© Copyright 2025

Matthew Michael James

Chitosan-Based Biomaterials for Renewal and Differentiation of Human Neural Stem Cells

Matthew Michael James

A dissertation

submitted in partial fulfillment of the

requirements for the degree of

Doctor of Philosophy

University of Washington

2025

Reading Committee:

Miqin Zhang, Chair

Jessica Young

Avik Som

Eleftheria Roumeli

Program Authorized to Offer Degree:

Materials Science and Engineering

University of Washington

Abstract

Chitosan Based Biomaterials for the Maintenance and Differentiation of Human Neural Stem Cells

Matthew Michael James

Chair of the Supervisory Committee:
Miqin Zhang
Materials Science and Engineering

Human neural stem cells (hNSCs) are critical for regenerative medicine and disease modeling due to their self-renewal and ability to differentiate into neurons, astrocytes, and oligodendrocytes. These traits make hNSCs ideal for repairing neural tissue and studying neurodegenerative disorders like Alzheimer's and Parkinson's, which are increasingly prevalent in aging populations and carry significant socioeconomic costs. Stem cell-based strategies offer transformative potential for therapeutic development and mechanistic studies. However, hNSC applications are hindered by current in vitro culture systems. Conventional 2D platforms, often using murine-derived extracellular matrix (ECM) coatings like Geltrex or Matrigel, fail to mimic the brain's 3D microenvironment. These materials are not chemically defined or xeno-free, posing regulatory and safety challenges for clinical translation. Cells grown on such substrates require extensive testing to meet current Good Manufacturing Practice (cGMP) standards, increasing costs and complexity. Moreover, 2D systems lack physiological relevance, contributing to the high failure rate of drug candidates in clinical trials.

This dissertation addresses these challenges through a systematic exploration of chitosan-based biomaterials as a versatile, next-generation platform for hNSC expansion, maintenance,

differentiation, and disease modeling. Chitosan, a biocompatible and biodegradable polysaccharide derived from chitin, closely mimics the glycosaminoglycans in the brain's ECM, offering a biomimetic substrate for neural cell culture. Its ability to be processed under mild conditions into various morphologies, such as films, scaffolds, or hydrogels, and chemically modified to tune mechanical and biological properties makes it an ideal candidate for advanced stem cell engineering applications.

The research began with the fabrication and characterization of composite thin films made from chitosan, alginate, and hyaluronic acid. These films were designed to optimize key parameters, including surface hydrophilicity, mechanical stiffness, nanoscale topography, and electrostatic interactions with hNSCs. By systematically varying polymer ratios, we found that pure chitosan films provided the most supportive environment for maintaining hNSC multipotency over a 4-day culture period, as evidenced by sustained expression of stemness markers (SOX2, nestin, Ki67, and SOX1) assessed via an alamarBlue assay, immunocytochemistry, and flow cytometry. These findings established pure chitosan as the foundational material for subsequent 3D scaffold development.

To address the limitations of 2D cultures and enable scalable production of functional stem cells, we designed 3D porous chitosan scaffolds optimized for dynamic culture conditions. Using an orbital shaker model to simulate perfusion and mechanical agitation, we demonstrated that these scaffolds maintained structural integrity under fluid shear stress while supporting hNSC viability and function. The porous architecture facilitated enhanced nutrient and oxygen diffusion, promoting physiologically relevant cell–cell and cell–matrix interactions. Compared to static 2D controls, these scaffolds significantly improved hNSC proliferation and multipotency, as measured by alamarBlue assay, live/dead staining, and SOX2, nestin, SOX1, and PAX6 staining. This

system supported long-term culture of hNSCs (over 21 days). Scaffolds with higher chitosan content (e.g., 4% w/v) exhibited superior mechanical resilience, making them well-suited for bioprocessing applications in large-scale cell manufacturing.

Recognizing the need for controlled, scalable stem cell production, we developed a custom, modular bioreactor system capable of supporting both macro- and microscale cultures. The bioreactor featured real-time, in-line monitoring of critical parameters, pH, dissolved oxygen, and CO_2, using integrated sensors connected to a microcontroller-based interface for precise environmental control. This system supported the culture of hNSCs for 7 days, as well as other cell types such as suspension-grown T cells and adherent tumor cell lines, demonstrating its broad applicability. The use of cost-effective, off-the-shelf components enhances the system's accessibility for academic research and its potential for adoption in translational settings, such as cGMP-compliant cell production facilities.

We then investigated chitosan scaffolds as a platform for directing hNSC differentiation into cortical neurons. Various surface modifications, including Geltrex coatings, medium conditioning with neurotropic factors (e.g., BDNF, GDNF), and pre-seeding techniques, were evaluated for their impact on lineage commitment. Pre-seeded scaffolds outperformed 2D controls, achieving higher neuronal yields and faster differentiation (within 14 days), with reduced astrocytic phenotypes, as confirmed by flow cytometry, immunocytochemistry, RT-qPCR analyses. These results highlight the scaffolds' ability to create a 3D microenvironment that closely mimics *in vivo* neural development.

To validate the platform's translational potential, we cultured human induced pluripotent stem cell (hiPSC)-derived neural progenitors from healthy donors and Alzheimer's disease (AD) patients on aligned porous chitosan scaffolds. These scaffolds supported the formation of

functional 3D neural networks, with AD-derived cultures exhibiting disease-specific hallmarks, including amyloid-beta peptide accumulation and dysregulated tau-related gene expression (e.g., MAPT, PSEN1). These phenotypes were quantified using ELISA and RNA sequencing, confirming the platform's utility as a scalable, physiologically relevant model for neurodegenerative disease research and preclinical drug screening.

In conclusion, chitosan-based biomaterials offer a chemically defined, xeno-free, and scalable solution to key challenges in hNSC culture, differentiation, and disease modeling. By meeting cGMP regulatory standards and enabling the transition from static cultures to dynamic bioreactor systems, these platforms support both research and therapeutic applications. This work advances the field of regenerative medicine and provides a robust, biomimetic tool for studying neurodegenerative disease mechanisms, paving the way to produce high-quality, clinically relevant neural cells.

Table of Contents

List of Figures 4
List of Tables 12
Acknowledgements 13

CHAPTER 1 INTRODUCTION AND RATIONALE 14

CHAPTER 2 BACKGROUND 19

2.1. Stem Cell Therapy and Disease Modeling 19
2.2. 2D Culture Limitations 20
2.3. Biomaterials for Stem Cell Culture 21
2.4. Chitosan: A Promising Culture Substrate 22
2.5. The Advantages of 3D Culture Modalities 24
2.6. Dynamic Culture Conditions and Bioreactors 25

CHAPTER 3 POLYSACCHARIDE THIN FILMS REGULATE THE CULTURE OF HUMAN NEURAL STEM CELLS 27

3.1 Introduction 27
3.2 Materials and Methods: 29
3.2.1 Preparation of CA, CHA, and CS films: *29*
3.2.2 Water Contact Angle *29*
3.2.3 SEM *30*
3.2.4 AFM *30*
3.2.5 FTIR *30*
3.2.6 Cell Culture *31*
3.2.7 Cell Morphology and Proliferation *31*
3.2.8 Flow Cytometry *32*
3.2.9 Immunocytochemistry *32*
3.2.10 Statistical Analysis *33*
3.3 Results and Discussion: 33
3.3.1 Hydrophilicity, topography, and mechanical strength: *33*
3.3.2 Cell behavior on CA/CHA/CS films: *39*
3.4 Supplemental Figures 52

CHAPTER 4 CHITOSAN SCAFFOLDS AS MICROCARRIERS FOR DYNAMIC CULTURE OF HUMAN NEURAL STEM CELLS 56

4.1 Introduction 56
4.2 Materials and Methods 60
4.2.1 Microcarrier fabrication *60*
4.2.2 FTIR and ^{1}H NMR Spectroscopy *60*
4.2.3 Microstructure characterization *61*
4.2.4 Mechanical properties *62*
4.2.5 Degradation test *62*
4.2.6 Cell culture *63*
4.2.7 Cell proliferation in a rotational bioreactor as a dynamic culture *63*
4.2.8 Flow Cytometry *64*
4.2.9 Immunocytochemistry for NSC marker proteins *65*
4.2.10 Statistical analysis *65*
4.3 Results and Discussion 65
4.3.1 Development of porous microcarriers for hNSC expansion in a defined environment condition *65*

4.3.2 Scaffold Microstructure Analysis *66*
4.3.3 Mechanical properties of the scaffolds *70*
4.3.4 Stability and degradation in culture medium *72*
4.3.5 Maintenance of hNSCs in dynamic cultures *74*

CHAPTER 5 CONTINUOUS FLOW BIOREACTOR WITH MULTI-SENSOR MONITORING FOR BIOMEDICAL APPLICATIONS 79

5.1 Introduction 79
5.2 Materials and Methods 81
5.2.1 Bioreactor and Its Components *81*
5.2.2 pH probe evaluation *82*
5.2.3 Oxygen Probe Evaluation *82*
5.2.4 CO2 Probe Evaluation *82*
5.2.5 RPM Probe Evaluation *83*
5.2.6 Scaffold fabrication *83*
5.2.7 Cell culture *84*
5.2.8 Cell metabolic activity and live/dead imaging *85*
5.2.9 Immunocytochemistry (ICC) and microscopy *85*
5.2.10 Flow cytometry analysis for NSC protein expression *86*
5.2.11 Statistical analysis *86*
5.3 Results and Discussion 86
5.3.1 Bioreactor Design and fabrication *86*
5.3.2 Process Monitoring and Control *90*
5.3.3 Evaluation of pH, oxygen, and CO2 probes *92*
5.3.4 Evaluation of RPM probe *96*
5.3.5 Evaluation of Tumor Model *98*
5.3.6 Design and Characterization of Micro-bioreactor *102*
5.3.7 Evaluation of a Nonadherent Cell Line for Both Bioreactors *105*
5.3.8 Evaluation of hNSC Model in the Microreactor *107*

CHAPTER 6 ENHANCED DIFFERENTIATION OF HUMAN NEURAL STEM CELLS INTO CORTICAL NEURONS USING 3D CHITOSAN SCAFFOLDS 109

6.1 Introduction 109
6.2 Materials and Methods 112
6.2.1 Preparation of CS scaffolds *112*
6.2.2 Physical Properties of CS Scaffolds *113*
6.2.3 SEM *113*
6.2.4 XPS *113*
6.2.5 hNSC Culture and cortical neuron differentiation *114*
6.2.6 Cell Metabolic Activity and Viability *115*
6.2.7 Flow Cytometry *115*
6.2.8 Immunocytochemistry *116*
6.2.9 PCR *117*
6.2.10 Statistical Analysis *117*
6.3 Results and Discussion 117
6.3.1 Scaffold coating procedure and cell culture protocol *117*
6.3.2 Physical characteristics of different coating conditions *119*
6.3.2 Cell viability and proliferation *124*
6.3.4 Cortical neuron differentiation from hNSCs *127*
6.3.5 mRNA expression in differentiated hNSCs *134*
6.4 Supplemental Information 137

CHAPTER 7 ALIGNED, POROUS SCAFFOLD AS A MORE EFFECTIVE MODELING CULTURE SUBSTRATE FOR ALZHEIMER'S DISEASE 145

7.1 INTRODUCTION 145
7.2 MATERIALS AND METHODS 149
7.2.1 Preparation of chitosan (CS) porous scaffolds 149
7.2.2 Microstructure characterized by scanning electron microscopy (SEM) 150
7.2.3 Physical Characterization of the Scaffolds 150
7.2.4 Cell Culture and hiPSC neuronal differentiation 151
7.2.5 Live/dead staining 152
7.2.6 Immunocytochemistry 152
7.2.7 Flow Cytometry 153
7.2.8 Functional Study 153
7.2.9 Quantification of gene expressions by real-time quantitative PCR (RT-qPCR) 153
7.2.10 Aβ 1–40 and 1–42 Analysis 154
7.2.11 Statistical analysis 155
7.3 RESULTS AND DISCUSSION 155
7.3.1 Scaffold Characterization 155
7.3.2 Adhesion and Morphology of hiPSCs 157
7.3.3 Maintenance of the Pluripotency of the hiPSCs 158
7.3.4 Adhesion and Morphology of hNPCs 164
7.3.5 hNPC Multipotency Maintenance and Differentiation Efficiency 166
7.3.6 hNPC Differentiation Efficiency 167
7.3.7 Functional Neuron Study 168
7.3.8 Amyloid Beta Analysis 173

REFERENCES 180

List of Figures

Figure 2.1 Outline highlighting the different ways hNSCs can be used to help treat or model neurodegenerative diseases. 20
Figure 2.2 A schematic showing the differences between a) 2D and b) 3D cell culture. 21
Figure 2.3 The chemical structures of a) alginate, b) hyaluronic acid, c) chitin, and d) chitosan.24
Figure 2.4 Illustration highlighting the important features of the scaffold. 25
Figure 2.5 Comparison of a) static and b) dynamic culture conditions.....26
Figure 3.1 Outline and physical characterization of the films. a) an illustration showing how the addition of chitosan aids in cell adhesion. Contact angle measurements taken by a goniometer for b) CA films ($n = 10$) and c) CHA films ($n = 10$) with varying ratios of 0:1, 1:3, 1:1, 3:1, and 1:0. AFM was used to measure the elastic moduli of d) CA films ($n > 239$) and e) CHA films ($n > 239$). Statistical significances of $p < 0.05$ and $p < 0.005$ are indicated by * and **, respectively. If no marks are present, there was no statistical significance between the samples. Illustrations of f) chitosan and alginate polyelectrolyte bond formation (red circle) and g) chitosan and hyaluronic acid polyelectrolyte bond formation (red circle). 36
Figure 3.2 Surface morphology and composition characterization of the films. (a) SEM images of the CA and CHA films with ratios of CS to alginate and CS to HA of 0:1, 1:3, 1:1, 3:1, and 1:0. Photographs of (b) CS:A and (c) CS:HA films immersed in PBS and taken after being prepared for cell culture. FTIR spectra of (d) CA and e) CHA films. Area under the highlighted peak in the FTIR spectra for f) CA and g) CHA films. 39
Figure 3.3 Cell morphology and live staining of hNSCs grown on CA films. Phase contrast and live (green) and dead (red) stained images showing the morphology of the cells grown on different films. The scale bar represents 50 μm. 40
Figure 3.4 Cell morphology and metabolic activity of hNSCs grown on CHA films. Phase contrast and live (green) and dead (red) stained images showing the morphology of cells grown on different films. The scale bar represents 50 μm. 42
Figure 3.5 Cell proliferation analysis on CS:A and CS:HA films. Graphs illustrating metabolic activity of hNSCS on (a) CS:A films and (b) CS:HA films with n=6. Percentage of live-stained area on (c) CS:A films and (d) CS:HA films with n=4. A p value of less than 0.05 was observed for all samples when compared to the 2D control at the same time point except for samples labeled with an *. 44
Figure 3.6 Flow cytometry analysis of cells cultured on CS:A and CS:HA Films. (a) Dot plots of SOX2 and Ki67 expression. (b) SOX1 positive populations. (c) Nestin positive populations. All samples have at least 5,500 cells analyzed. 46
Figure 3.7 Immunostaining analysis of cells cultured on CA films. Florescent images of (a) Geltrex control and films with CS:A ratios of (b) 0:1, (c) 1:3, (d) 1:1, (e) 3:1, and (f) 1:0. hNSC-H14 were stained for nestin (green), SOX2 (red) and nuclei (DAPI, blue). The scale bars are 50 μm. 48
Figure 3.8 Immunostaining analysis of hNSC-H14 cells cultured on CHA films. Florescent images of (a) Geltrex control and films with CS:HA ratios of (b) 0:1, (c) 1:3, (d) 1:1, (e) 3:1, and (f) 1:0. Cells were stained for nestin (green), SOX2 (red) and nuclei (DAPI, blue). The scale bars are 50 μm. 50
Supplemental Figure 3.9 Immunostaining analysis of cells cultured on CA films. Both the Ki67 and PAX6 appear to be expressed in the nucleus in the pure CS and Geltrex control. As more alginate is added, both Ki67 and PAX6 appear to be expressed more in the cytoplasm, indicating a loss of multipotency and proliferation capacity. Images showing a) Geltrex control, CA ratios of

(b) 0:1, (c) 1:3, (d) 1:1, (e) 3:1, and (f) 1:0. Fluorescent images of hNSC-H14 were stained for Ki67-green and PAX6-red. DAPI staining for nuclei are presented in blue. The scale bar is 50 µm. 52
Supplemental Figure 3.10 Immunostaining analysis of hNSC-H14 cells cultured on CHA films. PAX6 and Ki67 appear to remain mostly expressed in the nucleus in all of the CHA films conditions, with the exception of the pure HA film. This indicates that, other than the pure HA film, the CHA films are able to support cells in terms of Ki67 and PAX6 expression. Images showing a) Geltrex control, CS:HA ratios of (b) 0:1, (c) 1:3, (d) 1:1, (e) 3:1, and (f) 1:0. The cells were stained for nestin-green and SOX2-red. DAPI staining for nuclei are presented in blue. The scale bar is 50 µm. 54
Figure 4.1 Illustration depicting different culture methods in a dynamic bioreactor, including i) nonadherent suspension, ii) aggregate suspension, iii) nonporous microcarrier, and iv) porous microcarrier. 66
Figure 4.2 Spectroscopic analysis of scaffolds. The FTIR spectra acquired a) from chitosan, and b) collagen. c) ^{1}H NMR spectrum acquired from chitosan. 67
Figure 4.3 Microstructural analysis of porous scaffolds. (a) SEM images of dry porous scaffolds with a scale bar of 100 µm. (b) Pore diameters of the scaffolds measured from SEM images (n = 65). (c) Porosity through isopropanol displacement method (n = 5). (d) BET-specific surface area (n = 3). All data are presented as mean ± SD. Statistical significance, indicated by *, was determined using Tukey's test ($p < 0.05$). 70
Figure 4.4 Mechanical properties of the scaffolds. (a) Compressive modulus of the scaffolds in dry and wet conditions (n = 5). (b) Stress–strain curves of the scaffolds in a wet condition. The 05COL scaffold was too soft to be measured in a wet condition. (c) Elastic modulus of the scaffolds in a wet condition. (d) Degradation of the scaffolds in a dynamic condition. Degradation rate analysis was performed by comparing the initial weight of the dry scaffolds with the dried weight of the scaffolds after incubation. There are no significant changes in weight after 21 days of incubation (n = 4). The differences between the samples are considered significant when marked with * based on Tukey's test ($p < 0.05$).....73
Figure 4.5 Assessment of cell proliferation rates and cell fate in hNSC-H14 and ReNcell VM cell lines using alamarBlue and live/dead stain. a) Metabolic activity of hNSC-H14 measured by alamarBlue assay. b) Metabolic activity of ReNcell VM measured by alamarBlue assay. c) Fluorescent images of live (green) and dead (red cells stained with calcein-AM and ethidium homodimer-1, respectively. Scale bars represent 200 µm. An * means the difference between that sample and the respective 05COL sample is significant based on Tukey's test. 75
Figure 4.6 Flow cytometry analysis of cells collected from both cell lines over a 15-day period. Protein expression levels assessed for a) hNSC-H14 and b) ReNcell. c) Dot plots representing the expression of SOX1 and PAX6 in ReNcells on day 7. 77
Figure 4.7 Immunofluorescence staining of hNSCs for SOX2 (red), nestin (green), and DAPI (blue) on the 4CS scaffolds after 3 weeks for hNSC-H14 (top) and ReNcell VM (bottom). Scale bars are 200 µm. 78
Figure 5.1 a) schematic diagram of the dynamic bioreactor system. The bioreactor is connected to a nutrient reservoir and CO2 supply via a swivel connector, allowing for continuous nutrient and gas exchange. The system includes a water bath chamber for temperature control, a motor for agitation, and various valves, pumps, and sensors controlled by a computer through the system/stimuli control device. c) Exploded diagram of bioreactor chamber, housing, and swivel connector along with components that allow fluid flow to and from the chamber. Bioreactor system

illustrating components for operation for the c) macroreactor including 8) 12V DC motor with housing, 9) water bath chamber with heating element and bioreactor, 10) medium outlet, 11) medium inlet, 12) swivel connector housing, 13) peristaltic pump, 14) gas inlet, 15) gas outlet, 16) and main electronics system (Arduino Due, 12V DC power supply temperature controller, pH sensor, CO2 sensor, and oxygen sensor). Front panel close up of electronics housing with displays for 17) set RPM, 18) measured RPM, 19) temperature reading, 20) pH level, 21) measured CO2, 22) measured oxygen concentration, and 23) power switch with LED indicator. d) Image of bioreactor chamber and swivel connector assembly, with components labeled. 89
Figure 5.2 Python GUI front panel for displaying all BR functions. Functions of the Python GUI include a) Arduino COM selection interface; b) connection and error dialog box; c) RPM control; d) CO2 monitor; e) pH monitor; and f) oxygen monitor. 92
Figure 5.3 Data collected from the pH, oxygen, and CO2 probes. Data collected from the pH probe for a) standard solutions and b) used and fresh media. Data collected from the oxygen probe while the system is saturated with c) water and d) cell culture medium. Results from the CO2 e) longevity test and f) destabilization test. 96
Figure 5.4 RPM data collected from the BR system when the motor a) was directly connected to a DC power source for 1 hour, b) was connected to the Arduino and RPM was constantly monitored and adjusted for 1 hour, c) was directly connected to a DC power source for 21 hours, and d) had its RPM increased in increments of 10; arrows indicate where the RPM was changed, starting at 15 and ending at 65 RPM. 98
Figure 5.5 Sensor data collected from the macroreactor for a) pH, b) oxygen, c) CO_2, and d) RPM. 100
Figure 5.6 Fluorescent images of cells in 6CS scaffolds cultured statically and in the macroreactor. Cells were stained with Calcien AM (live, green) and propidium iodide (dead, red) for visualization on days 1, 3, 5, 7 and 10. The scale bar represents 250 μm. Viability data from the scaffolds cultured in static conditions and in the macroreactor for b) metabolic activity and c) percent area fluorescent. A p value of < 0.01 is indicated by an asterisk, and $n > 3$. 102
Figure 5.7 Bioreactor system illustrating components for operation for the a) microreactor including 1) 12V DC motor with housing, 2) water bath chamber with heating element and bioreactor, 3) medium outlet, 4) medium inlet, 5) swivel connector housing, 6) peristaltic pump, 7) gas inlet, 8) gas outlet, 9) and main electronics system (Arduino Due, 12V DC power supply temperature controller, pH sensor, CO2 sensor, and oxygen sensor). Front panel close up of electronics housing with displays for 10) set RPM, 11) measured RPM, 12) temperature reading, 13) pH level, 14) measured CO2, 15) measured oxygen concentration, and 16) power switch with LED indicator. b) Image of microreactor apparatus, with components labeled as 17) Individual culture reaction vessel, 18) 3D printed holder designed to hold 6 individual reaction chambers along with the central chamber, 19) connection to the central chamber, 20) tubing to connect the reaction vessel to the central chamber, 21) swivel connector, 22) housing for the swivel connector, and 23) tubing connection for CO_2. 103
Figure 5.8 Fluorescent images of cells in 6CS scaffolds cultured statically and in the microreactor. Cells were stained with Calcien AM (live, green) and propidium iodide (dead, red) for visualization on days 1, 3, 5, 7 and 10. The scale bar represents 250 μm. Viability data from the scaffolds cultured in static conditions and in the microreactor for b) metabolic activity and c) percent area fluorescent. A p value of < 0.01 is indicated by an asterisk, and $n > 3$. 105

Figure 5.9 Evaluation of the nonadherent cell line JURKAT in the macro- and microreactor. a) cell concentration and b) metabolic activity of JURKAT cells. A p value of < 0.01 is indicated by an asterisk, and n > 3. 106
Figure 5.10 Evaluation of hNSC-H14 grown on 6CS scaffolds in the microreactor. a) metabolic activity of the hNSCs grown in the microreactor. An * indicates a *p* value of less than 0.05 between the static and microreactor condition. b) protein expression results from hNSCs grown in the microreactor for 7 days. c) fluorescent images of live (green) and dead (red) stained cells. The scale bar indicates 250 μm. 108
Figure 6.1 Scaffold coating methods and experimental protocol for hNSC differentiation into cortical neurons. (a) Schematic representation of the various scaffold coating protocols for differentiating hNSCs into cortical neurons: medium-coated, Geltrex-coated, and pre-seeded scaffolds. (b) Diagram outlining the experimental protocol for hNSC culture and differentiation into cortical neurons. This includes cell seeding, cell interaction in 2D versus 3D environments, and the timeline for differentiation induction using BDNF, GDNF, and dBcAMP, followed by collection at 4 and 14 days. 119
Figure 6.2 Physical characterization of 6CS scaffolds across different coating conditions. (a) SEM image of a dry, 6CS scaffold showing its microstructure, with average pore sizes calculated from at least 50 pores. (b) Elastic compressive moduli of dry and wet 6CS scaffolds compared to typical brain ECM values (adapted with permission from*[276]) Copyright 2007 JSME. (c) Atomic composition data acquired from XPS for non-coated, Geltrex coated (GT), pre-seeded, and medium (Med) coated 6CS scaffolds for carbon, oxygen, and nitrogen. (d) Sulfur and phosphorous atomic composition data from XPS for the same scaffold conditions. A * indicates a *P*-value of less than 0.05, while unmarked values indicate no significant difference between samples. 122
Figure 6.3 Surface characterization of various scaffold coating conditions. SEM images of a) non-coated, b) medium-coated, c) Geltrex-coated, and d) pre-seeded scaffolds. The scale bar in the main images represents 10 μm and the scale bar in the inset images represents 1 μm. 123
Figure 6.4 Cell morphology, metabolic activity, and protein expression of non-differentiated hNSCs. Live (green) and dead (red) staining of cells at (a) 4X magnification and (b) 10X magnification. (c) Metabolic activity assessment using alamarBlue assay after 3 days of culture. (d) Quantification of fluorescence area percentage from scaffolds stained with CaAM and propidium iodide after 3 days of culture. Flow cytometry analysis showing (e) single positive populations of SOX2 and nestin and (f) the SOX2/nestin double positive populations. At least 2500 cells were collected from 3 separate scaffolds and analyzed for flow cytometry. Asterisks * indicate a *p*-value of less than 0.05, whereas absence of an asterisk denotes no statistical significance between samples. 126
Figure 6.5 Flow cytometry analysis of MAP2 and GFAP expression in hNSC-derived cortical neurons. hNSCs were differentiated on Geltrex coated 2D well plates (2D GT), medium treated 3D scaffolds (6CS Med), Geltrex coated 3D scaffolds (6CS GT), and pre-seeded 3D scaffolds (6CS Pre) for 7 and 14 days. (a) The single-positive population for MAP2B, highlighting the maturation of neurons (b) The single positive-population for GFAP, indicating astrocyte differentiation. (c) Dot plots showing the expression patterns of MAP2B and GFAP across the different conditions, demonstrating distinct neural lineage differentiation. (d) Histograms for MAP2B-postive populations, illustrating the increase in neuronal differentiation over time. At least 2500 cells were collected from 3 separate scaffolds and analyzed. 130

Figure 6.6 Flow cytometry analysis of TUBB3 and DCX in hNSC-derived cortical neurons. hNSCs were differentiated on different substrates for 7 or 14 days, including Geltrex coated 2D well plates (2D GT), medium treated 3D scaffolds (6CS Med), Geltrex coated 3D scaffolds (6CS GT), and pre-seeded 3D scaffolds (6CS Pre). The single-positive populations for (a) TUBB3 and (b) DCX. (c) Dot plots for TUBB3 and DCX. (d) Histograms for TUBB3-postive populations. At least 2500 cells were collected from 3 separate scaffolds and analyzed. 131
Figure 6.7 Immunostaining analysis of DAPI, TBR1, and MAP2 in -7-day differentiated hNSCs. Immunostaining images of hNSCs differentiated for 7 days, grown on different coating conditions: (a) Geltrex coated 2D well plates, (b) medium-treated 3D scaffolds, (c) Geltrex-coated 3D scaffolds, and (d) pre-seeded 3D scaffolds. TBR1 is presented as green, MAP2B as red, and DAPI, staining cell nuclei, is presented in blue. The scale bar is 50 μm.....133
Figure 6.8 Immunostaining analysis of DAPI, TBR1, and MAP2 in 14-day differentiated hNSCs. Immunostaining images of hNSCs differentiated for 14 days on various culture conditions: (a) Geltrex coated 2D well plates, (b) medium treated 3D scaffolds, (c) Geltrex coated 3D scaffolds, and (d) pre-seeded 3D scaffolds. Cells were stained with TBR1-green and MAP2B-red. DAPI, staining cell nuclei, is presented in blue. The scale bar is 50 μm.....134
Figure 6.9 Gene expression analysis of differentiation markers on day 7 and 14. Gene expression analysis of hNSC differentiation for 7 and 14 days, comparing cells grown on Geltrex coated 2D well plates (2DGT), Geltrex coated 3D scaffolds (3DGT), and pre-seeded 3D scaffolds (3DPre). Results for day 7 are shown as a bar chart in (a) and a heat map in (b). Corresponding data for day 14 are presented a bar chart in (c) and a heat map (d). An * indicates a *p* value lower than 0.05 when compared to the 2D sample at the same time point. 136
Supplemental Figure S6.10 Raw XPS spectra data for a) naked scaffolds survey scan, b) naked scaffolds sulfur scan, c) naked scaffolds phosphorous scan, d) medium-treated scaffolds survey scan, e) medium treated scaffolds sulfur scan, f) medium treated scaffolds phosphorous scan, g) Geltrex scaffolds survey scan, h) Geltrex scaffolds sulfur scan, i) Geltrex scaffolds phosphorous scan, j) pre-seeded scaffolds survey scan, k) pre-seeded scaffolds sulfur scan, and l) pre-seeded scaffolds phosphorous scan. The raw XPS scans show clear peaks for oxygen, nitrogen and carbon. The survey scans show clear peaks for sulfur and phosphorous for scaffolds that had a coating applied to them. 138
Supplemental Figure S6.11 Flow cytometry analysis of multipotency markers for 2D control (2D GT), medium treated 3D (6CS Med), Geltrex coated 3D (6CS GT), and pre-seeded 3D (6CS Pre). a) representative dot plots for SOX2 and nestin expression and b) histograms for SOX2 and nestin. The dot plot representation shows many cells are able expressing both SOX2 and nestin, indicating that both the 2D control and the scaffolds can support a healthy and multipotent cell population, with all conditions showing over 90% double expression. The histograms show the single positive populations for both SOX2 and nestin. Both the dot plots and histograms indicate that many of the cells are coexpressing both multipotency markers. At least 2500 cells were collected from 3 separate scaffolds and analyzed.....139
Supplemental Figure S6.12 Flow cytometry analysis taken from 2D well plates coated with Geltrex (GT 2D), medium treated 3D (6CS Med), Geltrex coated 3D (6CS GT), and pre-seeded 3D (6CS Pre), grown for 7 or 14 days. a) viable cell population after gating for dead cells and b) positive populations for SOX2. Viability of the cells shows that there are more viable cells in the scaffolds than there are in 2D across both time points, with there being the highest percentage in the pre-seeded scaffolds. Both the 2D control and the medium treated scaffolds saw a decrease in viability between day 7 and day 14, while the Geltrex coated and pre-seeded saw an increase in viability.

The 2D control saw an increase in SOX2 (a multipotency marker) expression over the 14-day period, and the 2D control had the greatest overall expression of SOX2. The Geltrex coated scaffolds saw an increase in SOX2 while both the medium treated and pre-seeded scaffold saw decreases over the 14-day period. At least 2500 cells were collected from 3 separate scaffolds and analyzed. 140
Supplemental Figure S6.13 Fluorescence images of hNSC-H14 cells cultured for 4 days and differentiated for 7-days using immunocytochemistry staining for CTIP2-green and MAP2B-red. DAPI staining for nuclei are presented in blue. a) Geltrex coated 2D well plates, b) medium treated 3D scaffolds, c) Geltrex coated 3D scaffolds, and d) pre-seeded 3D scaffolds. Cells grown in 2D showed CTIP2 stained appearing in the nucleus and MAP2B staining appearing in the dendrites, while also showing interactions between cells. In the 6CS medium treated scaffold, not CTIP2 staining can be seen. While the MAP2B does appear weakly in the dendrite, there is no connection to adjacent cells. In the Geltrex-coated scaffold, there appears to be a very weak CTIP2 expression, while there is a strong MAP2B expression in the dendrite that appears to be adherent to the scaffold wall. In the pre-seeded scaffold, the CTIP2 is expressed in the nucleus of the cells, while the MAP2B is expressed in the dendrites. The dendrite can be seen extending out to form connections with nearby cells. The scale bar is 50 μm. 141
Supplemental Figure S6.14 Immunostaining analysis for hNSCs differentiated on a) Geltrex coated 2D well plates, b) medium treated 3D scaffolds, c) Geltrex coated 3D scaffolds, and d) pre-seeded 3D scaffolds for 14 days. CTIP2-green and MAP2B-red. DAPI staining for nuclei are presented in blue. Cells were cultured on Matrigel coated plates, Geltrex coated scaffolds, and plain scaffolds. The scale bar is 50 μm. In the 2D control sample, CTIP2 and MAP2B stained cells can be seen, with CTIP2 appearing in the nucleus and MAP2B appearing in the dendrites and nucleus. The medium treated 6CS scaffold has poor staining, with CTIP2 not showing up and MAP2B being barely visible, indicating poor cell quality. The Geltrex coated scaffold shows weak CTIP2 staining, but the MAP2B staining appears strongly in the dendrites. The pre-seeded scaffold shows CTIP2 and MAP2B staining in the cells, and the dendrites can be seen extending out to the scaffold walls. 142
Supplemental Figure S6.15 Immunostaining analysis for hNSCs differentiated on a) Geltrex coated 2D well plates on day 7, b) Geltrex coated 2D well plates on day 14, c) pre-seeded 3D scaffolds for 7 days, and d) pre-seeded 3D scaffolds for 14 days. GFAP-green and MAP2B-red. DAPI staining for nuclei are presented in blue. Cells were cultured on Matrigel coated plates, Geltrex coated scaffolds, and plain scaffolds. The scale bar is 50 μm. In the 2D control samples, relatively high expression of GFAP stained cells can be seen, while in the pre-seeded 3D sample there is little to no staining of GFAP. This indicates the scaffolds produce a larger percentage of neurons and a low number of astrocytes compared to the 2D controls. 143
Supplemental Figure S6.16 Gene expression analysis of 7 and 14 day differentiated hNSCs grown on Geltrex coated 2D well plates (2DGT), Geltrex coated 3D scaffolds (3DGT), and pre-seeded 3D scaffolds (3DPre). a) bar chart and b) heat map and on day 14 as a c) bar chart and d) heat map. An * indicates a *p* value lower than 0.05 when compared to the 2D sample at the same time point. Between day 7 and 14, the multipotency markers SOX1, SOX2, PAX6, and nestin all increased for the 2D control group, while they decreased for the Geltrex coated and pre-seeded scaffolds. This indicates that the cells are becoming less multipotent and moving towards their differentiated state faster in 3D than they are in 2D. 144
Figure 7.1 Surface and physical characterization of the scaffolds. SEM images of the a) regular scaffold and SEM images of noncoated and Geltrex-coated scaffolds. The microstructure exhibits

overall isotropic interconnect pores. Geltrex coating left a net-like fibrous residue on the surface of the pores. Scale bars represent 100 μm. b) A columnar scaffold and SEM images from top and side, showing the vertical columnar microstructure. Scale bars represent 500 μm. e) The elastic compressive moduli of the nonaligned and aligned scaffolds, f) the alignment of the nonaligned and aligned scaffolds, and g) the pore size of the nonaligned and aligned scaffolds. An * indicates a p less than 0.05. An n value greater than 3 was used for both tests. 156
Figure 7.2 hiPSC adhesion and morphology evaluated via live (Calcien AM, green) and dead (propidium iodide, red) staining. CViA2, IID4, E9, and Swe22 cell lines were grown on nonaligned Geltrex coated scaffolds (Nonaligned GT), nonaligned conditioned medium treated scaffolds (Nonaligned CM), aligned Geltrex coated scaffolds (Aligned GT), and aligned conditioned medium treated scaffolds (Aligned CM). The scale bars indicate 250 μm. 158
Figure 7.3 Pluripotency expression from cells grown in the 3D scaffolds depicted as percent positive populations for a) SSEA4 expression, b) SOX2 expression, c) OCT4 expression, and d) Tra 1-60 expression. More than 3400 cells were analyzed in each condition, collected from 6 separate wells.....160
Figure 7.4 Fluorescence images of hiPSC-CViA2 cells cultured for 4 days using immunocytochemistry staining for TRA-1-60R-green and SOX2-red. DAPI staining for nuclei are presented in blue. The scale bar is 50 μm. 161
Figure 7.5 Fluorescence images of hiPSC-IID4 cells cultured for 4 days using immunocytochemistry staining for TRA-1-60R-green and SOX2-red. DAPI staining for nuclei are presented in blue. The scale bar is 50 μm. 162
Figure 7.6 Fluorescence images of hiPSC-E9 cells cultured for 4 days using immunocytochemistry staining for TRA-1-60R-green and SOX2-red. DAPI staining for nuclei are presented in blue. The scale bar is 50 μm. 163
Figure 7.7 Fluorescence images of hiPSC-Swe22 cells cultured for 4 days using immunocytochemistry staining for TRA-1-60R-green and SOX2-red. DAPI staining for nuclei are presented in blue. The scale bar is 50 μm. 164
Figure 7.8 hNPC adhesion and morphology evaluated via live (Calcien AM, green) and dead (propidium iodide, red) staining. CViA2, IID4, E9, and Swe22 cell lines were grown on nonaligned Geltrex coated scaffolds (Nonaligned GT), nonaligned conditioned medium treated scaffolds (Nonaligned CM), aligned Geltrex coated scaffolds (Aligned GT), and aligned conditioned medium treated scaffolds (Aligned CM). The scale bars indicate 250 μm. 165
Figure 7.9 Multipotency expression from cells grown in the 3D scaffolds depicted as fold changes compared to the 2D controls. a) SOX2 expression, b) Ki67 expression, c) nestin expression, and d) SOX1 expression. More than 2000 cells were analyzed in each condition, collected from 6 separate wells.....167
Figure 7.10 Differentiation efficiency of the cells grown in the scaffolds depicted a) percent positive population and b) fold change. More than 5400 cells were analyzed in each condition, collected from 6 separate wells. 168
Figure 7.11 Calcium imaging using Fluo4-AM in CViA2 cells cultured in different scaffold conditions. Graphs show intracellular uptake of calcium as $\Delta F/F_0$ with representative images below each graph showing calcium uptake and cell morphology. CViA2 cells grown on a) nonaligned Geltrex coated scaffolds, b) nonaligned conditioned medium treated scaffolds, c) aligned Geltrex coated scaffolds, and d) aligned conditioned medium treated scaffolds. 170
Figure 7.12 Calcium imaging using Fluo4-AM in Swe22 cells cultured in different scaffold conditions. Graphs show intracellular uptake of calcium as $\Delta F/F_0$ with representative images below

each graph showing calcium uptake and cell morphology. Swe22 cells grown on a) nonaligned Geltrex coated scaffolds, b) nonaligned conditioned medium treated scaffolds, c) aligned Geltrex coated scaffolds, and d) aligned conditioned medium treated scaffolds. 171
Figure 7.13 Calcium imaging using Fluo4-AM in a) CViA2 and b) Swe22 cells cultured in 2D conditions. Graphs show intracellular uptake of calcium as $\Delta F/F_0$ with representative images below each graph showing calcium uptake and cell morphology. 172
Figure 7.14 The mRNA expression normalized to the 2D cultured cell type for each cell type. The results are presented as fold changes as described previously. [350] The 2D differentiated cells were set as 1-fold for each cell type. 173
Figure 7.15 Quantification of Aβ 1-42 and Aβ 1-40 shown as the a) Aβ 1-42 to Aβ 1-40 ratio and b) Aβ 1-42 to Aβ 1-40 ratio fold change compared to the 2D control sample for each cell line. An * indicates a *p* value of less than 0.05. 174

List of Tables

Table 2.1 Summarization of important properties of alginate, HA, collagen, and chitosan. 22
Supplemental Table S6.1 The sequences of primers used in qPCR analysis. 137
Table 7.1 The sequences of primers used in qPCR analysis. 154

Acknowledgements

I have been incredibly fortunate to have been able to attend the University of Washington for my entire academic career. During my time pursuing a doctoral degree, I have grown tremendously as a researcher, teacher, student, team member, and person. This growth would not have been possible without the many wonderful individuals I have been fortunate enough to meet and work with during my time at the University of Washington. Among those individuals, Professor Miqin Zhang has had the most profound impact on me. Her guidance, leadership, and unwavering passion for the research our lab performs have been instrumental to my growth and enjoyment of my time learning under her tutelage. I would also like to thank my committee members Professor Jessica Young, Professor Avik Som, and Professor Eleftheria Roumeli for taking time out of their busy schedules to provide their support.

The research presented in this thesis (and many projects not able to fit in this thesis) would not have been possible without the help of many of my wonderful colleagues in the Zhang lab and collaborators who have been instrumental in making my time here enjoyable, especially Dr. Richard Revia, Dr. Fei-Chien Chang, Yang Zhou, Dr. Guanyou Lin, Dr. Dennis Edmondson, Dr. Dave Wood, Jianxi Huang, Dr. Xiaojie Lin, Dr. Ali Sadeghi, Dr. Yuanzhang Tang, Dr. Zachary Stephen, Jason Samson, Ty Spink, Jacob Belietzl, Picea Liu, and Baylie Philips.

Finally, I would like to thank my family for supporting and encouraging me during the pursuit of my degree. Thank you to my parents, Michael James and Jennifer James, and my brother, Joshua James, for their support during my entire academic career. A special thanks to my wife, Morgan James, for her unending love and support during this endeavor, I truly would not have been able to accomplish this without you.

Chapter 1 Introduction and Rationale

Neurodegenerative diseases, including Alzheimer's, Parkinson's, Huntington's, and multiple sclerosis, affect over 50 million people globally and are projected to rise sharply with aging populations, particularly in developed nations. Alzheimer's disease alone impacts nearly 8 million individuals in the United States, contributing to substantial healthcare costs and caregiver burdens. [1] Despite extensive research and numerous clinical trials targeting pharmacological interventions, no therapies currently halt or reverse disease progression, with most candidates showing limited long-term efficacy.[2] This persistent gap underscores the urgent need for innovative therapeutic strategies and advanced *in vitro* disease models to better understand pathological mechanisms and improve drug development outcomes.

Human neural stem cells (hNSCs) are a transformative tool for regenerative medicine and disease modeling due to their unique capacity for self-renewal and differentiation into neurons, astrocytes, and oligodendrocytes.[3,4] These properties enable hNSCs to replace damaged neural tissue in conditions like traumatic brain injury or neurodegenerative disorders and to create patient-specific models for studying disease mechanisms at the cellular and molecular levels.[3,4] Realizing hNSCs' full potential, however, requires scalable, safe, and physiologically relevant culture systems that support both research and clinical translation.

Current hNSC culture relies on 2D petri dishes coated with murine-derived extracellular matrix (ECM) proteins, such as Geltrex or Matrigel. While suitable for basic studies, these matrices are neither chemically defined nor xeno-free, posing significant regulatory hurdles for clinical applications and compromising experimental reproducibility due to batch-to-batch variability.[5-7] Human-derived ECMs, like vitronectin, address some regulatory concerns but are prohibitively

expensive and challenging to scale for large-scale production. Additionally, 2D systems fail to replicate the brain's 3D microenvironment, lacking critical mechanical cues, nutrient gradients, and complex cell–cell interactions essential for accurate disease modeling. [5-7]

This dissertation investigates chitosan, a biocompatible polysaccharide derived from chitin, as a modular platform for hNSC culture. Chitosan's structural similarity to brain ECM glycosaminoglycans, combined with its chemical tunability, antimicrobial properties, biodegradability, and cost-effectiveness, makes it an ideal candidate for biomedical applications. Its versatility allows processing into diverse formats, such as thin films, porous scaffolds, or microcarriers, enabling both static and dynamic culture systems suitable for research and therapeutic manufacturing.

The overarching research objectives of this dissertation are fourfold:

(1) to evaluate chitosan-based thin films for the maintenance of human neural stem cells (hNSCs) under chemically defined, xeno-free two-dimensional (2D) culture conditions;

(2) to engineer and optimize three-dimensional (3D) chitosan scaffolds capable of supporting dynamic culture environments for scalable hNSC expansion that recapitulates key features of the native extracellular matrix;

(3) to validate these scaffolds as effective platforms for the differentiation of hNSCs into cortical neurons and for modeling neurodegenerative disease using human induced pluripotent stem cell (hiPSC)-derived neural progenitors; and

(4) to develop a modular bioreactor system equipped with real-time monitoring of critical culture parameters, including pH, oxygen, and carbon dioxide, to support diverse cell types across macro- and microscale formats.

Collectively, these aims establish a flexible, chemically defined, and translationally relevant platform to advance stem cell-based therapies and create physiologically meaningful models for neurodegenerative disease research and drug development.

This dissertation is structured as follows:

Chapter 1 introduces the rationale, scope, and significance of the study, including the limitations of current hNSC culture systems and the need for scalable, xeno-free biomaterials.

Chapter 2 provides a comprehensive review of neurodegenerative diseases, challenges in stem cell-based therapies, and the design criteria for chitosan-based biomaterials. The chapter also discusses bioreactor integration for dynamic hNSC culture via medium perfusion and its effects on cell viability and performance.

Chapter 3 investigates the utility of chitosan, alginate, and hyaluronic acid thin films for supporting hNSC maintenance. Films with varying polymer compositions were characterized for mechanical and surface properties, followed by a 4-day hNSC culture study. Among all formulations, pure chitosan films most effectively maintained hNSC multipotency, as evidenced by cell morphology, proliferation, and sustained expression of key stemness markers (SOX2, nestin, Ki67, and SOX1) confirmed by immunocytochemistry and flow cytometry.

Chapter 4 presents a dynamic 3D culture model using porous chitosan scaffolds placed on an orbital shaker to enhance nutrient perfusion. Scaffolds fabricated at varying chitosan concentrations were evaluated for mechanical stability and biological performance. High-weight percent (4% w/v) scaffolds demonstrated superior mechanical integrity and better supported hNSC expansion, maintaining multipotency markers, and favorable morphology. Additionally, the high weight percent scaffolds were able to support the hNSCs for 3 weeks.

Chapter 5 describes the development and testing of a custom modular bioreactor system incorporating sensors for continuous, real-time monitoring of pH, dissolved oxygen, and carbon dioxide. The bioreactor supported both macro- and microscale formats and successfully cultured hNSCs, T cells, and cancer cells. Cell performance was evaluated by proliferation, morphology, and protein expression, demonstrating the system's versatility and utility for diverse biomedical applications.

Chapter 6 explores the differentiation of hNSCs into cortical neurons using chitosan scaffolds pre-treated with extracellular matrix coatings and supplemented with differentiation-inducing growth factors. Surface modifications were characterized using scanning electron microscopy (SEM) and X-ray photoelectron spectroscopy (XPS). Over a 2-week culture period, pre-seeded scaffolds promoted more efficient neuronal differentiation compared to 2D controls and reduced astrocyte generation, as shown by flow cytometry, qPCR, and immunocytochemistry analysis.

Chapter 7 focuses on Alzheimer's disease modeling using aligned porous chitosan scaffolds seeded with hiPSC-derived neural progenitors from both healthy individuals and

AD patients. These scaffolds supported neuronal differentiation and enabled disease-relevant phenotypes, including amyloid-beta accumulation and dysregulation of tau-related genes (MAPT, PSEN1). Validation was performed using ELISA and RNA sequencing, supporting the platform's potential for preclinical disease modeling and drug screening.

Chapter 8 synthesizes the findings across all experimental chapters, elucidating the key conclusions and implications for advancing hNSC-based regenerative therapies and high-fidelity in vitro models for neurodegenerative disease.

Chapter 2 Background

2.1. Stem Cell Therapy and Disease Modeling

Human neural stem cells (hNSCs) have become the focus of a plethora of research is the last 20 years due to their multifunctional use in the care of diseases.[8-10] Two of the most prominent uses are stem cell therapy and disease modeling. For stem cell therapy, large amounts of stem cells are required, and for use in patients, the cells must be harvested from cGMP compliant culture conditions.[3,11] If these conditions, chemical defined and xeno-free, are not met, additional characterizations of the hNSCs must be performed to ensure they are safe for use in humans.[12,13] The typical culture model uses uncoated petri dishes to ensure cGMP conditions are met. However, this causes the cells to form spheroids, and without any 3D structures present in the dish, these spheroids can grow to large and develop necrotic cores, causing cell death or differentiation.[14] Disease modeling is often used to determine how a disease progresses through the differentiation cycle of the affected cell and for drug discovery.[8,12,15] A multitude of drugs have been brought to clinical trials, and few have been approved for use in treating Alzheimer's disease.[16] However, none of these drugs have been shown to completely halt the disease progression, despite promising results *in vitro*. [17] This means that the current culture modality cannot effectively model the disease. **Figure 2.1** outlines the pathways for hNSC treatments and modeling for neurodegenerative diseases.

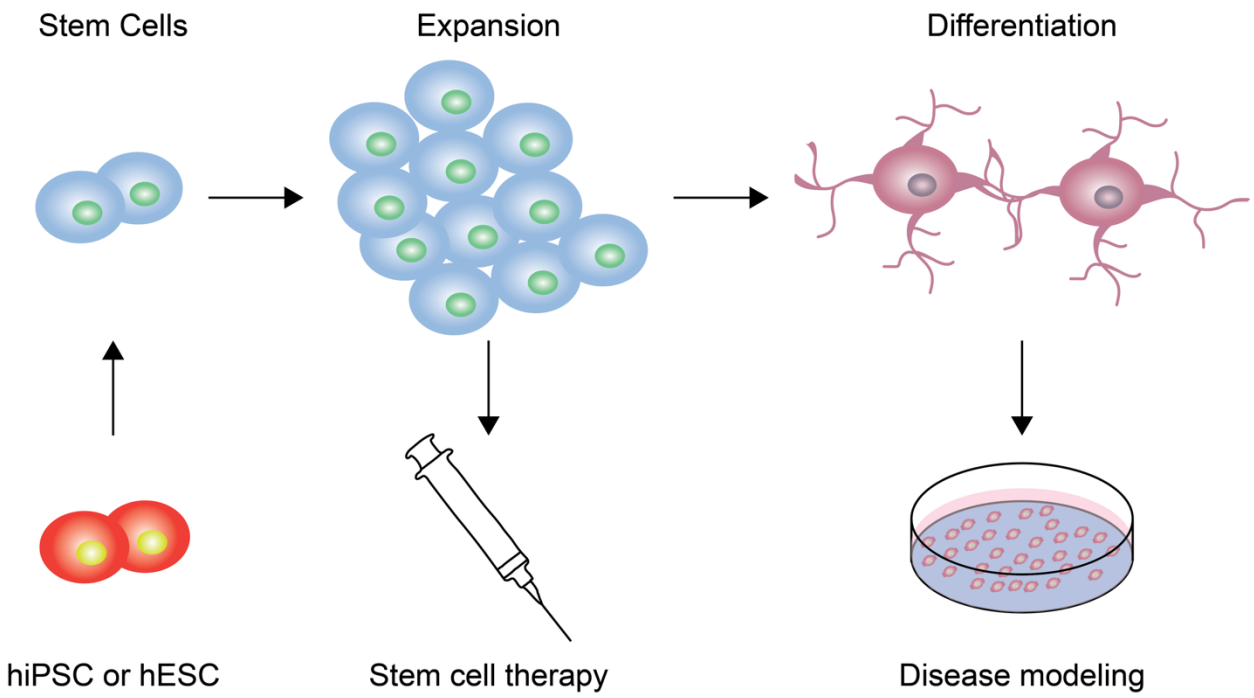


Figure 2.1 Outline highlighting the different ways hNSCs can be used to help treat or model neurodegenerative diseases.

2.2. 2D Culture Limitations

The gold standard for basic hNSC culture typically uses Geltrex or Matrigel coated petri dishes. Both protein cocktails are murine derived, meaning they are neither xeno-free nor chemically defined. Human derived protein cocktails, such as vitronectin, are xeno-free, but are expensive to scale up to meet the needs of clinical trials. Additionally, 2D cultures fail to replicate *in vivo* conditions such as failing to provide cells with sufficient cell-to-cell interaction, allow nutrients to reach the cell from all sides, and provide a surface with mechanical properties similar to those found *in vivo*. [5-7] 3D culture modalities, such as scaffolds, are able to better replicate *in vivo* culture conditions by allowing the cells to grow in 3 dimensions which gives them more realistic cell-to-cell interactions, allows nutrients to reach the cell from all directions, and gives the cells surfaces that are more mechanically similar to those found *in vivo*. **Figure 2.2a** and **2.2b** shows the differences between 2D and 3D culture, respectively.

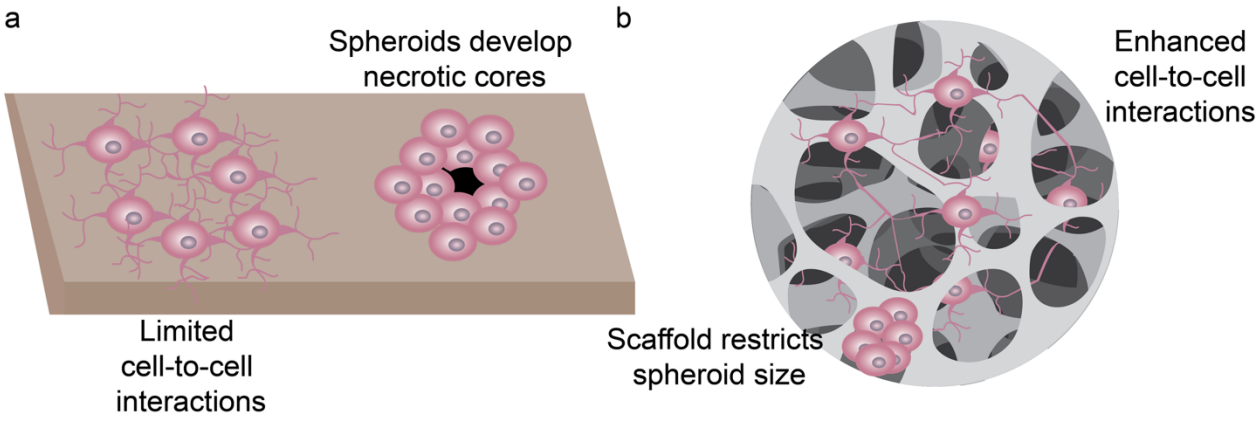


Figure 2.2 A schematic showing the differences between a) 2D and b) 3D cell culture.

2.3. Biomaterials for Stem Cell Culture

The culture modality needs a high degree of biocompatibility, mechanical properties similar to those found in the native brain ECM, and relevant surface chemistry to encourage cell attachment, thus material selection is important. A wide array of polymers exist that can meet these criteria, including alginate, hyaluronic acid, collagen, and chitosan. Alginate is an important polymer that is frequently incorporated into chitosan-based materials to improve their mechanical properties.[18,19] Alginate is a natural polysaccharide extracted from algae and is composed of linear chain structures of 1-4 linked mannuronic acid and l-guluronic acid. It is a hydrophilic, anionic copolymer and has a chemical structure similar to that of hyaluronic acid. Hyaluronic acid (HA) is one of the primary glycosaminoglycans found in the brain.[20] HA is also a common additive used to improve the microenvironment of chitosan based materials by promoting different receptors, such as CD44, TLR4, and RHAMM, that aid with cell attachment.[21,22] HA can also enhance the mechanical and physical properties of chitosan-based materials.[21] Collagen is one of the main ECM proteins found throughout the body, and has a prolific history as a biomaterial. Collagen is typically a cationic polymer at physiological pH, meaning its surface is positively charged, but does not have a structure similar to that of HA. Chitosan is a positively charged polysaccharide

with a chemical structure like that of HA. **Table 2.1** summarizes the differences in chemical structures and important properties of alginate, HA, collagen, and chitosan.

Table 2.1 Summarization of important properties of alginate, HA, collagen, and chitosan.

Biomaterial	Source	Charge	Biocompatibility	Mechanical Strength	Structure
Alginate	Seaweed or bacteria	Negative [23]	Fair [24]	Strong [25]	Polysaccharide
Hyaluronic Acid	Animal or human	Negative [26]	Good [27]	Strong [28]	Glycosaminoglycan [27]
Collagen	Animal or human	Negative [29]	Excellent [30]	Fair [29]	Fibrous protein
Chitosan	Crustacean or insect	Positive [29]	Good [31]	Fair [32]	Polysaccharide

2.4. Chitosan: A Promising Culture Substrate

CS is a deacetylated derivative of chitin, the primary structural polymer in insects and crustaceans. Its widespread availability and simple manufacturing process make it comparatively economical as a culture substrate when compared to other alternatives. CS is a linear polysaccharide with polycationic properties, rendering it biocompatible, non-antigenic, non-toxic, and biofunctional.[33-35] Additionally, It has excellent hemostatic, antiviral, and antibacterial properties,[36,37] making it suitable for applications such as wound dressings and drug delivery systems.[38,39] CS's positive charge and hydrophilic nature make it conducive for cell attachment,[40] further enhancing its suitability as a culture substrate. Its chemical structure closely resembles that of glycosaminoglycans (GAGs),[41] a major component of extracellular matrices found throughout the mammalian body.[42,43] This structural similarity to a prevalent bodily material adds to CS's appeal in various applications. CS has been extensively explored in biomaterials-related research,

particularly in the fabrication of thin films and microbeads for evaluating the effectiveness of various adhesion factors in hippocampal neuron cultures. Studies have demonstrated that CS supports rat hippocampal neurons effectively whether in the form of a film or microbead, regardless of the presence of adhesion factors.[44] Moreover, CS has been used as a copolymer to fabricate hydrogels for the cultivation and differentiation of human neural progenitor cells (hNPCs) and hNSCs.[45] These studies have highlighted the ability of CS films to maintain the multipotency of hNSCs, although some differentiation markers were observed after 2 weeks of culture. Additionally, hNPCs cultured on CS scaffolds were able to differentiate into both glial and neural lineages. Patterned CS thin films have also been used to investigate the differentiation and morphology of embryonic neuronal and glial cells derived from mice. The results indicate that CS promotes glial cell maturation and aids in aligning axonal growth.[46] The versatility of CS in such applications can be attributed to its advantageous properties such as its biocompatibility and ease of machinability. **Figure 2.3a, b, c,** and **d** show the differences in the chemical structure of alginate, hyaluronic acid, chitin, and chitosan, respectively.

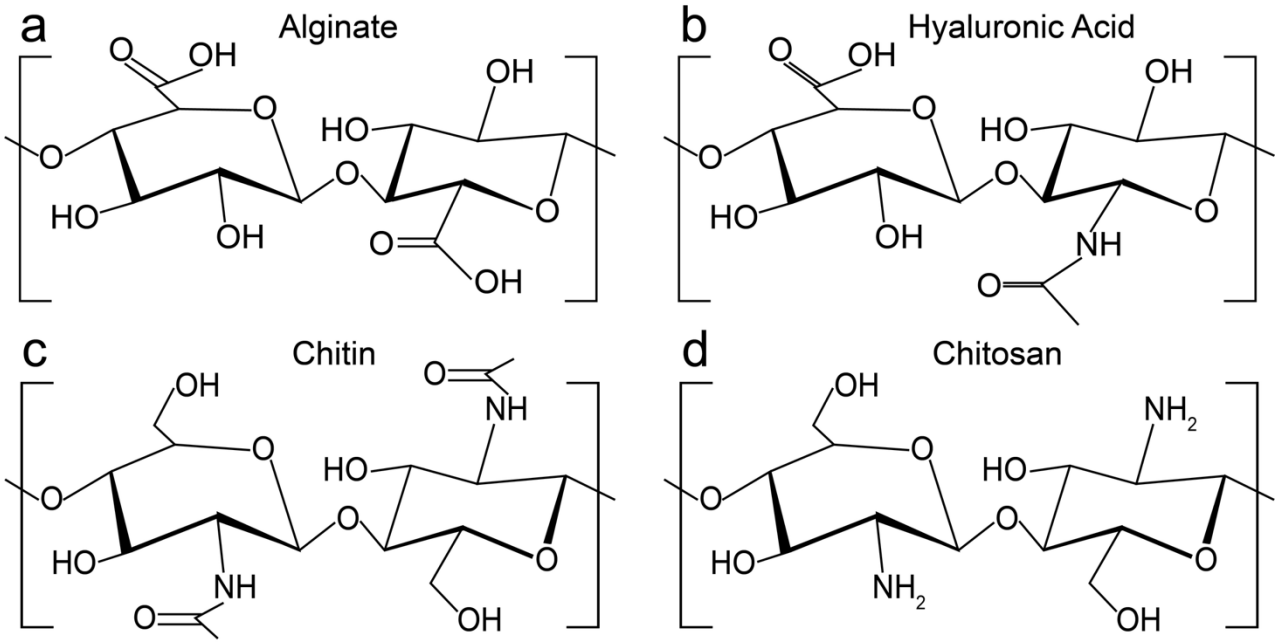


Figure 2.3 The chemical structures of a) alginate, b) hyaluronic acid, c) chitin, and d) chitosan.

2.5. The Advantages of 3D Culture Modalities

2D culture conditions, such as those found in the Geltrex or Matrigel coated petri dishes, fail to recapitulate *in vivo* conditions, such as cell-to-cell interactions in all 3 directions, and cell exposure to media and other growth factors from all directions.[5-7] 2D cell culture conditions do however provide an easy way to monitor cell morphology. 3D scaffolds can better model *in vivo* conditions by giving the cells a 3D matrix that they are able to grow in or adhere to.[47] If the cells are nonadherent or weakly adherent to the scaffolds, they may grow as spheroids, in which case the pose size of the scaffold becomes important. The pores of the scaffolds can physically restrict the spheroids from becoming too large, thus preventing the spheroids from becoming too large and avoiding necrotic cores. The scaffolds proved more cell-to-cell interactions by allowing the cells to grow in 3 dimensions instead of 2.[48,49] The scaffold can also be designed such that the mechanical properties and surface chemistry are more like native brain ECM, enhancing the cell interactions with the scaffold. The 3D scaffold also allows the cells to access nutrients from all

directions. However, media can have difficulty perfusing through the scaffolds and supplying fresh nutrients to all the cells.[50,51] **Figure 2.4** shows the different features of the scaffold.

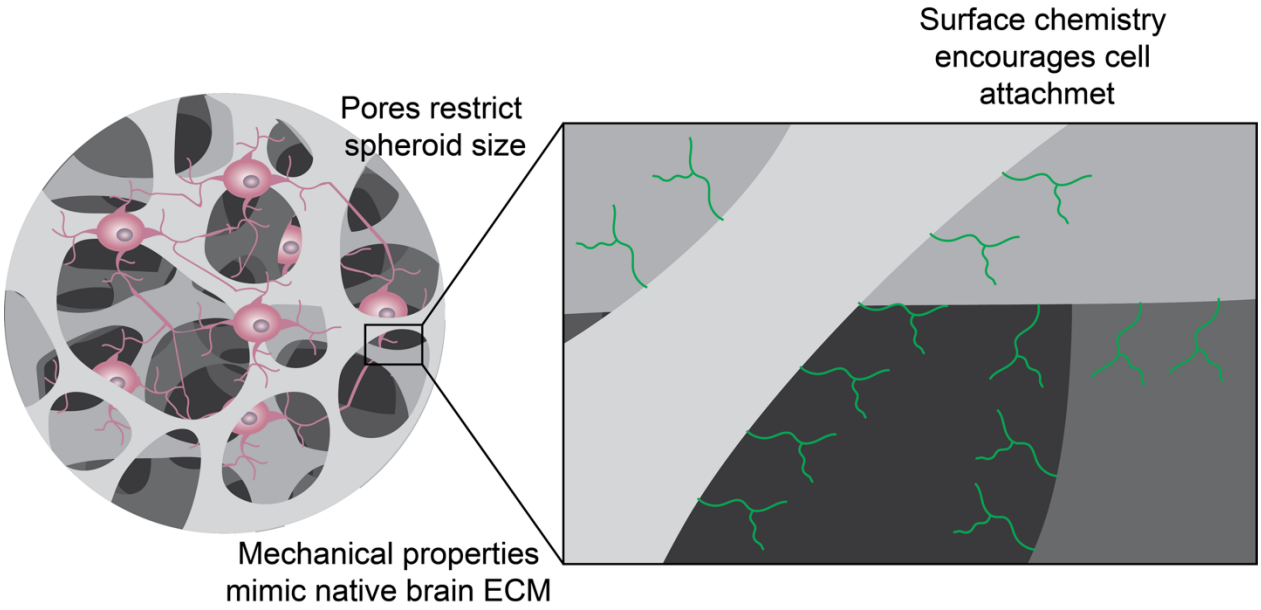


Figure 2.4 Illustration highlighting the important features of the scaffold.

2.6. Dynamic Culture Conditions and Bioreactors

Bioreactors can provide light stimulation to the cell culture conditions and can aid in perfusing the medium through the scaffold.[50,51] This constant perfusion of medium through the scaffold can prevent cell necrosis due to a lack of nutrients penetrating the scaffold. There are a multitude of different types of bioreactors, including rotating wall, shakers, and impeller drive bioreactors to name a few. Impeller driven bioreactors use an impeller to agitate the medium, but the mechanical impacts from the impeller can negatively impact cell fate.[52-54] Cell media culture condition are also important to monitor, and inline sensors can be used to for real time monitoring conditions such as pH, dissolved oxygen, and CO_2, to identify any drastic changes or trends. Orbital shakers provide a soft swirling motion to the media, which can enhance the homogeneity of the media, but the swirling motion can cause cells to aggregate at the center of the well if they

are nonadherent or weakly adherent. A rotating wall bioreactor provides soft agitation to the media and causes the cells or scaffolds to be constantly falling through the media, which acts as a sort of microgravity on the cells. [55,56] This additional mechanical stress on the cells can impact their proliferation and differentiation outcomes. **Figure 2.5a** and **2.5b** compares the differences between static and dynamic cultures, respectively.

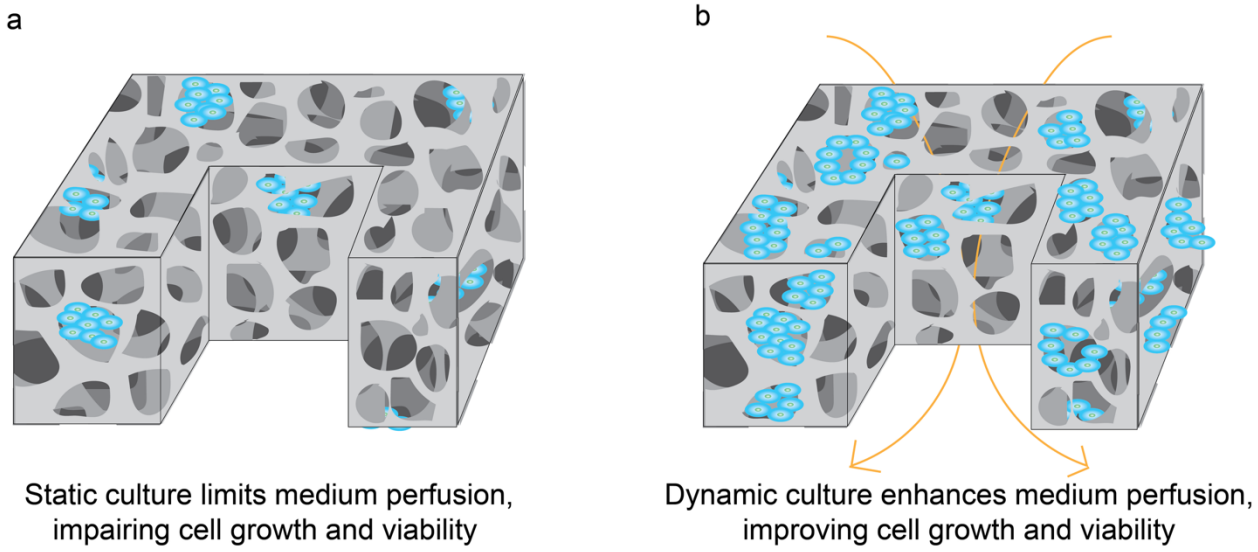


Figure 2.5 Comparison of a) static and b) dynamic culture conditions.

Chapter 3 Polysaccharide Thin Films Regulate the Culture of Human Neural Stem Cells

3.1 Introduction

Over the past two decades, human neural stem cells (hNSCs) have become central to pioneering research aimed at modeling and treating a broad spectrum of diseases, including cancer,[57-59] Alzheimer's disease,[60,61] Parkinson's disease,[61-65] cerebral palsy,[66,67] multiple sclerosis,[68-70] and many others.[71,72] These diseases can be targeted through hNSC implantation,[73-75] or by using hNSCs to model disease progression and assess drug efficacy.[76] However, the translation of these experimental approaches into clinical practice is hindered by the stringent requirements of current Good Manufacturing Practice (cGMP) culture conditions. These conditions necessitate the use of chemically defined, xeno-free environments to ensure safety and reproducibility.

Geltrex is the leading substrate for human neural stem cell (hNSC) growth, supporting adhesion, proliferation, and differentiation due to its ECM protein composition. However, derived from murine tumors, it is costly and unsuitable for xeno-free and chemically defined standards critical for clinical use. Human-derived extracellular matrices show promise as alternatives in supporting proliferation and differentiation of hNSCs,[77] but face scalability issues due to high production costs. These limitations highlight the need for affordable, reproducible, and clinically compatible materials, driving interest in innovative, scalable solutions for both research and clinical purposes.

To address these limitations, chitosan-based materials are being explored due to their well-established history as low-cost biomaterials with customizable properties.[78-82] Chitosan (CS) is a natural and known for its excellent biocompatibility, non-toxicity, and biofunctional properties such as antiviral and antibacterial effects, making it ideal for various biomedical applications.[33-39] Its versatility has been demonstrated in the fabrication of thin films and microbeads that support

the growth and differentiation of rat hippocampal neurons and human neural progenitor cells (hNPCs) into neural and glial lineages.[44] Additionally, CS-based copolymers have been used to create hydrogels for cultivating and differentiating hNPCs and human neural stem cells (hNSCs).[45] Furthermore, patterned CS thin films have facilitated studies on the differentiation and morphology of embryonic neuronal and glial cells.[46]

Building on this foundation, the present study investigates the modification of the microenvironment of hyaluronic acid (HA) and alginate (A) by incorporating chitosan. HA and alginate are two non-proteinaceous natural polymers that mimic the structure of glycosaminoglycans, a major component of the extracellular matrix (ECM). HA itself is a major ECM component in the brain.[75,76] Both HA and alginate are negatively charged, which allows them to effectively interact with positively charged chitosan to form films and enhance mechanical properties. Previous research has demonstrated that chitosan complexing with HA and alginate enhances cell attachment and the mechanical properties of biomaterials.[18,19,21,22]

In this study, we investigate chitosan-alginate (CA) and chitosan-hyaluronic acid (CHA) hybrid materials to form chemically defined, mechanically tunable, and xeno-free standards, and assess their suitability for supporting hNSC culture. By fabricating thin films from CS, CA, and CHA with varying ratios of CS to alginate and CS to HA (0:1, 1:3, 1:1, 3:1, and 1:0), we aimed to determine how these variations influence hNSC multipotency. These films, characterized by their transparency, uniform topography, and hydrophilicity, provided a conducive environment for studying hNSC adhesion, proliferation, and protein expression. The ability to fine-tune the physiochemical and mechanical properties of chitosan-based materials to optimize neural stem cell culture environments represents a significant advancement in stem cell-based therapies.

3.2 Materials and Methods:

3.2.1 Preparation of CA, CHA, and CS films:

0.3% (w/w) CS (Matexcel NAT-0300, degree of deacetylation: 97.3%), 0.3% (w/w) hyaluronic acid, and 0.3% (w/w) alginate were prepared in separate solutions of 1% acetic acid. 200 μL of the CS solution was added to a 48 well plate. The plate was then air dried in a chemical fume hood for 18 hours to form a base layer of CS. The CS base layer was then submerged in a neutralization solution consisting of 2.7% DI water, 6.4% NH_4OH, and 90.9% methanol for 30 minutes. Then, the films were washed extensively with DI water to remove the base solution and air dried for another 12 hours. Mixtures of CA were then prepared at ratios of CS:A of 0:1, 1:3, 1:1, 3:1, and 1:0 by combining the appropriate amounts of the solutions and using a blender to homogenize them. Mixtures of CHA were prepared at ratios of CS:HA of 0:1, 1:3, 1:1, 3:1, and 1:0. 100 μL of these mixtures were then added to the top of the base CS layer in the 48 well plate. The films were then air dried for 12 hours and then submerged in a neutralization solution for 30 minutes. The films were washed extensively with DI water and sterilized using 70% ethanol. Larger plates were also fabricated by scaling the amounts based on the surface area of the well plate.

3.2.2 Water Contact Angle

The films' surface wettability was examined using a goniometer (Ramé-Hart Instrument, Succasunna, NJ, USA) through measuring the water contact angle. Films were cast onto glass slides using the same protocol mentioned in section *2.1*. A 5 μL droplet of DI water was placed onto the coated glass slide, and the measurement was taken immediately at five random locations on the surface.

3.2.3 SEM

The CA, CHA, and CS films had their surface topographies examined using SEM. Films were prepared as described in *2.1*, except inside of petri dishes. Dried films were cut into 0.5 cm x 0.5 cm pieces and mounted onto stubs using carbon adhesive tape (NEM Tape, Nisshin Em. Co. Ltd. Tokyo, Japan). Samples were imaged with a TM3000 tabletop SEM (Hitachi, Tokyo, Japan) at 5 kV.

3.2.4 AFM

The CA, CHA, and CS films' mechanical properties were measured using a Nanosurf EasyScan atomic force microscope (Nanosurf AG, Switzerland). The mechanical properties were determined under ambient conditions using a ferromagnetic resonance tip with a nominal spring constant of 2.8 N m^{-1} and a resonance frequency of 60kHz. The topography of the sample was monitored using scanning probe microscopy in the force modulation mode while simultaneously taking nanomechanical measurements. The tip's position was controlled using an optical microscope in tandem with the AFM. Films were prepared as described in *2.1*, except inside petri dishes. The petri dishes were then fixed to an aluminum holder using tape and secured onto the AFM stage using magnets. Images were processed using Scanning Probe Image Processor software (SPIP; Image Metrology, Denmark).

3.2.5 FTIR

FTIR analysis of the chitosan films was performed using a Nicolet 5DXB spectrometer (Thermo Scientific, Boston, MA). The films were analyzed after being cast onto well plates. The films were scraped off the well plate using a razor blade and the shaving were combined with KBr powder.

The polymer and KBr mixture were then pressed to form a thin film. The films were analyzed by averaging 32 scans at a resolution of 2 cm^{-1} over a range of 500-4000 cm^{-1}.

3.2.6 Cell Culture

Human neural stem cells hNSC-H14 (WB0195) derived from the NIH-approved hESC-H14 (WA14) were obtained from WiCell Research Institute (Madison, WI, USA). The cells were expanded and cultured following the supplied protocol. Briefly, the cells were cultured on Geltrex- or Matrigel-coated tissue culture dishes prepared according to the WiCell protocol, and the cells were supplied with fresh NSC culture medium every other day. Human recombinant basic fibroblast growth factor (bFGF, Gibco) and epidermal growth factor (EGF, Gibco) were supplied every day at 20 ng mL^{-1} . The NSC culture medium consisted of Neurobasal medium (Gibco) supplemented with B27 (Gibco), N2 (Gibco), heparin (StemCell Technologies Inc), MEM NEAA (Gibco), and GlutaMAX (Gibco). The cells were passaged when they reached 90-95% confluency and were dissociated with Accutase. Cells that were seeded onto films had half-medium changes performed every day. BFGF and EGF were added every day at 20 ng mL^{-1}. Cells were maintained in a humidified incubator with 5% CO_2 at 37°C. For characterization experiments, cells were cultured for a maximum of 4 days because this is the typical amount of time it takes for cells to reach confluency in the Geltrex or Matrigel coated plates.

3.2.7 Cell Morphology and Proliferation

Cells were monitored using a Nikon Eclipse TE 2000-S (Nikon, Tokyo, Japan) inverted microscope. Live cells were stained with Calcien AM (ThermoFisher) and dead cells were stained with propidium iodide according to the manufacturer's protocol. The cells were then imaged using a Nikon TE 2000-S inverted microscope. Percent area fluorescent measurements were made using

ImageJ and were taken over 4 separate images with a total area analyzed of around 15 mm^2. Cell proliferation was monitored using an alamarBlue assay (Sigma Aldrich, St. Louis, MO, USA). Briefly, the total amount of medium in each well was measured and then the alamarBlue reagent (110 μg mL^{-1} resazurin) was added at 10% of the total volume. The cells were then incubated at 37ºC for 2 hours, and the fluorescence intensity of the solution was measured at 590 nm with excitation of 560 nm using a SpectraMax M2 microplate reader (Molecular Device, Sunnyvale, CA, US).

3.2.8 Flow Cytometry

The antibodies Alexa Fluor® 488 anti-Ki67 (350508) and Alexa Fluor® 647 anti-SOX2 (BDB560302) were purchased from BioLegend and BD Bioscience, respectively, and were used as suggested by the suppliers. Cells were dissociated from their respective coating or film with Accutase, rinsed with PBS, and then fixed in 4% paraformaldehyde for 15 minutes. Next, the cells were permeabilized in 0.1 %v/v Triton-X 100 in PBS and washed with PhosFlow PermWash Buffer (BD Bioscience, San Jose, CA). The cells were resuspended in 100 μL cell PermWash Buffer and incubated with fluorophore-conjugated antibodies for 30 minutes on ice in the dark. Next, the cells were washed with PermWash Buffer (Thermo Fisher Scientific, Waltham, MA, USA) and resuspended in 0.3 mL Cell Staining Buffer (BioLegend). The cells were analyzed on a LSRII flow cytometer (BD Bioscience) and quantified using the FlowJo software (Tree Star, Ashland, OR).

3.2.9 Immunocytochemistry

A Human Neural Stem Cell ICC kit (Cat. A24354, Thermo Fisher Scientific, Waltham, MA, USA) was used to characterize NSC marker protein expression (SOX2, nestin, and PAX6) following the

manufacturer's protocol. The cells were also stained with the cell proliferation marker protein Ki-67 (BioLegend: San Diego, CA 350508). Briefly, the cells were cultured as described above but on coated glass slides. After five days, the cells were rinsed with PBS, fixed with cold 4% paraformaldehyde for ten minutes on ice, permeabilized for ten minutes on ice, blocked for one hour on ice, and stained with primary antibodies at 4°C overnight. The cells were then washed and incubated with secondary antibodies for one to two hours on ice. Then, the cells were washed once and stained with DAPI before being mounted in Prolong Gold antifade reagent (Invitrogen; Carlsbad, CA). Fluorescence images were acquired using a Nikon Eclipse TE 2000-S (Nikon, Tokyo, Japan) inverted microscope.

3.2.10 Statistical Analysis

The statistical significance of the data was determined using an unpaired two-tailed Student's *t*-test to evaluate the *p*-value between two data sets. The number of independent measurements or experiments (*n*) is indicated in the figure captions. *P*-values that were less than 0.05 were considered statistically significant. Statistical analyses were performed in Microsoft Excel.

3.3 Results and Discussion:

3.3.1 Hydrophilicity, topography, and mechanical strength:

The integration of chitosan into alginate or HA films substantially affects cell adhesion by modifying surface chemistry and mechanical properties, as illustrated in **Figure 3.1a**. Hydrophilicity, a critical determinant of cell attachment and proliferation, generally favors more hydrophilic surfaces for optimal cell growth.[83,84] To assess the hydrophilicity of CA and CHA films, we measured the water contact angle immediately (within 60 seconds) after placing a water

droplet on the film using a goniometer. The films analyzed included varying ratios of CS:A and CS:HA at 0:1, 1:3, 1:1, 3:1, and 1:0.

Figure 3.1b shows that the contact angle for CA films decreased initially as the alginate content increased, and reached a minimum at the CS:A ratio of 1:1. There is a large increase in contact angle at 1:3, which may be due to the increase in precipitated alginate or CS. **Figure 3.1c** illustrates an increase in the water contact angle upon the introduction of HA to the base chitosan material, and a local minimum in water contact angle was observed at 1:1 ratio, suggesting that this ratio may represent an optimal balance where CS and HA aggregates are minimized.

When blended, alginate and CS form a polyelectrolyte complex via electrostatic interactions between the positively charged CS and the negatively charged alginate.[85,86] Although mammalian cells typically exhibit poor attachment to alginate;[87-90] CA demonstrates enhanced cell attachment due to its capability to absorb serum proteins.[91,92] As more alginate is added to the base CS material, electrostatic interactions increase until a threshold is reached where there is higher concentration of alginate than chitosan, resulting in subsequent decrease in electrostatic interactions and directly affecting the elastic modulus.[93,94] HA, an anionic, non-sulfated GAG, is a major component of some extracellular matrices.[95-97] When HA is combined with CS, a polyelectrolyte complex is formed.[21,98,99] Despite being a major component of many extracellular matrices, mammalian cells tend to exhibit poor adhesion to HA due to its negative charge.[100]

To understand how the elastic modulus of the films affects the cultivation of hNSCs, CA and CHA films were subjected to AFM nanomechanical measurements. **Figure 3.1d** shows that ss the amount of alginate in CA films increased a local maximum in elastic modulus was reached at a CS:A ratio of 1:1. The local maximum is likely due to an optimal amount of CS and alginate being present to maximize crosslinking. The bond strength from crosslinking is diminished when

either CS or alginate is removed from the film. A similar trend in CHA films is observed (**Figure 3.1e)**. The local maximum occurred at a CS to HA ratio of 1:1, indicating the optimal ratio that maximized crosslinking. As more HA was added to the base CS material, the elastic modulus increased up to a saturation point where the maximum electrostatic interaction occurred. Beyond this threshold, the electrostatic interaction weakened, leading to a decrease in elastic modulus.[101] An illustration of the polyelectrolyte bond that forms between CS and alginate and between CS and hyaluronic acid is presented in **Figure 3.1f** and **3.1g**, respectively. The electrostatic interaction occurs between the positively charged amine group on chitosan and the carboxylate group on alginate or hyaluronic acid.

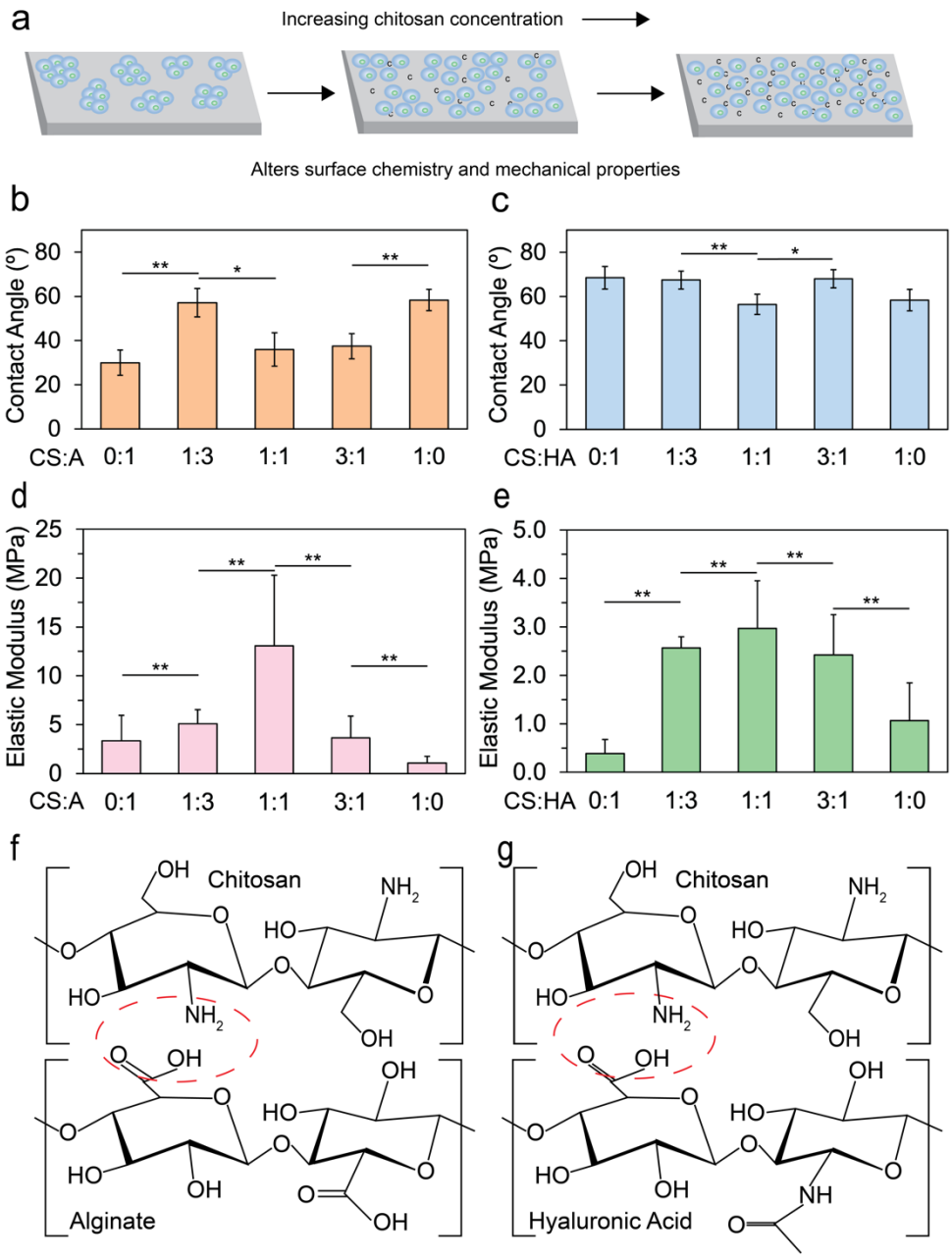


Figure 3.1 Outline and physical characterization of the films. a) an illustration showing how the addition of chitosan aids in cell adhesion. Contact angle measurements taken by a goniometer for b) CA films ($n = 10$) and c) CHA films ($n = 10$) with varying ratios of 0:1, 1:3, 1:1, 3:1, and 1:0. AFM was used to measure the elastic moduli of d) CA films ($n > 239$) and e) CHA films ($n > 239$). Statistical significances of $p < 0.05$ and $p < 0.005$ are indicated by * and **, respectively. If no marks are present, there was no statistical significance between the samples. Illustrations of f) chitosan and alginate polyelectrolyte bond formation (red circle) and g) chitosan and hyaluronic acid polyelectrolyte bond formation (red circle).

Surface topography plays a key role in cell growth, as sharp features, rough surfaces, and uneven textures can affect cell adhesion and proliferation.[102,103] CA and CHA films with ratios of CS to alginate or CS to HA of 0:1, 1:3, 1:1, 3:1, and 1:0 were cut into 0.5 cm by 0.5 cm squares for SEM imaging. The pure chitosan and CA films exhibited predominantly flat and smooth surfaces, while pure alginate films exhibited uneven textures (**Figure 3.2a**). This difference is likely due to the superior bonding between chitosan and alginate, which facilitates the formation of uniform films and minimizes the presence of aggregates. In contrast, the rougher surface of pure alginate can be attributed to the formation of alginate aggregates. Similarly, CHA films exhibited some uneven or rough surface features, likely attributable to the aggregation of CS or HA within the film matrix.

Figure 3.2b and **3.2c** show images of the various film blends after immesion in PBS following sterilization. All films appeared transparent, with no visible ridges or aggregates. **Figure 3.2d** and **3.2e** show the FTIR spectra of the CS:A and CS:HA films, respectively. In both cases, as more chitosan was added to the film, the number of carbons double bonded to oxygen was reduced, and the characteristic peak for this double bond was observed at around 1620 cm^{-1}. **Figure 3.2f** and **3.2g** show the area under the curve of this peak for the CA and CHA films, respectively. This area generally decreased as more chitosan was added into the film. Since chitosan has no carbon-oxygen double bond it is expected to have no peak here, but the degree of deacetylation of this chitosan is around 97%, so there will be some chitin, which does have a carbon-oxygen double bond.

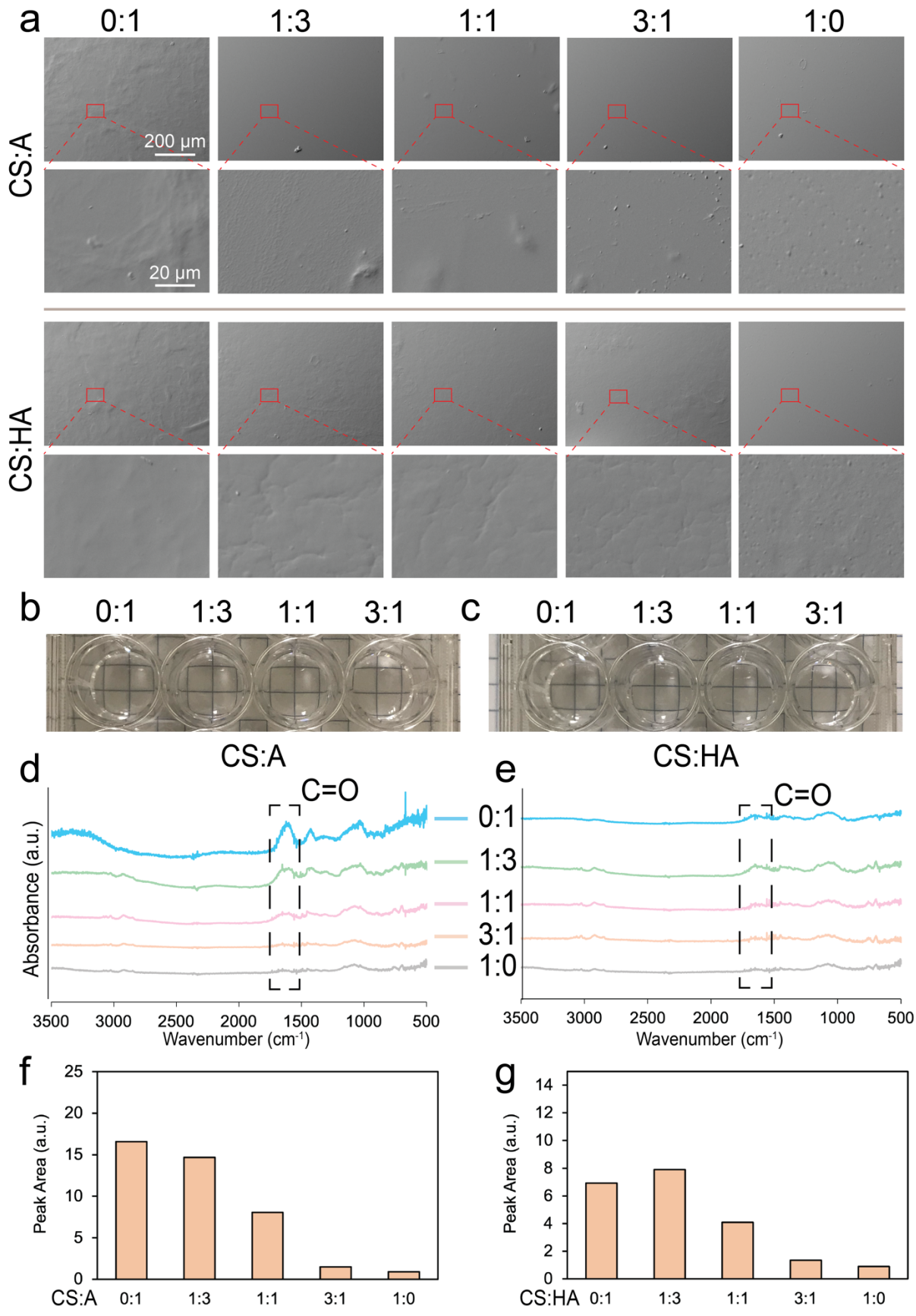

a
0:1
1:3
1:1
3:1
1:0
CS:A
CS:HA
200 μm
20 μm
b
0:1
1:3
1:1
3:1
c
0:1
1:3
1:1
3:1
d
CS:A
C=O
Absorbance (a.u.)
0:1
1:3
1:1
3:1
1:0
3500
3000
2500
2000
1500
1000
500
Wavenumber (cm-1)
e
CS:HA
C=O
3500
3000
2500
2000
1500
1000
500
Wavenumber (cm-1)
f
Peak Area (a.u.)
25
20
15
10
5
0
CS:A
0:1
1:3
1:1
3:1
1:0
g
Peak Area (a.u.)
14
12
10
8
6
4
2
0
CS:HA
0:1
1:3
1:1
3:1
1:0

Figure 3.2 Surface morphology and composition characterization of the films. (a) SEM images of the CA and CHA films with ratios of CS to alginate and CS to HA of 0:1, 1:3, 1:1, 3:1, and 1:0. Photographs of (b) CS:A and (c) CS:HA films immersed in PBS and taken after being prepared for cell culture. FTIR spectra of (d) CA and e) CHA films. Area under the highlighted peak in the FTIR spectra for f) CA and g) CHA films.

3.3.2 Cell behavior on CA/CHA/CS films:

After sterilization, hNSC-H14 were plated onto the films at 30k cm^{-2} cell density and cultured for up to four days. Cell morphology was examined for CS:A films of various chitosan to alginate ratios, including 0:1, 1:3, 1:1, 3:1, and 1:0. **Figure 3.3** shows images taken of the cells on days 1, 2, and 4. Cell morphology provides information on how the cells are attached to the substrates. The pure alginate film (CS:A = 0:1) promoted the formation of large cell clusters and had low cell adhesion. Cell adhesion decreased across the 4-day period for all the conditions, with the exception of the CS:A 1:0 ratio film (pure chitosan) and the Geltrex control (GT 2D) where cell adhesion increased or remained consistent. These decreases in cell adhesion are likely due to an unfavorable interaction between the cells and CA films, caused by either poor electrostatic interactions due to the negative charge of alginate, a lack of cell adhesion motifs, or a combination of the two.[104,105] This may also be caused by unfavorable mechanical properties of the films. Stem cells are influenced by the mechanical properties of their surroundings through a process known as mechanotransduction.[106-109] When the cells begin to grow as clusters, it becomes more difficult for nutrients to reach the cells in the core of the cluster, causing the center of the cluster to become necrotic. Pure CS films provide the most ideal surface with due to the presence of more protonated amine groups. They support the growth of single cells while the other film types tend to support the growth of cell clusters. As more alginate is added to the film, the number of protonated amine groups on the film is reduced and while the number of negatively charged carboxylic acid groups

increases. On day four, cells grew as cluster in the 0:1 and 1:3 conditions and weakly attached clusters for the rest of films except for the pure CS film and Geltrex control.

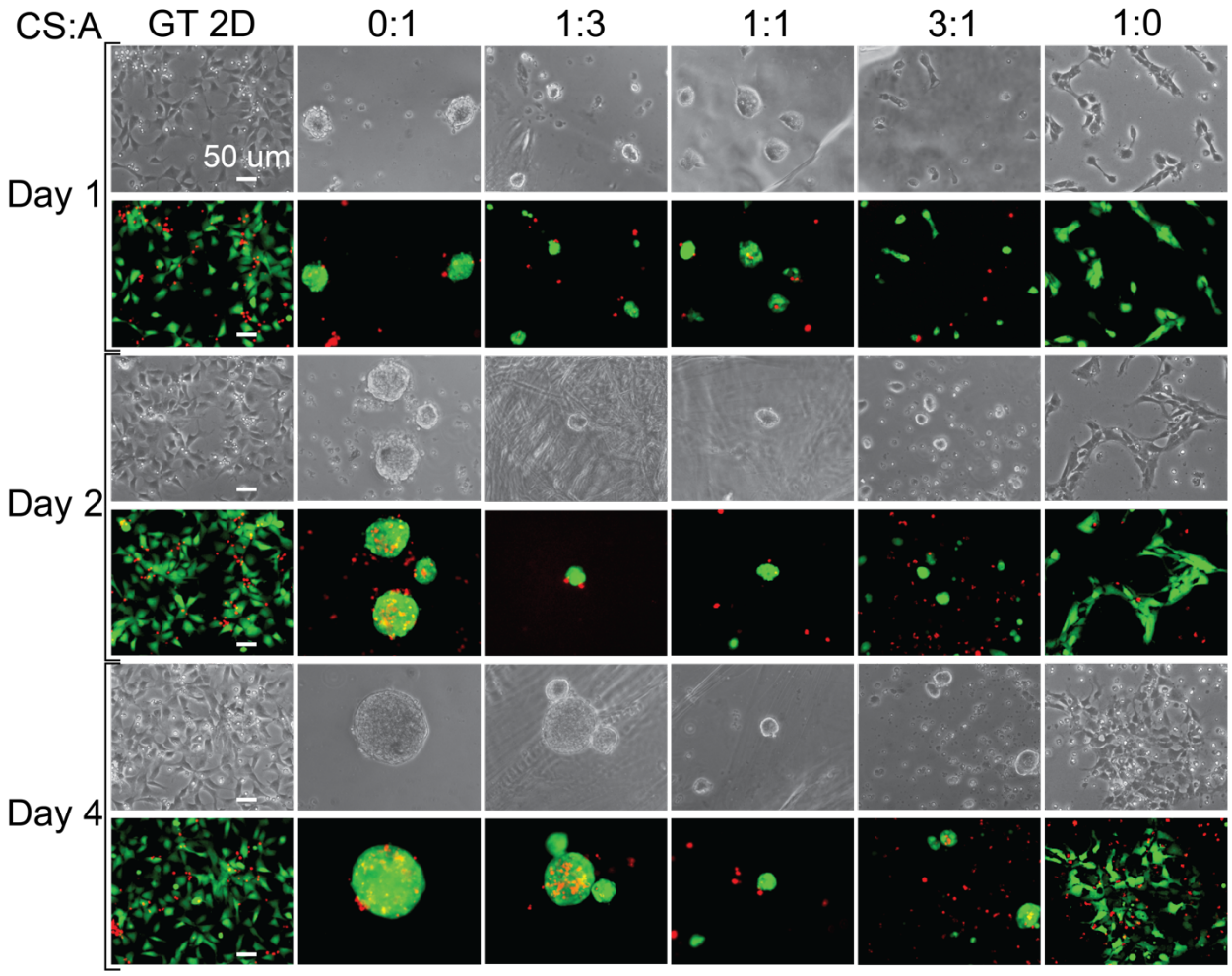


Figure 3.3 Cell morphology and live staining of hNSCs grown on CA films. Phase contrast and live (green) and dead (red) stained images showing the morphology of the cells grown on different films. The scale bar represents 50 μm.

Next, we examined cell morphology on the various CHA films. **Figure 3.4** shows the images of cells grown on CHA films taken on days 1, 2, and 4 of. The cells do not appear to adhere to the pure HA film, likely due to the negative surface charge of the film due to the hydroxide groups. The 1:3 ratio films do not appear adherent on day 1 but appear to be weakly adherent on day 2 and

4, while the 1:1 ratio film does not appear adherent on day 1 but appears to be more adherent on day 2 and 4 than the 1:3 ratio film. This is likely due to the addition of chitosan, which increases the surface charge. The 3:1 and 1:0 films appear more adherent than the other films conditions, and the pure chitosan film appears more adherent than the 3:1 film on day 1. This is likely due to a favorable interaction between the cells and CS:HA films, with an increasing surface charge as chitosan is added, and relevant surface receptors present in the films. Even though we are adding negatively charged hydroxides with the HA, we are also adding various surface receptors, which have been shown to enhance cellular activities.[110,111] These surface receptors enhance the cell adhesion making CS:HA films better substrate than CS:A films for cell adhesion.

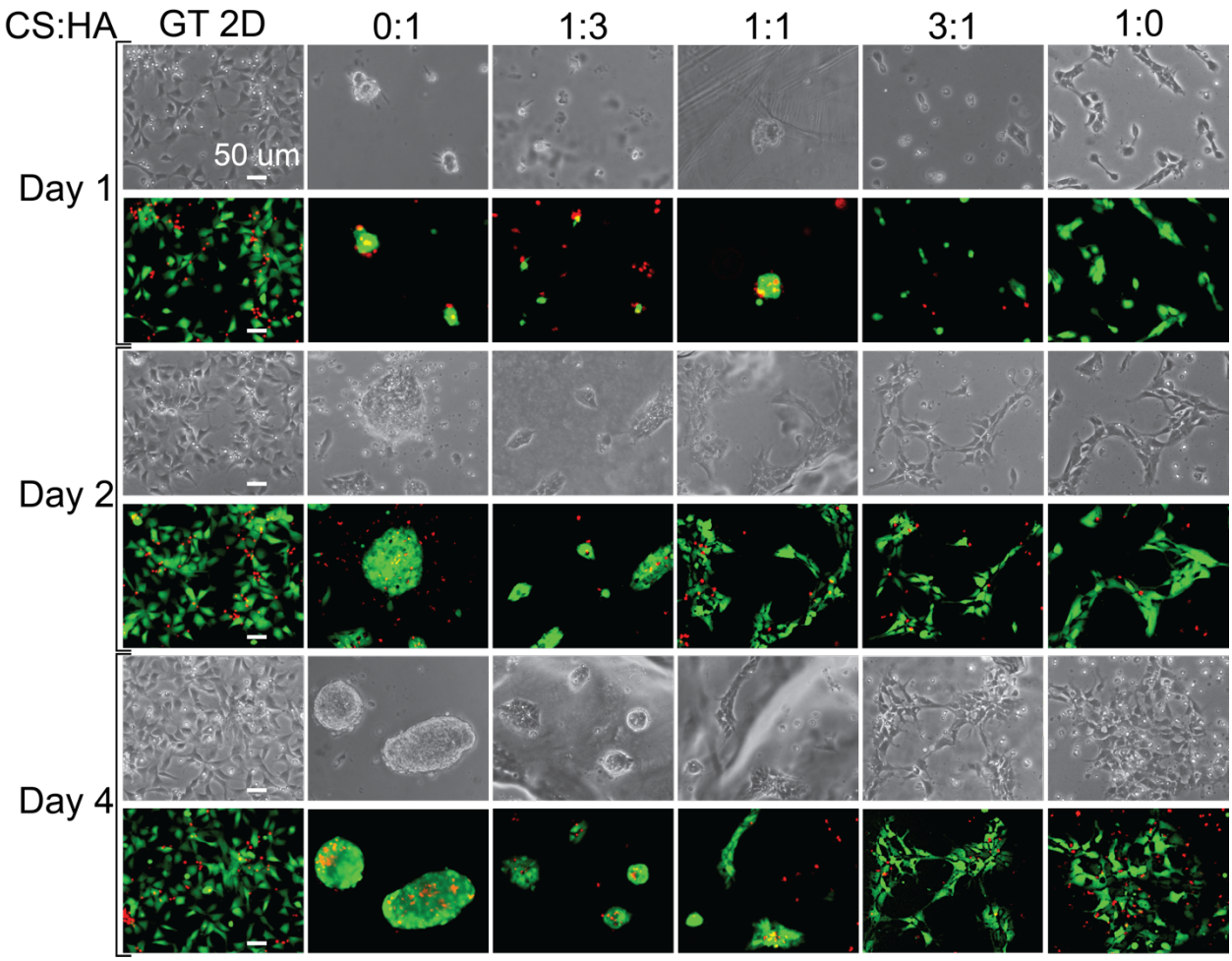


Figure 3.4 Cell morphology and metabolic activity of hNSCs grown on CHA films. Phase contrast and live (green) and dead (red) stained images showing the morphology of cells grown on different films. The scale bar represents 50 μm.

Figure 3.5a shows the percentage of area of CA films exhibiting Calcien AM staining, indicative of viable cells. The results largely corroborate previous observations in **Figure 3.3** and **Figure 3.4**, despite a notable exception: a decline in viable cell area is observed between days 2 and 4 for all CA films, save for the pure CS film, which demonstrates an increase during this period. **Figure 3.5b** illustrates the relationship between the percentage of fluorescent area and time for live-stained CHA films. Here, a consistent increase across all time points is observed for all films, aligning our previous observations of enhanced cell adhesion as seen in **Figure 3.3** and **Figure 3.4**. As

anticipated, The Geltrex control consistently outperformed all other culture methods in terms of cell proliferation and overall fluorescence area.

To access metabolic activity, an alamarBlue assay was conducted on days 1, 2, and 4. Cell viability is directionally proportional to metabolic activity.[112] This study investigate the effect of varying CS:alginate ratios on hNSCs. The data shown in **Figure 3.5c** indicates a strong trend that as chitosan is added to the film, metabolic activity increases. A consistent increase in cell proliferation was observed across all film conditions over the four-day period, with the pure CS film demonstrating most significant overall proliferation.

Figure 3.5d shows the metabolic activity data for CHA films. All CHA films exhibited an increase in metabolic activity over the four-day period, with the exception of 0:1 condition, which exhibited a decrease in cell proliferation between day 2 and 4. This decrease is likely attributable to necrosis within the formed spheroids, [this cannot be attributed to the material properties.]or cell loss during routine medium changes or characterization procedures.

While the pure CS films demonstrated the highest overall proliferation compared to CA films, no discernible difference in proliferation was observed between the CHA films with ratios of 1:3, 1:1, and 3:1 when compared to the pure CS film. This favorable interaction with the CHA films can be attributed to either the incorporation of surface receptors or the unique mechanical properties of these films. These results agree with the observed trends in cell adhesion in **Figure 3.3** and **Figure 3.4**.

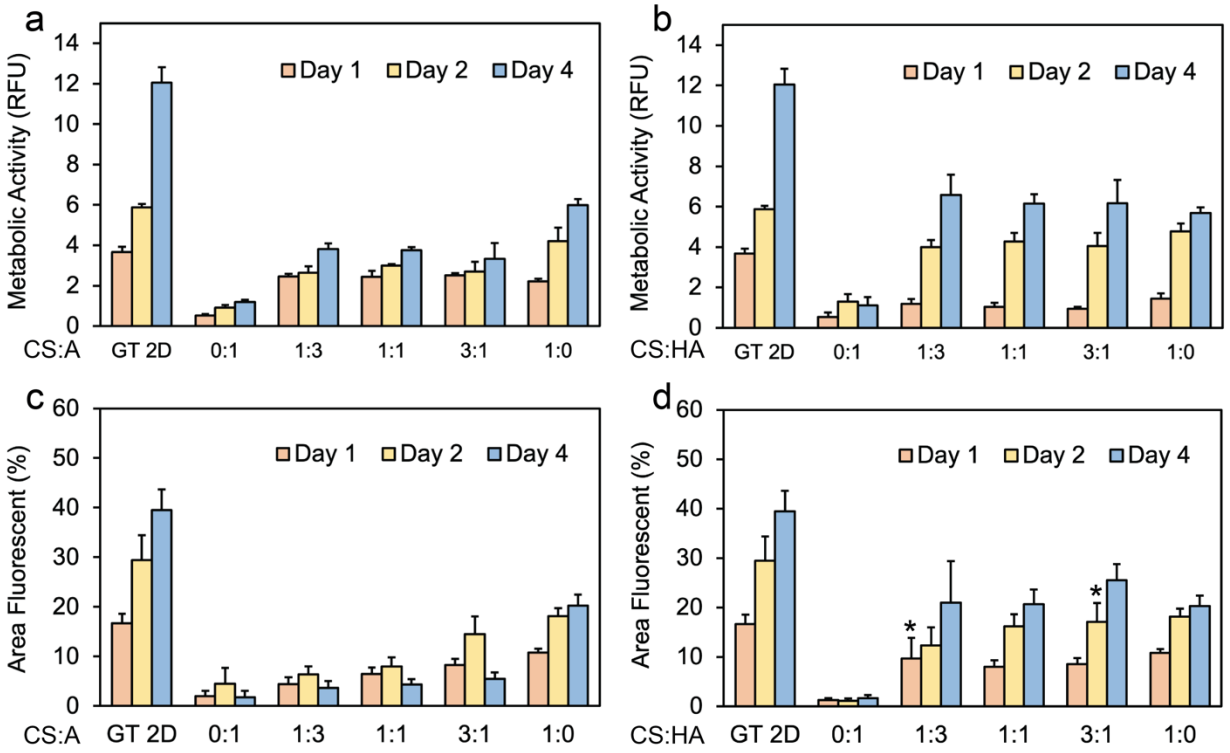


Figure 3.5 Cell proliferation analysis on CS:A and CS:HA films. Graphs illustrating metabolic activity of hNSCS on (a) CS:A films and (b) CS:HA films with *n*=6. Percentage of live-stained area on (c) CS:A films and (d) CS:HA films with n=4. A *p* value of less than 0.05 was observed for all samples when compared to the 2D control at the same time point except for samples labeled with an *.

Following a four-day culture period on their respective films, cells were collected and stained for flow cytometry analysis. The observed trends in SOX2 (a pluripotency marker responsible for gene regulation [113]) and Ki67 (a proliferation marker), as seen in **Figure 3.6a**, corroborate findings from both live/dead imaging and viability assays as seen in **Figure 3.3, 3.4,** and **3.5**.

The double-positive population for SOX2 and Ki67 generally increases as the chitosan content in the films increased for both the CA and CHA films. A minimal double positive population was observed at the CS:A ratio of 1:3. In contrast, the CHA films exhibited a local maximum in the SOX2/Ki67 double positive population at CS:HA ratio of 1:1, indicating an

optimal ratio where the negative impact from increasing HA negative charge is outweighed by the increased presentation of surface receptors. Notably, the pure alginate film demonstrated the lowest expression of this double-positive population, likely due to poor adhesion of the cells to the film surface.

Figure 3.6b shows the SOX1-positive population as histograms. For the CA films, SOX1 expression increases as chitosan concentration increases, while for the CHA films, we see and initial increase in SOX1 expression when chitosan is added, and then a large increase can be seen in the pure chitosan condition.

Figure 3.6c illustrates the expression of nestin, an intermediate filament protein. A significant increase in nestin expression was observed in the pure CS condition compared to other films conditions. In the CA films, nestin expression progressively increased with increasing chitosan content. However, for the CHA the film with the highest nestin expression, other than the pure chitosan film, was observed in the 1:3 ratio condition. The nestin expression decreased at the 1:1 ratio and then increased in at the 3:1 and pure CS conditions. This trend contrasts with the observed behavior of the SOX2/Ki67 double positive populations, where a local maximum was observed at the 1:1 CS:HA ratio. This discrepancy may be attributed to the influence of altered film mechanical properties on cellular cytoskeleton organization.

These findings collectively indicate that increasing chitosan content in the CA and CHA films positively affects cell proliferation and the expression of key hNSC markers. Across all markers, the pure CS films demonstrated superior performance, while the Geltrex control consistently exhibited the highest overall expression levels.

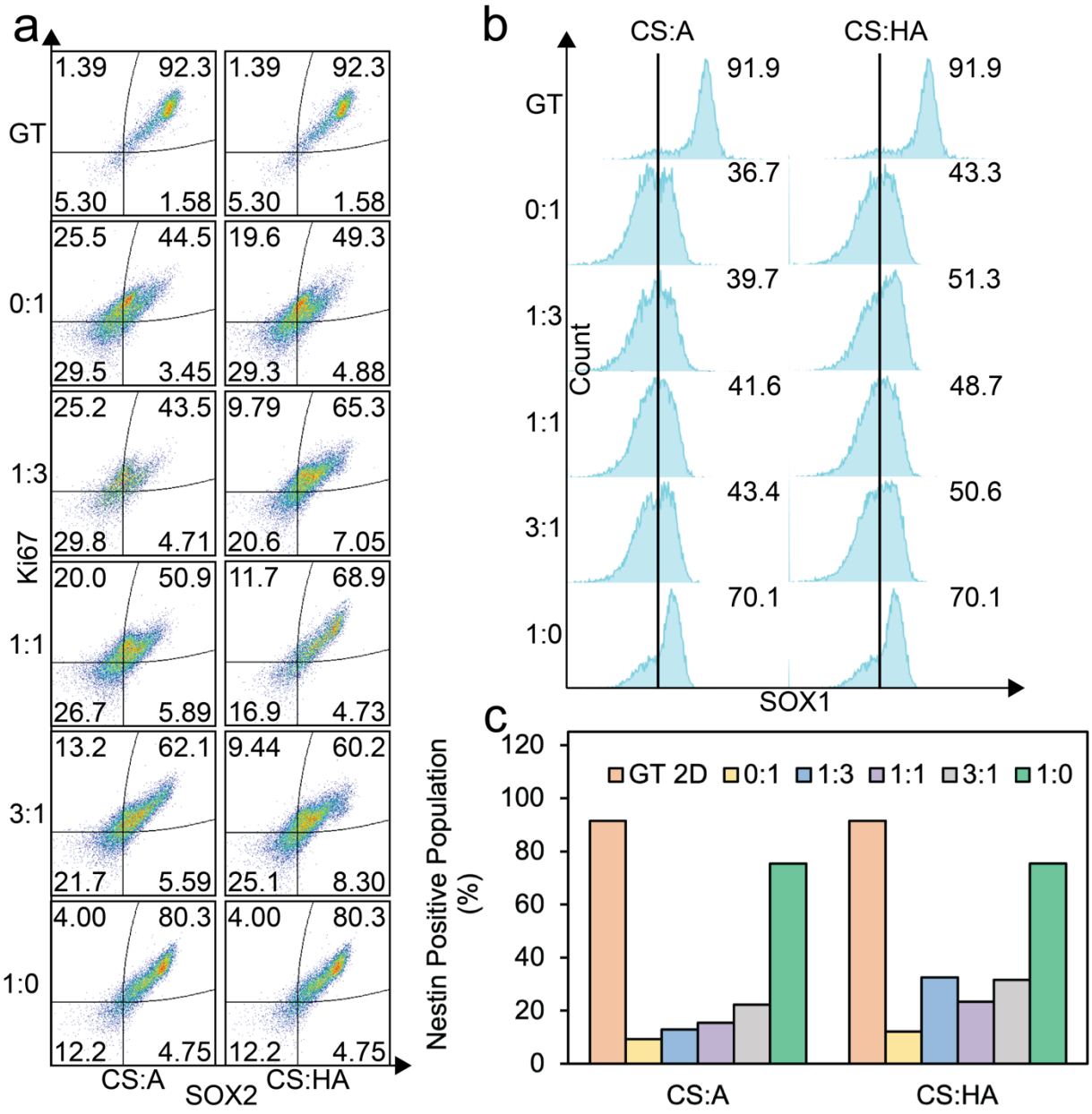


Figure 3.6 Flow cytometry analysis of cells cultured on CS:A and CS:HA Films. (a) Dot plots of SOX2 and Ki67 expression. (b) SOX1 positive populations. (c) Nestin positive populations. All samples have at least 5,500 cells analyzed.

Immunofluorescence imaging revealed a notable trend: as the concentration of either alginate (**Figure 3.7**) or HA (**Figure 3.8**) increased in the films, nestin expression became progressively less intense and exhibited a more uneven distribution. This downregulation of nestin expression

strongly suggests a decline in the overall health and differentiation status of the hNSCs, as alginate or HA content increased.

In contrast, immunofluorescence micrographs of pure CS films demonstrated a prominent nuclear translocation of SOX2, a critical transcription factor supporting hNSC multipotency and self-renewal. However, in the film conditions with increased alginate or HA ratios, SOX2 expression appeared to be predominantly localized in the cytoplasm rather than the nucleus. This cytoplasmic localization suggests a potential loss of long-term self-renewal and multipotency capabilities in hNSCs cultured on these substrates. **Supplemental Figures 3.9** and **3.10** show PAX6 and Ki67 expression in cells grown on CS:A and CS:HA films, respectively. The results seen here corroborate the previously described trends.

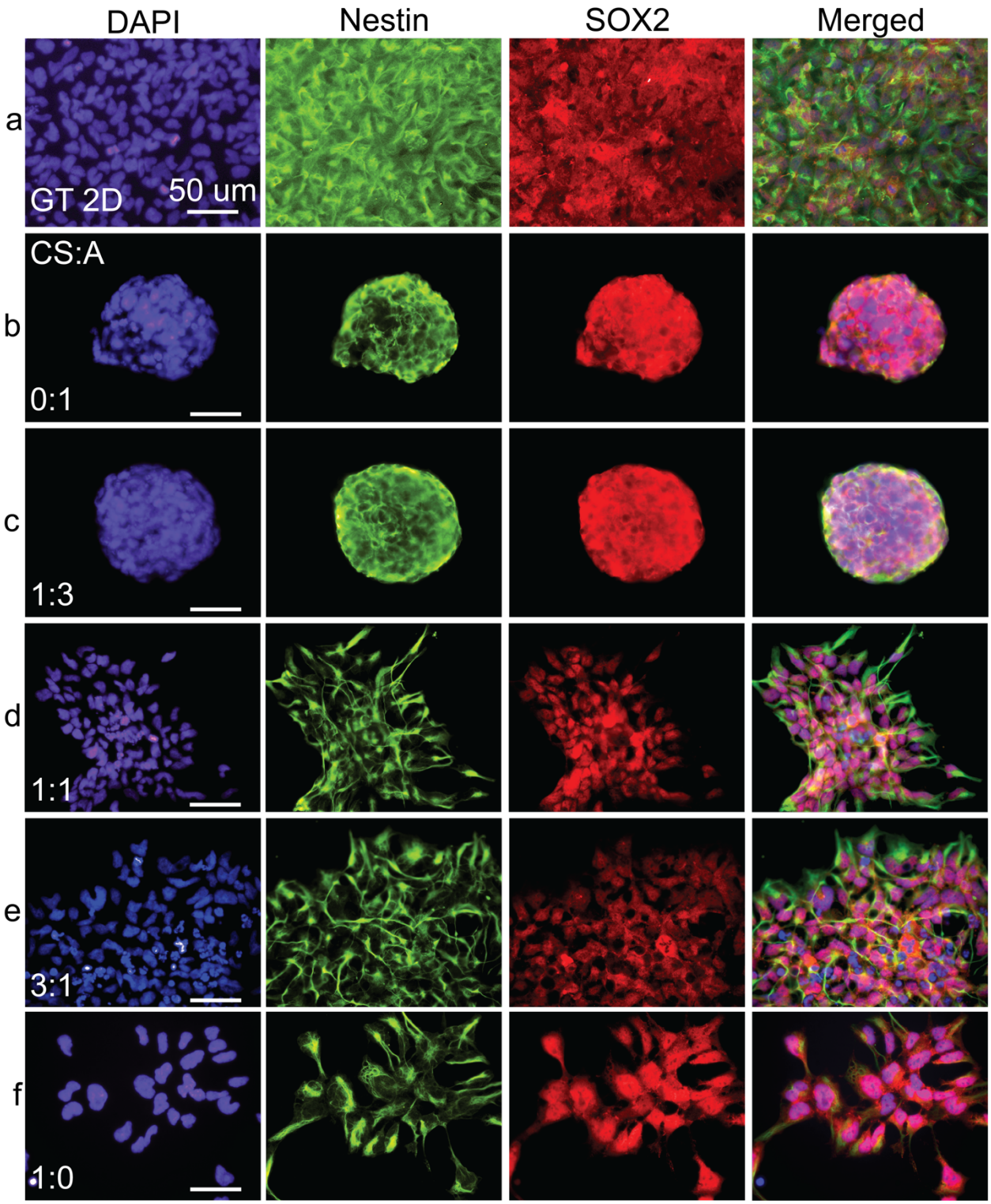


Figure 3.7 Immunostaining analysis of cells cultured on CA films. Florescent images of (a) Geltrex control and films with CS:A ratios of (b) 0:1, (c) 1:3, (d) 1:1, (e) 3:1, and (f) 1:0. hNSC-

H14 were stained for nestin (green), SOX2 (red) and nuclei (DAPI, blue). The scale bars are 50 μm.

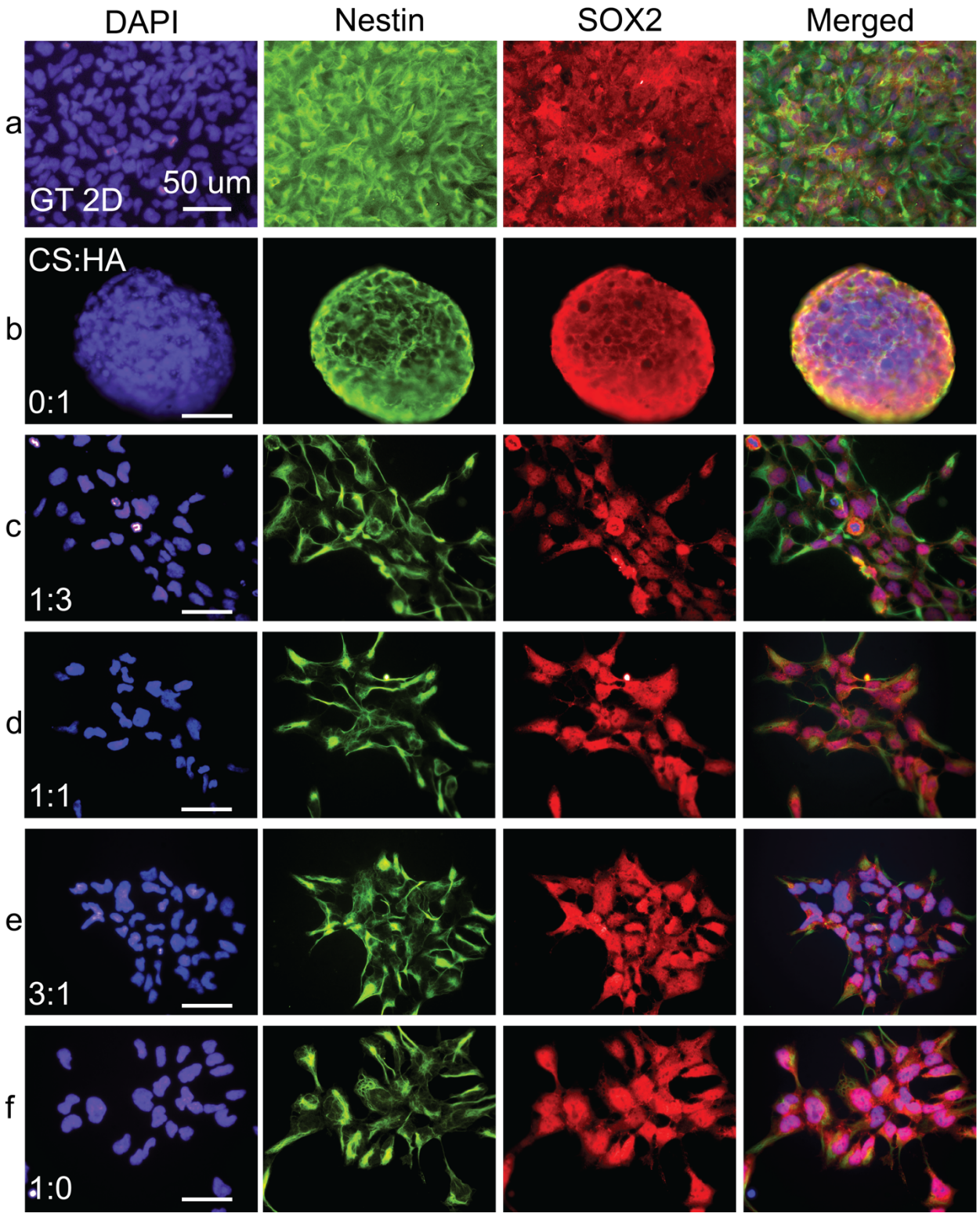
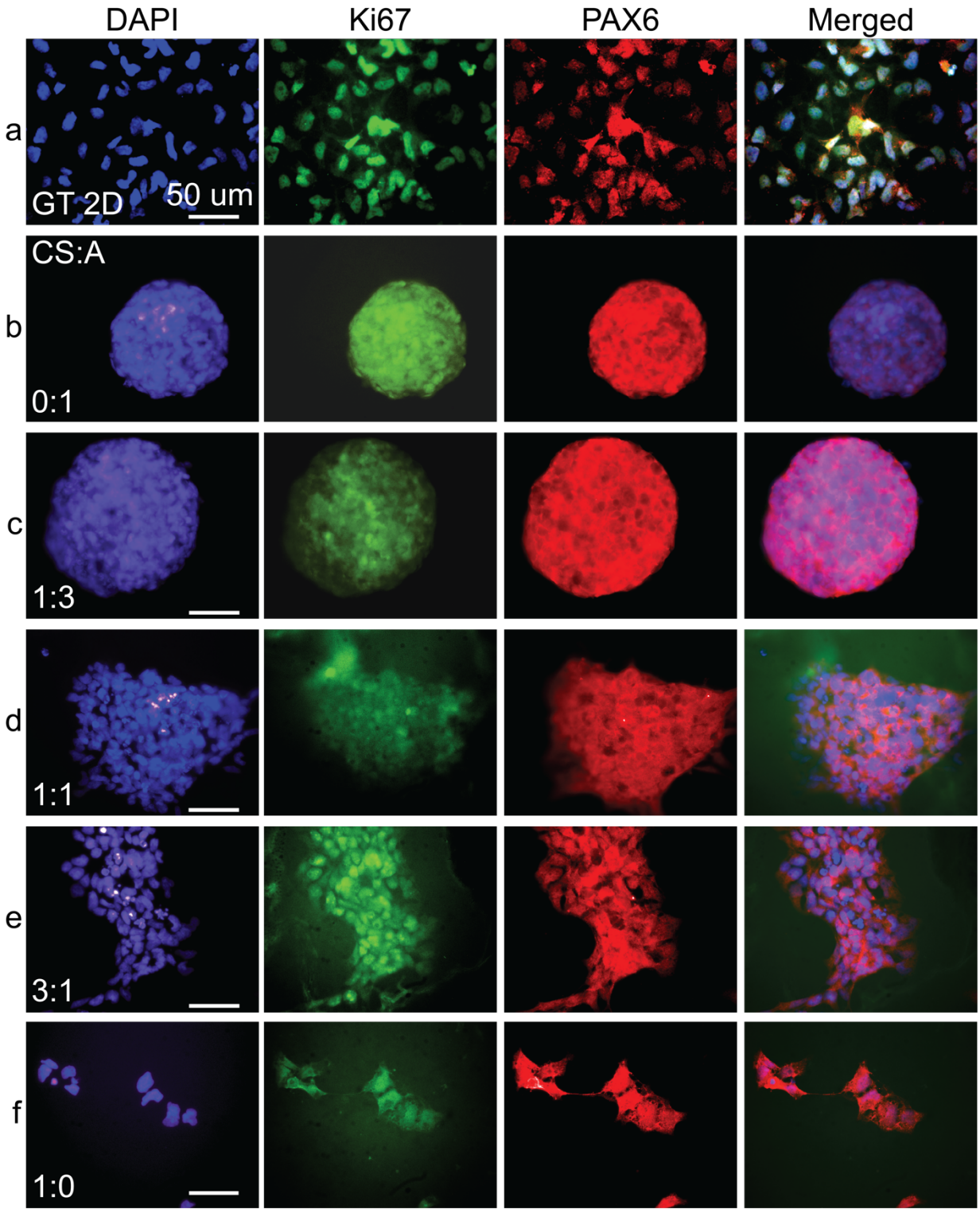


Figure 3.8 Immunostaining analysis of hNSC-H14 cells cultured on CHA films. Florescent images of (a) Geltrex control and films with CS:HA ratios of (b) 0:1, (c) 1:3, (d) 1:1, (e) 3:1, and (f) 1:0.

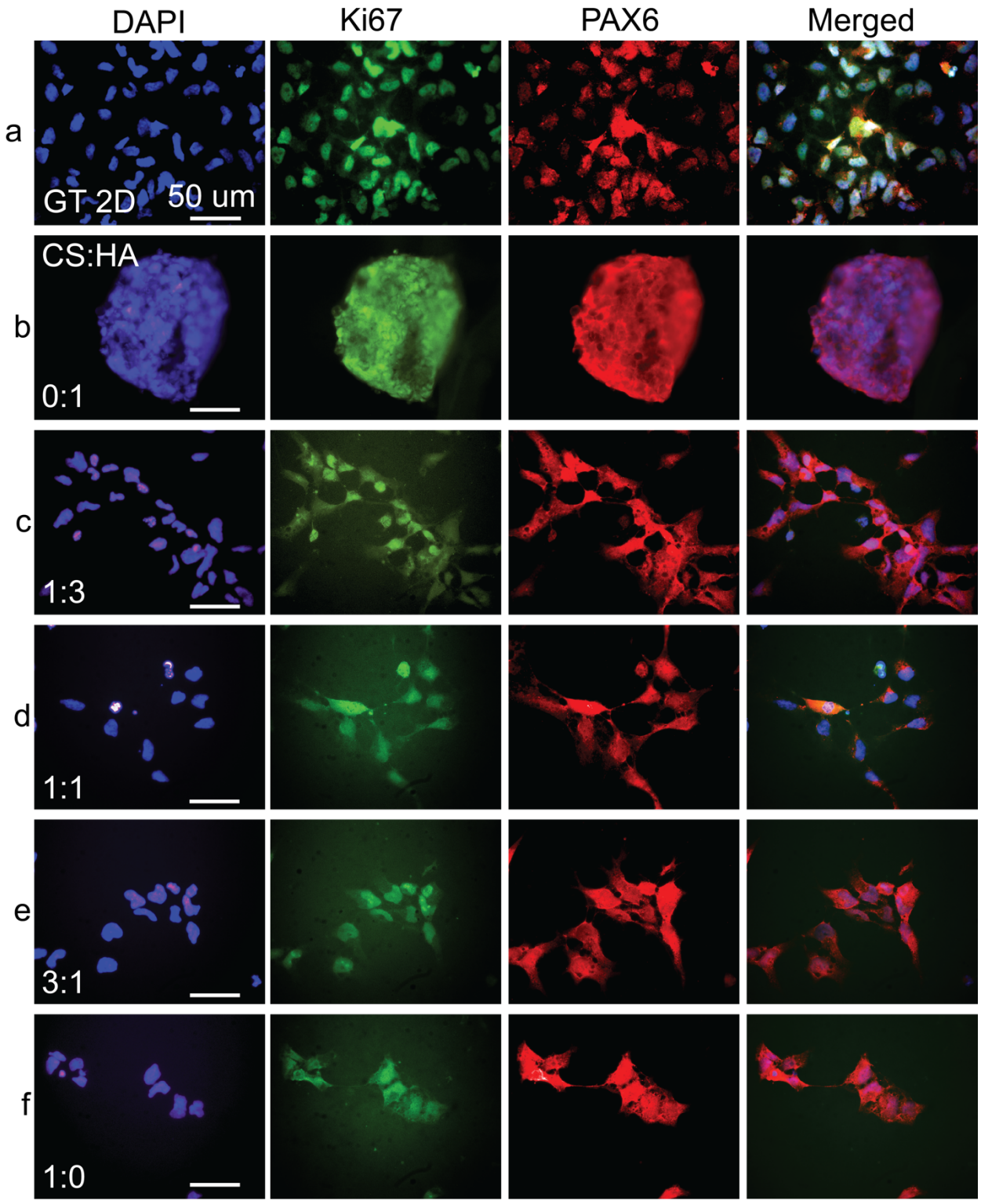
Cells were stained for nestin (green), SOX2 (red) and nuclei (DAPI, blue). The scale bars are 50 μm.

3.4 Supplemental Figures



Supplemental Figure 3.9 Immunostaining analysis of cells cultured on CA films. Both the Ki67 and PAX6 appear to be expressed in the nucleus in the pure CS and Geltrex control. As more

alginate is added, both Ki67 and PAX6 appear to be expressed more in the cytoplasm, indicating a loss of multipotency and proliferation capacity. Images showing a) Geltrex control, CA ratios of (b) 0:1, (c) 1:3, (d) 1:1, (e) 3:1, and (f) 1:0. Fluorescent images of hNSC-H14 were stained for Ki67-green and PAX6-red. DAPI staining for nuclei are presented in blue. The scale bar is 50 μm.



Supplemental Figure 3.10 Immunostaining analysis of hNSC-H14 cells cultured on CHA films. PAX6 and Ki67 appear to remain mostly expressed in the nucleus in all of the CHA films conditions, with the exception of the pure HA film. This indicates that, other than the pure HA

film, the CHA films are able to support cells in terms of Ki67 and PAX6 expression. Images showing a) Geltrex control, CS:HA ratios of (b) 0:1, (c) 1:3, (d) 1:1, (e) 3:1, and (f) 1:0. The cells were stained for nestin-green and SOX2-red. DAPI staining for nuclei are presented in blue. The scale bar is 50 μm.

Chapter 4 Chitosan Scaffolds as Microcarriers for Dynamic Culture of Human Neural Stem Cells

4.1 Introduction

The demand for human neural stem cells (hNSCs) is substantial in the fields of regenerative medicine and pharmacological development. These versatile cells play a crucial role in medical research and the treatment of challenging diseases such as Alzheimer's disease, Parkinson's disease, amyotrophic lateral sclerosis, Huntington's disease, and spinal cord injury.[114,115] These stem-cell based applications require the administration of tens of millions of purified cells for each patient. hNSCs are commonly grown on 2D plastic cultureware.[116,117] However, conventional 2D culture systems, commonly employed in hNSC growth, have limitations. These include restrict cell productivity due to limited growth area, the absence of microenvironmental cues resembling native tissues, and non-compliance with current good manufacturing practices (cGMP) guidelines, making mass production challenging and costly. As such, researchers have explored the utilization of three-dimensional (3D) culture systems for production of stem cells such as induced pluripotent stem cells (iPSCs), embryonic stem cells (ESCs), and mesenchymal stem cells to address these limitations and better mimic *in vivo* conditions.[118,119]

Despite extensive investigations into 3D culture systems,[120] customized technologies specifically targeting the long-term, large-scale production of hNSCs in these settings are yet to be explored. One of the primary obstacles encountered in the 3D production of stem cells is necrosis, primarily caused by the formation of stagnant zones in the system and the presence of large cell clusters. To address these challenges, dynamic culture conditions, those commonly found in bioreactors, have been identified as an effective means to eliminate stagnant zones in 3D cultures. The utilization of dynamic culture conditions may enable the production of a remarkable scale of 10^9 to 10^{12} high-quality cells per patient.[121-126]

Although bioreactors are widely utilized for large-scale, 3D production of microorganisms, such as bacteria or cells, in dynamic environments, their implementation for hNSCs presents significant challenges. Ideally, bioreactors should facilitate efficient nutrient and oxygen exchange essential for cell proliferation, metabolite removal, and abundant cell yield. However, there is currently a lack of scalable, dynamic cell culture methods, as well as bioreactor designs specifically tailored for hNSC production.[127] The dynamic environment in bioreactors generates shear stress, which poses threat to cell viability and can induce unintended cell differentiation, and yet the precise impact of shear stress on cell fate remains poorly understood.[128-130] Moreover, limited knowledge is available about the ability of bioreactors to maintain undifferentiated hNSC populations over extended periods. Most existing protocols focus on the production of ESCs or iPSCs immediately prior to differentiation.[131] These protocols typically involve initiating the culture with iPSC aggregates in suspension for neural differentiation to generate NSCs and neurons. However, these methods are not suitable for most purified hNSCs derived from patients, as the microenvironment of cell aggregates is not established by hNSCs themselves but rather by a mixed population of differentiating cells that aid in cell development and survival. As a result, patient-derived hNSC clusters exhibit low survival and proliferation rates in suspension cultures.[132-134] Although a few studies have explored bioreactor systems for inducing human neural precursor cells in matrix-free suspension, such approaches have not gained widespread popularity.[135-138] Matrix-free suspension cell cultures commonly suffer from issues such as spontaneous unwanted differentiation, particularly towards glial cells as well as necrosis resulting from inadequate nutrition and oxygen supply in the central region of cell aggregates.[134] To address these challenges, matrix-dependent dynamic systems utilizing microcarriers have been proposed as more reliable and applicable to a broader range of cell types.[139-141]

Microcarriers offer a 3D supportive matrix that enables cell adhesion and proliferation. However, the most hNSC cultures, including microcarriers and dish surfaces, the use of biologically relevant molecules such as Matrigel or laminin is necessary to achieve significant cell adhesion. Unfortunately, these molecules are expensive and do not meet cGMP standards. Therefore, there is a need for an appropriate microcarrier design that addresses these limitations and provide several advantages for culture in bioreactors. Firstly, an ideal microcarrier would allow cells to reside inside the microcarrier, protecting them from shear stress-induced apoptosis, detachment, and spontaneous differentiation. This would enable the utilization of various bioreactors and operating parameters. Secondly, the surface chemistry of microcarriers, whether through a cationic or biomimetic interface, could activate crucial cell surface receptors that promote cell adhesion, survival, and proliferation. Thirdly, the microstructure of microcarriers could regulate cell morphology and distribution, preventing necrosis and controlling the size of cell aggregates. Lastly, microcarriers offer the flexibility to tailor the microenvironment to better accommodate different tissue or cell subtypes by modifying the microcarrier design.

Too meet these criteria, researchers have been investigating porous microcarriers as a potential solution.[142-144] Porous materials can be made from metals or ceramics, But their high specific gravity makes them unsuitable for floating and flowing in a dynamic environment.[145] Therefore, biocompatible polymers such as chitosan, dextran, cellulose, collagen, alginate, poly (lactic-*co*-glycolic acid), polylactide, and polystyrene, are considered better candidates for porous microcarrier materials.[120,146-152] However, some of these materials have limitations such as being xenogenic, lacking the necessary surface chemistry to promote cell adhesion, or being expensive to scale up.

Chitosan, a natural polysaccharide derived from fungi or the shells of crustaceans like crabs or shrimp, is the second most abundant polymeric material after cellulose. It finds applications as a raw material for food, agriculture, and medical equipment industries.[153] Unlike collagen, chitosan does not harbor zoonotic pathogens, and the purification process removes allergenic crustacean proteins, minimizing the risk of allergic reactions in humans.[154] The cationic nature of chitosan along with its structural similarity to glycosaminoglycans enables mammalian cells to adhere to it effectively.[146] Additionally, chitosan exhibits a balanced hydrophilic-hydrophobic nature and possesses antimicrobial properties. Compared to collagen, chitosan has a higher elastic modulus, making it more suitable for maintaining structural integrity in dynamic cultures.[101] Importantly, chitosan has been proven to be compatible with neural tissue regeneration,[155] and it has been incorporated into numerous medical implants for nerve repair.[155-157]

This study introduces porous chitosan scaffolds constructed and optimized as microcarriers for the expansion of hNSCs in dynamic cultures. The scaffolds were fabricated through lyophilization using solutions with varying concentrations of chitosan, with collagen serving as a control. Compression tests and atomic force microscopy (AFM) were conducted to assess the elastic modulus and overall mechanical strength of the scaffolds. The chitosan scaffolds demonstrated excellent stability in the culture medium for a duration of three weeks. By tailoring the pore structure of the scaffolds specific for hNSCs, optimal 3D distribution and infiltration of the cells were achieved while providing protection against shear stress inducted by the dynamic environment. Cell adhesion, proliferation, and multipotency were characterized to identify the most suitable type of scaffolds for culturing hNSCs in a dynamic setting. The study presents these chitosan scaffolds as viable microcarriers capable of scaling up hNSC production in dynamic and well-defined cultures.

4.2 Materials and Methods

4.2.1 Microcarrier fabrication

All chemicals were purchased from MilliporeSigma (St. Louis, MO, USA) unless otherwise specified. To make chitosan porous scaffolds, chitosan (MW, 50–100 kDa; degree of deacetylation, 95%–98%; MarkNature, NY, USA) was dissolved homogeneously in 1 N acetic acid at chitosan concentrations of 0.5 wt% (05 CS), 2 wt% (2CS), and 4 wt% (4CS). To make collagen porous scaffolds, collagen was dissolved in 0.5 N acetic acid at 0.5 wt% (05COL). The solutions were cast into a 24-well plate and frozen at –20 °C for 8 h. Then, the frozen scaffolds were lyophilized in VirTis Virtual Lyophilizer (SP Scientific, NY, USA) for 1–3 days. No crosslinking steps were performed on the scaffolds. The samples were sectioned into 15 mm in diameter and 0.8-mm thickness for cell culture or 3.0-mm thickness for mechanical testing and dried in a desiccator for 24 h. The dried samples were neutralized with a basic solution (NH_4OH 33% 15 mL, deionized water (DI) 35 mL, ethanol 500 mL) for 30 min and rinsed with DI water to remove ammonia hydroxide and ethanol.

4.2.2 FTIR and ^1H NMR Spectroscopy

FTIR analysis of chitosan and collagen powders was performed using a Nicolet 5DXB spectrometer (Thermo Scientific, Boston, MA). The polymer powders were analysed by adding the polymer to KBr powder. The polymer and KBr mixture were then pressed to form a thin film. The films were analysed by averaging 32 scans at a resolution of 2 cm^{-1} over a range of 500-4000 cm^{-1}. ^1H NMR analysis was performed to verify the degree of deacetylation of the chitosan scaffold. Chitosan was first dissolved in 2.5% DCl D_2O at 10 mg/mL. A 300 MHz spectrometer (Bruker Avance III 300, Billerica, MA) was used to acquire the spectra in triplicates at 25 ºC. The degree of deacetylation was determined by calculating the integrals of the protons on the H-Acetyl

group and the protons on the H2/H6 group. The following equation was then used to determine the degree of deacetylation:

$$DD(\%) = \left[1 - 2\left(\frac{I_{H-Acetyl}}{I_{H2/H6}}\right)\right] x100 \qquad (1)$$

Where DD (%) is the degree of deacetylation in percentage, $I_{H\text{-}Acetyl}$ is the integral of the protons on the acetylated group, and $I_{H2/H6}$ is the integral of the protons on the monomer hexose rings.

4.2.3 Microstructure characterization

The microstructure of dry scaffolds was examined using scanning electron microscopy (SEM). To prepare SEM samples, the scaffolds were first neutralized with water and ammonia hydroxide and then sterilized with ethanol. Next, the scaffolds were dried under vacuum. The dried scaffolds were mounted on a carbon-conductive adhesive tape (NEM Tape, Nisshin EM. Co. Ltd. Tokyo, Japan). These were imaged at 5 kV using a TM3000 tabletop SEM (Hitachi High-Tech Corporation, Tokyo, Japan). From SEM images, pore diameters were calculated with ImageJ software (NIH, Bethesda, MD, USA).

The porosity of scaffolds was measured using a modified isopropanol displacement method. The dry scaffold volume (V, cm^3) and weight (W_1, g) were measured as follows. The scaffolds were fully immersed in 5 mL of isopropanol (ρ_s, 0.786 g/cm^3) under vacuum for 15 min to expel air from the pores. Saturated scaffolds were weighed (W_2, g) immediately upon removal from isopropanol bath. The volume of the scaffolds did not change after isopropanol saturation. The porosity (%) was calculated as follows (n = 10) and defined as the ratio of the volume of isopropanol absorbed by the scaffolds to the volume of the scaffold:

$$Porosity\ (\%) = \frac{W_2 - W_1/\rho_s}{\mathrm{V}} x100 \qquad (2)$$

Where V is the volume of the dry scaffold, W_2 is the weight after removal from the isopropanol bath, W_1 is the initial weight of the scaffold, and ρ_s is the density of isopropanol. The specific surface area of the scaffold was measured using the multipoint Brunauer–Emmett–Teller (BET) method in NOVA 4200e (Quantachrome Instruments, Boyton Beach, FL, USA). The scaffold was prepared and freeze dried again after the final wash. The dry scaffold was degassed at 50 °C for 12 h. Then, with as nitrogen the adsorbate, isotherms were acquired at 77K. A multipoint BET was then performed on the isotherms to determine the specific surface area of each scaffold.

4.2.4 Mechanical properties

Uniaxial compression tests were carried out to understand the macromechanical properties of scaffolds using Autograph Table-TOP Precision Universal Tester AGS-X (SHIMADZU CORPORATION, Kyoto, Japan) at room temperature. Dry scaffolds were compressed at 0.4 mm/min until at least 40% strain. The compressive Young's moduli of the scaffolds were calculated as the slope of the linear regions of the stress–strain curves within the range of 0%–15% strain.

AFM was performed with Nanosurf FlexAFM (Nanosurf AG, Liestal, Switzerland). A contact AFM probe mode with a spring constant of 0.2 N/m and resonance frequency of 13 kHz was used to obtain the elastic moduli of the scaffolds immersed in PBS.

4.2.5 Degradation test

The stability of the scaffolds was investigated by testing their degradation. Dry scaffolds were incubated in an Orbital Shaker PSU-10i (SIA Biosan, Riga, Latvia) with 37°C Neurobasal medium at 100 rpm. After 7, 14, and 21 days of incubation, the samples were removed, rinsed with distilled

water, and lyophilized. The remaining mass (%) of each scaffold after the incubation relative to the initial weight was calculated to assess the degradation.

4.2.6 Cell culture

hNSC-H14 (WB0195) cells, derived from NIH-approved hESC-H14 (WA14), were obtained from WiCell Research Institute (Madison, WI, USA). Following the WiCell hNSC protocol, the cells were cultured as monolayers on Geltrex-coated tissue culture dishes, and fresh media were supplied every other day. Human recombinant basic fibroblast growth factor (bFGF, Gibco®, Thermo Fisher Scientific, Waltham, MA, USA) and epidermal growth factor (EGF) were supplied daily at 20 ng/mL. The hNSC culture medium comprised a Neurobasal medium (Gibco®) supplemented with B 27, N2, MEM NEAA, heparin, and GlutaMAX. hNSCs were passaged every 3–5 days and dissociated with Accutase after reaching 90% confluency.

ReNcell VM was obtained from MillporeSigma (St. Louis, MO, USA). Following the manufacturer's protocol, the cells were cultured as monolayers on laminin (CC095-M, MillporeSigma)-coated culture dishes. Fresh medium (SCM005, MilliporeSigma), bFGF, and EGF at 20 ng/mL were supplied every other day. The cells were passaged every 3–5 days and dissociated with Accutase after reaching 80% confluency. All cells were incubated in a humidified incubator containing 5% CO_2 at 37°C.

4.2.7 Cell proliferation in a rotational bioreactor as a dynamic culture

One day after cell inoculation, scaffolds with hNSCs were transferred to a 15-mL flat-bottomed tube containing 1 mL of medium per two scaffolds. The samples were shaken at 65 rpm on an orbital shaker in the following culture period.

Cell proliferation was assessed by alamarBlue assay (MilliporeSigma) after 3, 5, 7, 11, and 15 days of culture. The scaffolds were transferred to a 24-well plate and gently rinsed with PBS. The medium was replaced with alamarBlue reagent (11 μg/mL resazurin in culture medium). After incubation at 37°C for 2 h, all solutions were transferred to 96-well black well plates to measure the fluorescence intensity at 590 nm with excitation at 560 nm using a SpectraMax M2 microplate reader (Molecular Devices LLC, San Jose, CA, USA).

Cell morphology and viability were monitored using a LIVE/DEAD™ Viability/Cytotoxicity Kit (Invitrogen Corporation, Waltham, MA, USA), following the manufacturer's protocol. Briefly, viable cells were stained with 1 μM calcein-AM, while dead cells were stained with 4 μM ethidium homodiemer-1 in a 1: 1 mixture of culture medium and phosphate buffered solution for 15–30 min. The scaffolds were imaged using a Nikon TE300 inverted microscope (NIKON CORPORATION, Tokyo, Japan).

4.2.8 Flow Cytometry

Single cell suspensions were collected from the scaffolds. A fixable yellow dead stain kit (Invitrogen) was used to identify dead cells. Cells were fixed with 4% paraformaldehyde for 10 min on ice, permeabilized in 1% v/v Triton-X 100, washed with PhosFlow Perm/Wash Buffer I (BD Biosciences, San Jose, CA, USA), and resuspended in a buffer. Antibodies PE anti-nestin (BDB561230), PerCP-Cy5.5 anti-SOX1 (BDB561549), Alexa Fluor 647 anti-SOX2 (BDB560302), and Alexa Flour 488 anti-PAX6 (BD561664) were added, incubated on ice for 1 h, and washed with a buffer. The cells were resuspended in 200 μL of buffer and stained with DAPI. All samples were analyzed on a LSRII flow cytometer (BD Biosciences), and data were plotted using a FlowJo software (Tree Star Inc., Ashland, OR, USA).

4.2.9 Immunocytochemistry for NSC marker proteins

Human neural stem cell ICC kits (Cat. A24354, Thermo Fisher Scientific) were used, following the manufacturer's instructions. Briefly, scaffolds bearing the cells were rinsed with PBS, fixed with cold 4% paraformaldehyde on ice for 10 min, permeabilized for 10 min, blocked for 1 h, and stained with SOX2 and nestin primary antibody overnight at 4°C. Secondary antibodies, Alexa Fluor 488 and 555, were added to the scaffolds the next day and the scaffolds were incubated for 1–2 h on ice, washed thrice with PBS, stained with DAPI, and mounted in a ProLong Gold anti-fade reagent (Thermo Fisher Scientific). Fluorescence images were acquired using a Nikon TE 300 inverted microscope.

4.2.10 Statistical analysis

All results are presented as mean ± standard deviation (SD). Statistical significance was determined using one-way analysis of variance with Tukey's multiple comparison test. Significant differences were set at p-value < 0.05.

4.3 Results and Discussion

4.3.1 Development of porous microcarriers for hNSC expansion in a defined environment condition

Four main culture modes commonly employed in bioreactors are nonadherent (matrix-free) suspension, aggregate suspension, adherent nonporous microcarriers, and adherent porous microcarriers (**Figure 4.1**). The utilization of microcarriers in adherent cultures allows for cell adhesion on controlled growth surfaces in dynamic culture conditions. The surface characteristics and microstructure of microcarriers play critical roles in cell quality and yield. In comparison to nonporous microcarriers, the porous design provides the largest growth surface area per volume and desirable interior porous structure to protect cells from shear stress. Therefore, we fabricated

porous scaffolds made of chitosan to serve as microcarriers for the expansion of hNSCs in a rotational dynamic bioreactor platform. Chitosan scaffolds with varying weight percentages were utilized to investigate the influence of structural and mechanical properties on cell fate under dynamic conditions. Collagen was used as a control sample due to its well-established role as a scaffold material in tissue engineering.[158-160] Although both chitosan and collagen have been applied in various tissue culture substrates, including neural tissues, they possess distinct physical properties and bioactivities on hNSCs.[160-165]

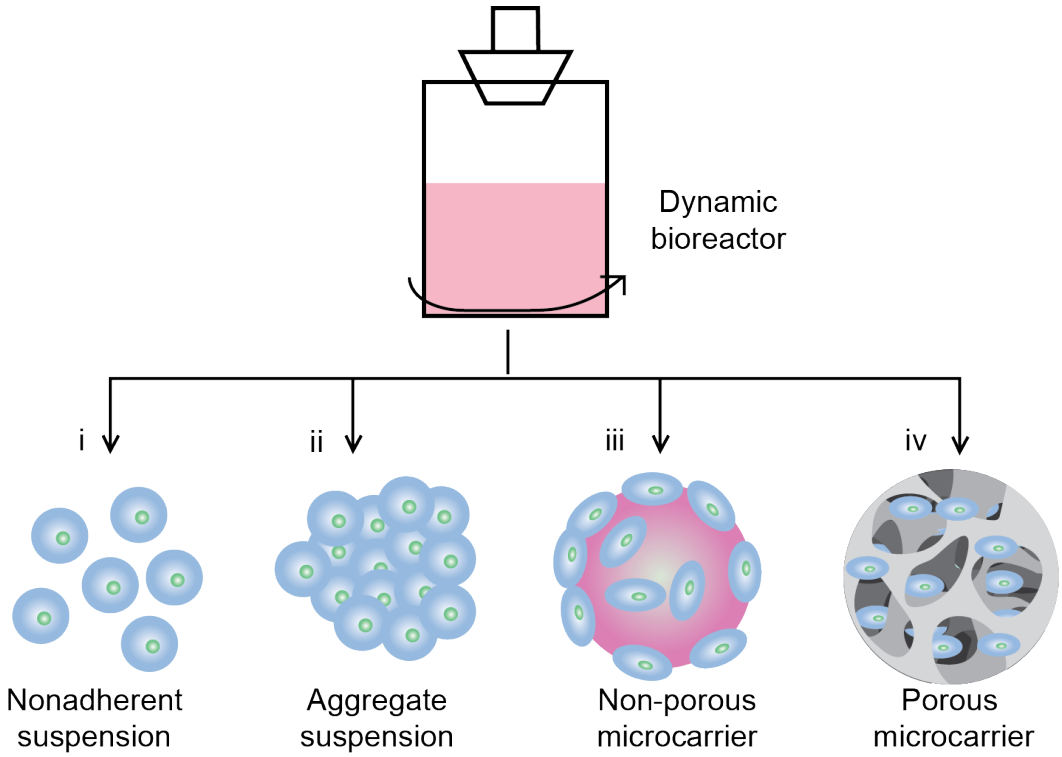


Figure 4.1 Illustration depicting different culture methods in a dynamic bioreactor, including i) nonadherent suspension, ii) aggregate suspension, iii) nonporous microcarrier, and iv) porous microcarrier.

4.3.2 Scaffold Microstructure Analysis

The microstructure of the scaffolds plays a crucial role in facilitating nutrient cycling and metabolite exchange. To achieve the desired porous structure, the scaffolds were prepared through

lyophilization, which involves phase separation during freezing and subsequent sublimation of the solvent. Precise control of nucleation and freezing solvent was employed to establish the desired porosity. Chitosan or collagen was mixed with KBr to form a pellet before FTIR analysis, while chitosan was dissolved in DCl/D_2O for ^{1}H NMR analysis. The FTIR spectra of chitosan and collagen are shown in **Figure 4.2a** and **4.2b**, respectively, and exhibit good agreement with previously reported.[166,167] The ^{1}H-NMR spectrum of chitosan, obtained at at 300 MHz, 2.5% DCl/D_2O, 25˚C:, displayed the following peaks: 4.80 (s, H-1 of GlcN), 4.50 (s, H-1 of GlcNAc), 3.03 (s, H-2 of GlcN), 2.75 – 4.15 (m, H-2/6), and 1.95 (s, H-Acetyl of GluNAc), as shown in **Figure 4.2c**. The degree of deacetylation was calculated to be 97% using Equation 1, which falls within the range provided by the supplier.[168,169]

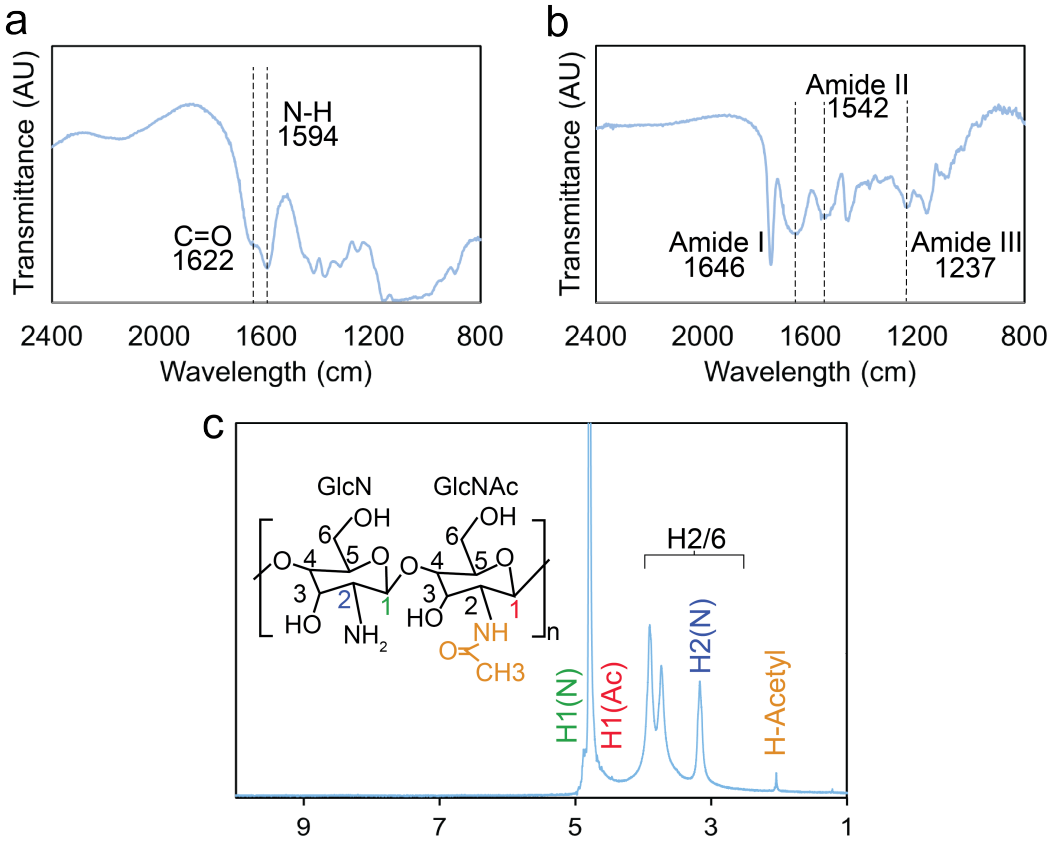


Figure 4.2 Spectroscopic analysis of scaffolds. The FTIR spectra acquired a) from chitosan, and b) collagen. c) ^{1}H NMR spectrum acquired from chitosan.

Following lyophilization, the scaffolds were mounted on stubs using carbon adhesive tape for imaging purpose. ImageJ software was utilized for manual measurement of pore diameters. **Figure 4.3a** presents SEM images displaying the cross-sections of various scaffolds, including 0.5 wt% collagen (05COL), 0.5 wt% chitosan (05CS), 2 wt% chitosan (2CS), and 4 wt% chitosan (4CS). Lower polymer concentrations resulted in visibly larger interconnected pores. Analysis of pore size analysis was performed by measuring the pore diameters from SEM images (**Figure 4.3b**). The average pore diameter for 05COL scaffolds was 289 ± 67 μm, similar to commercially available collagen scaffolds.[170] The selected collagen concentration of 0.5 wt% aligns with previous studies.[171-173] On the other hand, 05CS scaffolds exhibited an average pore diameter of 214 ± 48 μm, significantly different from that of 05COL scaffolds. As chitosan concentration increased, the pore diameter decreased, with average values of 85 ± 17 μm and 65 ± 13 μm for 2CS and 4CS scaffolds, respectively. All scaffolds possessed pore diameters suitable for stem cell growth,[174] particularly hNSCs,[146] providing ample internal surface area for cell proliferation. Moreover, the small pore sizes could limit the growth of hNSC clusters, mechanically preventing the formation of necrotic cores and aiding in the long-term culture and maintenance of hNSCs.

Scaffold porosity was determined using a modified isopropanol displacement method. Briefly, the scaffolds were immersed in isopropanol and subjected to vacuum to remove air bubbles. Weight measurements were recorded before and after submersion. The porosity (**Figure 4.3c**) decreased from 92.0% ± 1.2% to 86.2% ± 2.6% as chitosan concentration increased from 0.5% to 4%. The porosity of 05COL scaffolds was comparable to that of 05CS scaffolds at 92.3% ± 1.4% ($p > 0.05$, not significant). Additionally, specific surface area analysis using BET (**Figure 4.3d**) revealed an increase in specific surface area with higher chitosan concentrations: 15.34 ±

2.66 m^2/g, 12.2 ± 1.41 m^2/g, and 5.4 ± 1.89 m^2/g for 05CS, 2CS, and 4CS scaffolds, respectively. Porosity and surface area measurements account for the overall properties of the scaffold, encompassing both the internal intermolecular structures and the visible macropores (50–350 μm in diameter). Collagen and chitosan, being relatively hydrophilic materials, can form nanoscale crystals during freezing and leave voids after sublimation due to solvent (water) bonding in intermolecular spaces. The formation of intermolecular bonds via hydrophobic interactions and hydrogen bonding is more likely in chitosan than in collagen. Chitosan with a high uniform degree of deacetylation is known to exhibit higher crystallinity upon drying.[175] Higher polymer concentrations promote inter- and intramolecular interactions, resulting in reduced nanoscale interaction of polymer chains, which leads to lower material specific area at the nanoscale level and lower porosity in 05CS scaffolds compared to 05COL scaffolds.

The microstructure analyses confirm that the scaffolds meet the structural requirements of microcarriers, with highly interconnected pores possessing appropriate diameters to retain media, facilitate nutrient exchange, and provide a larger growth area compared to 2D flat surfaces. These characteristics make the scaffolds well-suited for their intended purpose of supporting hNSC expansion in a dynamic culture environment.

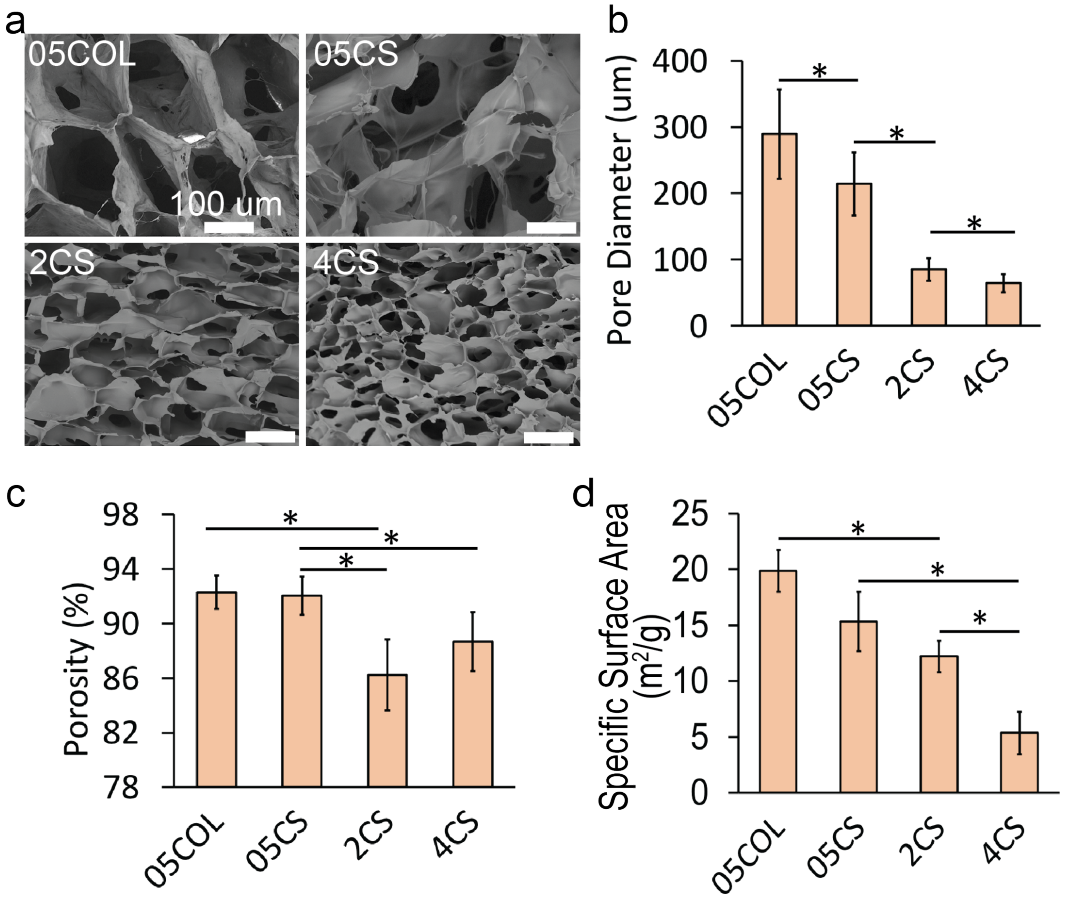


Figure 4.3 Microstructural analysis of porous scaffolds. (a) SEM images of dry porous scaffolds with a scale bar of 100 µm. (b) Pore diameters of the scaffolds measured from SEM images (n = 65). (c) Porosity through isopropanol displacement method (n = 5). (d) BET-specific surface area (n = 3). All data are presented as mean ± SD. Statistical significance, indicated by *, was determined using Tukey's test ($p < 0.05$).

4.3.3 Mechanical properties of the scaffolds

To understand the microenvironment provided by the scaffolds, their potential influence on cell mechanosensing, and their ability to withstand agitation in dynamic cultures, a detailed analysis of their mechanical properties was conducted. This analysis encompassed both dry scaffolds and those soaked in PBS. The compressive elastic moduli (**Figure 4.4a**) of dry chitosan scaffolds exhibited an increasing trend from 4.1 ± 0.9 kPa to 284.5 ± 22.9 kPa and 681.9 ± 43.0 kPa, corresponding to the increasing chitosan concentration of 05CS, 2CS, and 4CS, respectively. Dry

collagen scaffolds possessed a compressive elastic modulus of 10.0 ± 0.008 kPa. Considering that cell culture was conducted in a medium while the scaffolds were hydrated, compression tests were also performed on "wet" scaffolds. In the hydrated state, the elastic moduli were 1.2 ± 0.4 kPa, 7.4 ± 0.7 kPa, and 71.2 ± 9.3 kPa for 05CS, 2CS, and 4CS scaffolds, respectively. However, wet 05COL scaffolds could not be evaluated through compression tests as they became excessively soft upon hydration. The elastic moduli of both dry and wet 2CS and 4CS scaffolds were higher than those of dry collagen scaffolds.[146] Representative stress–strain curves of compression tests are presented in **Figure 4.4b**, demonstrating an increase in ultimate compressive strength with higher chitosan concentration. These results suggest that chitosan scaffolds may serve as superior protective structures for hNSCs compared to collagen scaffolds in dynamic cultures where microcarriers endure compression and shear forces.

To evaluate the micro- to nanoscale elastic moduli of wet scaffolds, AFM analysis was employed (**Figure 4.4c**). This analysis allowed the characterization of mechanical properties relevant to mechanosensing. While compression tests address macroscale structural integrity and the resistance of pore walls to buckling, AFM tips measure intermolecular attraction and the resistance of chitosan or collagen polymer chains on the interior surface of the pore walls. The 05COL scaffolds exhibited the lowest average elastic modulus (3.7 ± 17.9 kPa), whereas the values for chitosan scaffolds increased from 50.1 ± 123.9 kPa to 83.2 ± 62.3 kPa and 160.9 ± 121.5 kPa as the chitosan concentration increased from 05CS to 2CS and 4CS, respectively. The localized compression, tension, and nano- or microscale features of the substrate play a crucial role in regulating cell fate through cell transmembrane receptors, ultimately influencing cytoskeleton and cell morphology. In our previous paper, we compared chitosan thin films with differing degrees of deacetylation and its effect on the mechanical properties of the films.[82] We found that a higher

degree of deacetylation decreased the elastic modulus of the films, but increased cell attachment, proliferation, and multipotency. Additionally, increasing the molecular weight of the chitosan will increase the elastic modulus of the scaffold due to chain entanglement.[176]

In the subventricular zone and hippocampal dentate gyrus, where adult hNSC populations reside in humans and rodents, the reported elastic modulus is approximately 3 kPa.[177,178] However, there exists a considerable variation in measurement methods and results. Furthermore, the optimal elastic modulus for hNSC substrates remains uncertain, given the diverse outcomes observed in cell responses to softer substrates despite the success of conventional culture protocols on rigid plasticware. In this study, scaffolds with a wide range of mechanical properties were utilized to better assess the effect of these properties on cell fate. Mechanical properties, choice of materials, and resulting substrate surfaces collectively exert a coherent influence on cell responses.

4.3.4 Stability and degradation in culture medium

Understanding the stability and degradation characteristics of scaffolds is crucial for designing effective tissue engineering strategies. To evaluate the stability of the scaffolds, their weights were monitored over a three-week period in a culture medium under rotation at 37°C. Both chitosan and collagen have been shown to degrade *in vitro* and *in vivo*, with degradation rates depending on the specific conditions. Collagen, a widely used scaffold material, completely degrades after five weeks in a static culture medium.[179] Chitosan, on the other hand, can undergo partial depolymerization through hydrolysis within a few days when subjected to dynamic conditions in a medium.[153] Crosslinkers, such as genipin, can be added to the scaffolds to enhance mechanical properties and stability, however, they can also increase the autofluorescence of the scaffolds making it difficult to image the cells.[180]

In our study, all the scaffolds produced did not exhibit significant deterioration or degradation over the course of 21 days. Differences in the data may be due to scaffold-to-scaffold variability. They maintained over 90% of their weight after this period (**Figure 4.4d**). However, the 05COL scaffolds showed more variability and experienced a greater decrease in weight compared to the chitosan scaffolds. We expect our scaffolds to perform similarly through prolonged durations, the cells may also leave behind proteins that could adhere to the scaffold walls. These findings indicate that chitosan scaffolds are more durable in dynamic cultures, suggesting their suitability for long-term culture applications.

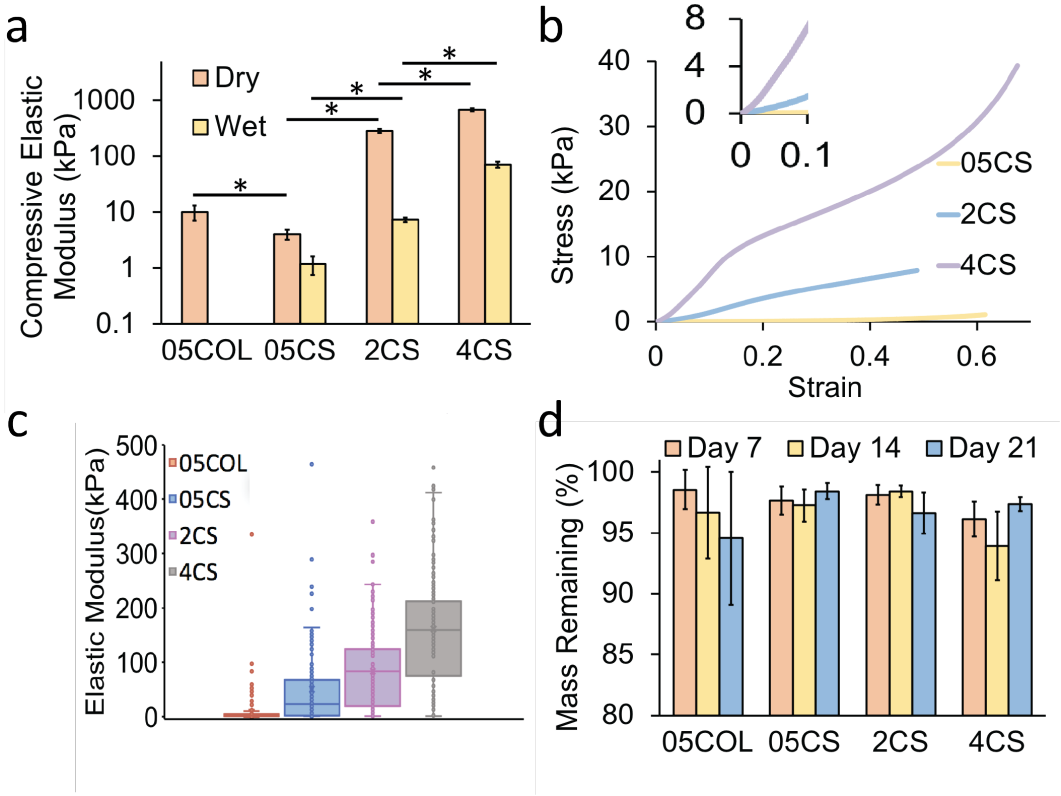


Figure 4.4 Mechanical properties of the scaffolds. (a) Compressive modulus of the scaffolds in dry and wet conditions (n = 5). (b) Stress–strain curves of the scaffolds in a wet condition. The 05COL scaffold was too soft to be measured in a wet condition. (c) Elastic modulus of the scaffolds in a wet condition. (d) Degradation of the scaffolds in a dynamic condition. Degradation rate analysis was performed by comparing the initial weight of the dry scaffolds with the dried weight of the scaffolds after incubation. There are no significant changes in weight after 21 days of

incubation (n = 4). The differences between the samples are considered significant when marked with * based on Tukey's test ($p < 0.05$).

4.3.5 Maintenance of hNSCs in dynamic cultures

We conducted dynamic culture experiments using porous scaffolds as microcarriers to support the growth of two different hNSC lines, namely hNSC-H14 and ReNcell VM. Initially, the cells were seeded onto the scaffolds in static well plates for one day and then transferred into dynamic culture vessels. The growth and proliferation of the cells were assessed using the alamarBlue viability/metabolic activity assay. The metabolic activity of hNSC-H14 and ReNcell in the scaffolds showed different trends (**Figure 4.5a** and **4.5b**). For hNSC-H14, the metabolic activity in chitosan scaffolds showed a slight decrease on day 3 of culture, followed by consistent increases until day 11. However, it decreased again on day 15, likely due to growth arrest caused by cell confluency. In contrast, cells in the 05COL scaffolds exhibited a modest increase on day 7 and overall limited growth after 15 days compared to those in chitosan scaffolds. As for ReNcell, the metabolic activity steadily increased in all scaffolds and reached its peak on day 11, followed by a decline on day 15, possibly due to confluency related factors. To accommodate longer culture periods, the initial cell seeding density could be decreased. Notably, the 4CS scaffolds demonstrated the highest overall metabolic activity for both hNSC-H14 and ReNcell. Consequently, the 05COL scaffolds exhibited restricted cell adhesion, which likely contributed to poorer activities compared to the 4CS scaffolds. Furthermore, the larger pore diameter of the 05COL and 05CS scaffolds might have failed to adequately protect or retain hNSC colonies.

To visualize cell adhesion and proliferation, the scaffolds were stained with calcein-AM and ethidium homodimer-1. **Figure 4.5c** illustrates the stained live and dead cells in the scaffolds, focusing on the hNSC-H14 cell line. As the culture progressed, the cells in the chitosan scaffolds exhibited more extensive expansion compared to those in collagen scaffolds. Moreover, the cells

in the 4CS scaffolds displayed polarized morphology more frequently than those in the 05COL scaffolds, suggesting a stronger adhesion to the 4CS scaffolds. Conversely, in the 05COL scaffolds, the cells formed larger clusters due to the preference for intercellular adhesion rather than cell-collagen interactions. Previous studies have reported that the increased surface positive charge resulting from the higher amino group content of chitosan promotes cell adhesion.[181] This favorable adhesion to chitosan scaffolds could further enhance cell proliferation.[181]

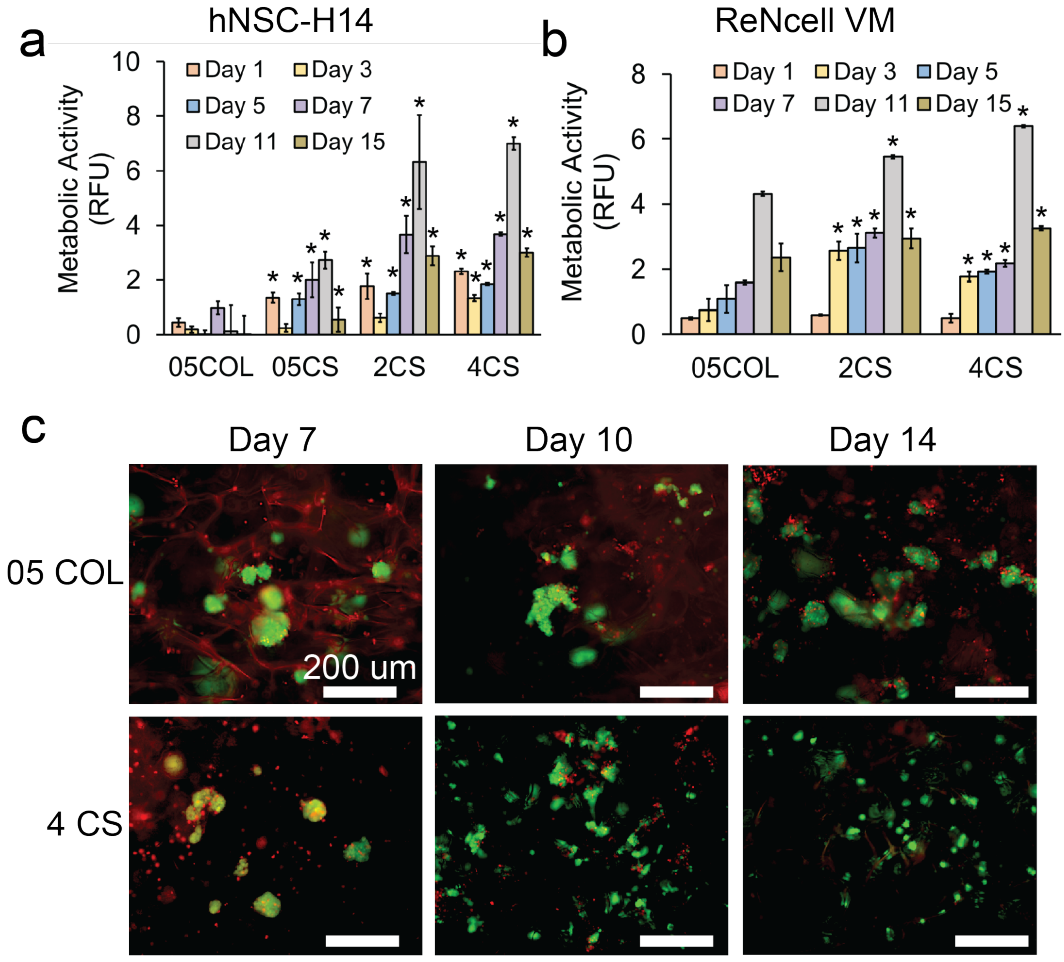


Figure 4.5 Assessment of cell proliferation rates and cell fate in hNSC-H14 and ReNcell VM cell lines using alamarBlue and live/dead stain. a) Metabolic activity of hNSC-H14 measured by alamarBlue assay. b) Metabolic activity of ReNcell VM measured by alamarBlue assay. c) Fluorescent images of live (green) and dead (red cells stained with calcein-AM and ethidium homodimer-1, respectively. Scale bars represent 200 µm. An * means the difference between that sample and the respective 05COL sample is significant based on Tukey's test.

Cells were harvested from the scaffolds over a period of 15 days, fixed, and then prepared for flow cytometry analysis. The multipotency of the cells collected from the microcarriers was assessed by staining for two crucial NSC protein markers, SOX2 and nestin. The time course of the populations positive for $SOX2^+/nestin^+$ in both cell lines is depicted in **Figure 4.6a** and **4.6b**. **Figure 4.6c** illustrates the cell populations gated for $SOX1^+/PAX6^+$ expression in ReNcells after seven days of culture, representing additional NSC protein markers. The 05COL scaffolds exhibited the highest populations of both $SOX2^+/nestin^+$ and $SOX1^+/PAX6^+$ cells, while among the chitosan conditions, the 4CS scaffolds showed the most favorable results. However, as the 05COL scaffolds have the largest pore size and lowest mechanical properties it is likely that only pristine cells are able to remain within the scaffolds, whereas non-pristine cells are likely able to remain in the chitosan-based scaffolds due to their smaller pore size and stronger mechanical properties. Notably, hNSC-H14 demonstrated the highest percentage of $SOX2^+/nestin^+$ population on the 11^{th} day of culture, which correlated with the metabolic activity data. Moreover, the porous scaffolds with large specific surface areas allowed hNSCs to proliferate for a longer duration compared to conventional 2D protocols, while preserving their proliferative and multipotent state. Typically, in regular 2D culture protocols, hNSCs require passage every 3–5 days upon reaching 90%–95% confluency to prevent growth arrest and spontaneous differentiation.[182] The growth kinetics and time course analysis of NSC proteins indicated that, in this study, the cells needed to be detached from the porous chitosan scaffolds before the 11^{th} day of culture to ensure effective expansion of the entire population. However, despite having the narrowest specific surface area and porosity, the 4CS scaffolds achieved the highest yield of hNSCs, suggesting a potential protective effect against shear stress in a bioreactor. Stem cells possess mechanisms to sense

mechanical stress, and the flow generated by agitation can induce cell death.[182,183] The higher compressive modulus of the 4CS scaffolds, compared to other chitosan scaffolds, may have shielded hNSCs from shear stress under dynamic conditions.

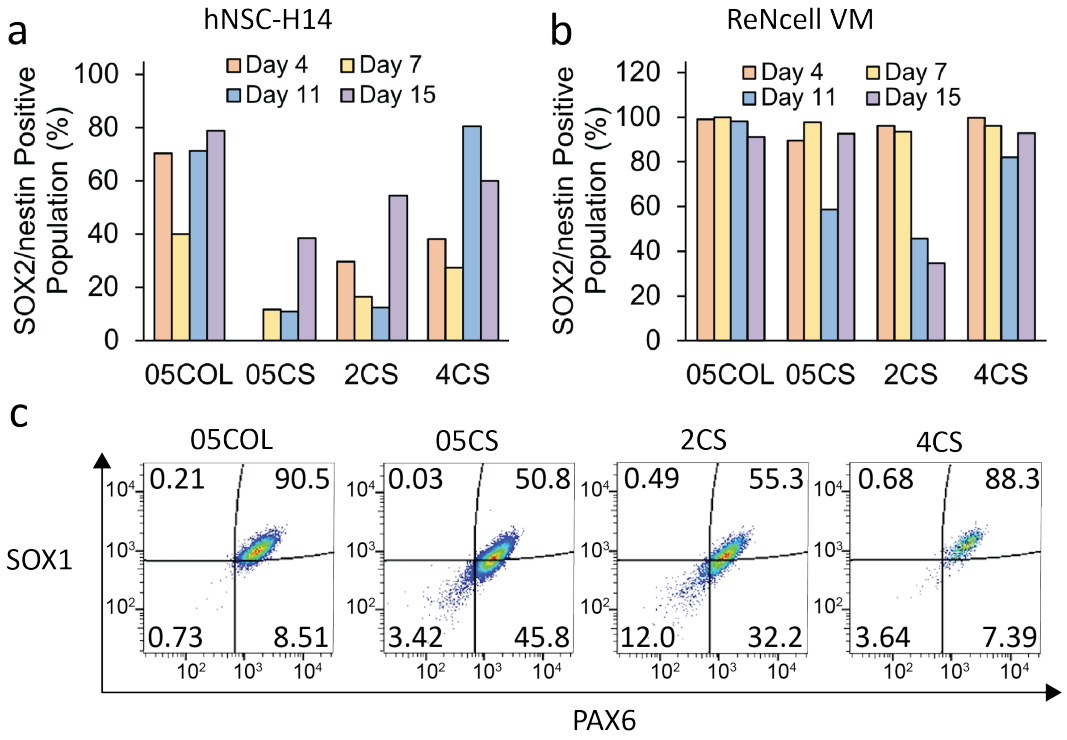


Figure 4.6 Flow cytometry analysis of cells collected from both cell lines over a 15-day period. Protein expression levels assessed for a) hNSC-H14 and b) ReNcell. c) Dot plots representing the expression of SOX1 and PAX6 in ReNcells on day 7.

Further investigation into longer culture periods, lasting up to three weeks, was conducted. Immunostaining for SOX2 and nestin (**Figure 4.7**) revealed that the cells were able to sustain expression of these crucial NSC marker proteins for an extended duration compared to regular 2D controls. Over the three-week culture period, hNSCs cultured on 4CS scaffolds formed adherent aggregates within the scaffold pores. SOX2 localization was predominantly observed in the nucleus, although some translocation into the cytoplasm was evident, indicating partial differentiation resulting from overcrowding within the pores. At this stage, some aggregates

reached confluency, occupying the pores without exceeding the desired size range of 300-500 µm in diameter to prevent necrosis.

Chitosan has been reported to promote the proliferation and differentiation of neurons and astrocytes.[183] However, its impact on hNSC maintenance has shown inconsistent results. In this study, multipotent hNSC colonies were successfully maintained in chitosan porous scaffolds optimized for use as microcarriers in dynamic cultures for up to three weeks. The chitosan scaffolds demonstrated their feasibility for long-term expansion of hNSCs in bioreactors under xeno-free and chemically defined culture conditions.

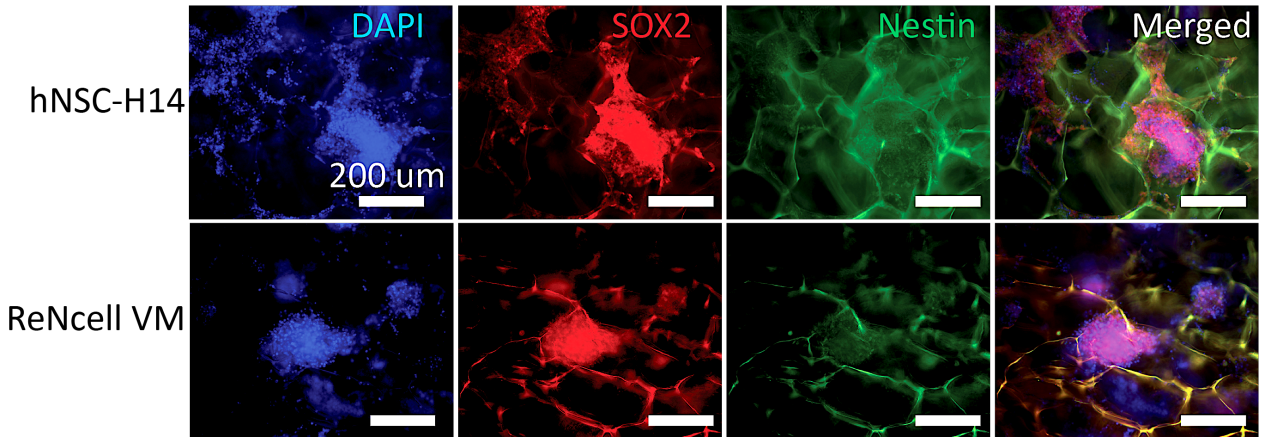


Figure 4.7 Immunofluorescence staining of hNSCs for SOX2 (red), nestin (green), and DAPI (blue) on the 4CS scaffolds after 3 weeks for hNSC-H14 (top) and ReNcell VM (bottom). Scale bars are 200 µm.

Chapter 5 Continuous Flow Bioreactor with Multi-Sensor Monitoring for Biomedical Applications

5.1 Introduction

Tissue engineering develops biological substitutes that restore, maintain, or enhance tissue function.[163,184,185] This field combines three-dimensional (3D) scaffolds, cells, and bioactive molecules to create tissue models that replicate the architecture and functionality of native tissues. However, traditional static in vitro culture methods often fall short, as they struggle to deliver adequate nutrients and oxygen to the interior of 3D scaffolds, resulting in hypoxic conditions that impair cell viability, proliferation, and differentiation.[186-189]

Bioreactors (BRs) have emerged as vital tools to address these challenges by providing dynamic culture environments that better mimic physiological conditions.[50,190,191] These systems enhance mass transport, improve cell seeding efficiency, and support cellular differentiation through controlled fluid flow, mechanical stimulation, and precise regulation of environmental parameters. Various BR designs, such as perfusion, wave-motion, and rotational systems, have been developed to optimize tissue culture. Perfusion BRs pump media through cell-seeded scaffolds,[192-194] wave-motion BRs oscillate fluid over samples,[195-198] and rotational BRs create microgravity-like conditions with laminar flow and low shear stress, suspending cells or constructs in circulating media.[199-201]

Despite decades of use in tissue engineering, no single BR system has emerged as an ideal, widely adopted solution.[202-207] Current designs face limitations, including restricted size, complexity, maintenance challenges, sterility issues, and high costs.[208,209] For example, perfusion BRs cannot provide microgravity, wave-motion BRs may generate turbulent flow with elevated shear stress, and impeller-driven BRs risk damaging cells through physical impact. Rotational BRs, however, offer microgravity and consistent low shear forces without direct cell impact,

though designing user-friendly, cost-effective systems that simultaneously monitor and control multiple parameters to mimic in vivo conditions remains a challenge.

Effective operation of BR systems requires precise control of key variables, including pH, temperature, dissolved oxygen, CO_2, medium flow, and rotation speed (RPM). Optimal pH and temperature ranges, adequate oxygen levels to prevent hypoxia, balanced CO_2, and consistent nutrient supply are essential for maintaining a suitable environment for cell growth.[210] Medium flow and RPM must be carefully adjusted to provide beneficial mechanical stimulation through fluid shear generated by flask rotation and media circulation, without causing harmful shear stress.[56,196,211] Mechanical stimulation, which mimics in vivo dynamic forces like muscle and joint loading, supports various cell types, although the ideal level depends on the tissue type.[212-215] While methods like magnetic stir bars and impellers can enhance mass transport, they often generate turbulence and cause cell damage, hindering tissue growth.[56]

To address these issues, we developed a novel rotational, continuous-flow BR system with integrated multi-sensor monitoring and control. Our design incorporates real-time sensors for pH, oxygen, CO_2, and temperature to maintain stable, optimal conditions for cell growth. A regulated nutrient supply system ensures consistent media delivery, while a speed-controlled rotational mechanism generates low shear forces and enhances mass transport, simulating physiological environments. A custom swivel connector prevents tubing tangles, enabling uninterrupted gas and media exchange during rotation. These components are unified by a control system that adjusts settings dynamically based on sensor feedback.

This integrated design improves reproducibility and stability in cell culture experiments. Its versatility is demonstrated through both macro- and micro-bioreactor configurations, accommodating diverse culture volumes and applications. Testing showed the system accurately

monitors and maintains pH, oxygen, CO_2, and RPM over extended periods, detecting subtle changes in culture conditions and tuning RPM for consistency. Additionally, the BR successfully cultured cancer cells on scaffolds for short-term experiments, underscoring its adaptability. By offering a precise, dependable, and adaptable platform, this BR system holds promise for advancing tissue engineering, regenerative medicine, and other biomedical applications.

5.2 Materials and Methods

5.2.1 Bioreactor and Its Components

The bioreactor contains the following the off-shelf components including: 12V DC motor (Servocity, Winfield, Kansas) providing rotation to the BR chamber; a rubber base chamber adaptor to hold the BR chamber; filter sterilization flasks serving as the BR chambers; flat bottomed tubes serving as reaction chambers for the microreactor (Fisher Scientific, Hampton, NH); sterile silicone tubing (Masterflex, Gelsenkirchen, Germany) and Tygon® tubing to conduct fluid and gas media to the BR chambers; four stage Masterflex peristaltic pump (Masterflex, Gelsenkirchen, Germany) to move fluid and gas media; barbed fittings (McMaster-Carr, Elmhurst, Illinois) to connect tubing ends, incubator (Thermo Scientific, Waltham, Massachusetts) to maintain cell culture medium temperature and maintain 5% CO2 atmosphere; electric coil heater (McMaster-Carr, Elmhurst, Illinois) maintaining BR housing temperature; sensors that measure oxygen (Atlas Scientific, Long Island City, New York) and CO2 (Sandbox Electronics); a micro-pH sensor (Atlas Scientific, Long Island City, New York); an Arduino Due (Arduino, Ivrea, Italy) controlling the DC motor and interfacing with sensors and computer; a Hall effect sensor and magnet (McMaster-Carr, Elmhurst, Illinois) monitoring motor RPM; and a motor shield (Adafruit, New York, New York) interfacing the motor and Arduino. The CO2 atmosphere is generated in the incubator and then pump through the bioreactor using a peristaltic pump.

5.2.2 pH probe evaluation

The BR chamber and tubing were first saturated with water using the peristaltic pump to assess the long-term efficacy of the pH probe. Next, 250 mL of a pH 10 standard solution (MilliporeSigma, Burlington, MA) was introduced, displacing the water. After one hour, this was replaced with 250 mL of a pH 4 standard solution (MilliporeSigma, Burlington, MA). The Arduino and Python program measured and recorded pH values throughout. To evaluate the probe's precision, fresh culture medium was circulated via the peristaltic pump until readings stabilized. Then, used culture medium replaced the fresh medium, and pH values were again recorded using the Arduino and Python system.

5.2.3 Oxygen Probe Evaluation

Water was first boiled for one hour to remove entrained oxygen from the water to evaluate the efficiency of the oxygen probe. This boiled water was then cooled down to room temperature and stored without exposure to air. The BR chamber and tubing were first saturated with room temperature water using the peristaltic pump, and then boiled water was allowed to saturate the system. The preciseness of the oxygen probe was evaluated by first saturating the BR chamber and tubing with used medium. After the reading was stable for 4 minutes, fresh media was added to the system and allowed to circulate.

5.2.4 CO2 Probe Evaluation

The BR system's ability to maintain CO_2 levels throughout the BR chamber and tubing for prolonged periods of time was assessed by monitoring the CO_2 level of the system for 1 hour. CO_2 readings were taken once per rotation of the bioreactor vessel. The system's ability to recover after destabilization was evaluated by first allowing the system to come to equilibrium at 5% CO_2. Then

air was introduced into the system by disconnecting the inlet tube fitting and allowing air from the outside to enter the tubing. Finally, the tubing was reconnected, allowing the system to equilibrate to 5% CO_2.

5.2.5 RPM Probe Evaluation

The RPM sensor was first evaluated by directly connecting the motor to a DC power source and the output voltage was adjusted such that the RPM was set near 16 and was monitored for 1 hour. Next, the motor was connected to the Arduino system and the RPM was set again to 16. The initial starting RPM was deliberately set to 14 to show how the Arduino and controlling python program slowly changes the power output to adjust the RPM to within 1% of a given value. RPM was monitored and adjusted throughout the duration of the experiment. Then, the motor was connected to a DC power source and voltage was adjusted such that the RPM started near 50, and RPM was again monitored throughout the duration of the experiment. Finally, to see the preciseness and adjustability of the system the motor was connected to the Arduino and RPM was varied in increments of 10 starting at 15 and ending at 65RPM.

5.2.6 Scaffold fabrication

Chitosan scaffolds were fabricated via freeze-drying. Briefly, chitosan (MilliporeSigma, St Louis, MO, USA) was purchased with a molecular weight of 50-100kDa and was dissolved homogenously in 1N acetic acid at a concentration of 6 wt% (6CS). The solution was cast into a 24 well plate and frozen at -20ºC for 8 hours. Then, a VirTis Virtual Lyophilizer (SP Scientific, NY, USA) was used to lyophilize the scaffolds for 1-3 days. The scaffolds were cut into 0.4mm sections using a vibratome. The dried samples were neutralized with a mild basic solution (15mL

33% NH_4OH, 35mL DI water, and 500mL ethanol) for 30 minutes and then rinsed three times with 70% ethanol and PBS to sterilize.

5.2.7 Cell culture

U-87 MG human glioblastoma cells were purchased from the American Type Culture Collection (ATCC, Manassas, VA). Cells were maintained in DMEM and were fully supplemented with 10% FBS and 1% Pen Strep in a humidified incubator with 5% CO2 at 37 °C. After plating the cells onto the scaffolds at 200,000 cells/scaffold, the seeded scaffolds were incubated for 4 days. After 4 days, the scaffolds were placed into the macroreactor running at RPM of 5 maintained for the duration of the experiment. In the macroreactor, a constant volume of 60 mL of medium was maintained in the reaction vessel. In the microreactor, cell-laden scaffolds were prepared the same method as was as in the macroreactor, with only difference being the usage of 750 µL of medium per scaffold per day.

Human neural stem cells hNSC-H14 (WB0195), derived from the NIH-approved hESC-H14 (WA14), were obtained from WiCell Research Institute (Madison, WI, USA). The cells were expanded and cultured according to WiCell NSC protocols. Briefly, the cells were cultured on Geltrex®-coated tissue culture dishes with medium refreshed every other day. Human recombinant basic fibroblast growth factor (bFGF, Gibco®) was supplied every day at 20 ng/mL. The NSC culture medium contains Neurobasal medium (Gibco®) supplemented with bFGF, B27, MEM NEAA, and GlutaMAX™. Cells were passaged every 3–5 days and dissociated with Versene when the growth area is over 90% confluent. The day of passaging was considered culture day 0. For the culture in 3D scaffolds, the cells were plated at 0.2 million cells in each 24-well sized scaffold following regular passaging procedures. The cells used in the experiments were at P34. Cells were maintained in a humidified incubator with 5% CO_2 at 37°C. After 4 days of culture the cell laden

scaffolds were placed into the micro-reactor. 2mL of medium was added every other day, and bFGF was added every day at a concentration of 20 ng/mL.

5.2.8 Cell metabolic activity and live/dead imaging

Cell metabolic activity was evaluated using an alamarBlue assay (Sigma Aldrich, St Louis, MO, USA). The scaffolds were removed from the BR or their respective well and placed into a new well. The new well was then filled with a diluted alamarBlue solution (10X dilution with DMEM culture medium, 110 μg/mL resazurin) and incubated for 80 minutes in an incubator. The fluorescence intensity of the solution was measured at 590 nm using an excitation of 560 nm on a SpectraMax M2 microplate reader (Molecular Devices, Sunnyvale, CA, USA). All the measured fluorescence intensities were normalized to a standard control well. Cell viability was evaluated using a LIVE/DEAD Viability/Cytotoxicity Kit (Invitrogen, Thermo Fisher Scientific) according to the manufacturer's protocol. Briefly, cells were stained with Calcien AM at 1 μM for viable cells and propidium iodide (Thermo Fisher) was used at 10 μM for 15 minutes at room temperature. The samples were imaged using a Nikon TE3000 Inverted Microscope (Nikon, Tokyo, Japan).

5.2.9 Immunocytochemistry (ICC) and microscopy

The primary antibodies SOX2 (Biolegend) and nestin (Biolegend) were used to characterize hNSC marker protein expression following the manufacturer's protocol. Briefly, the hNSCs were cultured as described above. After 7 days, the cells were rinsed with PBS, fixed with cold 4% paraformaldehyde for 10 minutes on ice, permeabilized for 10 minutes, blocked for 1 hour, and stained with primary antibodies at 4°C overnight. Cells were then incubated with secondary antibodies for 2 hours on ice, washed three times and stained with DAPI before mounted in Prolong

Gold antifade reagent (Invitrogen; Carlsbad, CA). Fluorescence images were acquired using a Nikon TE300 inverted microscope (Nikon, Tokyo, Japan).

5.2.10 Flow cytometry analysis for NSC protein expression

Cells were dissociated from the scaffolds with Accutase and washed in PBS. The cells were subsequently fixed in 4% paraformaldehyde for 10 minutes, permeabilized in 1 %v/v Triton-X 100 in PBS, and then washed with PhosFlow Perm/Wash Buffer (BD Biosciences, San Jose, CA). The cells were resuspended in 100 µL cell Perm/Wash Buffer, incubated with fluorophore-conjugated antibodies SOX2, nestin, Ki67, and SOX1 for 60 minutes on ice in the dark, washed with Perm/Wash Buffer, and resuspended in 0.3 mL Cell Staining Buffer (BioLegend; San Diego, CA). Cells were analyzed on a LSRII flow cytometer (BD Biosciences) and using FlowJo software (Tree Star Inc., Ashland, OR). The antibody PE anti-nestin (BDB561230), Alexa Fluor® 647 anti-SOX2 (BDB560302), Ki67, and SOX1 were purchased from BD Bioscience (BD Biosciences).

5.2.11 Statistical analysis

Statistical significance was assessed using an unpaired, two-tailed Student's t-test to determine the p-value. The number of independent measurements or experiments (n) is provided in the figure captions. A p-value of less than 0.01 was considered statistically significant. All statistical analyses were conducted in Microsoft Excel using a student's t-test.

5.3 Results and Discussion

5.3.1 Bioreactor Design and fabrication

The dynamic bioreactor is engineered to support continuous nutrient and gas exchange, critical for cell culture and fermentation processes. It comprises a bioreactor chamber linked to a nutrient reservoir and CO_2 supply via a swivel connector, ensuring uninterrupted media flow. The system

incorporates a water bath for precise temperature regulation and a motor for consistent agitation. Integrated valves, pumps, and sensors, managed by a computer through a stimuli control device, enable seamless operation. Fabrication focuses on assembling these components to maintain sterility, efficiency, and reliability.

As illustrated in **Figure 5.1a**, the dynamic bioreactor system features a motor-rotated chamber with sensors monitoring oxygen, CO_2, and pH to optimize cell culture conditions. **Figure 5.1b** provides an exploded view of the swivel connector The design includes a rubber base adaptor and filter-sterilized flasks as chambers, with flat-bottomed tubes serving as reaction vessels for the microreactor. Sterile tubing, driven by a peristaltic pump, delivers fluid and gas media. An incubator regulates the cell culture medium's temperature and CO_2 atmosphere, while an electric coil heater maintains the bioreactor housing's temperature. An Arduino interfaces with sensors and computer, controlling the motor, with a Hall effect sensor tracking RPM for consistent performance.

The integration of Arduino boards and custom Python programs enhances the flexibility of multi-parameter monitoring and control in bioreactor (BR) processes. Leveraging affordable, widely available Arduino components increases system modularity, thanks to compatibility with a broad range of sensors, modules, and devices. Similarly, Python enables rapid integration of Arduino hardware and custom interfaces into the BR system, streamlining operation and customization.

The integration of Arduino boards and custom Python programs enhances the flexibility of multi-parameter monitoring and control in BR processes. By utilizing inexpensive and available Arduino components, modularity of the system is increased due to the wide variety of compatible modules, sensors, and devices compatible with Arduino.[216] Similarly, Python enables rapid

integration of Arduino hardware and custom interfaces into the BR system, streamlining operation and customization.

A standout feature of our design is the dynamic swivel-joint connector, which ensures leak-proof media and gas isolation. The BR chamber-swivel connector system is designed for easy disassembly, cleaning, and replacement of u-cup seals, with expandable housing porting to support additional transport options. **Figure 5.1c** depicts the realized macroreactor, while **Figure 5.1d** shows the assembled unit. The tubing, fittings, and seals maintain sterility during medium and air transport. By eliminating internal rotors, this design reduces cell shearing and impact forces, instead using gentle shear against the chamber wall to stimulate cells and promote flow. Off-the-shelf components enhance modularity and adaptability, supporting applications like scaffold-based cell cultures or high-volume suspension cultures. The system can also be adapted for small-volume cultures by modifying the motor shaft to accommodate microliter-scale vessels.

Our BR system is not restricted to a specific number of samples per chamber, as other designs may be, and can accommodate multiple samples in a soft rotating / tumbling modality or through the use of a sample holder of various potential configurations. The BR chamber can also be used in a non- rotating configuration, only allowing fluid to pass over and through, e.g., porous mesh stainless steel wire cage holding seeded scaffolds.

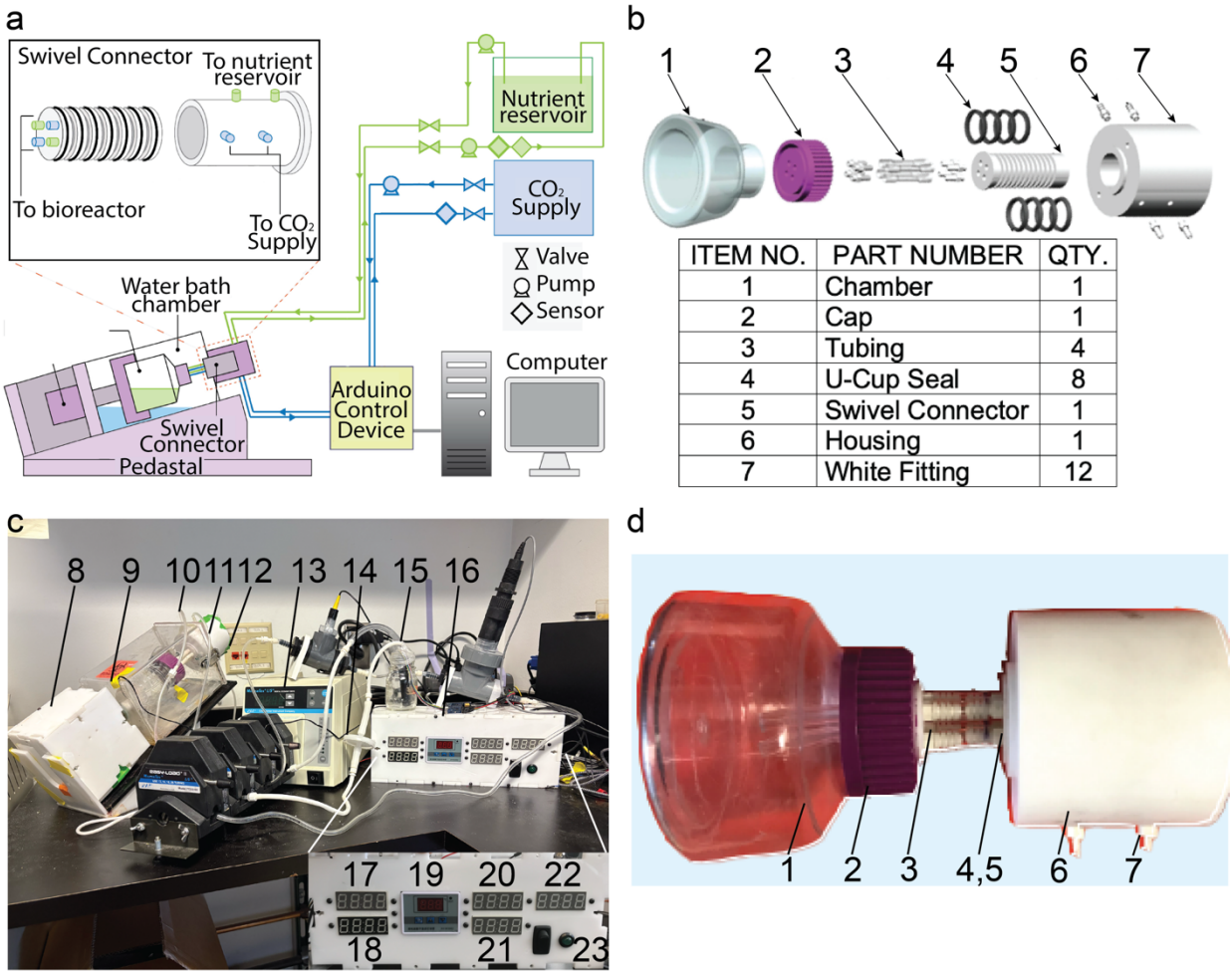


Figure 5.1 a) schematic diagram of the dynamic bioreactor system. The bioreactor is connected to a nutrient reservoir and CO2 supply via a swivel connector, allowing for continuous nutrient and gas exchange. The system includes a water bath chamber for temperature control, a motor for agitation, and various valves, pumps, and sensors controlled by a computer through the system/stimuli control device. c) Exploded diagram of bioreactor chamber, housing, and swivel connector along with components that allow fluid flow to and from the chamber. Bioreactor system illustrating components for operation for the c) macroreactor including 8) 12V DC motor with housing, 9) water bath chamber with heating element and bioreactor, 10) medium outlet, 11) medium inlet, 12) swivel connector housing, 13) peristaltic pump, 14) gas inlet, 15) gas outlet, 16) and main electronics system (Arduino Due, 12V DC power supply temperature controller, pH sensor, CO2 sensor, and oxygen sensor). Front panel close up of electronics housing with displays for 17) set RPM, 18) measured RPM, 19) temperature reading, 20) pH level, 21) measured CO2, 22) measured oxygen concentration, and 23) power switch with LED indicator. d) Image of bioreactor chamber and swivel connector assembly, with components labeled.

The macroreactor employs a 250 mL flask as its standard chamber, but its design allows for flexibility, chamber size can be adjusted or swapped for alternative geometries (e.g., larger or smaller volumes) or supplemented with additional bioreactor assemblies (e.g., trays, hollow fibers, membranes) using adaptors. This adaptability supports a variety of tissue types. The Arduino framework enables the addition of multiple motors to operate several BR chambers simultaneously, along with extra sensors for greater complexity. The versatile Python program can be easily adapted to manage multiple motors and sensors, facilitating parallel experiments with different cell types or testing conditions.

The open-ended system design supports diverse applications, such as testing the effects of varying growth factor (GF) concentrations on identical cell lines under intermittent or continuous rotation within separate chambers. It also allows trials with distinct parameter sets across individual chambers, where cell secretions from one chamber can be channeled into a second, third, or fourth chamber via the novel swivel connectors, all while accommodating different chamber sizes. This flexibility enhances the system's utility for complex tissue engineering experiments.

5.3.2 Process Monitoring and Control

The BR system operation starts by launching the Python program and connecting the Arduino Due via a drop-down list of available COM ports, as shown in **Figure 5.2a**. Upon initialization, the Python GUI front panel displays all BR functionalities, with a confirmation message indicating a successful connection or failure (**Figure 5.2b**). The user sets the chamber rotation speed using the dial in **Figure 5.2c**, triggering the DC motor to spin and self-adjust via a Hall effect sensor near the motor shaft. The measured RPM is relayed to the Arduino and shown in the "Measured" textbox (**Figure 5.2c**). Sensors connected to the Arduino monitor CO_2, pH, and oxygen, with

readings displayed in the Python GUI under their respective labels (**Figures 5.2d–f**). CO_2 auto-calibrates at startup, while pH and oxygen probes can be calibrated with standard solutions before placement in the outlet line. The water bath temperature is set using the controller on the device's front panel (**Figure 5.1b**), and a Masterflex peristaltic pump regulates nutrient media and gas flow into and out of the BR chamber.

Settings and readings from the Python GUI are mirrored on the device's front-panel LEDs for quick reference, with time-series data for CO_2, pH, and oxygen graphed in **Figures 5.2d–f**. Once RPM is set, a text file logs RPM, pH, oxygen, CO_2, and timestamps until the user stops it, facilitating data analysis. Python's flexibility allows future customization with additional modules or components. The 12V DC motor, operating at 0–116 RPM, connects to an Adafruit Motor Shield interfacing with the Arduino Due and Python GUI. Motors are interchangeable for higher RPM needs, and if the set and measured RPM differ by more than 1% (via Hall effect sensor readings), the Arduino adjusts the motor speed to maintain the target. The swivel connector assembly features a shaft with 10 grooves, four active ones sealed by dynamic U-cup seals (AN6226, Parker-Hannifin, Lexington, KY), preventing leakage between active and inactive grooves.

Sensors for oxygen, CO_2, pH, and temperature provide feedback to the Arduino Due, Python GUI (**Figure 5.2**), and device front panel (**Figure 5.2, 17-23**). The oxygen sensor detects 0–150% saturation (0–27 mg/L) with a resolution of 0.01 mg/L, while the CO_2 sensor ranges from 0–100,000 ppm. A 5% CO_2 atmosphere, maintained in an incubator and pumped through a HEPA filter into the BR system, ensures a stable cell culture environment. The pH sensor measures 0–14 ± 0.01, and a thermocouple in the water bath monitors temperatures from 25.0–70.0 °C ± 0.1°C. These sensors interface with the Arduino Due within the BR housing (**Figures 5.1** and **5.2**), which

connects to the Python program via USB. The system continuously adjusts RPM to match the set value. To regulate pH, dissolved oxygen (DO), and CO_2, the peristaltic pump's flow rate can be manually adjusted based on probe readings. Temperature is controlled separately via the water bath, not the Arduino or Python, though such capabilities could be added with minimal effort.

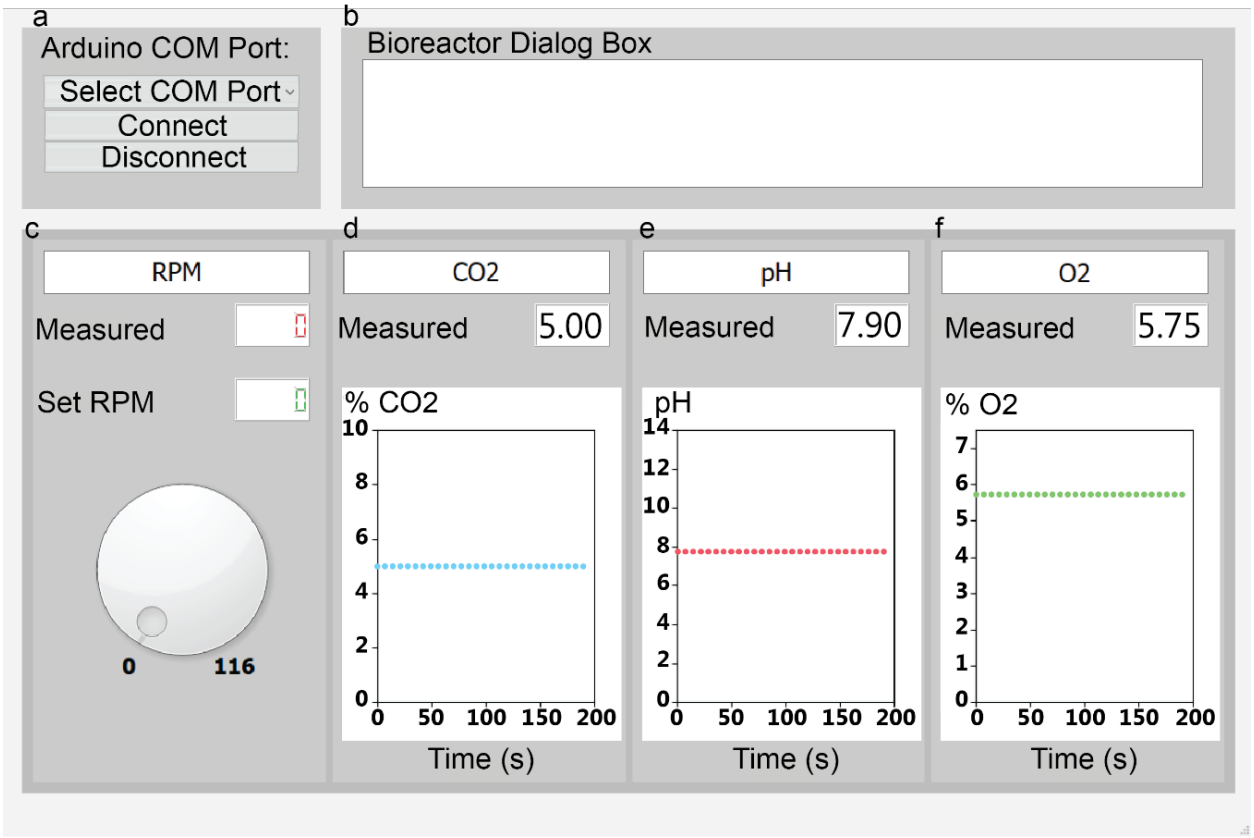


Figure 5.2 Python GUI front panel for displaying all BR functions. Functions of the Python GUI include a) Arduino COM selection interface; b) connection and error dialog box; c) RPM control; d) CO2 monitor; e) pH monitor; and f) oxygen monitor.

5.3.3 Evaluation of pH, oxygen, and CO2 probes

Our dynamic BR design incorporates several sensors and controllers to monitor conditions within the BR chamber. One of the most important parameters to monitor is the pH of media, which can significantly impact cell fate.[217] Even small changes in pH can affect a myriad of different biomaterials.[218] Thus, it is imperative to control and monitor the pH of culture media in real time

to ensure it remains within acceptable limits. To accomplish this, the medium was constantly cycled through the BR, and a pH probe was installed in line with the media outlet channel. As cells grow, they secrete waste which makes the medium more acidic. We counteract the tendency of cell culture media to increase in acidity by automatically exchanging the cell culture media with fresh medium with a basic pH, usually around 7.5-8.0 depending on the type of medium

To demonstrate our system's pH monitoring and control capabilities, the system was saturated with two different pH standard solutions by using the peristaltic pump. When switched from water to solution of pH 10 and then from solution of pH 10 to solution of pH 4, the pH sensor showed relatively quick changes in pH readings, and once it reached the target pH, the readings were consistent. This test demonstrated the system's ability to monitor pH over long term periods as well as track changes in pH. **Figure 5.3a** shows the pH value detected by the pH sensor as a function of time for this experiment. In **Figure 5.3b**, fresh medium was first allowed to saturate the system and stabilize, then used media was introduced into the system and allowed to stabilize. We again see relatively fast responses to changes in the culture medium state between the fresh and used medium. This test demonstrates the system's ability to track small changes in pH.

Oxygen is essential to the metabolic activity of cells and is another major factor that can affect cell fate.[219,220] To ensure oxygen is within an acceptable range, it was monitored in the same way as pH was with one caveat. Here, our oxygen probe will consume a small amount of oxygen as it takes readings, and if the flow rate is not fast enough stagnation will occur and a constant decrease in the reading should be observed as time goes by because the probe is consuming oxygen. To conserve medium, our flow rates are low enough such that we can sometimes see a change in the readings due to oxygen consumption from the probe, however, when stagnation occurs the system usually recovers on its own. As cells grow, they will consume oxygen in the

medium, leading the used medium to have an overall lower amount of oxygen than the fresh medium.

Figure 5.3c demonstrates the system's ability to detect oxygen changes by using fresh and boiled water. A constant reading of around 8.0 mg/mL is maintained when fresh water has saturated the system. After boiled water is added to the system, a change down to around 7.0 mg/mL is observed. The system's sensitivity to changes in the oxygen of culture medium showed in **Figure 5.3d**. Here, the reading holds steady at around 6.5 mg/mL when the used medium has saturated the system. After new medium is added, an increase in oxygen level was observed, but stagnation occurs. The BR system manages to correct itself and constant reading around 7.5 mg/mL is observed for the new medium. These tests demonstrate the system's ability to follow and monitor changes in oxygen.

CO2 is another critical parameter that can impact cell culture outcomes. CO2 helps the system buffer against drastic changes in pH when biological products are produced. Therefore, careful monitoring and regulating of CO2 is necessary to ensure the system is properly buffered. To achieve this, air with 5% CO2 is continually pumped through the system, and a CO2 sensor was installed in line with the output gas to monitor CO2 levels. During an experiment, certain treatments, such as chemotherapeutics, may need to be administered to the BR chamber. Thus, it is important for the BR chamber and tubing to be able to come back to 5% CO2 quickly after being destabilized.

To determine the long-term CO2 stability of the system, the CO2 level was monitored for 1 hour in the system. **Figure 5.3e** shows a constant reading of around 4.8% for the duration of the experiment. This deviation from 5% is likely due to placement of the gas inlet tubing being too close to the door or general fluctuations of CO2 inside of the incubator. To evaluate the

effectiveness of the CO2 sensor, the CO2 level was first stabilized at 5% by allowing the peristaltic pump to cycle air through the system for 30 minutes. Then, the BR chamber and tubing were destabilized by loosening one of the inlet connections and allowing air into the BR system and finally allowed to equilibrate again by securing the inlet connections with results presented in **Figure 5.3f**. In our BR system, a 5% CO2 atmosphere is constantly maintained in an incubator, and a peristaltic pump is used to pump that atmosphere through the BR. When the system is destabilized, regular air is introduced into the system. The results of this test indicate that the system can not only maintain an atmosphere of 5% CO2 but can quickly recover if any changes need to be made during the experiment.

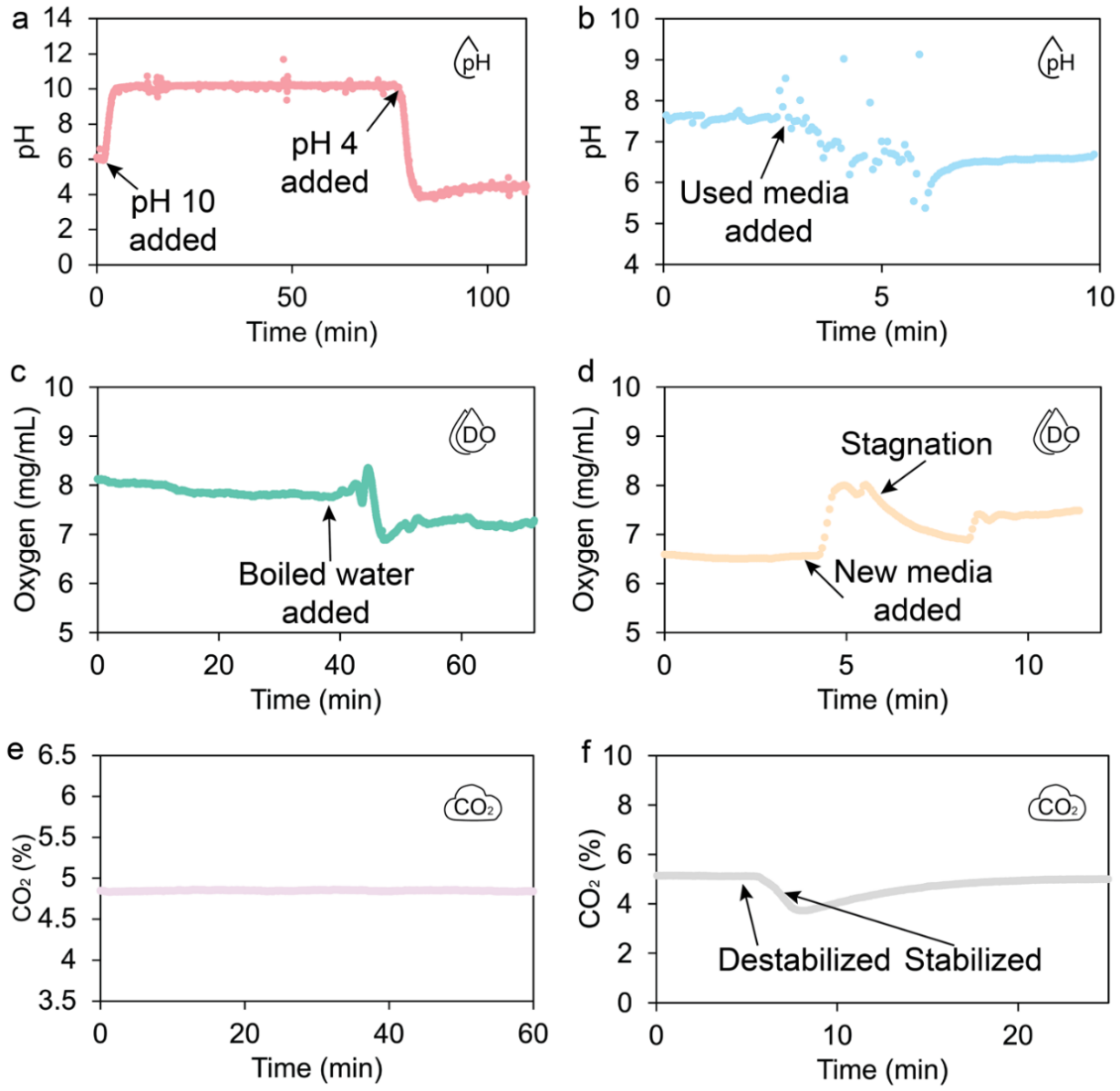


Figure 5.3 Data collected from the pH, oxygen, and CO2 probes. Data collected from the pH probe for a) standard solutions and b) used and fresh media. Data collected from the oxygen probe while the system is saturated with c) water and d) cell culture medium. Results from the CO2 e) longevity test and f) destabilization test.

5.3.4 Evaluation of RPM probe

The BR system must maintain consistent rotational speed over extended periods to ensure uniform shear forces on cells and adequate medium agitation to prevent stagnation. Precise RPM control is critical, especially for applications requiring variable shear forces. To achieve this, a Hall effect

sensor and magnet continuously monitor RPM, and the Arduino adjusts motor power based on these readings. The acceptable deviation range is programmable, but here, adjustments occur when the measured RPM deviates by more than 1% from the set value.

When powered by a DC source alone, the motor's speed fluctuated slightly over one hour, as shown in **Figure 5.4a**, averaging 16.68 ± 2.05 RPM at a target of 16 RPM. This variability highlights the inadequacy of a DC power source for precise control, even at low speeds. In contrast, **Figure 5.4b** illustrates the motor's stability when regulated by the Arduino, which uses Hall effect sensor data to maintain a steady 16.15 ± 1.55 RPM. The RPM starts below 16 and incrementally rises to the target, demonstrating fine adjustment capability. **Figure 5.4c** shows that a DC motor connected solely to a power source fails to sustain a high RPM, exhibiting a gradual decline over time. However, **Figure 5.4d** showcases the Arduino and Python program's precise, near-instantaneous control, as RPM increases from 15 to 65 in 10-RPM increments with minimal transition time.

RPM settings are easily adjusted via the Python GUI (**Figure 5.2**), allowing real-time variation during experiments to meet diverse shear force requirements. This flexibility and precision enhance the BR system's reliability for long-term cell culture applications.

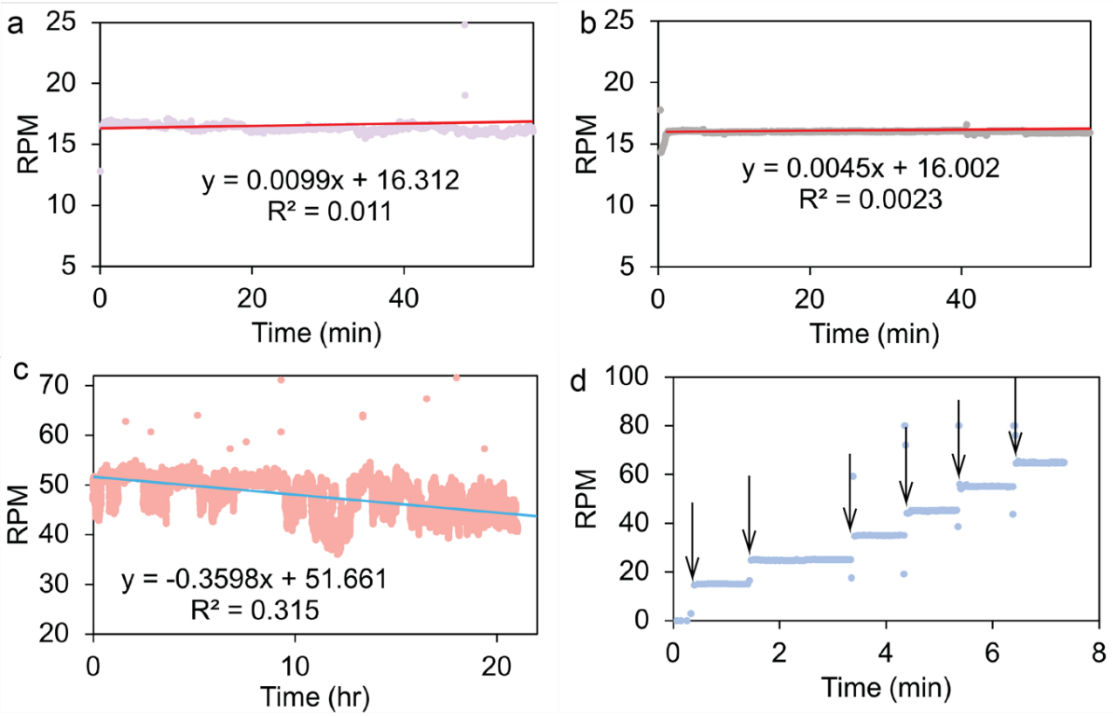


Figure 5.4 RPM data collected from the BR system when the motor a) was directly connected to a DC power source for 1 hour, b) was connected to the Arduino and RPM was constantly monitored and adjusted for 1 hour, c) was directly connected to a DC power source for 21 hours, and d) had its RPM increased in increments of 10; arrows indicate where the RPM was changed, starting at 15 and ending at 65 RPM.

5.3.5 Evaluation of Tumor Model

The macroreactor was evaluated on its ability to support the tumor cell line U87. U87 is a glioblastoma cell line, which is one of the most common brain cancers.[221-223] U87 is an adherent cell line and therefore was cultured on chitosan scaffolds. Prior to plating, 6CS scaffolds were treated with medium by incubating them for 30 minutes. The scaffolds were introduced into the macroreactor on day 4, meaning that they had not been exposed to the macroreactor until that point. **Figure 5.5a** and **5.5b** show the sensor data for the pH and oxygen sensors, respectively, collected from the macroreactor during the experiment. In the pH and oxygen data, the sharp change in the data is due to leaving the program running to collect data while performing medium

changes and cell analysis, which causes air to enter the line and affects the readings. The pH and oxygen see slight decreases over time between medium changes. Precise pH regulation is essential, as even small deviations can profoundly affect cellular processes.[224] For instance, a pH shift of 2 units has been shown to alter protein secretion and extracellular vesicle uptake, with implications for transfection and drug delivery.[225] Our BR's accurate pH monitoring supports such applications and opens avenues for further investigation. Similarly, oxygen control is critical, as hypoxic conditions, common in tumors, can modify gene expression and drive invasive phenotypes.[226] Unlike traditional systems that rely on pumped media flow, our rotational design minimizes shear stress and allows hypoxia to be induced by sealing the gas outlet, offering flexibility for specialized studies.

Figure 5.5c shows the CO_2 data. The large dips in the data are caused by opening of the incubator door or from performing medium changes and cell analysis, but otherwise the CO_2 levels remain consistent around 5% CO_2. Stable CO_2 levels are vital, acting as a buffer to prevent abrupt pH swings.[227] Our system effectively maintains CO_2 concentrations and quickly recovers from disruptions, ensuring a dependable culture environment.

Figure 5.5d shows the RPM sensor data. Fluid shear and microgravity, regulated through precise RPM adjustments, enhance mass transport and replicate in vivo mechanical cues. The motor speed averaged 4.98 ± 0.12 RPM over the duration of the experiment. The modular design accommodates various flask geometries, enabling fine-tuned shear forces and optimized culture conditions tailored to specific needs. Mechanical stimulation is a key driver of cell proliferation and differentiation.[228] The 30° canted-axis rotating chamber generates gentle shear forces through soft vortex circulation, improving fluid mixing while minimizing cell damage. This contrasts with conventional paddle or impeller-based systems, which often produce turbulent flow and excessive

mechanical stress. The adaptability of our design makes it well-suited for sensitive cell types, such as stem cells and cancer cells, broadening its utility.

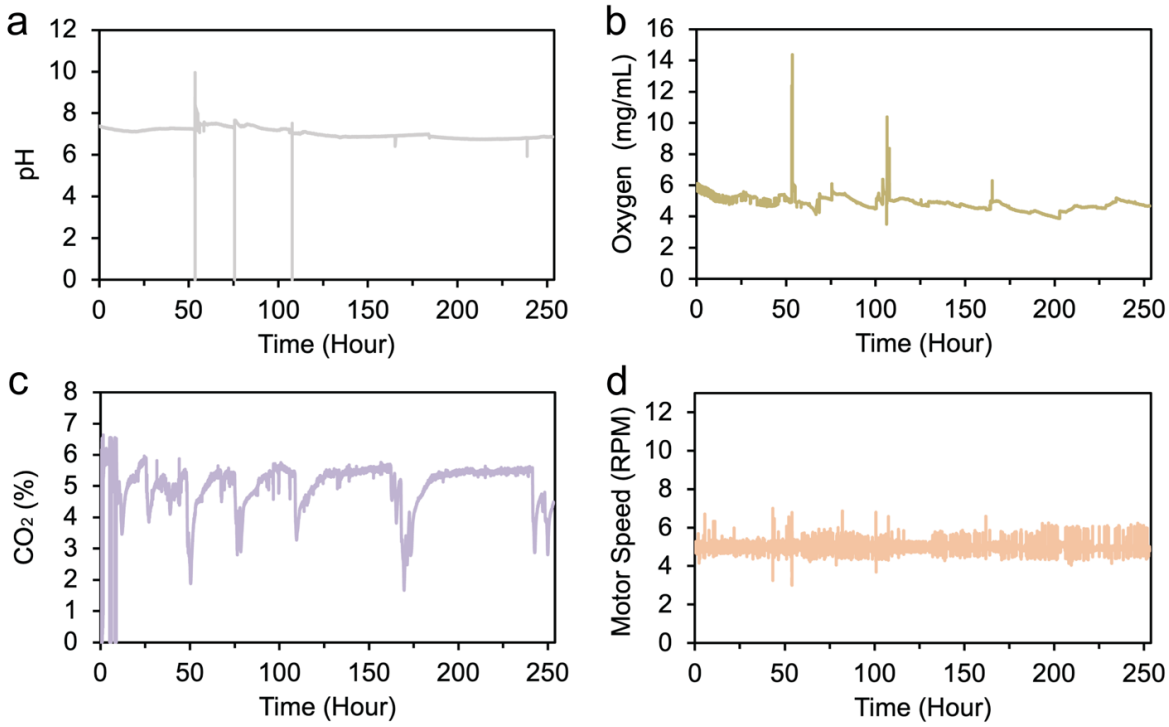


Figure 5.5 Sensor data collected from the macroreactor for a) pH, b) oxygen, c) CO_2, and d) RPM.

Figure 5.6a shows live/dead imaging of the cells in the scaffold. In the macroreactor a healthy population of cells can be observed with clusters and single cells present, and minimal or no dead cells visible. However, in the static condition, dead cells can be observed. It is worth noting that the cells in the macroreactor appear to spread more evenly throughout the scaffold, whereas in the static condition the cells tend to remain closer to the edges of the scaffold. It is also interesting to note that the metabolic activity in the static condition is higher than that of the macroreactor on day 10, but the live/dead images indicate there are more cells present in the macroreactor scaffolds. This is likely due to a decrease in the metabolic activity of the cells in the macroreactor caused by the dynamic conditions.

The cells were also stained with Calcien-AM and the percent area fluorescent was quantified and can be seen in **Figure 5.6b**. In the static condition, the cells saw a consistent increase in percent area fluorescence across the 10-day period. The macroreactor saw an initial increase in percent area fluorescence on day 3, but a decrease in percent area fluorescence on day 5, followed by a consistent increase for the remainder of the experiment. As the cells are adjusting to their new environment, some of the weakly attached cells are likely falling off or dying.

The cell metabolic activity on the scaffolds was measured over time, and the results are presented in **Figure 5.6c**. Upon introducing the scaffolds into the macroreactor, there was an initial decrease in cell metabolic activity on day 3. However, the macroreactor showed a general increase in metabolic activity after day 3. The initial decrease in the macroreactor is likely attributed to an initial adjustment period for the cells, where the cells are undergoing an adjustment with the added mechanical stresses on them. Once the cells were acclimated to the environment, they can start proliferating and spreading throughout the scaffolds.

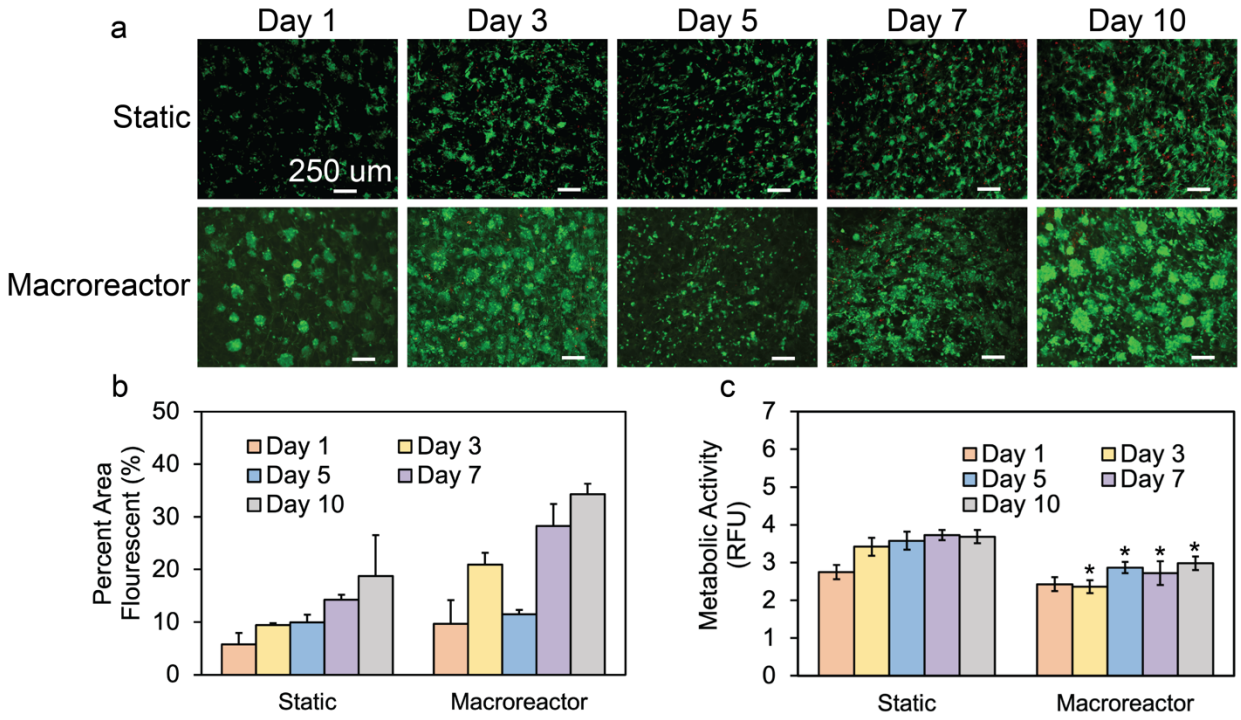


Figure 5.6 Fluorescent images of cells in 6CS scaffolds cultured statically and in the macroreactor. Cells were stained with Calcien AM (live, green) and propidium iodide (dead, red) for visualization on days 1, 3, 5, 7 and 10. The scale bar represents 250 µm. Viability data from the scaffolds cultured in static conditions and in the macroreactor for b) metabolic activity and c) percent area fluorescent. A p value of < 0.01 is indicated by an asterisk, and $n > 3$.

5.3.6 Design and Characterization of Micro-bioreactor

To demonstrate the versatility of the bioreactor and accommodate for high throughout testing in the bioreactor, we designed a microbioreactor with small volumes that can culture up to 6 different reaction vessels at a time. Thus, a microreactor was also designed to accommodate multiple reaction vessels that can culture cells using small volumes. To achieve this, a 3D printed holder was created, capable of holding 6 individual reaction chambers. These chambers were connected to a central chamber through tubing to enable passive air exchange. The central reaction chamber was directly connected to a modified version of the swivel connector, providing a secure connection for air or medium exchange, if desired. **Figure 5.7** shows the realized microreactor.

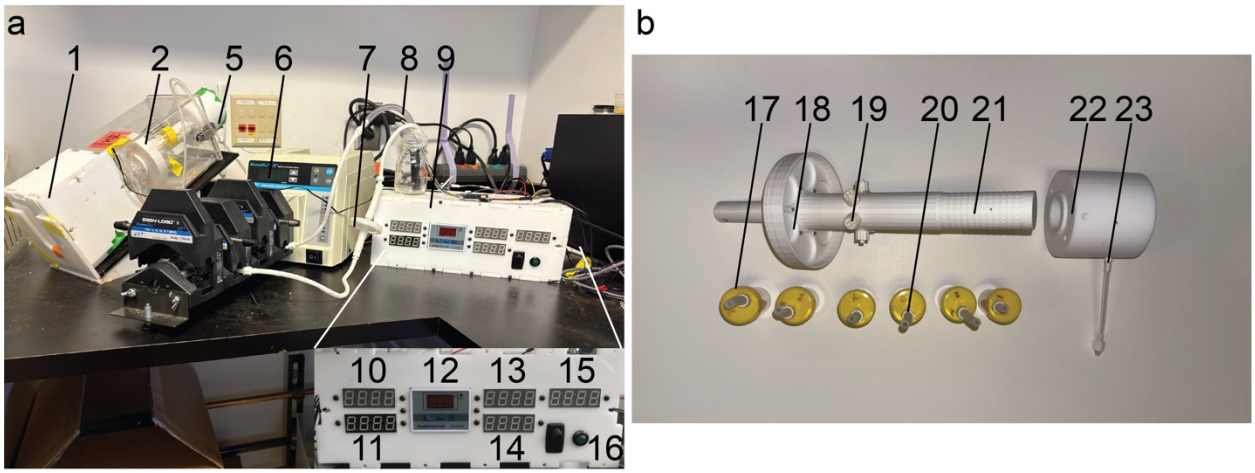


Figure 5.7 Bioreactor system illustrating components for operation for the a) microreactor including 1) 12V DC motor with housing, 2) water bath chamber with heating element and bioreactor, 3) medium outlet, 4) medium inlet, 5) swivel connector housing, 6) peristaltic pump, 7) gas inlet, 8) gas outlet, 9) and main electronics system (Arduino Due, 12V DC power supply temperature controller, pH sensor, CO2 sensor, and oxygen sensor). Front panel close up of electronics housing with displays for 10) set RPM, 11) measured RPM, 12) temperature reading, 13) pH level, 14) measured CO2, 15) measured oxygen concentration, and 16) power switch with LED indicator. b) Image of microreactor apparatus, with components labeled as 17) Individual culture reaction vessel, 18) 3D printed holder designed to hold 6 individual reaction chambers along with the central chamber, 19) connection to the central chamber, 20) tubing to connect the reaction vessel to the central chamber, 21) swivel connector, 22) housing for the swivel connector, and 23) tubing connection for CO_2.

Figure 5.8a presents live/dead imaging of cells within the scaffold. In the microreactor, a healthy cell population is observed, with both single cells and clusters present, and minimal to no dead cells visible. In contrast, the static condition shows a noticeable presence of dead cells. Additionally, the cells in the microreactor appear to be more evenly distributed throughout the scaffold, whereas in the static condition, they tend to remain near the scaffold edges. In the macroreactor, cells seem to form denser clusters. Interestingly, metabolic activity in the static condition is higher than in the microreactor on day 10, yet live/dead imaging suggests a greater number of cells in the microreactor scaffolds. This discrepancy is likely due to a decrease in metabolic activity caused by the dynamic conditions in the microreactor.

Cells were also stained with Calcien-AM, and the quantified percent area fluorescence is depicted in **Figure 5.8b**. In the static condition, fluorescence increased consistently over the 10-day period. In the microreactor, fluorescence initially increased on day 3, followed by a decline on day 5, before steadily rising for the remainder of the experiment. This fluctuation may be attributed to weakly attached cells detaching or dying as they adapt to the new environment.

Cell metabolic activity on the scaffolds was measured over time, as shown in **Figure 5.8c**. After scaffold introduction into the microreactor, an initial decline in metabolic activity was observed on day 3. However, metabolic activity generally increased after day 3, with the microreactor displaying higher metabolic activity on day 10 compared to the macroreactor. The static condition exhibited the highest overall metabolic activity, though a slight decline was noted on day 10. The initial drop in both BR systems is likely due to an adaptation period, where cells experience mechanical stress. Once acclimated, they begin to proliferate and spread throughout the scaffolds.

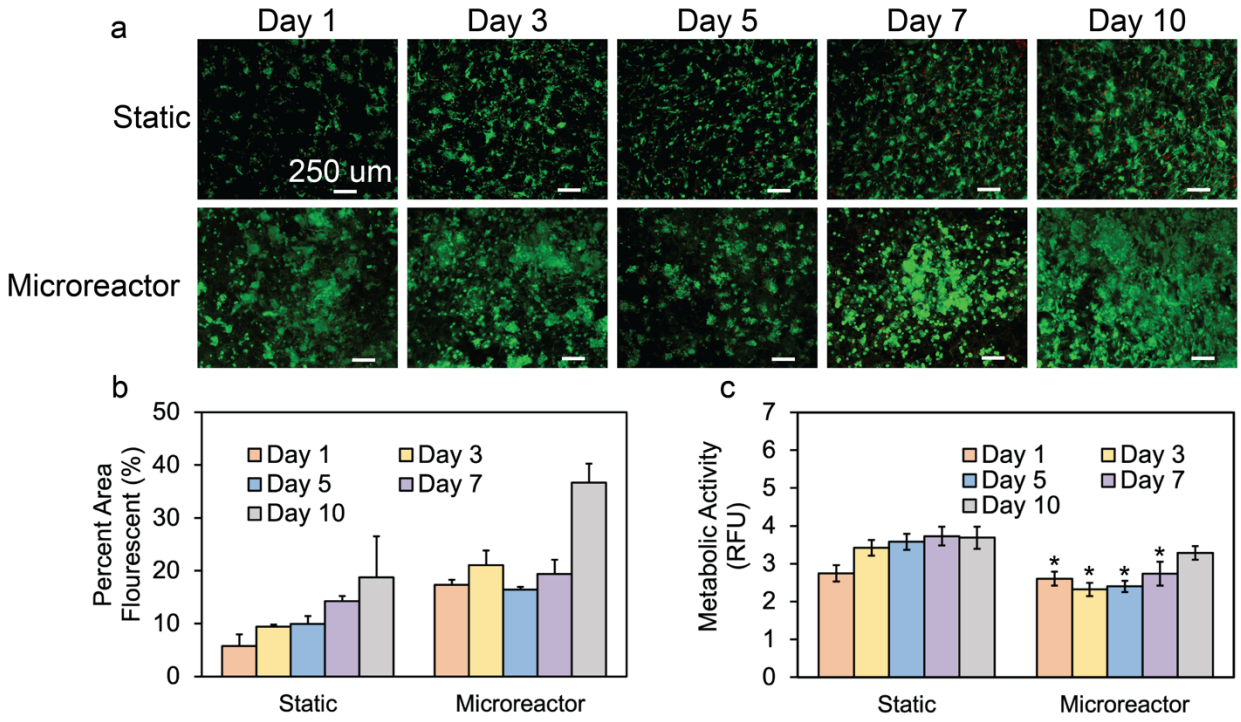


Figure 5.8 Fluorescent images of cells in 6CS scaffolds cultured statically and in the microreactor. Cells were stained with Calcien AM (live, green) and propidium iodide (dead, red) for visualization on days 1, 3, 5, 7 and 10. The scale bar represents 250 μm. Viability data from the scaffolds cultured in static conditions and in the microreactor for b) metabolic activity and c) percent area fluorescent. A p value of < 0.01 is indicated by an asterisk, and $n > 3$.

5.3.7 Evaluation of a Nonadherent Cell Line for Both Bioreactors

The macroreactor and microreactor were compared on their ability to support the nonadherent human T-cell line JURKAT. The JURKAT cell line was chosen because T-cells are among the most common cells used in cell therapy, and their production is important to scale up.[229,230] The JURKAT cells are nonadherent and therefore were not cultured with scaffolds. After plating, the JURKAT cells were allowed to grow for 1 day before beginning rotation. Both the metabolic activity and the overall cell concentration were measured over a 10-day period and the results are shown in **Figure 5.9a** and **5.9b**, respectively. The metabolic activity and cell concentration agree with each other for the macroreactor, microreactor, and static conditions. The macroreactor saw nearly a 170% increase in cell concentration over the 10-day period, while the microreactor saw

an almost 280% increase in cell concentration. This discrepancy is likely due to the greater force acting on the cells in the macroreactor compared to the microreactor. Since the macroreactor vessel is larger than the microreactor, the cells have farther to fall during rotation.

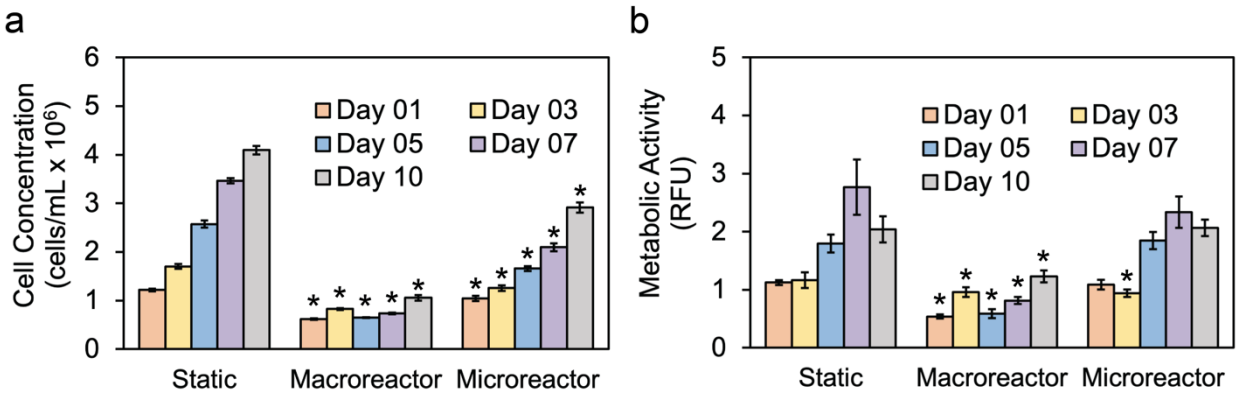


Figure 5.9 Evaluation of the nonadherent cell line JURKAT in the macro- and microreactor. a) cell concentration and b) metabolic activity of JURKAT cells. A p value of < 0.01 is indicated by an asterisk, and $n > 3$.

The system, built on an Arduino and Python framework, demonstrated robust performance in maintaining U-87 MG glioblastoma cells on chitosan scaffolds and nonadherent JURKAT cells, showcasing its versatility for various tissue engineering applications. Unlike conventional bioreactors that rely on impellers or mechanical stirring, our system eliminates direct contact with cells through its innovative swivel connector and rotation-based fluid circulation. This approach reduces cell damage, enhances mass transport, and provides a more physiologically relevant culture environment by simulating low-shear microgravity conditions. The ability to reduce turbulence and avoid direct mechanical stress makes this system especially advantageous for fragile or sensitive cell types. Additionally, the versatility of this system could enable high-throughput drug screening, multi-sample processing for personalized medicine, and large-scale tissue regeneration for clinical use. Scalability allows miniaturization through modified motor

shafts, smaller vessels, and micro-scale sensors, opening possibilities for portable bioreactors suited to point-of-care diagnostics or space research. Its precise control and real-time monitoring also support advanced bioprocessing, such as optimizing stem cell-derived organoids or engineering tissue constructs for transplantation.

5.3.8 Evaluation of hNSC Model in the Microreactor

The microreactor was evaluated on its ability to support a multipotent population of hNSCs cultured in the chitosan scaffolds. hNSCs were chosen because hNSCs are used in many stem cell therapies,[3] and scaling up their culture is important for accommodating the large number of cells required for stem cell therapy. **Figure 5.10a** shows the metabolic activity of the cells grown in both static conditions and in the microreactor. It can be seen that the cells grown in the micro-reactor have a greater proliferation after the 7-day period. **Figure 5.10b** shows the ability of the microreactor and scaffolds ability to maintain the multipotency of the hNSCs. The microreactor has a larger multipotent population than the cells grown in the static condition, with SOX2, nestin, Ki67, and SOX1 all having larger positively expressing populations in the microreactor than in the static condition, but not in the 2D control. Live/dead stained images of the cells in both the static and microreactor conditions can be seen in **Figure 5.10c**. Over the course of 7 days, it can be seen that the cells continue to grow throughout the scaffold in both the static and microreactor condition, however, the cells appear to be more confluent in the microreactor than in the static condition after 7 days.

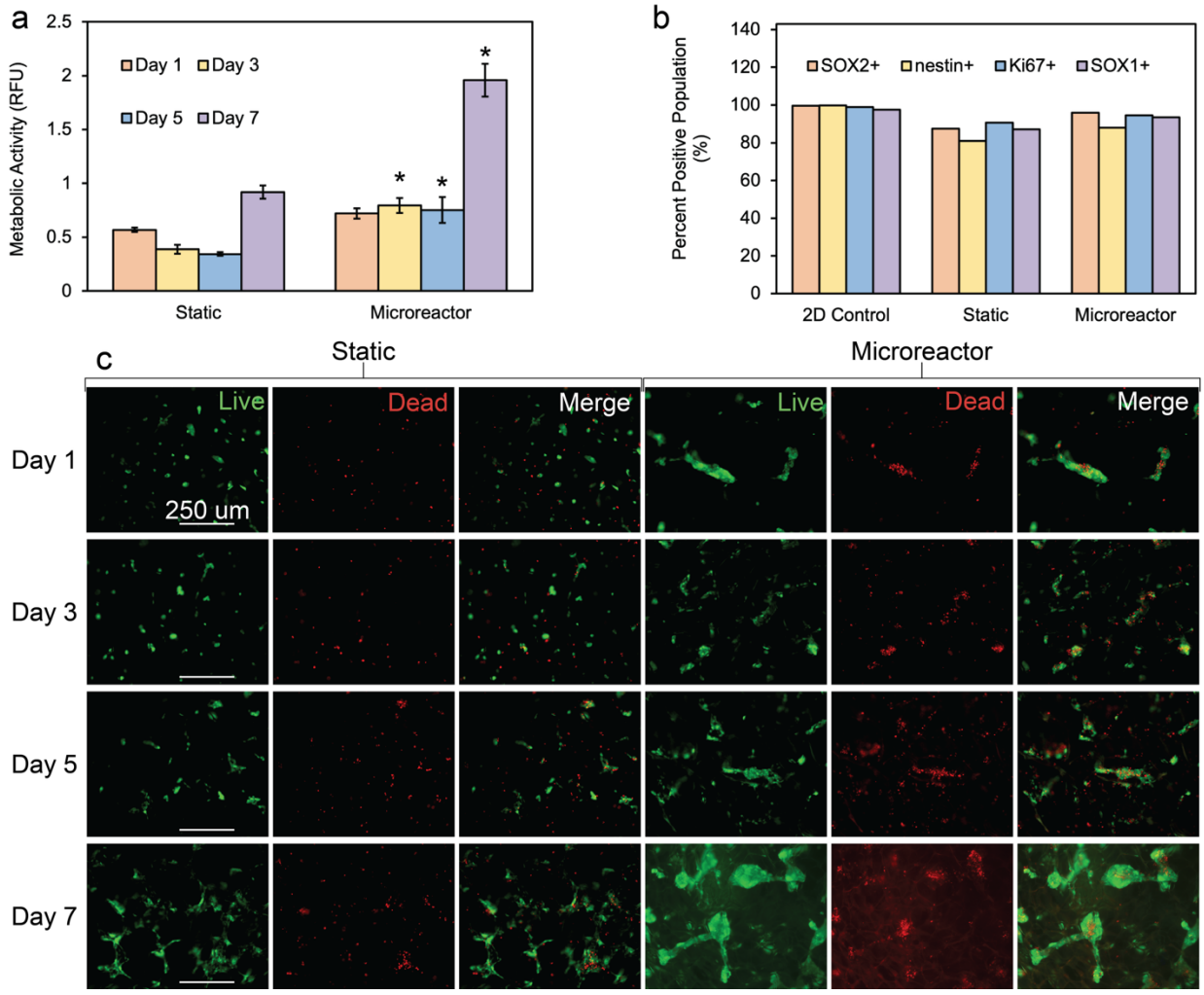


Figure 5.10 Evaluation of hNSC-H14 grown on 6CS scaffolds in the microreactor. a) metabolic activity of the hNSCs grown in the microreactor. An * indicates a *p* value of less than 0.05 between the static and microreactor condition. b) protein expression results from hNSCs grown in the microreactor for 7 days. c) fluorescent images of live (green) and dead (red) stained cells. The scale bar indicates 250 μm.

Chapter 6 Enhanced Differentiation of Human Neural Stem Cells into Cortical Neurons Using 3D Chitosan Scaffolds

6.1 Introduction

Human neural stem cells (hNSCs) are self-renewing, multipotent cells with the intrinsic capability to differentiate into specialized cell types of the central nervous system, including astrocytes, oligodendrocytes, and neurons.[231,232] Among these, cortical neurons are particularly important, as they constitute a major population in the cerebral cortex and play a significant role in the pathophysiology of neurodegenerative diseases, such as Alzheimer's disease. The study of cortical neurons can provide vital insights into the mechanisms underlying neurodegenerative disorders such as Alzheimer's, Parkinson's, and multiple sclerosis.[3,233,234] By differentiating stem cells into functional neurons, researchers can track the progression of diseases at different developmental stages.[235] Additionally, fully differentiated neurons offer an invaluable platform for evaluating the efficacy of therapeutic interventions.[236] A complicating factor, however, is frequent emergence of cells types, such as astrocytes, during the differentiation process, necessitating additional cell sorting to obtain purified populations of cortical neurons.[237] In this regard, in vitro three-dimensional (3D) disease models have shown great promise, and recent advancements have yielded encouraging results in treating these conditions.[235,238]

While traditional 2D culture substrates offer advantages in terms of imaging convenience and ease of handling for passaging and evaluation,[6] 3D culture systems more accurately emulate the in vivo environment, facilitating more natural cell responses.[239,240] In 3D cultures, cell-cell and cell-matrix interactions occur in all directions and cells experience enhanced exposure to nutrients and biologically relevant signals,[241] leading to more physiologically relevant cellular networks, synaptic transmissions, and morphological features.[242] These aspects are thought to underline the

superior differentiation efficiency observed in 3D cultures,[45,165] positioning 3D culture systems as a key tool for more rapid and efficient differentiation of hNSCs into cortical neurons.

Moreover, 3D culture systems present certain manufacturing advantages over their 2D counterparts,[243] especially when using versatile materials such as chitosan. These systems offer tunable properties, such as pore size and stiffness, which can significantly influence cell growth and differentiation.[244] By contrast, 2D substrates made of glass or hard plastic are inadequate in replacing the mechanical cues found *in vivo.* Additionally, 2D culture substrates usually require coating for hNSC culture, and these coatings are typically derived from murine tumors, have limited shelf life (up to 1 month), and can be used only once. In contrast, polymer based 3D culture systems, composed of readily available chemicals, can replicate these in vivo mechanical properties, fostering improved cell growth and differentiation.[245] These features could enhance the efficiency and speed of the differentiation of hNSCs into cortical neurons.

Synthetic polymers, such as polypyrrole, have been developed as fibrous and porous scaffolds to differentiate neural stem cells,[246,247] yet they lack the necessary surface chemistry to promote cell adhesion.[248] Natural polymers, therefore, present an appealing alternative. Matrigel and Geltrex, natural protein cocktails derived from murine tumors, are considered the gold standard for coatings in 2D cultures, and can also be used as a gel or scaffold material to culture and differentiate hNSCs.[249,250] Chitosan, another commonly used biomaterial, offers advantages such as controllable material properties and cost-effectiveness.[251,252] Derived from chitin, a major component found in insects, crustaceans, and some fungi, chitosan is obtained via a simple deacetylation reaction.[253] This biocompatible and biofunctional polycationic, hydrophilic, and linear polysaccharide,[254,255] presents an attractive surface for cell attachment due to its positive

charge and hydrophilic nature.[181,256] Its structural similarity to glycosaminoglycans, a major component of extracellular matrices, further enhances its suitability for use in culture systems.[257] Chitosan has been utilized to fabricate various culture systems for neural tissue engineering,[258,259] where it supports the growth and differentiation of hNSCs when used in hydrogel form.[45] Chitosan membranes have also demonstrated efficacy in maintaining the proliferation and multipotency of hiPSCs.[165] In 3D printing applications, chitosan-based inks have shown potential to enhance hNSC differentiation,[260] and chitosan scaffolds have been used to promote the differentiation of human dental pulp stem cells into neurons, astrocytes, and oligodendrocytes. [261]

Several methods exist for producing cortical neurons, including differentiation from dental pulp stem cells,[261] human induced pluripotent stem cells (hiPSCs),[262] and hNSCs.[242] While hiPSCs offer some advantages including the ability to model neurogenesis and pathogenesis,[263-265] they are patient-derived and may contain pathological phenotypes.[266,267] Moreover, hiPSCs are often associated with a higher risk of tumorgenicity than embryonic cells.[268-270] Embryonic stem cells, in contrast, tend to exhibit greater specificity and differentiation efficiency than hiPSCs.[271] hNSCs, however, remain a compelling option, as they are multipotent and capable of differentiating into functional neural cells.[272] Traditionally, hNSC differentiation into cortical neurons involves seeding cells as a monolayer on two-dimensional (2D) surfaces coated with Matrigel or Geltrex. Neurotrophic factors such as BDNF and GDNF can be used to enhance the process, however, this typically results in the simultaneous production of astrocytes, oligodendrocytes, and other neurons, necessitating additional purification steps to isolate cortical neurons. Hence, the protracted differentiation period and low yield of target cells, particularly cortical neurons, remain major challenges in advancing neurodegenerative disease treatments for neurodegenerative diseases.[237,273] Achieving fully mature cortical neurons often require 2-8 weeks.[274,275]

In this study, we introduce a novel strategy to enhance the differentiation efficiency of hNSCs into cortical neurons using chitosan scaffolds. These scaffolds provide a chemically defined, 3D platform that promotes cell growth and fosters increased cell-cell interactions compared to 2D cultures. We optimized the fabrication of chitosan scaffolds to produce an interconnected, 3D porous space suitable for hNSC culture, characterizing its pore size and compressive elastic modulus. To demonstrate the versatility of the chitosan scaffolds, we explored neuronal differentiation using scaffolds with various surface coatings: native hNSC ECM, Geltrex, culture medium, or uncoated scaffolds. Specifically, the native ECM was deposited on a sacrificial passage of hNSCs. The deposition on the surface was evaluated using SEM and XPS. Initial hNSC adhesion, viability as well as differentiation was characterized. The efficiency of cortical neuron differentiation over 2 weeks was compared among scaffold conditions using representative markers for neuronal linage cells and cortical neurons.

6.2 Materials and Methods

6.2.1 Preparation of CS scaffolds

The 6CS scaffolds were prepared by mixing medical grade chitosan (degree of deacetylation of 98.3 ± 0.1%, Matexcel, Shirley, NY) in ultrapure deionized water with 4% w/w acetic acid such that a 6wt% chitosan solution was made. The mixing was performed in two steps. The first step was performed 3-5 times in a Thinky Mixer (ARM 300, ThinkyUSA, Laguna Hills, CA) at 2000 rpm for 3 minutes. The second step was performed in a household blender 2 times at the highest setting for 5 minutes or until the solution was homogenous. The 6CS solution was cast into a well plate and then lyophilized overnight. Scaffolds were then sliced into 400 μm thick slices using a vibrating microtome. Then the scaffolds were neutralized in ammonium hydroxide/water/methanol (7%/3%/90%) solution and rinsed 3 times with sterile water. Scaffolds

were then rinsed 3 times in sterile ethanol (70% v/v), and then the scaffolds were rinsed 3 times with sterile PBS. Scaffolds were stored at 4ºC in sterile PBS.

6.2.2 Physical Properties of CS Scaffolds

The compressive elastic modulus of both dry and wet scaffolds was determined using an AGS-X Series Universal Tester (Shimadzu, Kyoto, Japan). Scaffolds were compressed at a rate of 0.4 mm/min until a strain of at least 0.4 was reached. Wet scaffolds were soaked in PBS for at least 24 hours before testing. The elastic compressive modulus was calculated from the linear region. Pore size was determined from SEM images by measuring and averaging the pore diameters of at least 50 pores using ImageJ.

6.2.3 SEM

The non-coated, Geltrex coated, pre-seeded, and medium treated scaffolds had their surface topographies examined using SEM. Scaffolds were prepared as normal and had the appropriate coating applied to them. Scaffolds were then freeze dried. Dried scaffolds were sputter coated with platinum using a SC7620 Sputter Coater (Quorum, Lewes, United Kingdom), and then mounted onto stubs using carbon adhesive tape (NEM Tape, Nisshin Em. Co. Ltd. Tokyo, Japan) in preparation for SEM. Samples were imaged with a JSM-6010 Plus (JEOL, Akishima, Japan) at 5 or 10 kV. Pore diameters were measured and calculated using ImageJ software (NIH, Bethesda, MD).

6.2.4 XPS

The non-coated, Geltrex coated, pre-seeded, and medium treated scaffolds had elemental analysis performed on their surfaces via XPS. Samples had their respective coatings applied to them, and then the scaffolds were rinsed with water before being freeze dried. Samples we attached to the

sample holder using carbon adhesive tape. Samples were examined with an Axis Ultra DLD X-ray Photoelectron Spectrometer (Kratos, Tokyo, Japan).

6.2.5 hNSC Culture and cortical neuron differentiation

Human neural stem cells hNSC-H14 (WB0195) derived from the NIH-approved hESC-H14 (WA14) were obtained from WiCell Research Institute (Madison, WI, USA). The cells were expanded and cultured following the supplier's protocol. Briefly, Geltrex- or Matrigel-coated tissue culture dishes were prepared according to the WiCell protocol for expansion, and hNSCs were cultured on these dishes as monolayers. The hNSC culture medium consists of Neurobasal medium (Gibco) supplemented with B27 (Gibco), N2 (Gibco), heparin (StemCell Technologies Inc), MEM NEAA (Gibco), and GlutaMAX (Gibco). The cells were supplied with fresh hNSC culture medium every other day. Human recombinant basic fibroblast growth factor (bFGF, Gibco) and epidermal growth factor (EGF, Gibco) were supplied every day at 20 ng/mL. Cells were passaged once they reached 90-95% confluency and were dissociated with Accutase or Versene. Cells used in this experiment were collected from passage number 33-38. Cells were seeded onto scaffolds at 100,000 cells per scaffold and had half-medium changes performed every day and bFGF and EGF added every day at 20 ng/mL.

Pre-seeding scaffolds was accomplished by seeding the scaffolds at 100,000 cells per scaffold. The sacrificial cells were collected from passage number 42. These scaffolds had half medium changes performed every day and bFGF and EGF added every day at 20 ng/mL. After 3 days, scaffolds were placed directly in PBS and stored at 4C. All hNSCs were maintained in a humidified incubator with 5% CO_2 at 37°C. Medium coated scaffolds were incubated in fresh, fully supplemented culture medium for 1 hour at room temperature before use. Geltrex coated

scaffolds were coated the same way 2D plates were coated, at a Geltrex concentration of 0.34 mg/mL. Scaffolds were plated with 200,000 cells per scaffold.

The differentiation of the hNSCs was initiated after 3 to 4 days by removing growth factors and adding in BDNF and GDNF at 20ng/mL to the NSC culture medium. dBcAMP was also added in at 0.5mM. Fresh hNSC culture medium supplemented with BDNF, GDNF, and dBcAMP was added every 2 days to 2D controls and 3D samples.

6.2.6 Cell Metabolic Activity and Viability

An alamarBlue assay (Sigma Aldrich, St Louis, MO, USA) was used to monitor cell metabolic activity. The scaffolds were placed into a new well, and then the new well was filled with a alamarBlue working solution (10X dilution with DMEM culture medium, 110μg/mL resazurin). The scaffolds were then incubated in an incubator. After 80 minutes, the fluorescence intensity of the solutions was measured at 590 nm using an excitation wavelength of 560 nm on a SpectraMax M2 microplate reader (Molecular Devices, Sunnyvale, CA, USA). A LIVE/DEAD Viability/Cytotoxicty Kit (Invitrogen, Thermo Fisher Scientific) was used to evaluate cell viability according to the manufacturer's protocol. Cells were stained with Calcien AM at 1 μM for viable cells and propidium iodide (Thermo Fisher) was used at 10 μM to stain for dead cells. The scaffolds were incubated for 15 minutes at room temperature before imaging. The samples were imaged using a Nikon TE3000 Inverted Microscope (Nikon, Tokyo, Japan). Percent area fluorescence was determined using the Python modules Numpy and Pillow.

6.2.7 Flow Cytometry

The antibodies SOX2-AF647 (BD Biosciences, 560302), nestin-PE (BD Biosciences, 561230), MAP2B-AF647 (BD Biosciences, 560382), DCX-PE (BD Biosciences, 561505), GFAP-AF488

(BD Biosciences, 561449), TUBB3-PerCP/Cy5.5 (BioLegend, 801216), SOX2-AF647 (BD Biosciences 560302), NeuN-PE (EMD Millipore, FCMAB317PE), and Ki67-PerCP/Cy5.5 (BioLegend, 350520) were purchased, and the antibodies were used as suggested by the supplier. Cells were dissociated from their respective coating or scaffold with Accutase into a single cell suspension, rinsed with PBS, and then stained for 15 minutes on ice with a dead stain (BioLegend, 891723). Cells were then fixed in 4% paraformaldehyde for 10 minutes on ice and stored in 0.5mL Cell Staining Buffer (BioLegend) at 4ºC until use. Next, the cells were permeabilized in 0.1 %v/v Triton-X 100 in PBS and then washed with PhosFlow PermWash Buffer (BD Bioscience, San Jose, CA). The cells were resuspended in 100 µL cell PermWash Buffer and then incubated with fluorophore-conjugated antibodies for 40 minutes on ice in the dark. Next, the cells were washed with PermWash Buffer, resuspended in 200 µL of buffer, and stained with DAPI. Cells were analyzed on a LSRII flow cytometer (BD Bioscience) and analyzed using the FlowJo software (Tree Star, Ashland, OR).

6.2.8 Immunocytochemistry

Cells were stained with MAP2 (Abcam, ab92434), CTIP2 (Abcam, ab18465), and TBR1 (Abcam, 31940) primary antibodies and Alexa-Fluor 594 (Invitrogen, A11042), Alexa-Fluor 488 (Invitrogen, A11006), and Alexa-Fluor 488 (Invitrogen, A11008) following the manufacturers protocol. Briefly, the cells were cultured as described above but on Geltrex coated glass slides or on their respective scaffolds. After the differentiation period was completed, the cells were rinsed with PBS, fixed with cold 4% paraformaldehyde for 10 minutes on ice, permeabilized for 10 minutes on ice, blocked for 1 hour on ice, and stained with primary antibodies at 4°C overnight. Cells were then washed and incubated with secondary antibodies for 1 to 2 hours on ice. Then, the cells were washed once and stained with DAPI before being mounted in Prolong Gold antifade

reagent (Invitrogen; Carlsbad, CA). Fluorescence images were acquired using a Nikon Eclipse TE 2000-S (Nikon, Tokyo, Japan) inverted microscope.

6.2.9 PCR

PCR was performed using SsoAdvanced SYBR Green Supermix (Bio-Rad) with a Bio-Rad CFX96 Real-Time PCR Detection System. RNA was isolated using an RNeasy Mini Kit (Qiagen, Valencia, CA) for each scaffold condition and time point. Reverse transcription was conducted with an iScript cDNA synthesis kit (Bio-Rad, Hercules, CA). PCR cycles were run at 95°C for 3 minutes followed by 40 cycles at 95°C for 15 seconds, 58°C for 40 seconds, and 72°C for 30 seconds. The primer sequences were 90-110% efficient and the sequences are provided in Supplemental Table S1. Targeted mRNA gene expression was normalized to GAPDH mRNA levels. Relative fold changes in gene expression compared to the nondifferentiated 2D day 3 condition were calculated with Cq values analyzed using Bio-Rad CFX Manager software.

6.2.10 Statistical Analysis

The statistical significance of the data was determined using an unpaired two-tailed Student's *t*-test to evaluate the *p*-value between two data sets. The number of independent measurements or experiments (*n*) is indicated in the figure captions. *P*-values that were less than 0.05 were considered significantly different. Statistical analyses were performed in Microsoft Excel using a student's t-test.

6.3 Results and Discussion

6.3.1 Scaffold coating procedure and cell culture protocol

Noncoated scaffolds were used directly after sterilization and rinsing with PBS. Medium coated scaffolds (Med-coated) were fabricated by incubating non-coated scaffolds in supplemented

culture medium for 1 hour. Geltrex coated scaffolds (GT-coated) were made by incubating the non-coated scaffolds in a Geltrex solution prepared following the manufacturer's protocol. Pre-seeded scaffolds (pre-seeded) were prepared by culturing a sacrificial cell passage on non-coated scaffolds for 3 days, after which the medium was replaced with PBS, and the scaffolds were stored in a fridge. The different coating protocols are summarized in **Figure 6.1a**. hNSCs were plated onto scaffolds at 200,000 cells per scaffold. After 4 days, differentiation was initiated by introducing BDNF, GDNF, and dBcAMP. The differentiation was allowed to proceed for 7 and 14 days, after which cells were collected for further analysis. This process is illustrated in **Figure 6.1b**, highlighting the difference in cell-cell interactions between 2D and 3D cell culture systems. In 2D systems, cells are restricted to interactions in the X-Y plane, whereas in 3D systems, cells can interact in all directions, including the Z-axis. This 3D interaction more closely mimics the in vivo environment, fostering more physiologically relevant cellular behaviors.

The mechanical properties and microstructure of the scaffolds play a key role in supporting the proliferation and differentiation of hNSCs. The porous structure, stiffness, and overall architecture of the scaffolds directly influence cell attachment, growth, and the efficiency of neuronal differentiation.

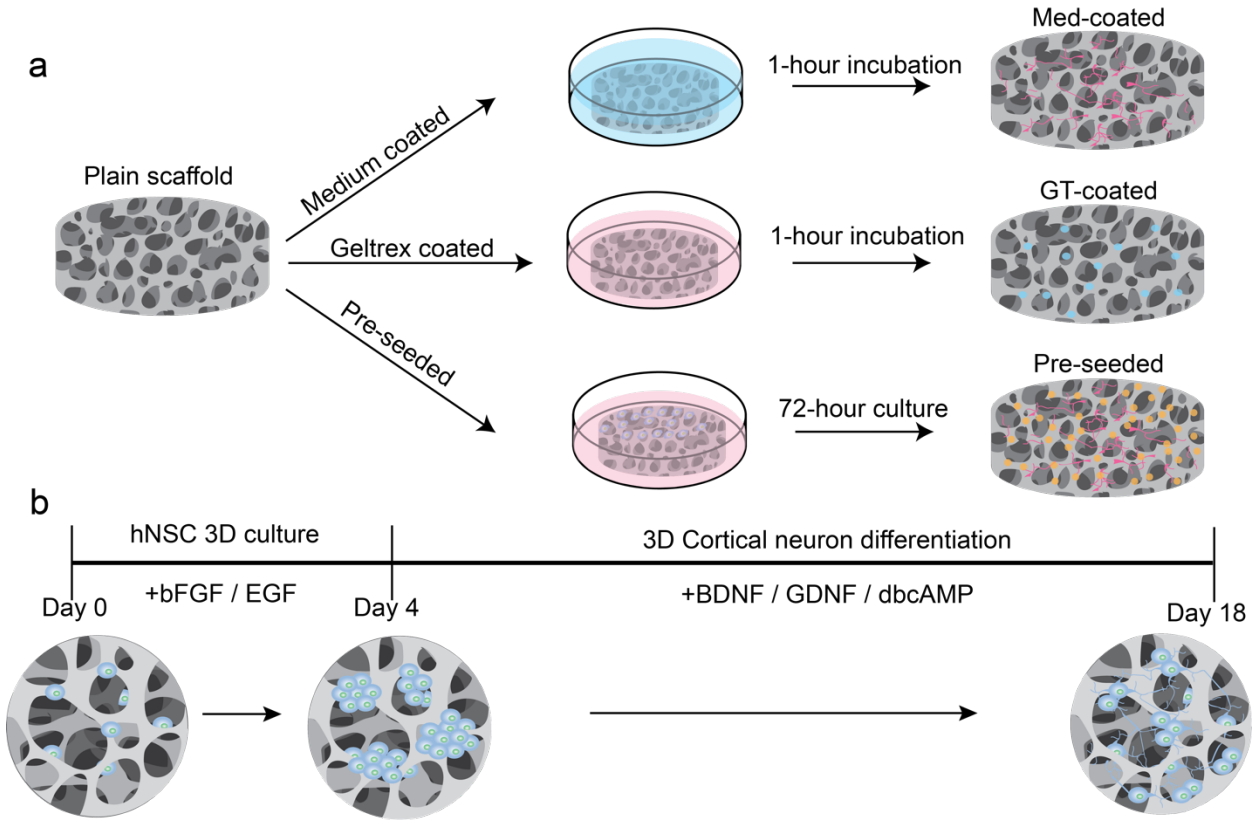


Figure 6.1 Scaffold coating methods and experimental protocol for hNSC differentiation into cortical neurons. (a) Schematic representation of the various scaffold coating protocols for differentiating hNSCs into cortical neurons: medium-coated, Geltrex-coated, and pre-seeded scaffolds. (b) Diagram outlining the experimental protocol for hNSC culture and differentiation into cortical neurons. This includes cell seeding, cell interaction in 2D versus 3D environments, and the timeline for differentiation induction using BDNF, GDNF, and dBcAMP, followed by collection at 4 and 14 days.

6.3.2 Physical characteristics of different coating conditions

For SEM analysis, scaffolds were sputter coated and mounted on stubs using carbon tape prior to imaging. The scaffolds demonstrated sufficient mechanical integrity to retain their structure following removal from the culture well. The microstructure of the 6CS scaffold, shown in **Figure 6.2a**, shows uniformity throughout the scaffold, with open pores visible, allowing the penetration of hNSCs into deeper regions of the scaffold. The average pore diameter of the 6CS scaffold was $63 \pm 23\mu m$.

The elastic compressive moduli of both dry and hydrated 6CS scaffolds and brain ECM are shown in **Figure 6.2b**. Since scaffolds are wet during cell culture, the hNSCs experience a bulk compressive elastic modulus of 100kPa. For comparison, typical brain ECM has a compressive elastic modulus around 5.7 kPa,[276] although reported values for brain ECM moduli can range from 0.1kPa to 100kPa.[277,278]

Figure 6.2c and **4.6d** present XPS results for all scaffold coating conditions. **Supplemental Figure S6.10** shows the raw XPS spectra data for each coating condition, with survey scans identifying the elemental compositions of sulfur and phosphorous. The carbon composition across all scaffolds of different coating conditions remains relatively constant at around 60%. Oxygen composition is the highest in the non-coated scaffold at 30% and the lowest in the pre-seeded scaffold at 21%, with medium treated and Geltrex coated scaffolds falling between these values at 25%. Nitrogen composition peaks for the Geltrex and medium coated scaffolds at around 10.5% and is lowest in the non-coated scaffold at 7% with the pre-seeded scaffolds showing nearly 10% nitrogen content.

The sulfur composition is highest in the medium coated scaffolds and lowest in the non-coated scaffold, with the Geltrex coated and pre-seeded scaffolds ranking between the two. The non-coated scaffold has no sulfur in it. Phosphorous, another key element commonly found in the extracellular matrices, is most abundant in the pre-seeded condition, indicating that the pre-seeded scaffolds likely have a higher amount of protein adsorbed onto their surfaces. The presence of phosphorous on the non-coated scaffold can likely be attributed to residual phosphate from PBS wash during scaffold preparation.

Proteins typically found in Geltrex and produced by cells to form the ECM, such as laminin, collagen, and heparan sulfate, contain both sulfur and phosphorus. As chitosan itself

contains no sulfur, the observed increase in sulfur content in the coasted scaffolds is due to the adsorption of these proteins onto the scaffold surfaces. Moreover, the variations in oxygen and nitrogen composition provide further insight into protein coating. The oxygen content in chitosan is around 40%, whereas in laminin and collagen, it is around 20%. Nitrogen content in laminin and collagen is near 16%, while in chitosan it is around 7%. This means that introducing proteins to the chitosan scaffolds reduces the overall oxygen atomic percentages while increasing nitrogen content.

These data suggest that the pre-seeded scaffold has more overall protein coating than the Geltrex-coated scaffold, though the Geltrex-coated scaffold exhibits a slightly higher sulfur content, likely from sulfur-containing heparan sulfate. These findings highlight the different surface chemistry across the various scaffold coating conditions, with implications for hNSC attachment and differentiation.

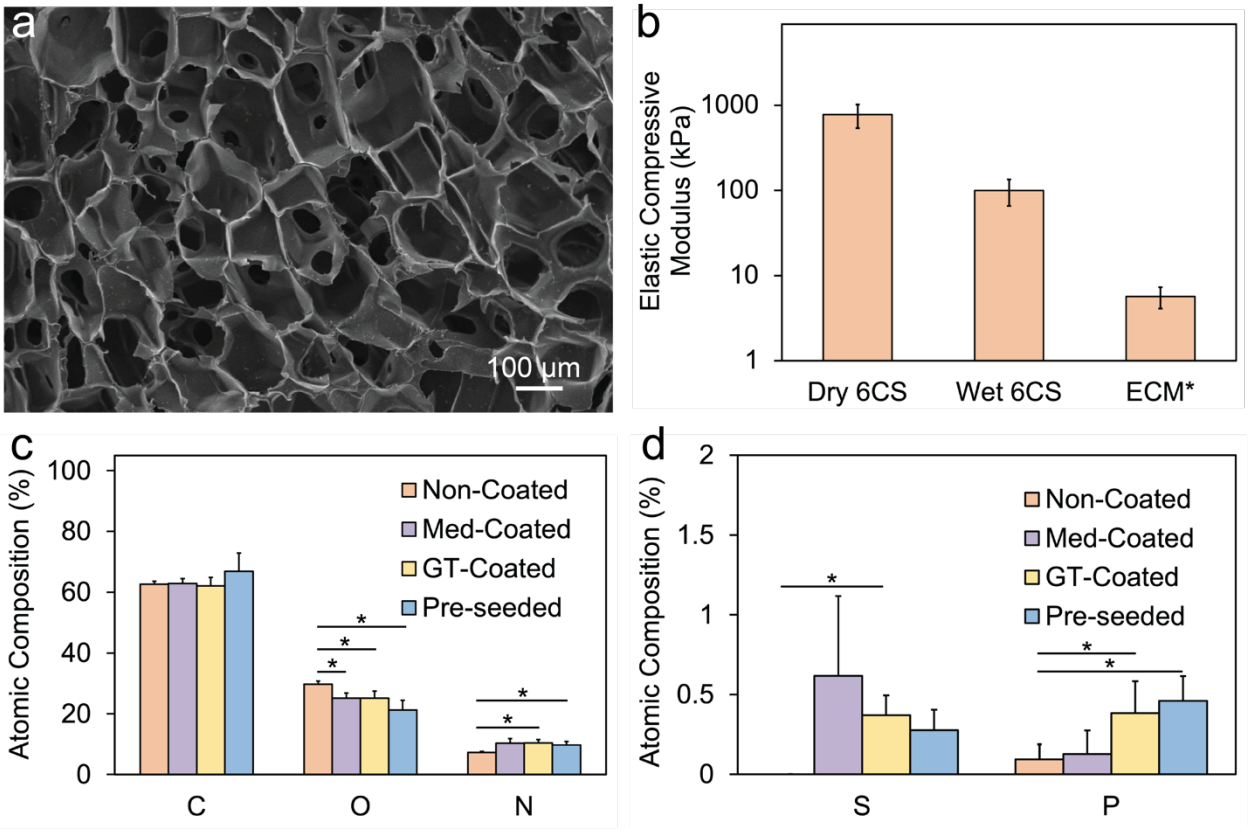


Figure 6.2 Physical characterization of 6CS scaffolds across different coating conditions. (a) SEM image of a dry, 6CS scaffold showing its microstructure, with average pore sizes calculated from at least 50 pores. (b) Elastic compressive moduli of dry and wet 6CS scaffolds compared to typical brain ECM values (adapted with permission from*[276]) Copyright 2007 JSME. (c) Atomic composition data acquired from XPS for non-coated, Geltrex coated (GT), pre-seeded, and medium (Med) coated 6CS scaffolds for carbon, oxygen, and nitrogen. (d) Sulfur and phosphorous atomic composition data from XPS for the same scaffold conditions. A * indicates a *P*-value of less than 0.05, while unmarked values indicate no significant difference between samples.

Figure 6.3 shows SEM images of scaffolds across the different coating conditions along with corresponding XPS results. **Figure 6.3a** shows the non-coated scaffolds surface, which appears relatively flat and free of debris, providing hNSCs ample surface area for attachment and proliferation. The medium coated scaffolds shown in **Figure 6.3b** show string-like proteins and some debris from the medium. These string-like proteins can also be seen, though less prominently, on pre-seeded scaffolds, indicating the cells may have used these proteins in their growth cycle. In

Figure 6.3c, the Geltrex coated scaffold shows clump-like proteins visible on the surface, indicating potential uneven coating, or possible damage to the Geltrex layer during SEM sample preparation.

Figure 6.3d shows that the pre-seeded scaffolds have an even protein coating and cell debris layer, indicating that cells growing on the scaffolds generate ECM and other proteins that may attach to the scaffold. Upon cell death additional proteins and cell debris contribute further to this coating. Overall, these results indicate that pre-seeded scaffolds yield a more uniform and consistent layer across the scaffold surface to compared to Geltrex or medium coated scaffolds, enhancing attachment sites for hNSCs.

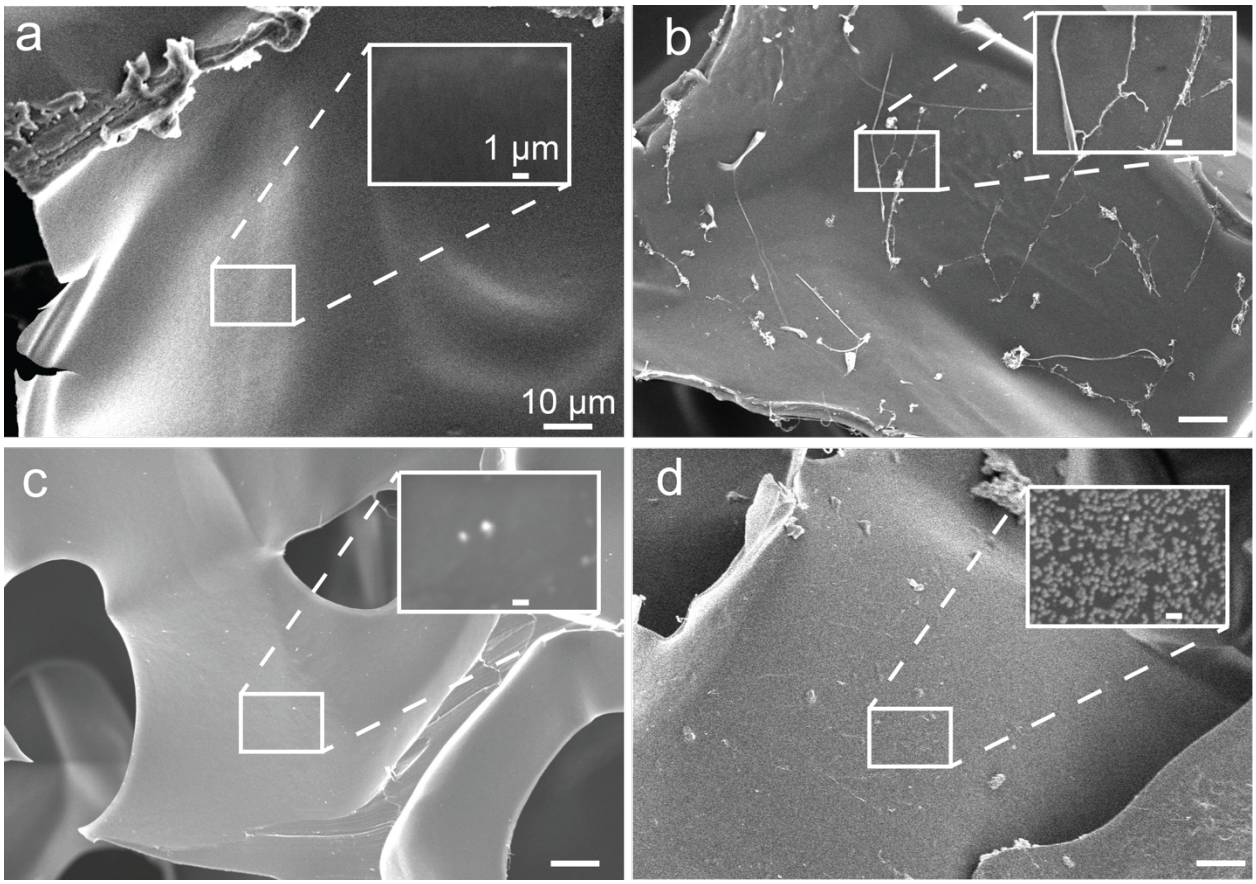


Figure 6.3 Surface characterization of various scaffold coating conditions. SEM images of a) non-coated, b) medium-coated, c) Geltrex-coated, and d) pre-seeded scaffolds. The scale bar in the main images represents 10 µm and the scale bar in the inset images represents 1 µm.

6.3.2 Cell viability and proliferation

Cell attachment across various scaffold coating conditions can be seen in **Figure 6.4a** and **6.4b** at 4X and 10X magnifications, respectively. In the noncoated scaffold cells appear in small clusters with limited adherence. Similarly, cells grown in medium coated scaffolds form small clusters but lack significant attachment to the substrate. For the Geltrex coated scaffolds, the cells can be seen to be growing as single cells or small clusters and do appear to be adherent. The cells grown in the pre-seeded condition can be seen to be growing in large clusters that appear to be somewhat adherent to the scaffold wall.

Figure 6.4c shows the metabolic activity of the cells grown on different scaffold conditions, revealing that pre-seeded scaffolds exhibited the highest metabolic activity among the 3D conditions, followed by the Geltrex-coated scaffolds. The non-coated and medium-coated scaffolds showed minimal metabolic activity after 3 days of culture. **Figure 6.4d** quantifies the percent area fluorescence of the Calcien-AM and propidium iodide-stained scaffolds after 3 days of culture, showing agreement with the results from the alamarBlue assay. While both the Geltrex coated and pre-seeded scaffolds have a similar percent area fluorescence for live stained cells, the cells on the Geltrex coated scaffold are more spread out while the cells on the pre-seeded scaffold tend to grow closer to one another, and a high cell density yields better differentiation results due to cell to cell interactions.[279] A population of dead cells remains in the scaffold during culture since the scaffold's pore structure acts to shield the cells from being removed from the scaffold.

Sex determining region Y-related high mobility group box 2 (SOX2) is an important transcriptional regulator in neural stem cells.[280] SOX2 regulates gene expression in NSCs, to both maintain the multipotency of the cells and to help direct differentiation.[281] Nestin is an intermediate filament protein that plays a role in the formation of tunneling nanotubes, which help regulate the

multipotency of hNSCs.[282] Flow cytometry analysis results in **Figure 6.4e** and **6.4f** show high expression of multipotency markers SOX2 and nestin across all conditions, with detailed dot plots and histograms in **Supplemental Figure S6.11a** and **S6.11b**, respectively. The non-coated scaffolds have the lowest overall metabolic activity, and therefore, the non-coated condition was eliminated from the subsequent characterizations. Overall, the live/dead images and the metabolic activity data strongly correlate, suggesting the enhanced cell viability and proliferation provided by the pre-seeded scaffolds.

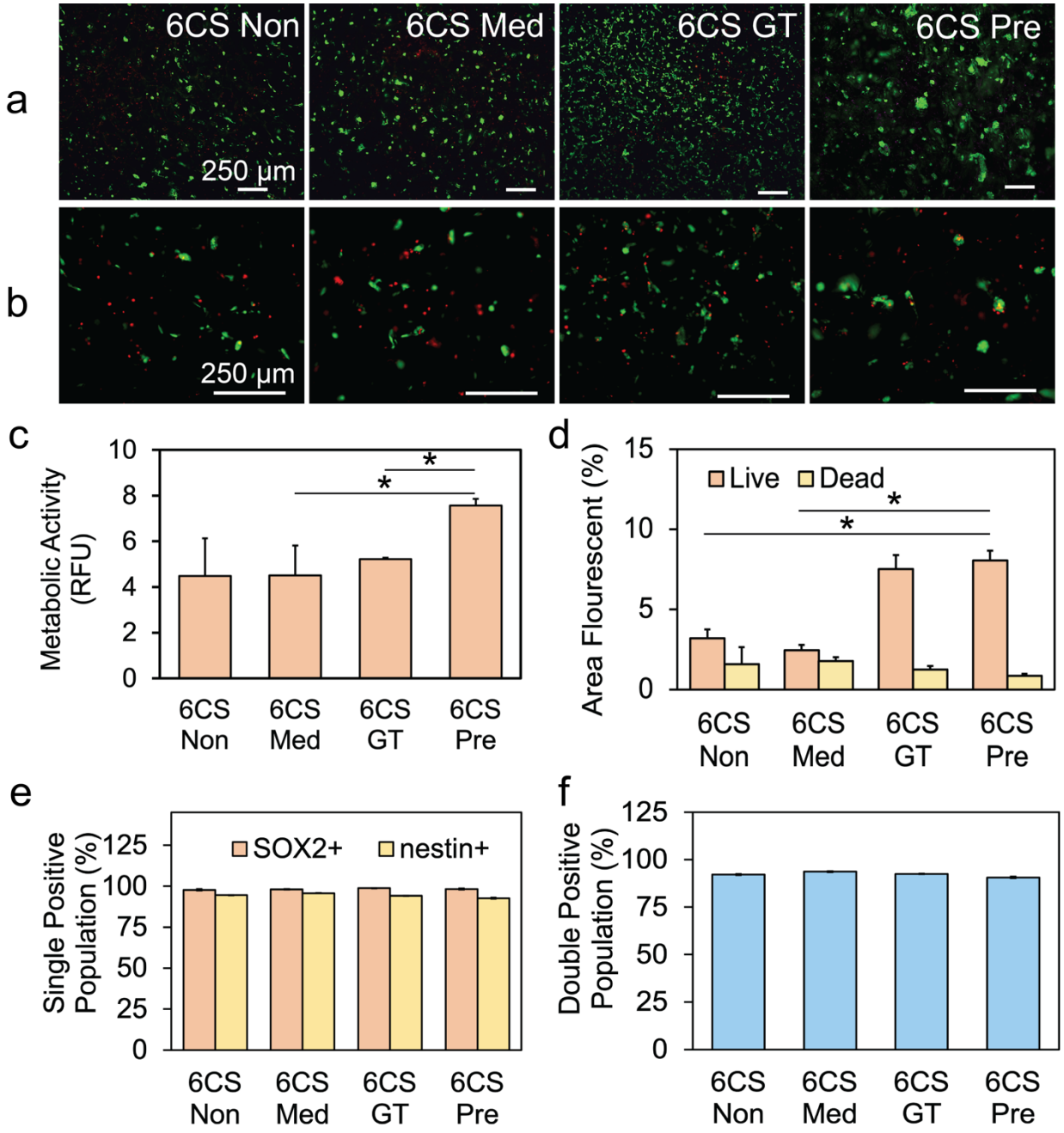


Figure 6.4 Cell morphology, metabolic activity, and protein expression of non-differentiated hNSCs. Live (green) and dead (red) staining of cells at (a) 4X magnification and (b) 10X magnification. (c) Metabolic activity assessment using alamarBlue assay after 3 days of culture. (d) Quantification of fluorescence area percentage from scaffolds stained with CaAM and propidium iodide after 3 days of culture. Flow cytometry analysis showing (e) single positive populations of SOX2 and nestin and (f) the SOX2/nestin double positive populations. At least 2500 cells were collected from 3 separate scaffolds and analyzed for flow cytometry. Asterisks * indicate a *p*-value of less than 0.05, whereas absence of an asterisk denotes no statistical significance between samples.

6.3.4 Cortical neuron differentiation from hNSCs

To evaluate the progression of hNSCs towards cortical neuron lineage, cells were collected from the scaffolds after 7 and 14 days of differentiation, followed by fixation. Flow cytometry was performed to assess the expression of key neuronal and glial markers. The expression levels of microtubule-associated protein 2B (MAP2B), a cytoskeletal protein crucial for dendritic stability and neuronal functionality,[283] and glial fibrillary acidic protein (GFAP), an intermediate filament protein expressed in mature astrocytes, which is essential for maintaining cellular architecture and intercellular communication of the cells.[284] **Figure 6.5a** shows an increase over time for the expression of MAP2B in the pre-seeded and 2D control groups, indicating the cells have begun the differentiation process and are moving towards maturing as neurons with around 50% total expression for the pre-seeded group and around 20% for the 2D control group on day 14. Both the medium coated and Geltrex coated scaffolds had a decrease in MAP2B expression over the 14-day period, likely due to the cells in the medium coated and Geltrex coated scaffold being more spread out or scaffold environment being unable to support mature neurons. **Figure 6.5b** shows how the expression of GFAP increases for all the conditions, with a notable rise in the pre-seeded scaffolds (from 4% on day 7 to 24% on day 14) and a more modest increase in the 2D control group (from 3% on day 7 to 6% on day 14). Maintaining a healthy astrocyte population is essential for neuron health and function.

Dot plots in **Figure 6.5c** reveal that the population of double-positive cells for MAP2B and GFAP remained minimal for all groups on day 7 and day 14, which is expected because MAP2B and GFAP are indicative of distinct neural lineages, with the former marking neuronal differentiation and the latter marking astrocytic differentiation. **Figure 6.5d** displays the histograms for MAP2B positive populations, which shows the cell distributions for each condition.

Figure 6.6a shows the expression of beta-tubulin 3 (TUBB3), an immature neuronal protein that regulates cell structure and migration.[242] The TUBB3-positive population increased significantly over time across all scaffold conditions. Notably, the pre-seeded scaffolds exhibited a higher expression rate (84% at day 7 and 95% at day 14, respectively) compared to either Geltrex coated scaffolds (72% and 88%, respectively) and the 2D control samples (47% and 67%, respectively). This suggests that the pre-seeded scaffolds provide a more conducive environment for early neuronal differentiation.

Figure 6.6b shows the positive populations for doublecortin (DCX), an early microtubule associated protein essential to neurite outgrowth and migration.[285] the DCX-positive population increased over time for the Geltrex coated, pre-seeded, and 2D control groups, while it decreased for the medium-coated scaffold. Specifically, the pre-seeded scaffold showed a significant increase from 25% on day 7 to 52% on day 14, and the 2D control increased from 8% to 23% over the same period. This means that the Geltrex coated scaffold can support migratory neurons (DCX positive), but not mature neurons (MAP2B positive), while the pre-seeded scaffold is able to support both. This pattern highlights the enhanced differentiation capabilities of the pre-seeded scaffold condition.

Dot plots in **Figure 6.6c** shows an increase in the double-positive population for TUBB3, and DCX for all scaffold conditions, except for the medium treated scaffolds. This trend suggests a progression of hNSCs from expressing immature neuronal markers (TUBB3) to more mature, intermediary markers (DCX). The presence of double-positive cells indicates an overlap in the expression of these proteins during the transitional phase of neuronal differentiation. **Figure 6.6d** displays the histograms for the TUBB3 positive populations, reinforcing the higher differentiation potential of the pre-seeded scaffolds.

Analysis of cell viability (**Supplemental Figure S6.12a**) revealed that 7 days after plating the pre-seeded and Geltrex-coated scaffolds had similar viable cell populations, around 53%, while the medium-treated scaffolds had a slightly higher viability at 68%. The 2D control had the lowest viability at 20%. By day 14, the pre-seeded scaffold condition displayed the highest viable cell population (85%), followed by the Geltrex-coated scaffolds (73%), while the medium-treated scaffolds decreased to 58%. The 2D control further declined 14%, indicating superior overall survival rate in 3D scaffolds compared to the 2D controls. The medium coated scaffolds likely lacked proteins on their surface needed for long term cell attachment, which affected their ability to differentiate because cell attachment plays a role in cell differentiation.[286]

Supplemental Figure S6.12b shows the SOX2 positive population of the various scaffold conditions. SOX2 is a transcription factor essential for maintaining stem multipotency.[287] Over the 14-day period, SOX2 expression decreased in the medium coated and pre-seeded scaffold conditions, indicating a reduction in stemness as cells differentiated In contrast, the 2D control and Geltrex coated scaffolds showed an increase in SOX2 expression, with the 2D control reaching the highest levels. This suggests that the differentiation environment in 3D scaffolds, particularly in pre-seeded scaffolds, may more effectively promote neuronal lineage commitment, as indicated by the declining expression of this multipotency marker.

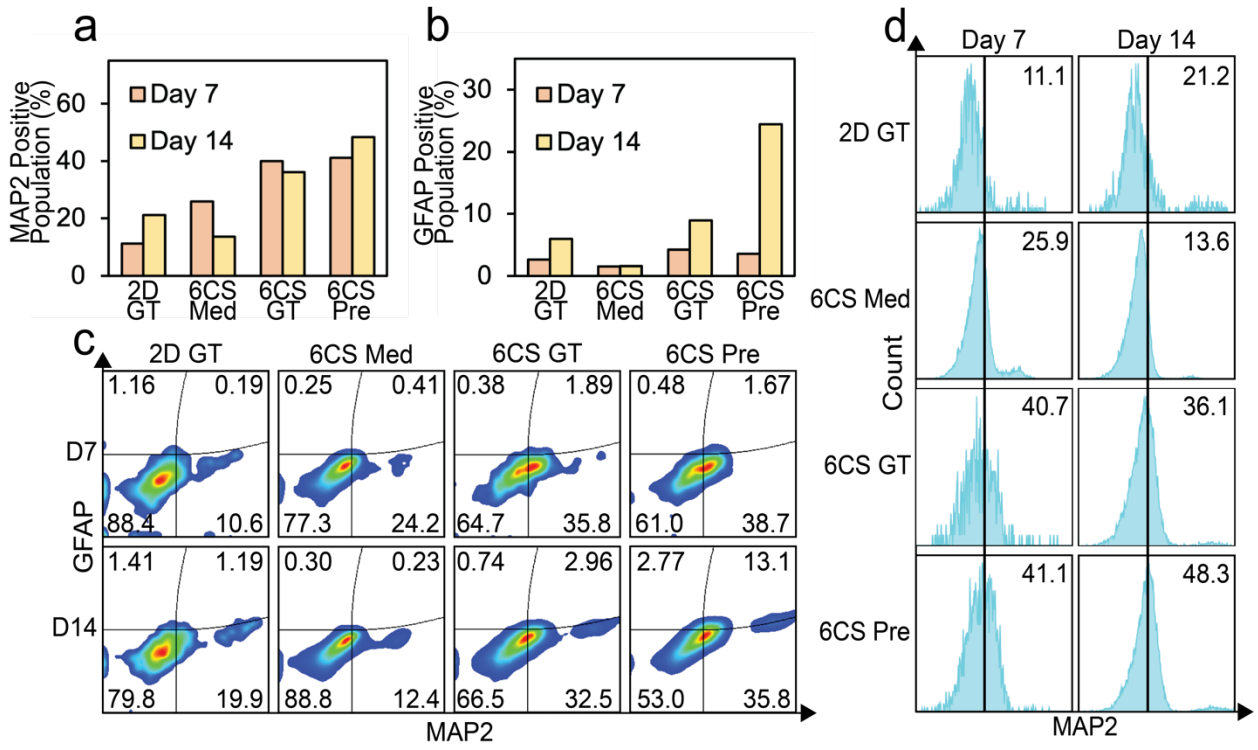


Figure 6.5 Flow cytometry analysis of MAP2 and GFAP expression in hNSC-derived cortical neurons. hNSCs were differentiated on Geltrex coated 2D well plates (2D GT), medium treated 3D scaffolds (6CS Med), Geltrex coated 3D scaffolds (6CS GT), and pre-seeded 3D scaffolds (6CS Pre) for 7 and 14 days. (a) The single-positive population for MAP2B, highlighting the maturation of neurons (b) The single positive-population for GFAP, indicating astrocyte differentiation. (c) Dot plots showing the expression patterns of MAP2B and GFAP across the different conditions, demonstrating distinct neural lineage differentiation. (d) Histograms for MAP2B-postive populations, illustrating the increase in neuronal differentiation over time. At least 2500 cells were collected from 3 separate scaffolds and analyzed.

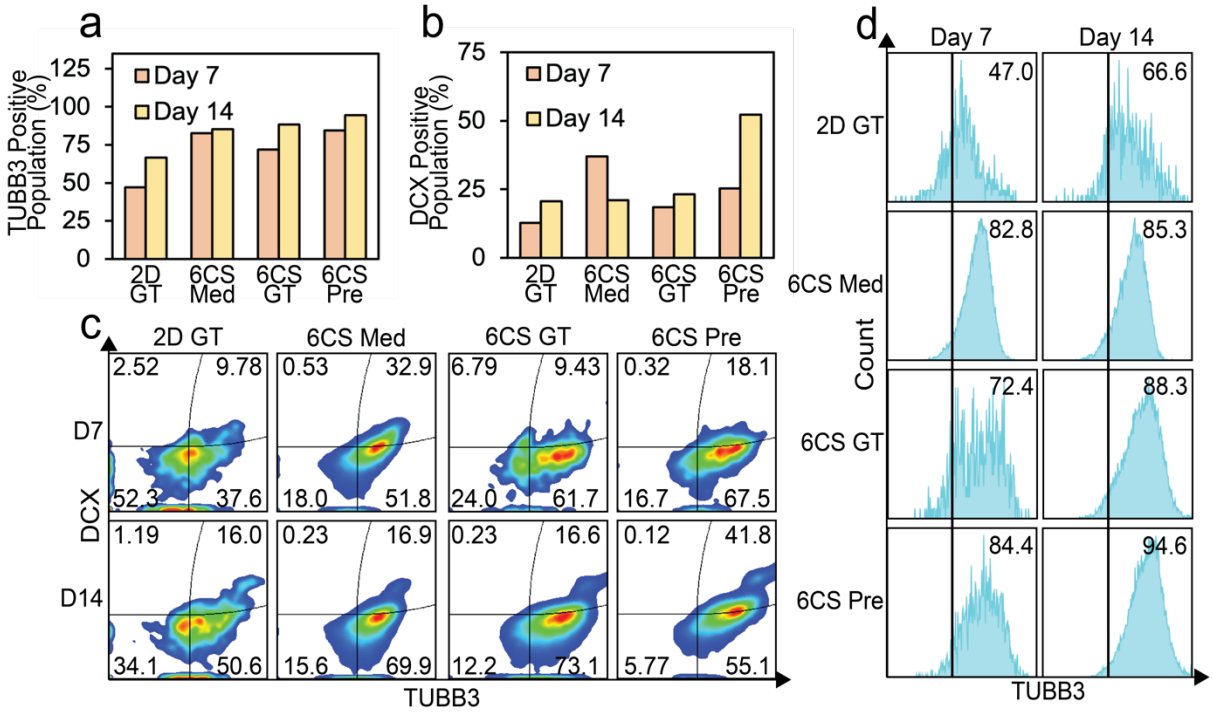


Figure 6.6 Flow cytometry analysis of TUBB3 and DCX in hNSC-derived cortical neurons. hNSCs were differentiated on different substrates for 7 or 14 days, including Geltrex coated 2D well plates (2D GT), medium treated 3D scaffolds (6CS Med), Geltrex coated 3D scaffolds (6CS GT), and pre-seeded 3D scaffolds (6CS Pre). The single-positive populations for (a) TUBB3 and (b) DCX. (c) Dot plots for TUBB3 and DCX. (d) Histograms for TUBB3-postive populations. At least 2500 cells were collected from 3 separate scaffolds and analyzed.

200,000 cells were seeded onto each scaffold and allowed to proliferate for 4 days before initiating differentiation. Cells were collected and fixed after 7 and 14 days of differentiation, followed by immunocytochemistry to examine the intracellular localization of key proteins. MAP2B expression, shown in **Figures 6.7** and **6.8** (**a** represents the Geltrex 2D control, **b** represents the medium treated scaffolds, **c** represents the Geltrex coated scaffolds, and **d** represents the pre-seeded scaffolds)**,** was consistently detected throughout the study and became increasingly concentrated in the dendrites over time, indicating ongoing dendritic development. **Supplemental Figures S6.13** and **S6.14** further illustrate this trend, showing an increase in the expression of

mature cortical neuron markers, t-box brain 1 (TBR1) and COUP-TF-interacting protein 2 (CTIP2). TBR1, a transcription factor that regulates the development and maintenance of cortical neurons and aids in axon pathfinding,[288] and CTIP2, a transcription factor that regulates neuron fate, increased over time,[289] indicating progressive neuronal maturation. CTIP2 can hardly be seen in the scaffold conditions due to the autofluorescence of the scaffolds and can be seen for day 7 and day 14 in **Supplemental Figures S6.13** and **S6.14**, respectively.

TBR1 was mainly localized in the cell body and not in the dendrites in both for the pre-seeded and Geltrex coated scaffolds, but was scarcely expressed in the medium treated scaffolds on both day 7 and 14. In the medium treated scaffolds, MAP2B staining revealed that dendrites often terminated close to the cell body on day 7, and by day 14, dendrites were no longer visible, indicating suboptimal differentiation conditions. Cells in the Geltrex and pre-seeded scaffolds appeared randomly distributed; however, those with positive marker expression adhered well to the scaffold walls, indicating that cell attachment significantly influences differentiation success. Additionally, dendrites formed by cells in the pre-seeded and Geltrex-coated scaffolds showed higher interconnectivity between cells, even when the cells are located a long distance from each other, while the medium coated scaffolds exhibited poor dendritic connectivity. As a result, the medium coated scaffolds were excluded from further experiments due to their insufficient support for differentiation.

Supplemental Figure S6.15 shows GFAP and MAP2 staining for both 2D controls and pre-seeded scaffolds on day 7 and 14. GFAP expression was relatively low in cells grown in the scaffolds compared to those grown in the 2D controls (**Supplemental Figure S6.15a** and **S6.15b** for 2D control; **S6.15c** and **S6.15d** for pre-seeded scaffolds), indicating reduced astrocytic differentiation in the 3D scaffold environments.

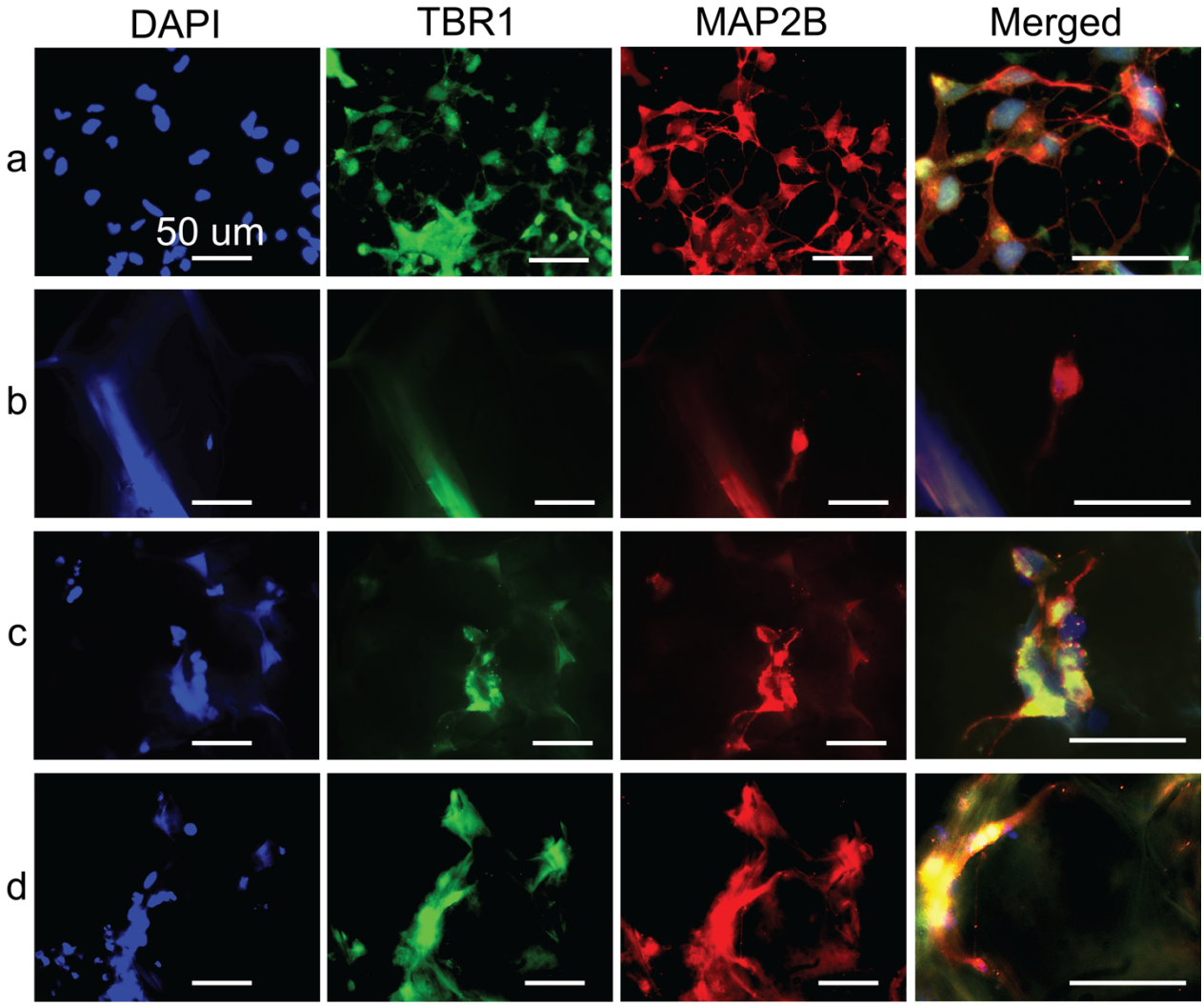


Figure 6.7 Immunostaining analysis of DAPI, TBR1, and MAP2 in -7-day differentiated hNSCs. Immunostaining images of hNSCs differentiated for 7 days, grown on different coating conditions: (a) Geltrex coated 2D well plates, (b) medium-treated 3D scaffolds, (c) Geltrex-coated 3D scaffolds, and (d) pre-seeded 3D scaffolds. TBR1 is presented as green, MAP2B as red, and DAPI, staining cell nuclei, is presented in blue. The scale bar is 50 µm.

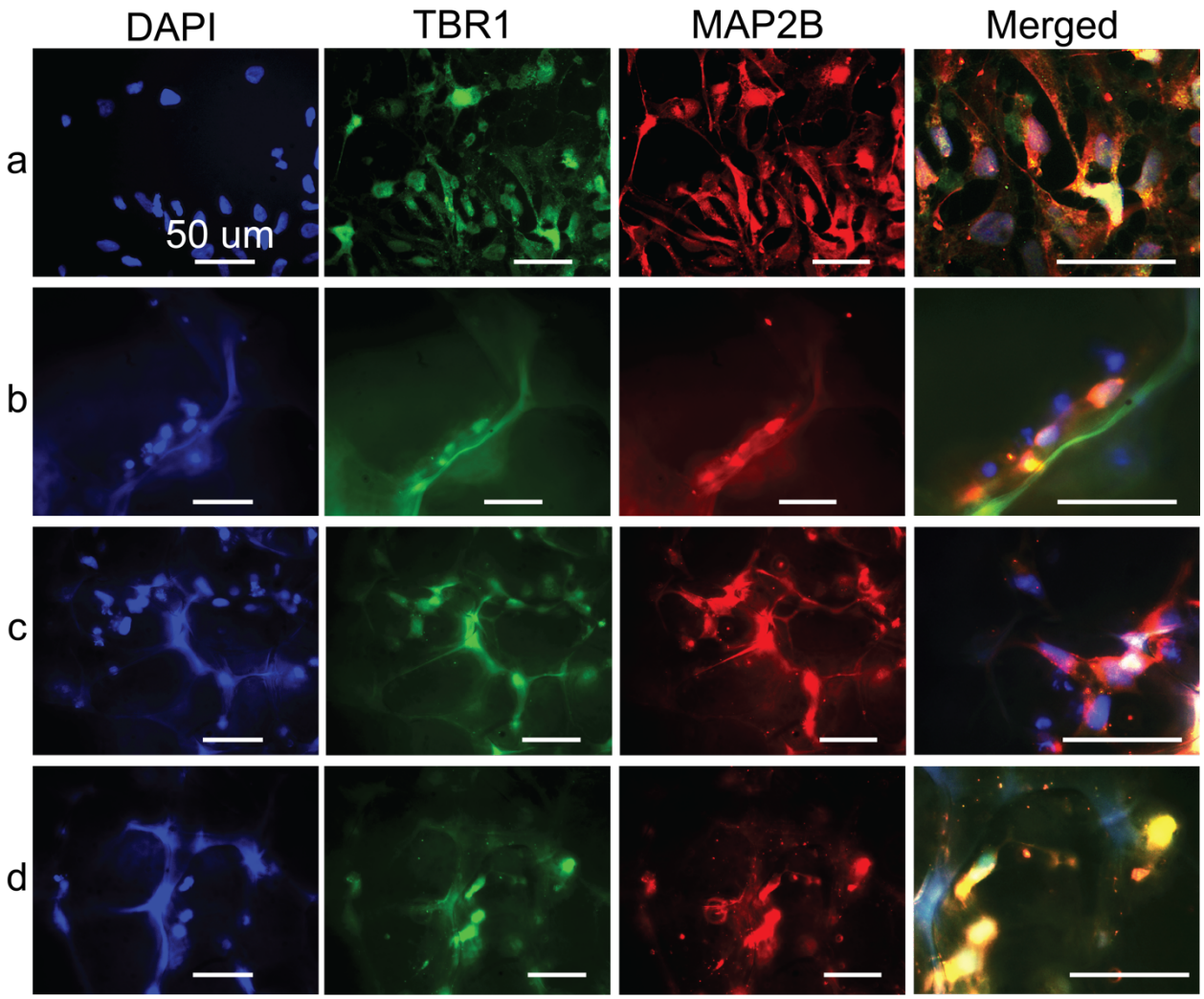


Figure 6.8 Immunostaining analysis of DAPI, TBR1, and MAP2 in 14-day differentiated hNSCs. Immunostaining images of hNSCs differentiated for 14 days on various culture conditions: (a) Geltrex coated 2D well plates, (b) medium treated 3D scaffolds, (c) Geltrex coated 3D scaffolds, and (d) pre-seeded 3D scaffolds. Cells were stained with TBR1-green and MAP2B-red. DAPI, staining cell nuclei, is presented in blue. The scale bar is 50 μm.

6.3.5 mRNA expression in differentiated hNSCs

PCR analysis was conducted to assess mRNA expression of key differentiation markers. Markers analyzed include *GFAP* (a mature astrocyte marker), oligodendrocyte transcription factor 2 (*OLIG2*), a gene that regulates oligodendrocyte differentiation,[290] *DCX*, *MAP2*, *TBR1*, and *CTIP2* (**Figure 6.9**).[291] **Figure 6.9a** shows the gene expression on day 7, while **Figure 6.9b** shows the data represented as a heat map. **Figure 6.9c** shows the gene expression on day 14 and **Figure 6.9d**

presents the gene expression as a heat map. All data were normalized to undifferentiated hNSCs control.

The cells from 3D scaffolds showed higher levels of differentiation markers compared to the 2D controls. Notably, the pre-seeded scaffolds exhibited higher expression of *GFAP* and *OLIG2*. *GFAP* is a mature astrocyte marker and *OLIG2* is a mature oligodendrocyte marker. This result indicates that the cells from the pre-seeded scaffolds exhibited faster progression towards mature astrocytes and oligodendrocytes than the cells from the Geltrex coated scaffolds. *DCX* and *MAP2* are immature and mature, microtubule associated neuronal markers, respectively. The initial higher *DCX* expression in the pre-seeded scaffolds, followed by a decrease by by 14 days, indicates rapid transition to maturity. Conversely, *MAP2* expression was higher in Geltrex-coated scaffolds than in the pre-seeded scaffolds, indicating that the pre-seeded scaffolds may be more supportive of maturation. *TBR1*, an earlier mature neuron marker, and *CTIP2*, a mature cortical neuron marker, were more expressed in the pre-seeded scaffolds, but decreased over time, indicating a transition to mature neuron differentiation. In contrast, , all differentiation markers increased In the 2D control over the 14-day period, potentially reflecting an earlier differentiation stage than in the scaffolds, where mRNA expression declined, possibly due to cellular maturation and senescence,[292-294] meaning the cells differentiated into mature cortical neurons.

Multipotency markers including SRY-box transcription factor 1 (*SOX1*), *SOX2*, paired box protein 6 (*PAX6*) (a transcription factor that regulates proliferation, multipotency, and neurogenesis),[295] and *nestin*, a cytoskeletal filament protein, were assessed and shown in **Supplemental Figure S6.16**. Gene expression on day 7 and on day 14, along with their heat maps, revealed a general decrease in these markers over time in 3D scaffold samples, suggesting advanced differentiation. *SOX1*, *SOX2*, *PAX6*, and *nestin* were shown generally decreasing in the

3D samples over time. These markers all increased for the 2D control samples. These markers help control neuronal differentiation and decreases in these markers indicate the progression of differentiation.

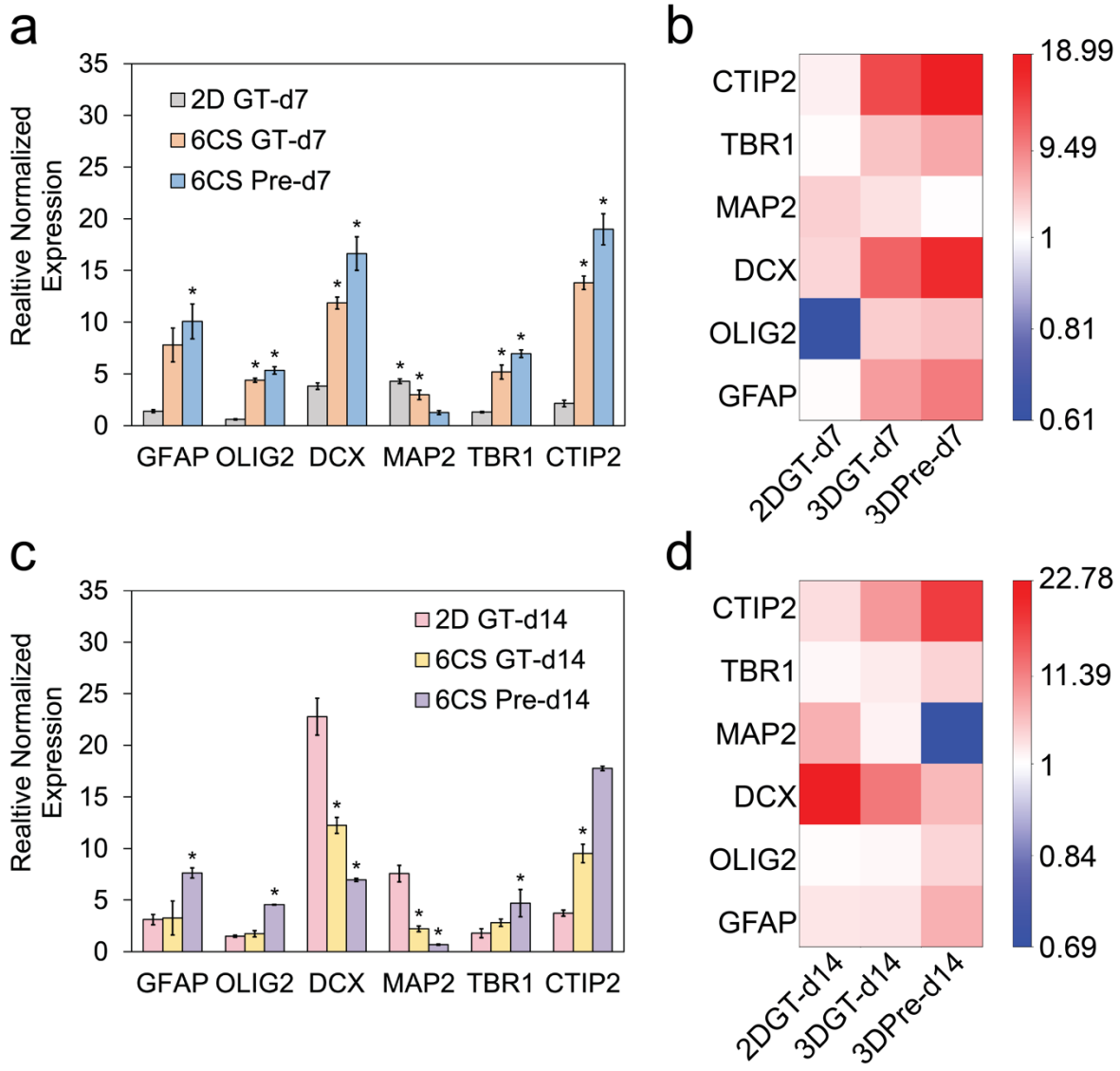
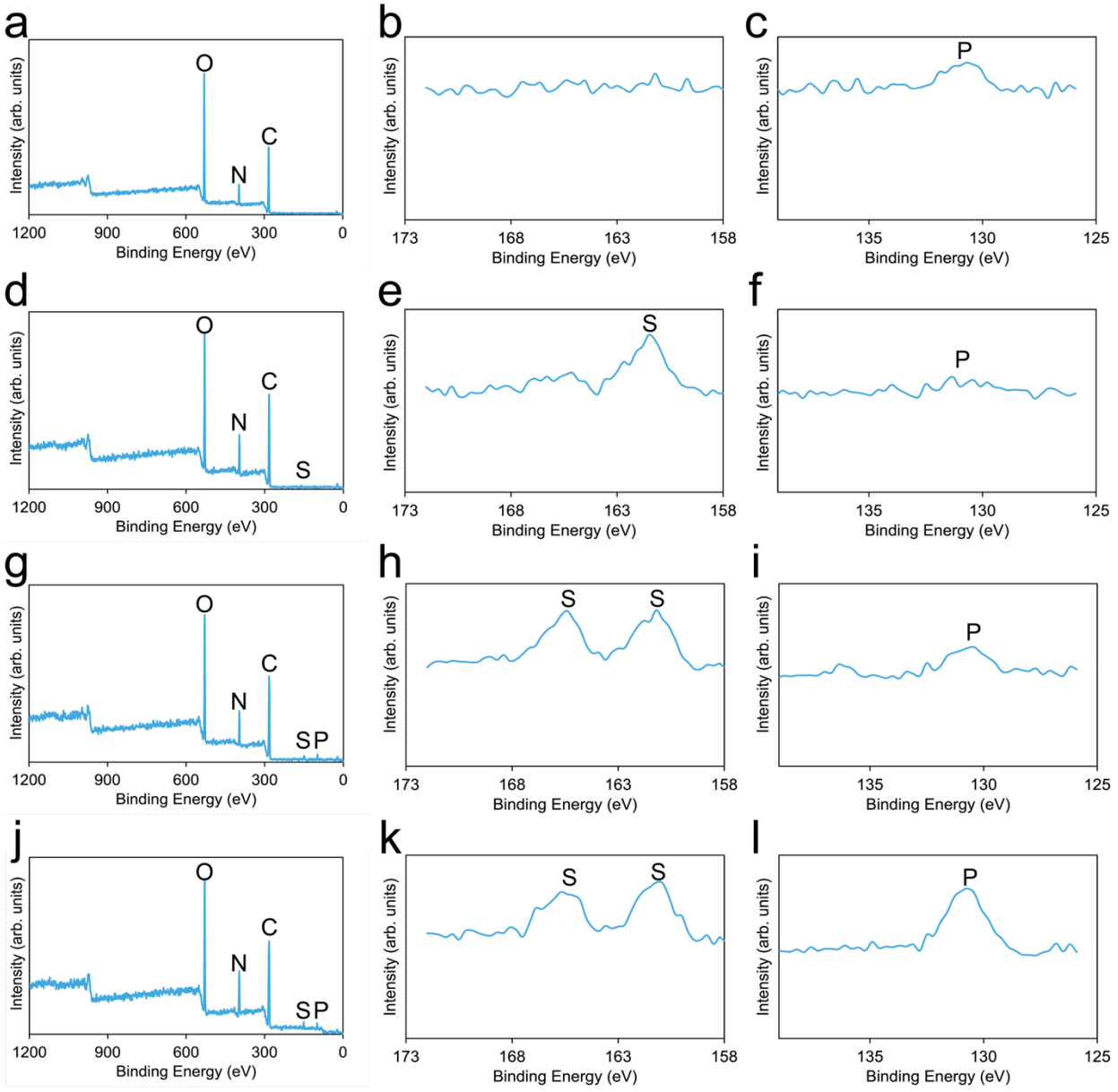


Figure 6.9 Gene expression analysis of differentiation markers on day 7 and 14. Gene expression analysis of hNSC differentiation for 7 and 14 days, comparing cells grown on Geltrex coated 2D well plates (2DGT), Geltrex coated 3D scaffolds (3DGT), and pre-seeded 3D scaffolds (3DPre). Results for day 7 are shown as a bar chart in (a) and a heat map in (b). Corresponding data for day 14 are presented a bar chart in (c) and a heat map (d). An * indicates a *p* value lower than 0.05 when compared to the 2D sample at the same time point.

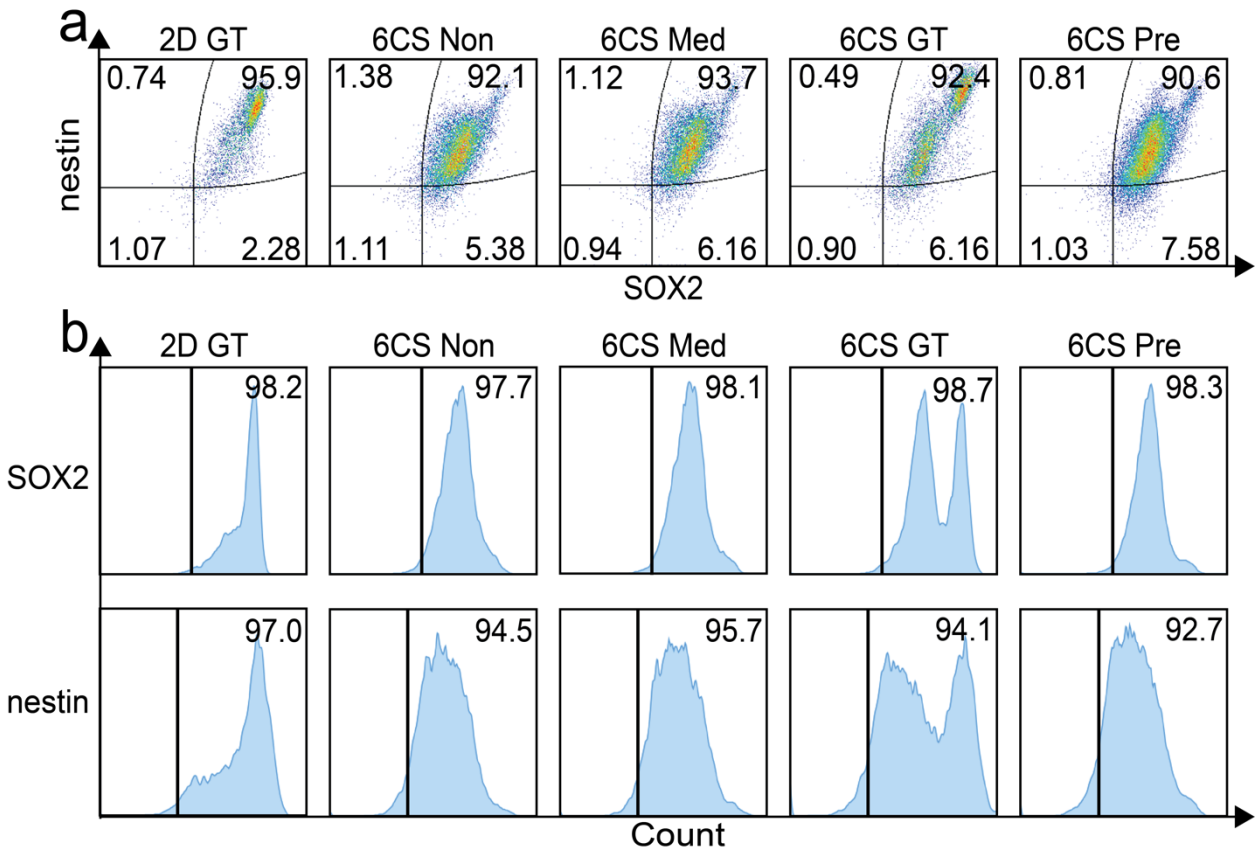
6.4 Supplemental Information

Supplemental Table S6.1 The sequences of primers used in qPCR analysis.

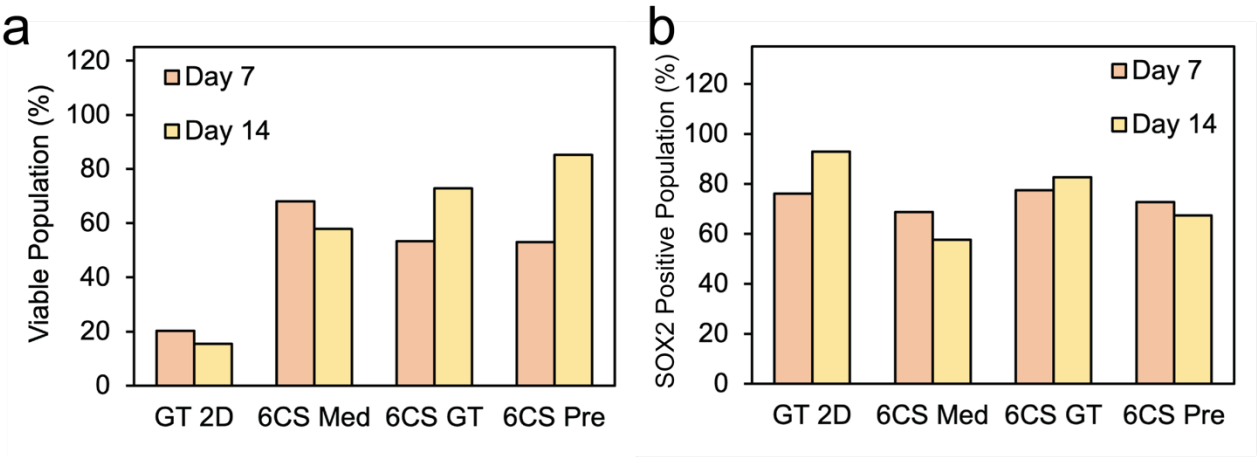
Primer	Sequence
GAPDH Forward	GGTGTGAACCATGAGAAGTATGA
GAPDH Reverse	GAGTCCTTCCACGATACCAAAG
SOX1 Forward	GCAAGATGGCCCAGGAGAA
SOX1 Reverse	CCTCGGACATGACCTTCCA
SOX2 Forward	GCGAACCATCTCTGTGGTCT
SOX2 Reverse	GGAAAGTTGGGATCGAACAA
PAX6 Forward	AACAGACACAGCCCTCACAAACA
PAX6 Reverse	CGGGAACTTGAACTGGAACTGAC
nestin Forward	TCCAGAGCTGTCAATGACTCTAAG
nestin Reverse	GACCACTCCAGTTTAGAGGCTAAG
GFAP Forward	GAGGTTGAGAGGGACAATCTGG
GFAP Reverse	GTGGCTTCATCTGCTTCCTGTC
OLIG2 Forward	AACAGTTTGGGTTATTTGGG
OLIG2 Reverse	GGAGGAGTTTACCATTTGTG
DCX Forward	TATGCGCCGAAGCAAGTCTC
DCX Reverse	TACAGGTCCTTGTGCTTCCG
MAP2 Forward	TTGTCTCTAACCGAGGAAGCA
MAP2 Reverse	TCGTTGTGTCGTGTTCTCAA
TBR1 Forward	ATGGGCAGATGGTGGTTTTA
TBR1 Reverse	GACGGCGATGAACTGAGTCT
CTIP2 Forward	CAGAGCAGCAAGCTCACG
CTIP2 Reverse	GGTGCTGTAGACGCTGAAGG



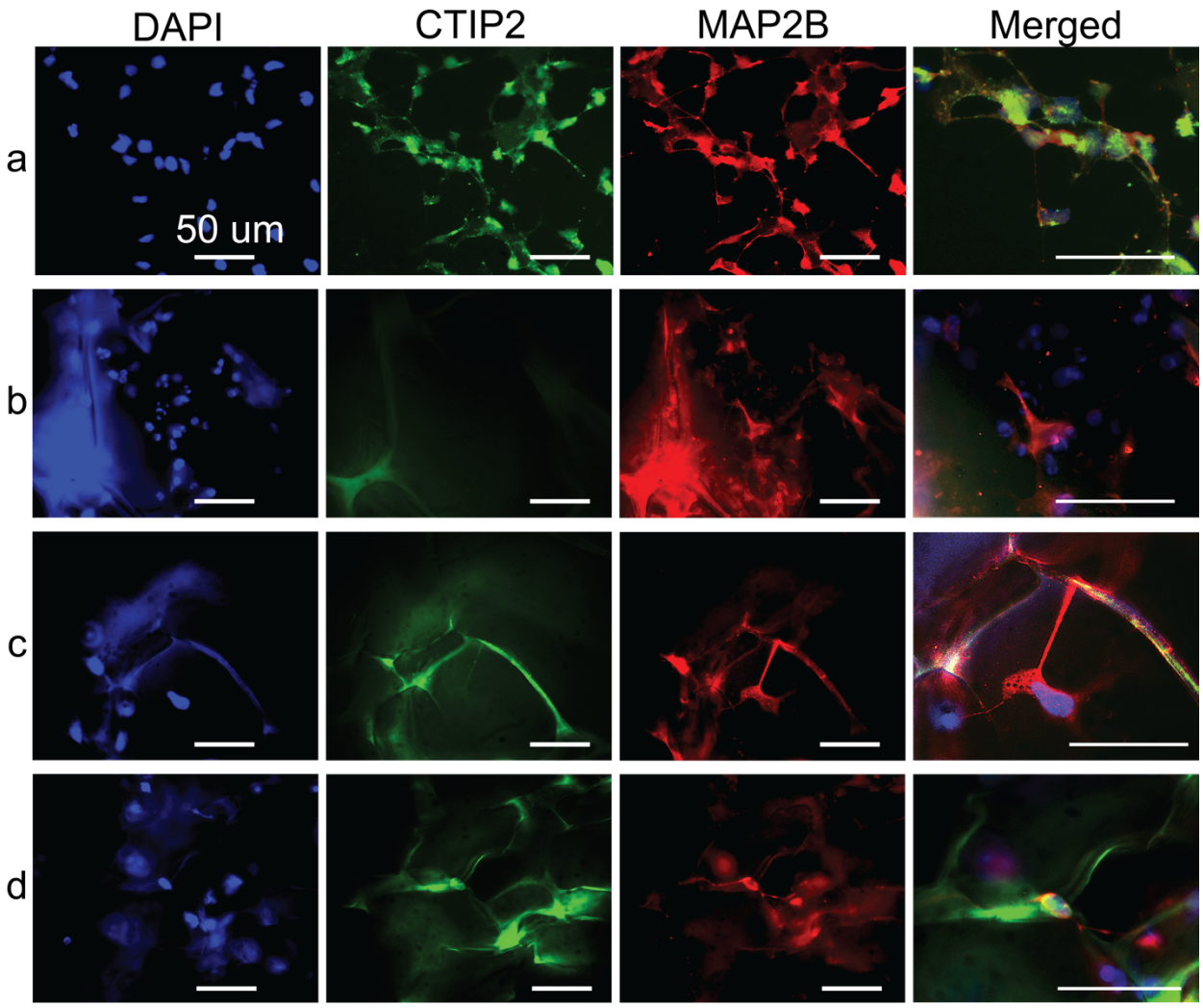
Supplemental Figure S6.10 Raw XPS spectra data for a) naked scaffolds survey scan, b) naked scaffolds sulfur scan, c) naked scaffolds phosphorous scan, d) medium-treated scaffolds survey scan, e) medium treated scaffolds sulfur scan, f) medium treated scaffolds phosphorous scan, g) Geltrex scaffolds survey scan, h) Geltrex scaffolds sulfur scan, i) Geltrex scaffolds phosphorous scan, j) pre-seeded scaffolds survey scan, k) pre-seeded scaffolds sulfur scan, and l) pre-seeded scaffolds phosphorous scan. The raw XPS scans show clear peaks for oxygen, nitrogen and carbon. The survey scans show clear peaks for sulfur and phosphorous for scaffolds that had a coating applied to them.



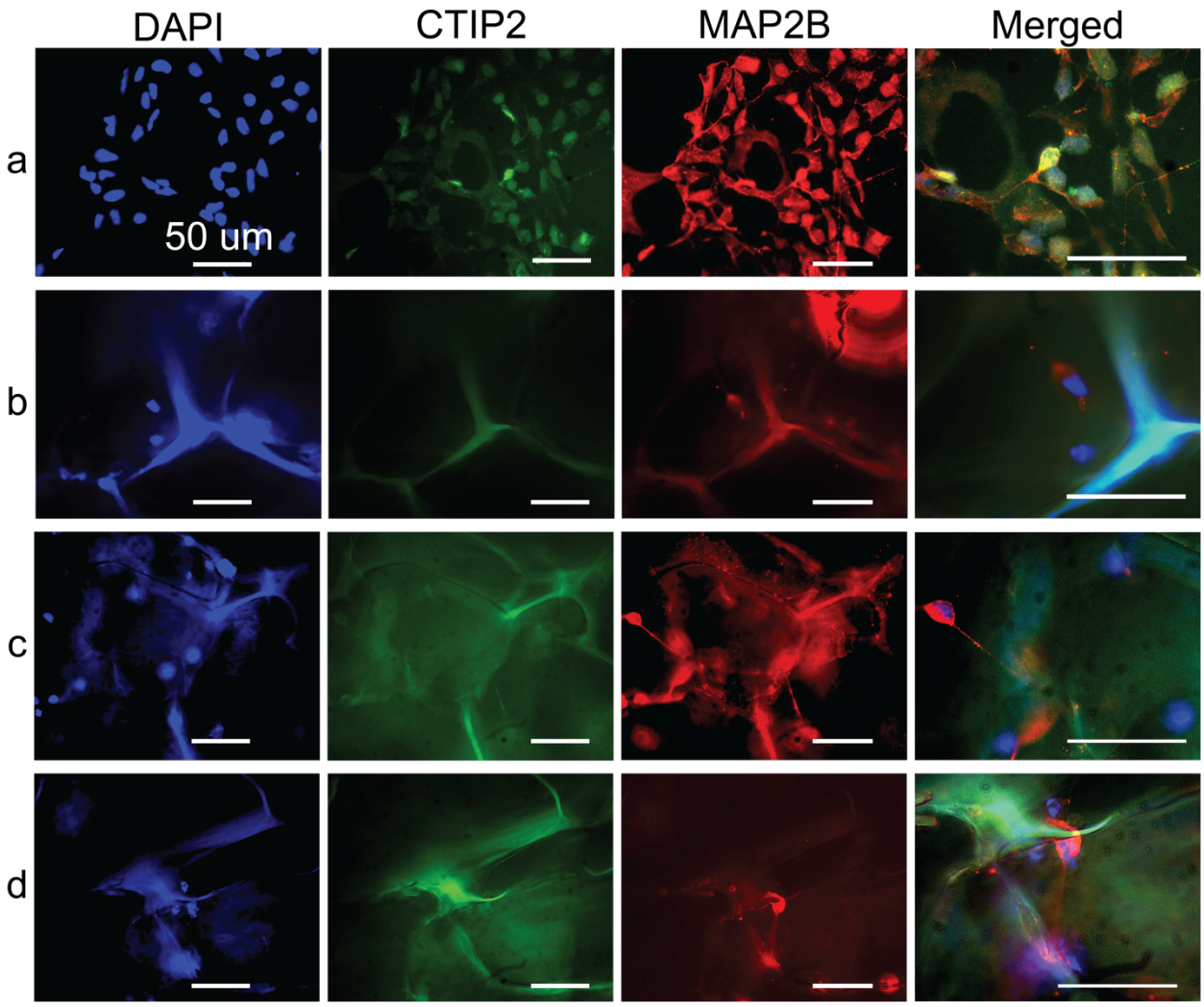
Supplemental Figure S6.11 Flow cytometry analysis of multipotency markers for 2D control (2D GT), medium treated 3D (6CS Med), Geltrex coated 3D (6CS GT), and pre-seeded 3D (6CS Pre). a) representative dot plots for SOX2 and nestin expression and b) histograms for SOX2 and nestin. The dot plot representation shows many cells are able expressing both SOX2 and nestin, indicating that both the 2D control and the scaffolds can support a healthy and multipotent cell population, with all conditions showing over 90% double expression. The histograms show the single positive populations for both SOX2 and nestin. Both the dot plots and histograms indicate that many of the cells are coexpressing both multipotency markers. At least 2500 cells were collected from 3 separate scaffolds and analyzed.



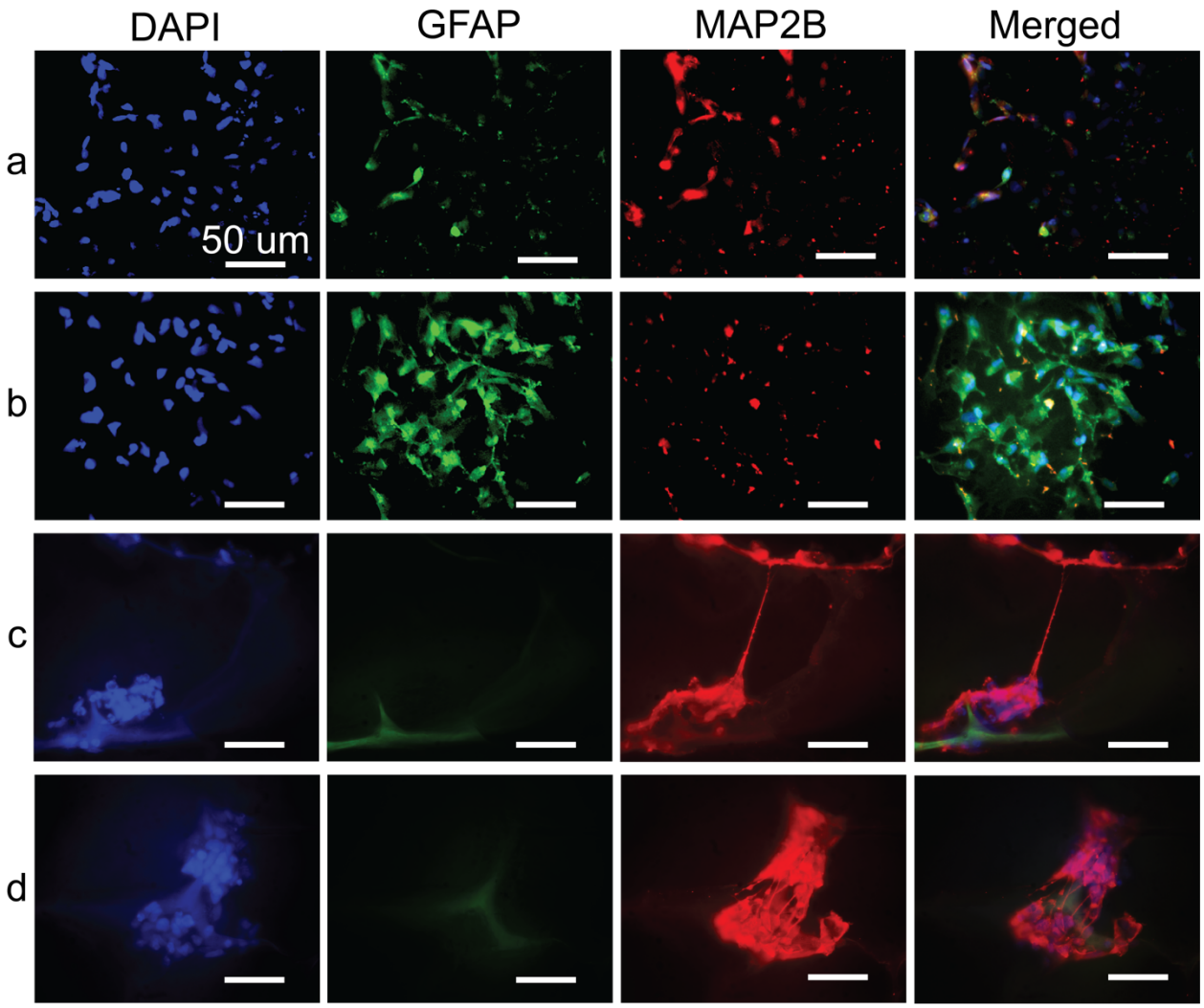
Supplemental Figure S6.12 Flow cytometry analysis taken from 2D well plates coated with Geltrex (GT 2D), medium treated 3D (6CS Med), Geltrex coated 3D (6CS GT), and pre-seeded 3D (6CS Pre), grown for 7 or 14 days. a) viable cell population after gating for dead cells and b) positive populations for SOX2. Viability of the cells shows that there are more viable cells in the scaffolds than there are in 2D across both time points, with there being the highest percentage in the pre-seeded scaffolds. Both the 2D control and the medium treated scaffolds saw a decrease in viability between day 7 and day 14, while the Geltrex coated and pre-seeded saw an increase in viability. The 2D control saw an increase in SOX2 (a multipotency marker) expression over the 14-day period, and the 2D control had the greatest overall expression of SOX2. The Geltrex coated scaffolds saw an increase in SOX2 while both the medium treated and pre-seeded scaffold saw decreases over the 14-day period. At least 2500 cells were collected from 3 separate scaffolds and analyzed.



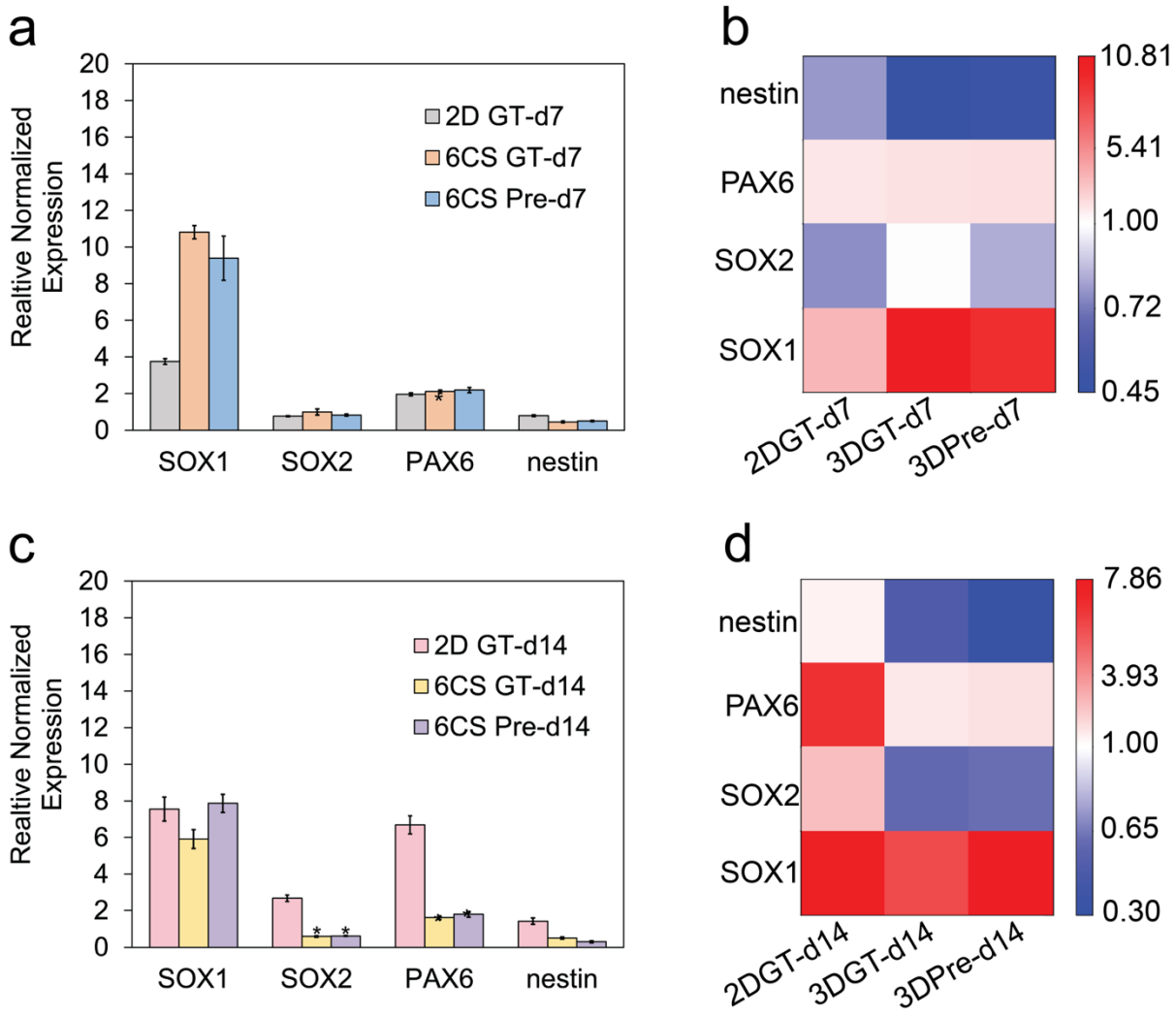
Supplemental Figure S6.13 Fluorescence images of hNSC-H14 cells cultured for 4 days and differentiated for 7-days using immunocytochemistry staining for CTIP2-green and MAP2B-red. DAPI staining for nuclei are presented in blue. a) Geltrex coated 2D well plates, b) medium treated 3D scaffolds, c) Geltrex coated 3D scaffolds, and d) pre-seeded 3D scaffolds. Cells grown in 2D showed CTIP2 stained appearing in the nucleus and MAP2B staining appearing in the dendrites, while also showing interactions between cells. In the 6CS medium treated scaffold, not CTIP2 staining can be seen. While the MAP2B does appear weakly in the dendrite, there is no connection to adjacent cells. In the Geltrex-coated scaffold, there appears to be a very weak CTIP2 expression, while there is a strong MAP2B expression in the dendrite that appears to be adherent to the scaffold wall. In the pre-seeded scaffold, the CTIP2 is expressed in the nucleus of the cells, while the MAP2B is expressed in the dendrites. The dendrite can be seen extending out to form connections with nearby cells. The scale bar is 50 µm.



Supplemental Figure S6.14 Immunostaining analysis for hNSCs differentiated on a) Geltrex coated 2D well plates, b) medium treated 3D scaffolds, c) Geltrex coated 3D scaffolds, and d) pre-seeded 3D scaffolds for 14 days. CTIP2-green and MAP2B-red. DAPI staining for nuclei are presented in blue. Cells were cultured on Matrigel coated plates, Geltrex coated scaffolds, and plain scaffolds. The scale bar is 50 µm. In the 2D control sample, CTIP2 and MAP2B stained cells can be seen, with CTIP2 appearing in the nucleus and MAP2B appearing in the dendrites and nucleus. The medium treated 6CS scaffold has poor staining, with CTIP2 not showing up and MAP2B being barely visible, indicating poor cell quality. The Geltrex coated scaffold shows weak CTIP2 staining, but the MAP2B staining appears strongly in the dendrites. The pre-seeded scaffold shows CTIP2 and MAP2B staining in the cells, and the dendrites can be seen extending out to the scaffold walls.



Supplemental Figure S6.15 Immunostaining analysis for hNSCs differentiated on a) Geltrex coated 2D well plates on day 7, b) Geltrex coated 2D well plates on day 14, c) pre-seeded 3D scaffolds for 7 days, and d) pre-seeded 3D scaffolds for 14 days. GFAP-green and MAP2B-red. DAPI staining for nuclei are presented in blue. Cells were cultured on Matrigel coated plates, Geltrex coated scaffolds, and plain scaffolds. The scale bar is 50 µm. In the 2D control samples, relatively high expression of GFAP stained cells can be seen, while in the pre-seeded 3D sample there is little to no staining of GFAP. This indicates the scaffolds produce a larger percentage of neurons and a low number of astrocytes compared to the 2D controls.



Supplemental Figure S6.16 Gene expression analysis of 7 and 14 day differentiated hNSCs grown on Geltrex coated 2D well plates (2DGT), Geltrex coated 3D scaffolds (3DGT), and pre-seeded 3D scaffolds (3DPre). a) bar chart and b) heat map and on day 14 as a c) bar chart and d) heat map. An * indicates a *p* value lower than 0.05 when compared to the 2D sample at the same time point. Between day 7 and 14, the multipotency markers SOX1, SOX2, PAX6, and nestin all increased for the 2D control group, while they decreased for the Geltrex coated and pre-seeded scaffolds. This indicates that the cells are becoming less multipotent and moving towards their differentiated state faster in 3D than they are in 2D.

Chapter 7 Aligned, Porous Scaffold as a More Effective Modeling Culture Substrate for Alzheimer's Disease

7.1 Introduction

Alzheimer's disease (AD) is the seventh-leading cause of death for all adults in 2021 in the United States.[296-298] None of commonly prescribed pharmacologic treatments, such as acetylcholinesterase inhibitors, methyl-D-aspartate receptor antagonists, β-amyloid removal agents, and various β-amyloid targeting therapies, are effective in restoring or preventing further progression of AD symptoms, which are typically characterize by the degradation of neurons. Effective treatments and early detection of early onset AD are urgently needed to enable timely intervention. Despite over three decades of research since the identification of β-amyloid plaques and phosphorylated tau in neurofibrillary tangles, it is becoming clear that AD pathology is far more complex than the traditional amyloid and tau hypotheses suggest..[299-302] A 99% failure rate of AD drugs in clinical trials, showing no difference between the placebo and drug treated groups,[303] has led to the need for improvement of drug development tools as well as disease models to help aid in the fundamental understanding of AD biology. The common preclinical targets include Aβ (20%), tau (12%), neuroinflammation (12%), APOE, lipids, and proteostasis. While the interplay between Aβ accumulation, neurofibrillary tangles (NFTs), and cognitive decline involves complex mechanisms, genetic mutations that disrupt Aβ production and clearance are strongly linked to Alzheimer's disease.

The ALZFORUM (alzforum.org) website has logged 196 preclinical mouse and 17 preclinical rat models with different AD pathophysiology features. However, it is difficult to predict drug efficacy in human subjects based on success in rodent models due to inherent differences, such as disease progression, between laboratory rodents and human subjects.[304] Rodents do not naturally develop similar AD histopathological hallmarks such as NFT, neuronal

loss, or cognitive impairment.[305] Variations between rodents and humans, including genetic makeup, brain structure, age-related neurological decline, and immune function, hinder the translation of successful animal studies to human patients.[306] Due to these issues, an increase in interest in harnessing human stem cell technology has been seen in the past decade.[307] Human induced pluripotent stem cell (hiPSC) technology enables disease modeling and drug discovery by allowing researchers to use patient-derived cells, either healthy or diseased, to investigate disease-related mutations and screen for potential therapeutics.[304,308] Additionally, stem cell therapy using hiPSC-derived cells for neurodegenerative disorders has also shown promising results.[309,310] The use of patient-derived hiPSC cells allows the disease to be recapitulated in vitro to yield insights for neuropathological mechanisms and patient specific drug screening. The genetic mutations and their downstream pathways are able to be profiled to look for resulting gain and loss of other potentially relevant physiological functions.[311]

Cell culture in three-dimensions (3D) allows for more physiologically relevant interactions between neurons, glial cells, and extracellular matrices, which establishes an more realistic model, with tissue-like spatial and morphological cellular organization. 3D models, including matrix-free spheroids,[312] organoids, and matrix-dependent cultures were developed for more efficient generation of neural lineage cells and for the pathological features that were initially challenging to recapitulate in 2D culture models.[313-321] More efficient differentiation in 3D than in 2D has been demonstrated, showing an increase in neuronal and glial cell maturation and an elevation in neurotransmitter expresson.[322,323] However, these systems may not be readily translatable to hiPSC models if the system was developed using immortalized cell lines such as ReNcells.[238,316,324,325] The key challenges for disease modeling include heterogeneity across different batches,[326]

inability to recreate spatiotemporal signaling dynamics, and insufficient maturation or aging for age-related neurodegenerative disease models like AD.[316,327,328]

Involvement of a matrix material into the modeling system provides a few advantages to overcome these challenges. The matrix material simulated real AD brain microenvironment better by retaining Aβ in the surrounding area and allowing for more Aβ aggregation. Human 4 repeat tau isoform (4RTau) was expressed earlier or substantially higher in both a gel-based 3D model and in brain of AD patients than in a 2D model.[322,329,330] The matrix-supported culture models could allow for long-term culture to be more stable by minimizing necrotic cores, via pore size restrictions, to prevent immature neurons and simulated aging.[331] Appropriate matrix materials can be tailored to support specific cell types, enabling 3D culture of cells at any stage neural differentiation pathway, as well as non-neural cells like endothelial cells. Additionally, the matrix can shield cells from shear stress and abrupt microenvironmental changes during culture handling.

The most popular material to facilitate 3D cell growth is Matrigel, a protein cocktail derived from mouse sarcoma basement membrane ECM extract. Matrigel can be used as a 3D embedding layer at the bottom of wells, microfluidic chips,[331-334] or microspheres in suspension,[335] either alone or with other stabilizing polymers.[336] However, Matrigel presents a few drawbacks as a matrix for hiPSC disease modeling, such as the varied and undefined composition of Matrigel leading to inconsistency in experiments or xenogenic affects.[337] Material selection for 3D matrices in Alzheimer's disease modeling is critical due to the complex interactions between ECM components and Aβ or tau deposition. While natural and synthetic polymers, often used in other tissues, have been explored, hydrogels remain common for their compatibility with pipetting, multi-well formats, and familiarity. However, hydrogels may isolate cells, limiting interactions and providing insufficient structure for neurite growth and migration. Their use is further

constrained by the need for high hydrophilicity and cell encapsulation. In contrast, porous 3D scaffolds offer customizable architectures that better guide cell processes and expand design flexibility in mechanical and surface properties.

A wider range of synthetic and natural polymers can be used to fabricate 3D scaffolds, as the process does not require cell compatibility. For example, a honeycomb structure with around 30 μm thick walls and 240 μm wide pores was 3D printed from commercial resin using high-resolution laser technology to support hiPSC neuronal differentiation, followed by coating with Geltrex and laminin.[338] This study demonstrated that the 3D scaffold culture systems enabled long-term cortical neuronal differentiation over 120 days whereas 2D controls could only be properly maintained up to 50 days. Importantly, formation of neuronal network with synaptogenesis occurred along the microstructure of the scaffolds. The elasticity of the resin was much higher than the native tissue, with tensile elastic modulus at 1-2 GPa and the compressive elastic modulus at 0.2 GPa.[339] Most studies reported softer matrices for hydrogels, similar to brain tissue, supported neurogenesis better than stiffer gels, such as the case of collagen-alginate gels.[340] Stiffness and degradability can also affect NPC maintenance.[341,342] Conversely, for porous scaffolds, the choice of material, surface, and mechanical properties resulted in a profound effect on NSC maintanence and expansion,[338] where even though the modulus was much higher than the native tissue, the scaffolds were still able to support neurogenesis and synaptogenesis.

We previously showed that 3D porous scaffolds made from pure chitosan outperformed chitosan-alginate, chitosan-HA, and collagen scaffolds in supporting hNSC maintenance and neuronal differentiation. Three hNSC lines favored scaffolds with higher chitosan concentrations, which correlated with increased elastic modulus and reduced negative surface charge. Higher

chitosan content enhanced cell adhesion, proliferation, and multipotency, ultimately promoting differentiation into cortical neurons.

Therefore, here we utilized similar 3D chitosan-based scaffolds to explore their potential in establishing 3D AD model using hiPSC-derived neurons. The scaffold surface was either coated with Geltrex or treated with conditioned medium. The neurons were derived from wild type or hiPSC harboring Swedish APP mutation or PSEN1 mutation. HiPSCs were first cultured in the scaffolds and then differentiated into human neural progenitor cells (hNPCs). Next, the hNPCs were differentiated into neurons in their respective scaffold conditions. The overall differentiation efficiency and the ability of the scaffolds to maintain the hiPSCs, hNPCs, and neurons were evaluated. The production of Aβ40 and Aβ42 were compared between 3D and 2D controls. Gene expression analysis compared key genes associated with AD pathogenesis including for Aβ, tau, β-secretase, γ-secretase, synapses, metalloprotease, APOE, oxidative stress, and aging.

7.2 Materials and methods

7.2.1 Preparation of chitosan (CS) porous scaffolds

All scaffolds were prepared by lyophilizing polymer solutions in multiwell plates or tubes. The solutions were prepared by dissolving the polymer and mixed in a Thinky mixer (ARM300, Thinky USA, Laguna Hills, CA) at 2000 rpm for 3 minutes for 3–5 times. The solutions were then homogenized in a blender for 5 minutes twice. Afterwards, the solutions were further homogenized in the Thinky mixer to remove bubbles. To prepare for lyophilization, the solution was casted in 24-well plates or 15-mL tubes. The columnar structure was established by unidirectional freezing utilizing precooled metal shelves at –80˚C. The pure chitosan scaffolds were prepared by dissolving medical grade chitosan (degree of deacetylation 98.3± 0.1%, Matexcel, Cat. NAT-0030, Shirley, NY) at 6 wt% (6CS) in acetic acid 1-4 wt% to form homogeneous solutions.

The lyophilized scaffolds were sectioned to 500 μm thickness, sterilized in 70% ethanol, and rinsed in PBS. The coating of 3D scaffolds included Geltrex (GT; ThermoFisher, Cat. A1413201) at 0.34 mg/mL protein and conditioned medium. The conditioned medium was prepared by collecting medium before performing a medium change from 2D wells of CViA2 or IID4 cell lines.

7.2.2 Microstructure characterized by scanning electron microscopy (SEM)

Scaffolds were examined using SEM to observe the microstructure before coating. To prepare samples for SEM, the lyophilized scaffolds were sectioned into small pieces and attached on SEM pin stubs by carbon conductive adhesive tape (NEM Tape, Nisshin EM. Co. Ltd. Tokyo, Japan). Platinum conductive coating was applied in a mini sputter coater (SC7620, Quorum Technologies, United Kingdom). The samples were imaged using a JSM-6010PLUS/LA analytical SEM (JEOL, Tokyo, Japan) operating at 10 or 5 kV. For each type of scaffolds, 6–8 images were used for measuring pore diameter with ImageJ to acquire 50 different measurements.

7.2.3 Physical Characterization of the Scaffolds

Uniaxial compression tests were conducted to evaluate the compressive elastic moduli of the scaffolds using the Autograph Table-TOP Precision Universal Tester AGS-X (SHIMADZU CORPORATION, Kyoto, Japan) at room temperature. The scaffolds were soaked in PBS before testing. The wet scaffolds were compressed at a rate of 0.4 mm/min until they reached at least 40% strain. The compressive Young's modulus was determined from the slope of the linear portion of the stress–strain curve, specifically within the 0% to 15% strain range. Alignment of the scaffolds was determined using the Python packages numpy, pillow, scipy, and skimage.

7.2.4 Cell Culture and hiPSC neuronal differentiation

The cell lines wild type control (CViA2 and IID4), cell line harboring PSEN1 ΔE9 (E9), and cell line harboring APP Swedish mutation (Swe22) were kindly provided Dr. Jessica E. Young (Department of Laboratory Medicine and Pathology, University of Washington, Seattle).[343-347] hiPSCs were cultured under feeder-free conditions and differentiated to hNPCs following published protocols utilizing dual-SMAD inhibition. Briefly, hiPSCs were plated on Matrigel (Corning, cat no. 356230) coated plates and fed with MTeSR medium (Stemcell Technologies). Accutase (Thermo Fisher Scientific, cat no. A1110501) and 10 μM Rho-associated protein kinase (ROCK) inhibitor Y-27632 (R&D Systems, cat no. 1254) were used for passaging. Neural differentiation was induced by replacing the medium with Basal Neural Maintenance Medium (BNMM) (1:1 DMEM/F12 + Neurobasal, 0.5% N2 supplement, 1% B27 supplement, 0.5% GlutaMax, 0.5% insulin-transferrin-selenium, 0.5% NEAA, 0.2% β-mercaptoethanol; Gibco, Waltham, MA) containing 10 mM SB-431542 and 0.5 mM LDN-193189 (Biogems, Westlake Village, CA). The cells were fed daily for 8 days and replated. The day following passaging, the medium was replaced with BNMM with 20 ng/mL FGF (R&D Systems, Minneapolis, MN) and fed daily. Cells were expanded and passaged when confluent.

Neuronal differentiation of NPCs to cortical neurons was performed in previously published research.[347-349] Briefly, NPCs were grown in 10-cm Matrigel-coated dishes until confluent and differentiated in neural differentiation medium (ND), consisting of BNMM with GDNF (20 ng/mL PeproTech, Rocky Hill, NJ, USA), BDNF (20 ng/mL PeproTech, Rocky Hill, NJ, USA) and dbcAMP (250 ug/mL Sigma, St. Louis, MO, USA) for 3 weeks. After 3 weeks, the cells were passaged using accutase and replated into wells using ND medium and RI at 10uM. After 1 day, the medium was changed to Brainphys medium (Stemcell Technologies) with GDNF

(20 ng/mL PeproTech, Rocky Hill, NJ, USA), BDNF (20 ng/mL PeproTech, Rocky Hill, NJ, USA) and dbcAMP (250 ug/mL Sigma, St. Louis, MO, USA) and were cultured for 4 weeks.

7.2.5 Live/dead staining

The viability and morphological features were monitored on a Nikon TE300 inverted microscope (Nikon, Tokyo, Japan) after incubation with Calcein AM at 1 μM and ethidium homodimer-1 at 4 μM in complete culture medium for 15 minutes.

Confocal imaging was performed on a Leica SP8X confocal fluorescence microscope at the University of Washington Keck Imaging Center. Image processing was performed on Leica LAS X software (Leica Microsystems, Wetzlar, Germany) and IMARIS software (Bitplane, Zurich, Switzerland).

7.2.6 Immunocytochemistry

The cell-scaffold constructs were fixed with cold 4% paraformaldehyde for 10 minutes at room temperature. The fixed samples were permeabilized for 10 minutes with 0.5% Triton X-100 in DPBS, blocked for 30 minutes and then incubated with primary and secondary antibodies diluted in BD Phosflow™ Perm/Wash Buffer I (BD Bioscience). The incubation was at 4°C overnight for primary and 1-2 hours for secondary antibodies and stained with DAPI. After washing 3 times, the samples were embedded with Prolong Gold Antifade mounting medium (Invitrogen; Carlsbad, CA, Cat. P36930) on glass slides. Fluorescence microscopy was done using a Nikon TE300 inverted microscope or SP8X confocal microscope as previously described. The following antibodies were used: SOX2, Tra-1-60R, and nestin.

7.2.7 Flow Cytometry

Cells were collected from the 2D controls or from scaffolds using accutase. The cells were then fixed using 4% paraformaldehyde and stored in cell staining buffer (Biolegend) until ready for staining. For intracellular staining, cells were permeabilized for 10 minutes on ice using 1% Triton X-100 in PBS. For surface staining, the cells were not permeabilized. The samples were blocked for 30 minutes before being stained with the antibodies according to the manufacturers protocol. The antibodies used are OCT4 (Biolegend 653704), SSEA-4 (Biolegend 330412), TRA-1-60-R (Biolegend 330618), SOX2 (Biolegend), nestin (Biolegend), Ki67 (Biolegend), SOX1 (Biolegend), CD44 (Biolegend 397508), CD184 (Biolegend 306506), CD24 (Biolegend 311110), and CD271 (Biolegend 345112).

7.2.8 Functional Study

Cells were collected from the 2D controls and scaffolds after differentiating for 3 weeks and were then plated onto 2D wells. After culturing in Brainphys medium (Stemcell Technologies) for 4 weeks, Fluo4-AM (ThermoFisher F14201) was added to the wells according to the manufacturers protocol. Images were acquired using a Nikon TE300 inverted microscope.

7.2.9 Quantification of gene expressions by real-time quantitative PCR (RT-qPCR)

Total RNA was isolated using RNeasy Mini Kit (Qiagen, Valencia, CA). Reverse transcription was performed with iScript cDNA synthesis kit (Bio-Rad, Hercules, CA). Quantitative PCR was carried out using SsoAdvanced SYBR Green Supermix (Bio-Rad) or PowerUp SYBR Green Mastermix (Applied Biosystems) with a Bio-Rad CFX96 Real-Time PCR Detection System. PCR cycles were run for 3 minutes at 95°C followed by 40 cycles of 95°C for 15 seconds, 58°C for 40 seconds, and 72°C for 30 seconds. The primer sequences were with 90-110% efficiency and

provided in **Table 7.1**. Targeted mRNA gene expression was normalized to GAPDH mRNA levels. Relative fold changes in gene expression were calculated with Cq values analyzed using Bio-Rad CFX Manager software.

Table 7.1 The sequences of primers used in qPCR analysis.

Primer	Sequence 5' - 3'
APP Forward	CGAAATGCTTTAGGGTGT
APP Reverse	AAGTGGAATCTTTGGAACAG
MAPT Forward	AAGTCGCCGTCTTCCGCCAAG
MAPT Reverse	GTCCAGGGACCCAATCTTCGA
3RTau Forward	AGGCGGGAAGGTGCAAATAG
3RTau Reverse	TCCTGGTTTATGATGGATGTT
4RTau Forward	GAAGCTGGATCTTAGCAACG
4RTau Reverse	GACGTGTTTGATATTATCCT
SYNGR3 Forward	CGTCCTGGGTGTTCTCCATC
SYNGR3 Reverse	CTGCTGATTTGCTGGAAGCG
SHANK2 Forward	CTGGCGAGCTGGGGTGATTA
SHANK2 Reverse	TCAATGGGTGTGTCAGCTTTG
PSD95 Forward	CTCAGGGTCAACGACAGCAT
PSD95 Reverse	AAGCCAAGACCTTTAGGCCC
NRF2 Forward	AAACCAGTGGATCTGCCAAC
NRF2 Reverse	GACCGGGAATATCAGGAACA
KEAP1 Forward	ATTGGCTGTGTGGAGTTGC
KEAP1 Reverse	CAGGTTGAAGAACTCCTCTTGC
BACE1 Forward	GGGCTGGCCTATGCTGAGATTGC
BACE1 Reverse	GCACCACAAAGCTGCAGGGAGAA
PSEN1 Forward	TCTAGGGCCTCATCGCTCTA
PSEN1 Reverse	GGCTGTTGCTGAGGCTTTAC
PSEN2 Forward	CGCTGCTACAAGTTCATCCA
PSEN2 Reverse	ATGATGAGGTAGGCCTGCTG
ADAM10 Forward	ATGGGAGGTCAGTATGGGAATC
ADAM10 Reverse	ACTGCTCTTTTGGCACGCT

7.2.10 Aβ 1–40 and 1–42 Analysis

Aβ peptides were measured as previously described.[145] The conditioned medium of was harvested from each culture condition 72 hours after replacing with the same volume of medium to measure

secreted Aβ peptides. Concentration of Aβ 1–40 and Aβ 1–42 was assessed using a human V-plex Aβ Peptide Panel 1 (6E10) ELISA kit (Cat. K15200E-2, Meso Scale Discovery, Rockville, MD, USA) following manufacturer's instructions.

7.2.11 Statistical analysis

All data are presented as mean ± standard deviation unless otherwise specified. Statistical significance was evaluated on GraphPad Prism v.9 (GraphPad Software Inc., La Jolla, CA, USA). Depending on the data set, unpaired two-tailed Student's *t*-test, one-way ANOVA or two-way ANOVA and Tukey's test for post-hoc multiple comparison analysis were used and indicated in captions. The number of replicates and *p*-values are stated in results and figure captions. Differences were considered statistically significant at p-value < 0.05.

7.3 Results and Discussion

7.3.1 Scaffold Characterization

The nonaligned and aligned scaffolds were imaged using SEM, and the images of the nonaligned and aligned scaffolds can be seen in **Figure 7.1a** and **7.1b**, respectively. From the images, the width of the pore size of the nonaligned scaffold is 81 ± 25 μm and the aligned scaffold pore size is 189 ± 49 μm. These pore sizes allow plenty of room for cells to grow as clusters but also prevent the cells from becoming too large and developing necrotic cores. **Figure 7.1c** shows the measured compressive elastic moduli for the nonaligned scaffold and for the aligned scaffold in the direction of the alignment. Both compressive elastic moduli are similar to what we expect the brain ECM elastic compressive modulus to be. **Figure 7.1d** shows the relative pore alignment of both the nonaligned and aligned scaffolds. The aligned scaffold's pores are more aligned than the

nonaligned scaffold pores. This means that the pore structure of the aligned scaffolds could help the hNPCs and neurons to align in the direction of the pores.

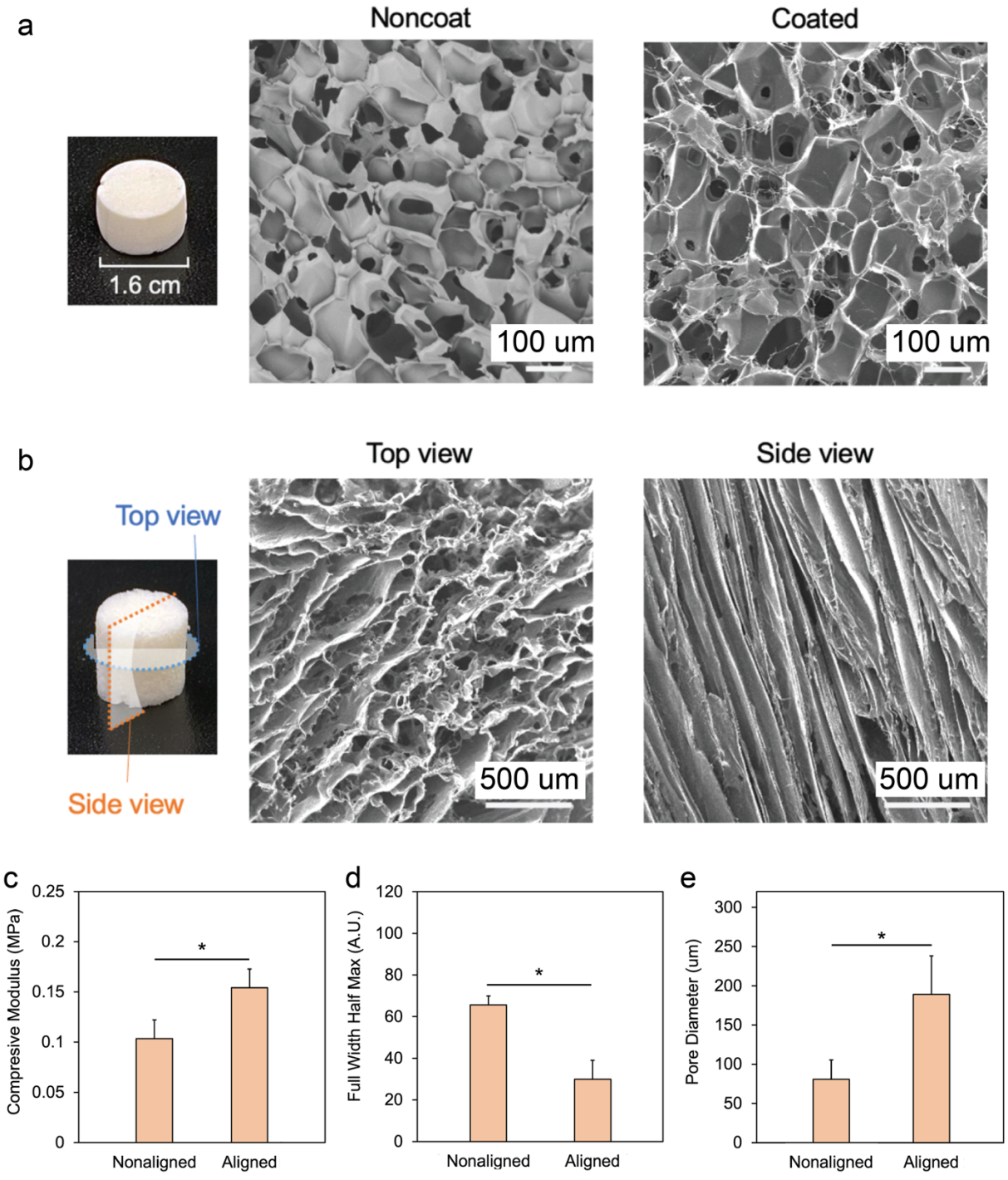


Figure 7.1 Surface and physical characterization of the scaffolds. SEM images of the a) regular scaffold and SEM images of noncoated and Geltrex-coated scaffolds. The microstructure exhibits

overall isotropic interconnect pores. Geltrex coating left a net-like fibrous residue on the surface of the pores. Scale bars represent 100 μm. b) A columnar scaffold and SEM images from top and side, showing the vertical columnar microstructure. Scale bars represent 500 μm. e) The elastic compressive moduli of the nonaligned and aligned scaffolds, f) the alignment of the nonaligned and aligned scaffolds, and g) the pore size of the nonaligned and aligned scaffolds. An * indicates a p less than 0.05. An n value greater than 3 was used for both tests.

7.3.2 Adhesion and Morphology of hiPSCs

The hiPSCs were plated onto nonaligned Geltrex coated, nonaligned condition medium treated, aligned Geltrex coated, and aligned conditioned medium treated scaffolds for all 4 cell lines. The hiPSC morphology and adhesion to the nonaligned and aligned scaffolds was evaluated using a live/dead stain, and the images of the different scaffold conditions can be seen in **Figure 7.2**. The hiPSCs adhere well to the Geltrex coated scaffolds and form clusters in the conditioned medium treated scaffolds. The cells appear to adhere to the scaffold walls in the Geltrex coated scaffolds, and the alignment of the pores can significantly impact the morphology of the cells. The cells grown in the nonaligned scaffolds appear to be growing in random directions, while the cells grown in the aligned scaffolds can clearly be seen to be growing along with the alignment of the pores.

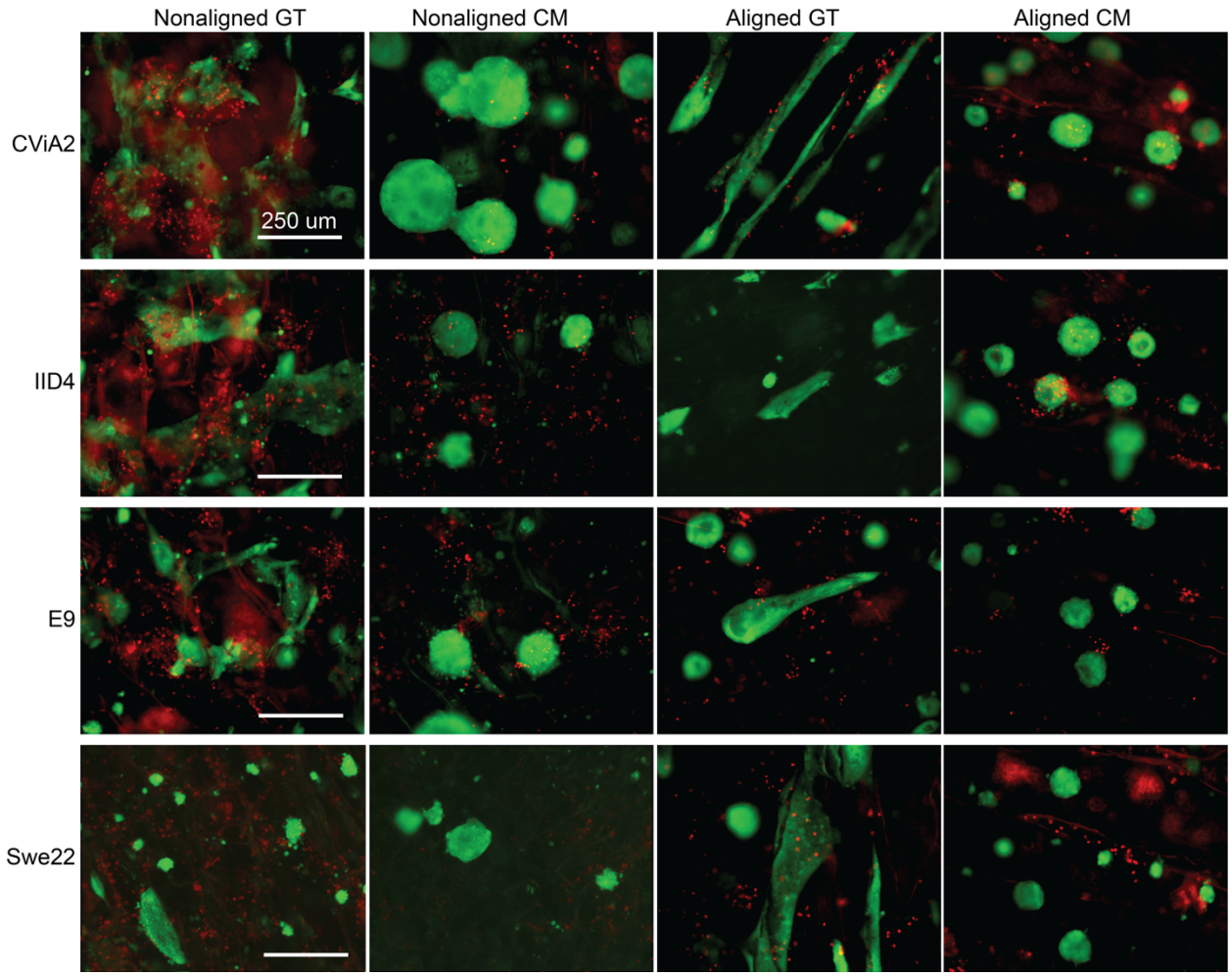


Figure 7.2 hiPSC adhesion and morphology evaluated via live (Calcien AM, green) and dead (propidium iodide, red) staining. CViA2, IID4, E9, and Swe22 cell lines were grown on nonaligned Geltrex coated scaffolds (Nonaligned GT), nonaligned conditioned medium treated scaffolds (Nonaligned CM), aligned Geltrex coated scaffolds (Aligned GT), and aligned conditioned medium treated scaffolds (Aligned CM). The scale bars indicate 250 µm.

7.3.3 Maintenance of the Pluripotency of the hiPSCs

The hiPSCs were collected for flow cytometry analysis after 4 days of culture. Flow cytometry analysis of key pluripotency markers revealed that the scaffolds were able to maintain the pluripotency of the hiPSCs when compared to the 2D controls. **Figure 7.3a** and **7.3b** show the percent positive populations for SSEA4 and SOX2, respectively. These markers were maintained across all scaffold and cell conditions, with only a slight decrease being seen when compared to

the 2D. The percent positive population for the pluripotency marker OCT4 can be seen in **Figure 7.3c**. OCT4 was generally maintained across all conditions, except for the nonaligned Geltrex condition for CViA2 and Swe22, the nonaligned conditioned medium treated condition for CViA2 and Swe22, the aligned Geltrex condition for E9, and the aligned conditioned medium treated condition for CViA2. While there was a difference in these conditions, it was relatively small (~0.2). The decrease could also be due to the 3D condition not being ideal for somatic cell reprogramming. **Figure 7.3d** illustrates the percent positive populations for Tra 1-60, and the Tra 1-60 expression was well maintained across all the conditions. **Figures 7.4**, **7.5**, **7.6**, and **7.7** show the immunostaining images for CViA2, IID4, E9, and Swe22, respectively. The Geltrex coated scaffolds appear to be adherent to the scaffold, while the conditioned medium treated scaffolds appear to be weakly adherent or nonadherent across all the cell lines. Cells grown in 2D showed SOX2 staining appearing in the nucleus and TRA-1-60R staining appearing in the cytoplasm. In the Geltrex coated scaffolds, the cells appear to be more adherent. While in the Geltrex coated aligned scaffolds, the cells can be seen growing along with the aligned pores. SOX2 appears to be mostly located in the nucleus and TRA-1-60 appears to be in the cytoplasm for the medium coated scaffolds, indicating good maintenance of the hiPSCs in the scaffolds.

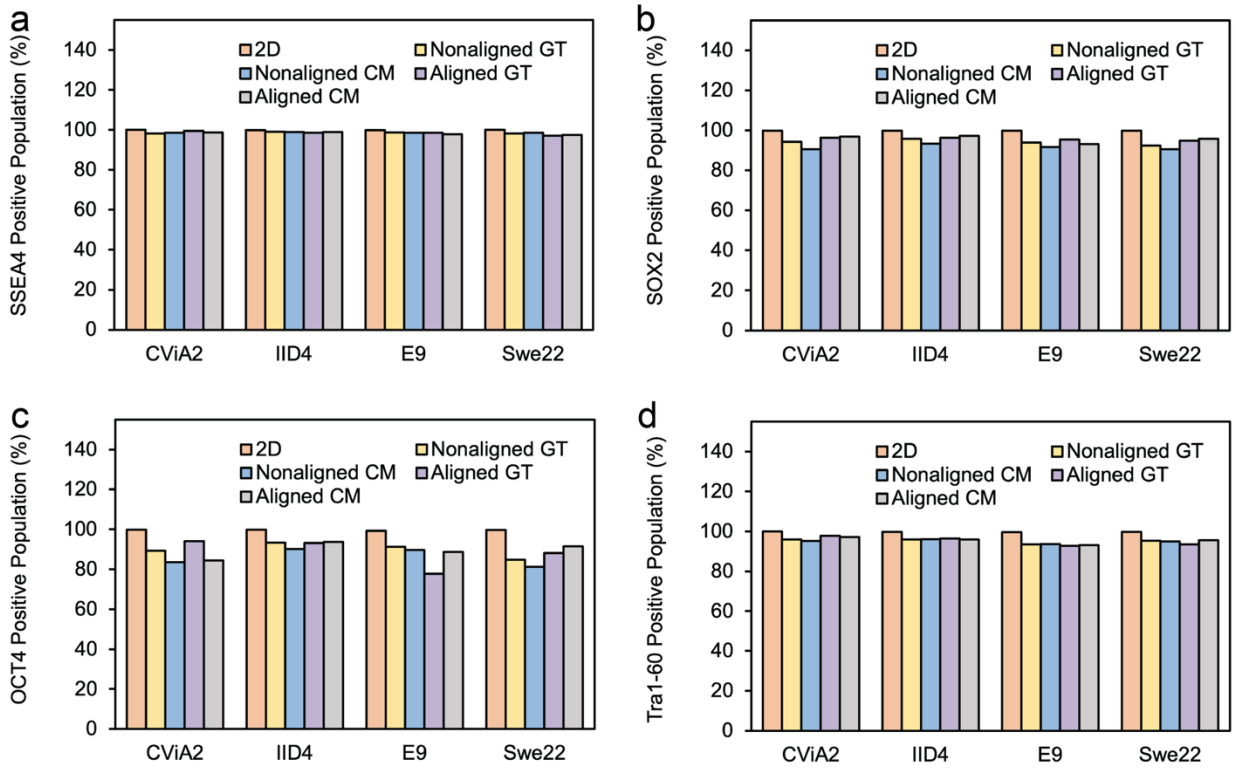


Figure 7.3 Pluripotency expression from cells grown in the 3D scaffolds depicted as percent positive populations for a) SSEA4 expression, b) SOX2 expression, c) OCT4 expression, and d) Tra 1-60 expression. More than 3400 cells were analyzed in each condition, collected from 6 separate wells.

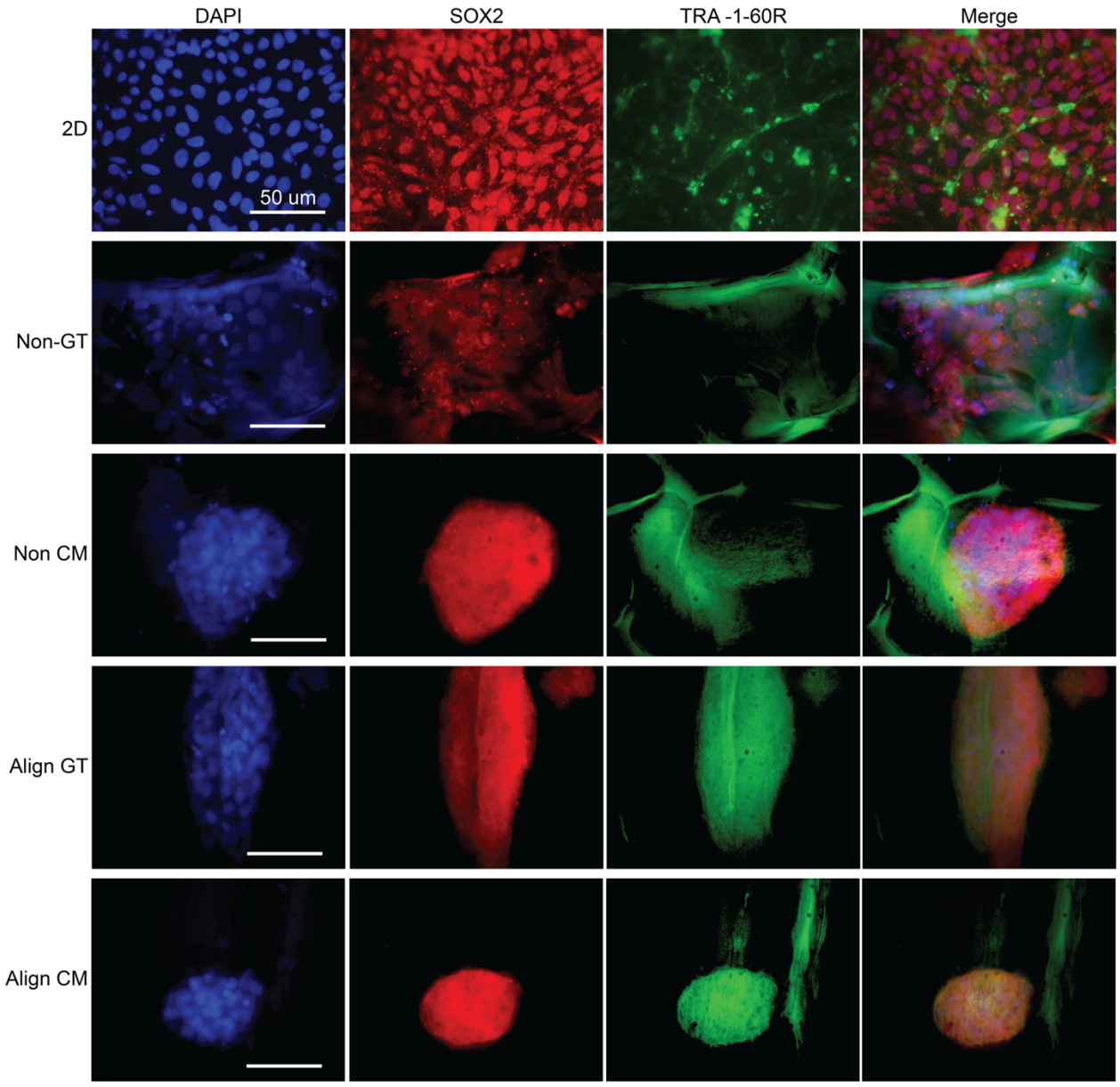


Figure 7.4 Fluorescence images of hiPSC-CViA2 cells cultured for 4 days using immunocytochemistry staining for TRA-1-60R-green and SOX2-red. DAPI staining for nuclei are presented in blue. The scale bar is 50 µm.

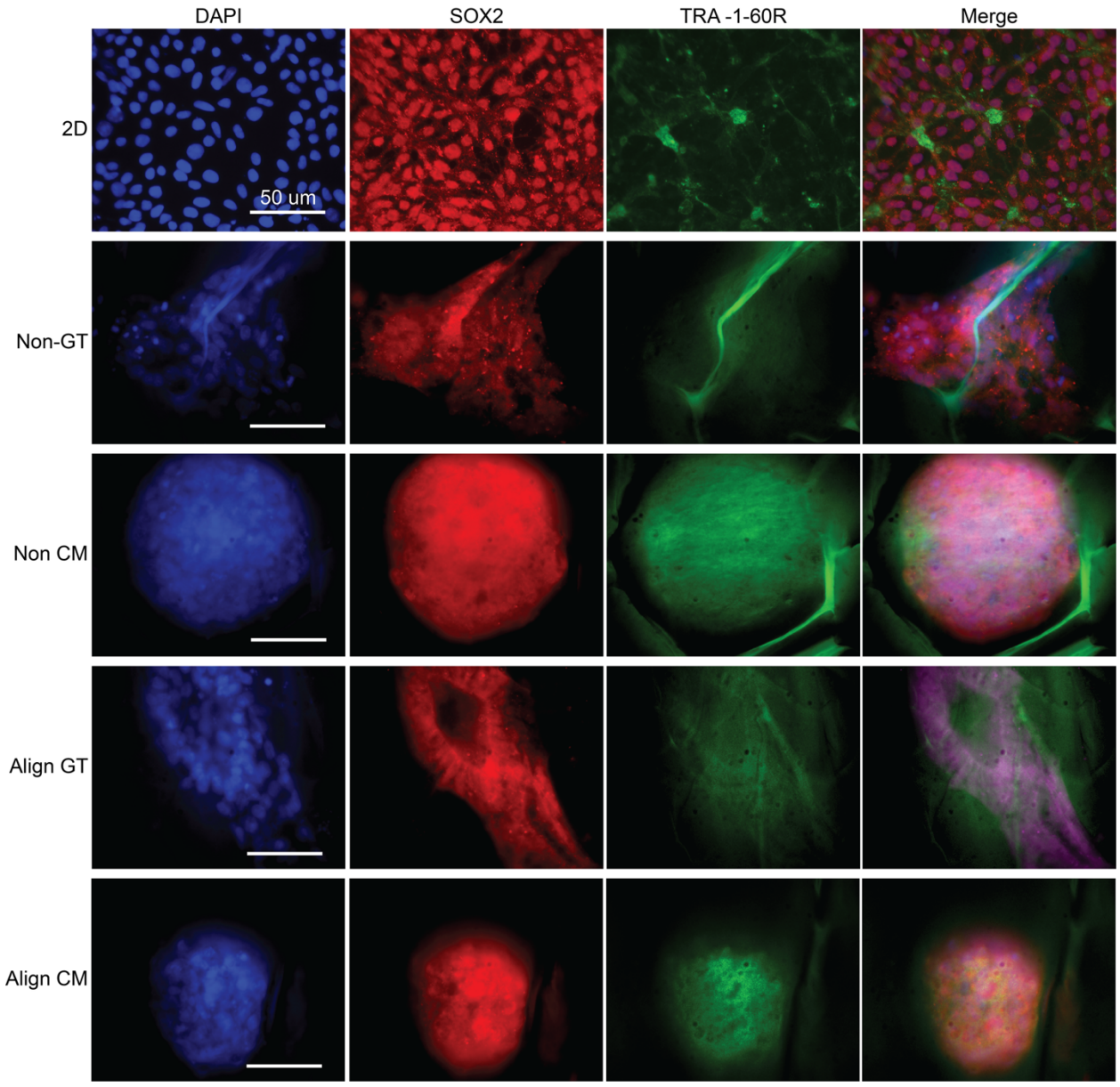


Figure 7.5 Fluorescence images of hiPSC-IID4 cells cultured for 4 days using immunocytochemistry staining for TRA-1-60R-green and SOX2-red. DAPI staining for nuclei are presented in blue. The scale bar is 50 µm.

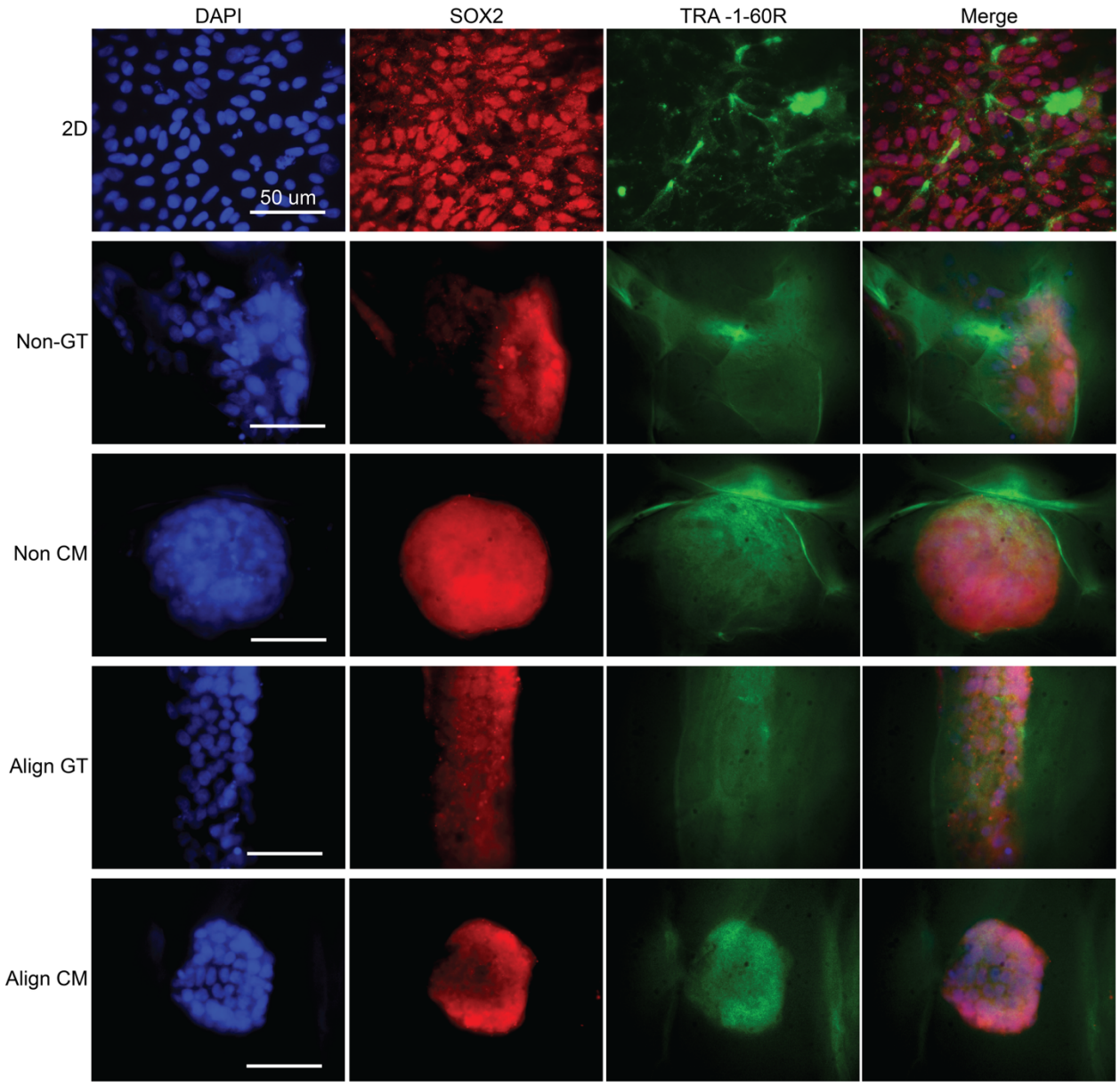


Figure 7.6 Fluorescence images of hiPSC-E9 cells cultured for 4 days using immunocytochemistry staining for TRA-1-60R-green and SOX2-red. DAPI staining for nuclei are presented in blue. The scale bar is 50 µm.

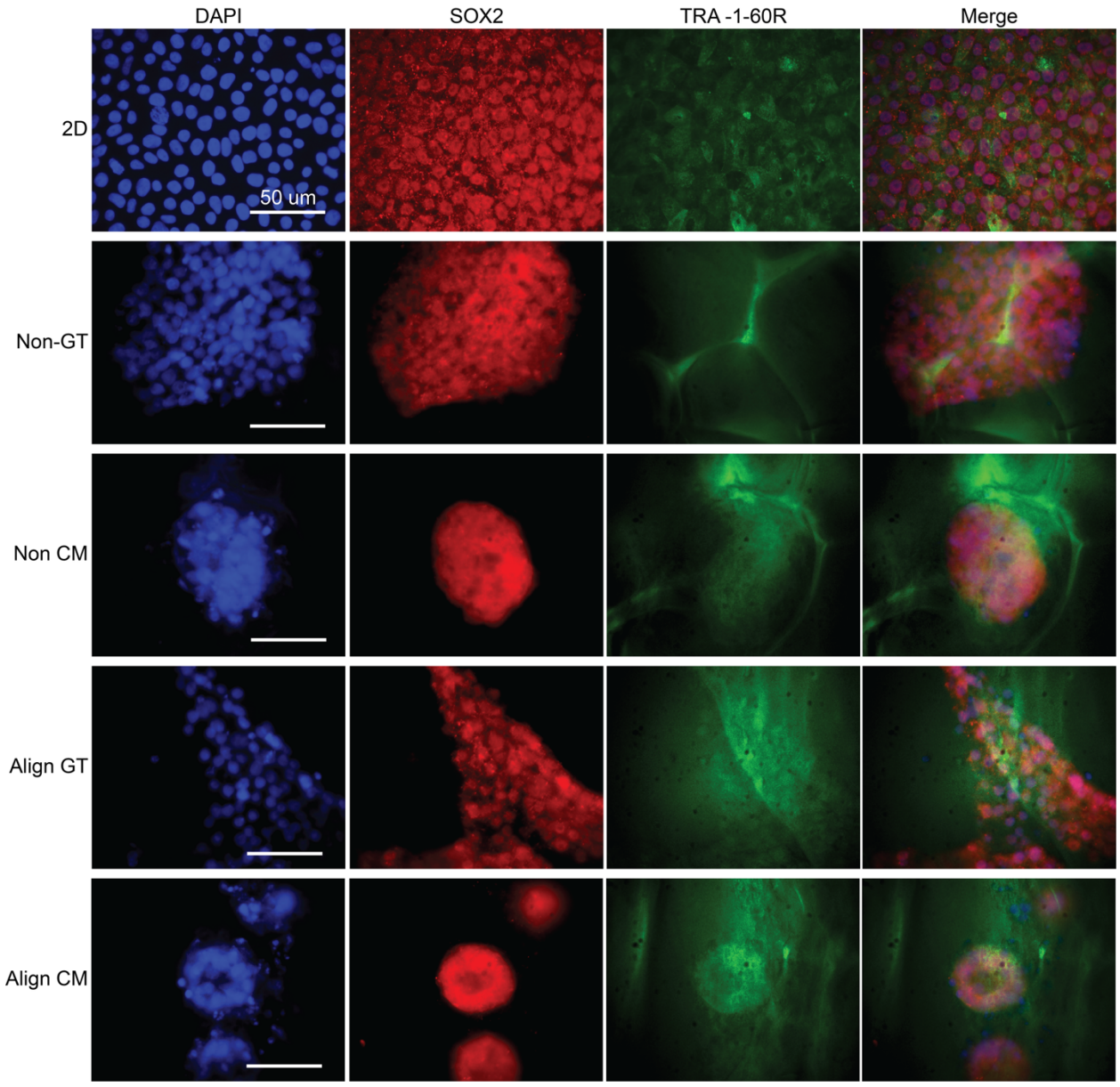


Figure 7.7 Fluorescence images of hiPSC-Swe22 cells cultured for 4 days using immunocytochemistry staining for TRA-1-60R-green and SOX2-red. DAPI staining for nuclei are presented in blue. The scale bar is 50 µm.

7.3.4 Adhesion and Morphology of hNPCs

The hiPSCs were then differentiated into hNPCs for 16 days. After differentiation, the hNPCs were expanded twice in their respective scaffold condition before being used for subsequent experimentation. The hNPC morphology and adhesion to the nonaligned and aligned scaffolds was

evaluated using a live/dead stain, and the images of the different scaffold conditions can be seen in **Figure 7.8**. The hNPCs adhere well to the scaffold walls in both scaffold conditions. The alignment of the pores can significantly impact the morphology of the cells. The cells grown in the nonaligned scaffolds appear to be growing in random directions (around the edges of the pores), while the cells grown in the aligned scaffolds can clearly be seen to be growing along with the alignment of the pores.

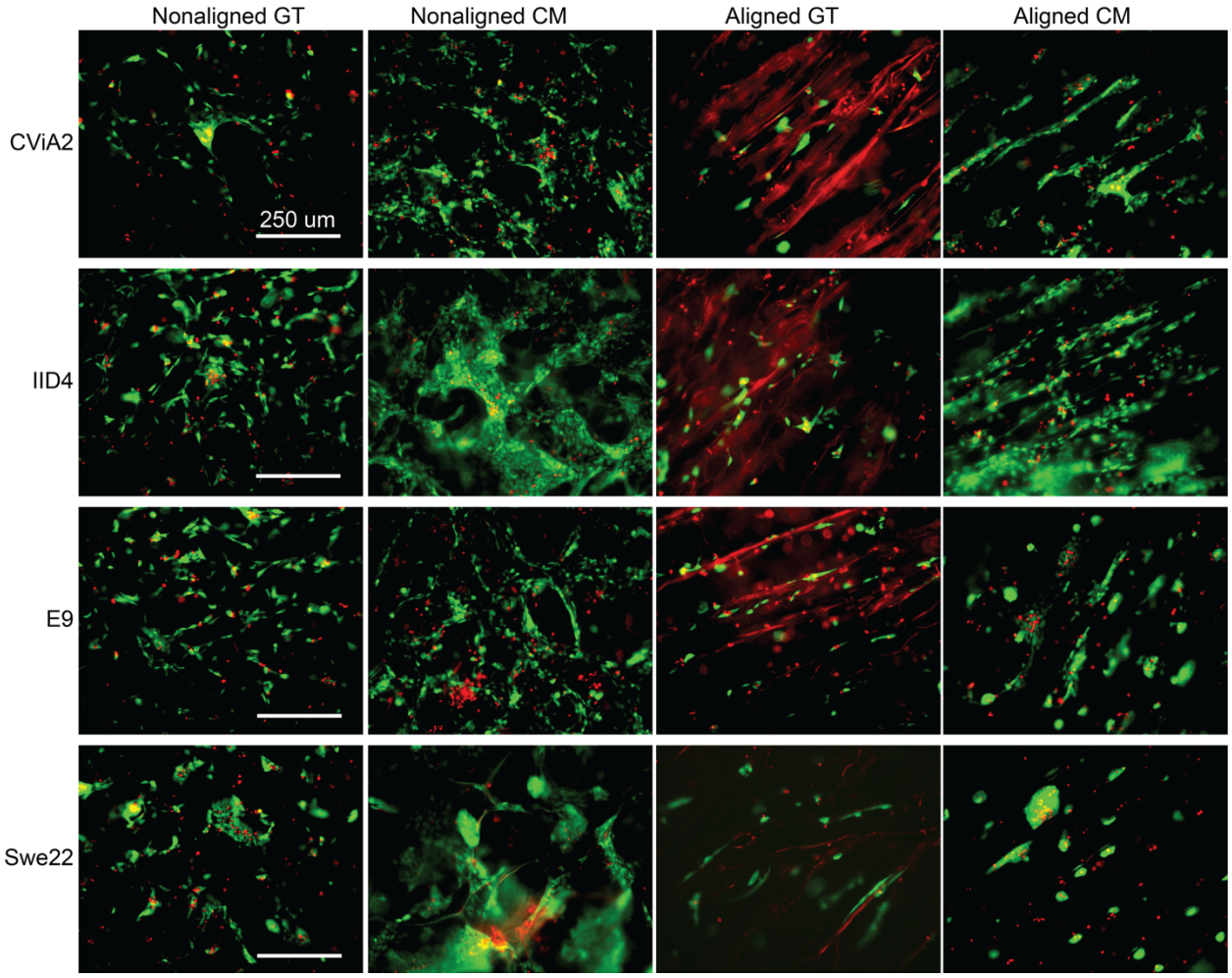


Figure 7.8 hNPC adhesion and morphology evaluated via live (Calcien AM, green) and dead (propidium iodide, red) staining. CViA2, IID4, E9, and Swe22 cell lines were grown on nonaligned Geltrex coated scaffolds (Nonaligned GT), nonaligned conditioned medium treated scaffolds (Nonaligned CM), aligned Geltrex coated scaffolds (Aligned GT), and aligned conditioned medium treated scaffolds (Aligned CM). The scale bars indicate 250 μm.

7.3.5 hNPC Multipotency Maintenance and Differentiation Efficiency

After the cells were differentiated into hNPCs from hiPSCs, the hNPCs cultured for 4 days before collecting for flow cytometry analysis. Flow cytometry analysis of key multipotency markers revealed that the scaffolds were able to maintain the multipotency of the hNPCs after differentiation when compared to the 2D controls. **Figure 7.9a** shows the percent positive population for SOX2. This marker was maintained across all scaffold and cell conditions, with a few exceptions such as the nonaligned Geltrex coated conditions for E9 and Swe22. The percent positive population for the proliferation marker Ki67 can be seen in **Figure 7.9b**. Ki67 was generally maintained across all conditions, except for the nonaligned Geltrex coated conditions for E9 and Swe22 and the aligned condition medium treated scaffold for Swe22. **Figure 7.9c** and **7.9d** illustrates the percent positive population for the multipotency markers nestin and SOX1, and the nestin and SOX1 expressions were well maintained across all the conditions except for the nonaligned Geltrex coated conditions for E9 and Swe22 and the aligned condition medium treated scaffold for Swe22.

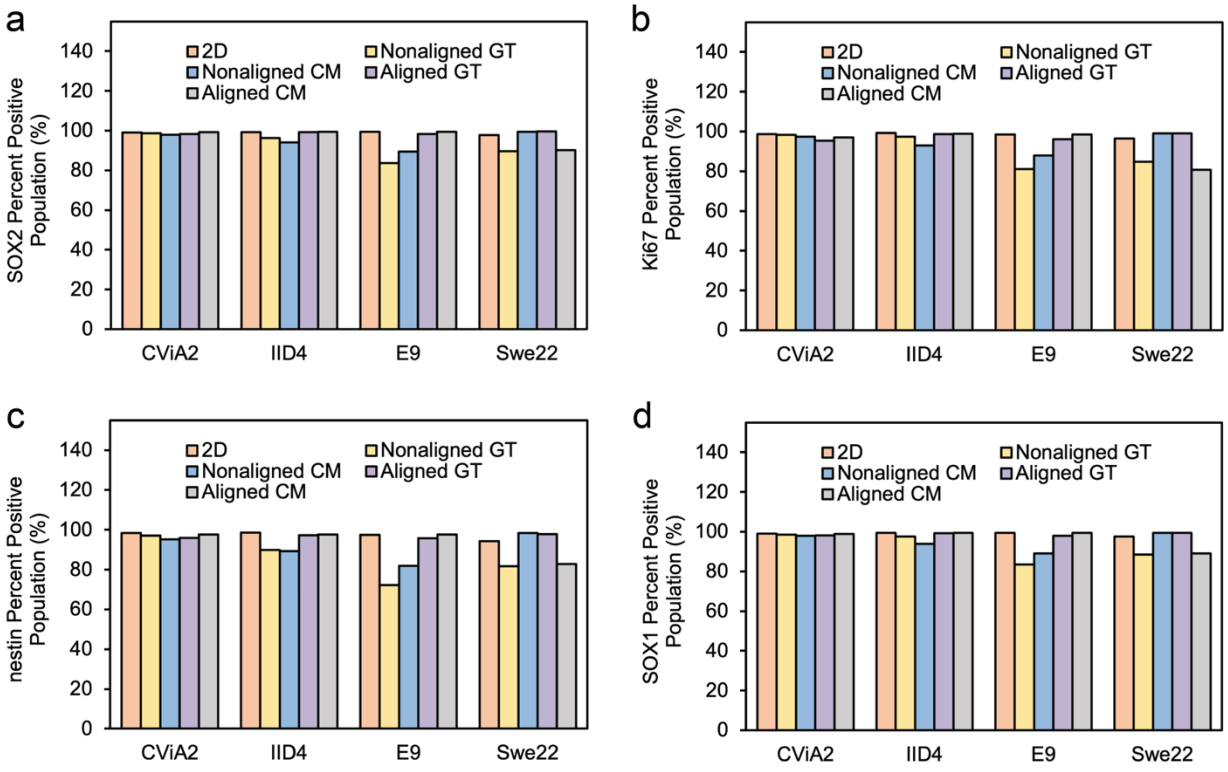


Figure 7.9 Multipotency expression from cells grown in the 3D scaffolds depicted as fold changes compared to the 2D controls. a) SOX2 expression, b) Ki67 expression, c) nestin expression, and d) SOX1 expression. More than 2000 cells were analyzed in each condition, collected from 6 separate wells.

7.3.6 hNPC Differentiation Efficiency

Figure 7.10a and **7.10b** illustrate the differentiation efficiency from hiPSCs into hNPCs for the cell lines CViA2, IID4, E9, and Swe22 in terms of the fold change and the overall percent positive populations, respectively. In the 2 control cell lines, the 2D condition offered the best overall differentiation efficiency. Among the scaffold conditions, the results indicate that the aligned Geltrex coated scaffold offered the best efficiency for the CViA2 cells and the nonaligned conditioned medium treated scaffold offered the best efficiency for the IID4 cells. **Figure 7.10c** shows the histograms for CViA2, E9, and Swe22 cells grown in 2D and in the aligned CM scaffold conditions, showing good distributions of the populations. Both the E9 and Swe22 cells had better differentiation efficiency than the 2D controls across all of the scaffold conditions, however, the

aligned conditioned medium treated scaffold offered the best efficiency.

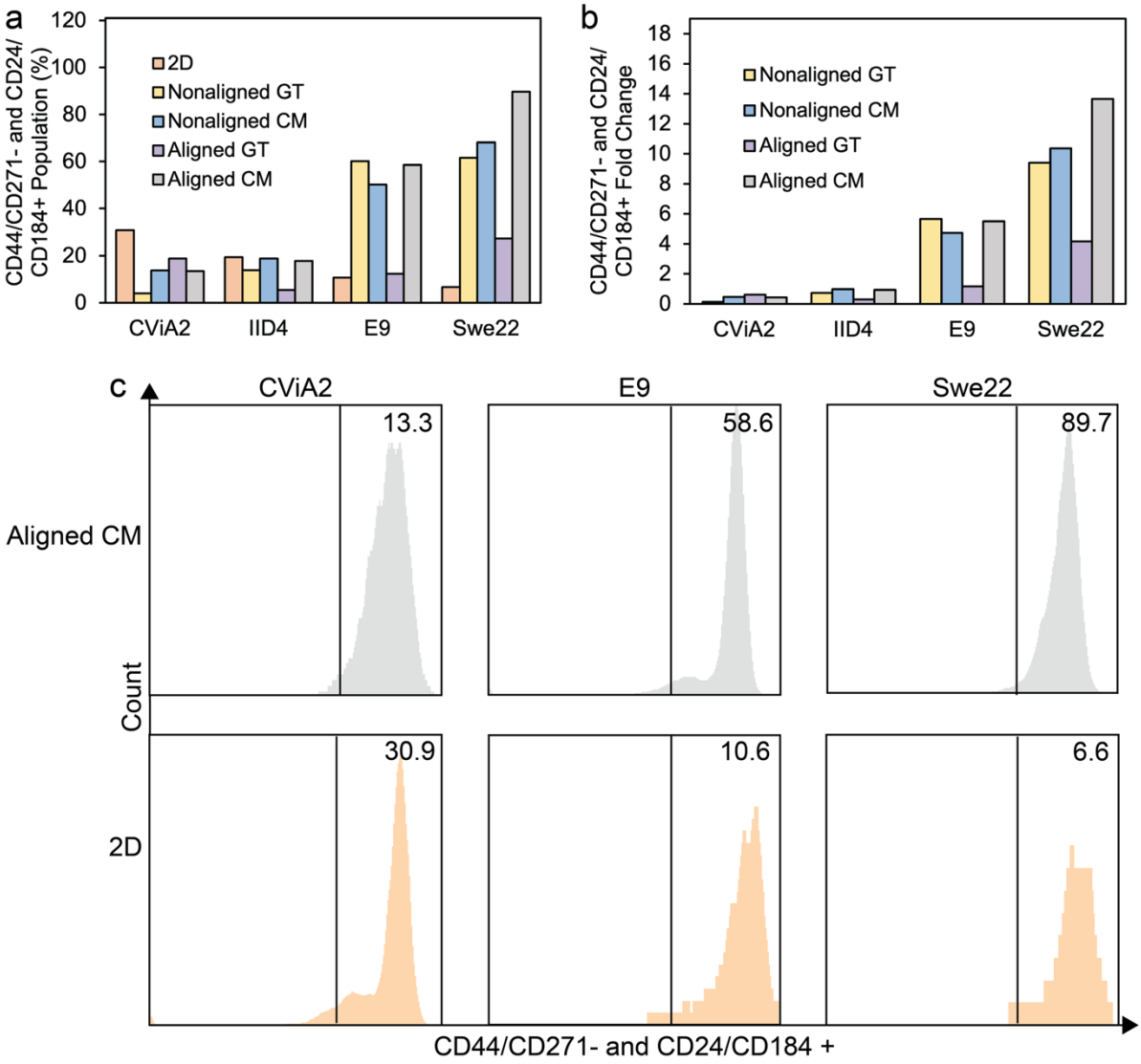


Figure 7.10 Differentiation efficiency of the cells grown in the scaffolds depicted a) percent positive population and b) fold change. More than 5400 cells were analyzed in each condition, collected from 6 separate wells.

7.3.7 Functional Neuron Study

After the initial 3 week differentiation period, the cells were passaged and replated into new 2D wells and were subsequently differentiated for an additional 4 weeks before being stained with Fluo-4 AM. **Figure 7.11a**, **b**, **c**, and **d** show the change in fluorescence divided by the initial fluorescence for CViA2 cells grown in nonaligned Geltrex coated, nonaligned condition medium

treated, aligned Geltrex coated, and aligned condition medium treated scaffolds, respectively. The neurons were able to uptake calcium and subsequently release it. The cells that were originally grown in 2D wells did not show any spontaneous signaling as seen in **Figure 7.13a**. **Figure 7.12a**, **b**, **c**, and **d** show the change in fluorescence divided by the initial fluorescence for Swe22 cells grown in nonaligned Geltrex coated, nonaligned condition medium treated, aligned Geltrex coated, and aligned condition medium treated scaffolds, respectively. The neurons were able to uptake calcium and subsequently release it. The Swe22 cells that were originally grown in 2D wells did not show any spontaneous signaling as seen in **Figure 7.13b**. The cells grown on the aligned scaffolds tended to exhibit more elongated morphologies and well defined neurite-like structures extending between cells. Cells cultured in the scaffolds also tended to have more defined calcium uptake and release, indicating the scaffolds help direct cell differentiation towards neurons when compared to the 2D controls.

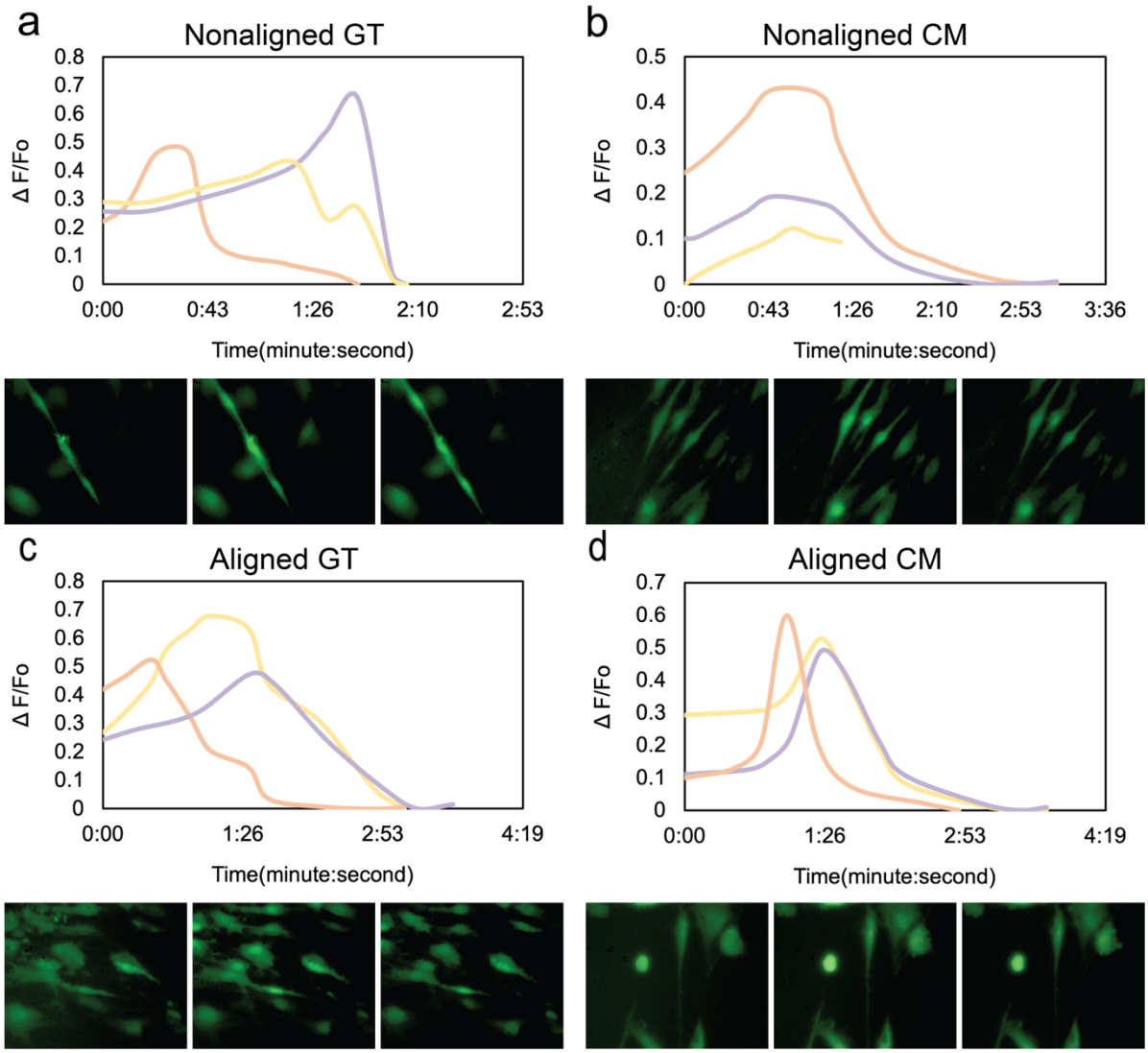


Figure 7.11 Calcium imaging using Fluo4-AM in CViA2 cells cultured in different scaffold conditions. Graphs show intracellular uptake of calcium as $\Delta F/F_0$ with representative images below each graph showing calcium uptake and cell morphology. CViA2 cells grown on a) nonaligned Geltrex coated scaffolds, b) nonaligned conditioned medium treated scaffolds, c) aligned Geltrex coated scaffolds, and d) aligned conditioned medium treated scaffolds.

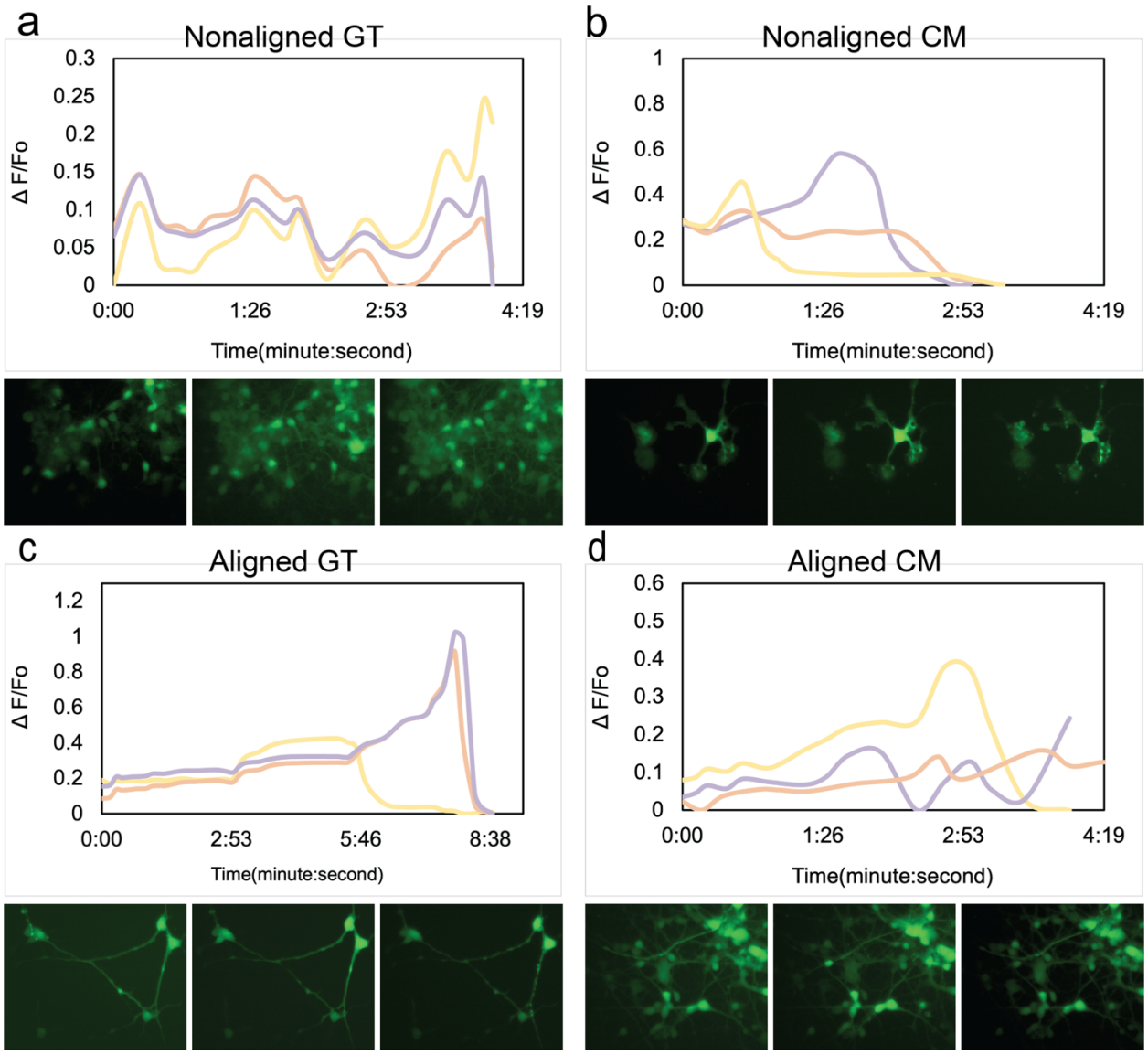


Figure 7.12 Calcium imaging using Fluo4-AM in Swe22 cells cultured in different scaffold conditions. Graphs show intracellular uptake of calcium as $\Delta F/F_0$ with representative images below each graph showing calcium uptake and cell morphology. Swe22 cells grown on a) nonaligned Geltrex coated scaffolds, b) nonaligned conditioned medium treated scaffolds, c) aligned Geltrex coated scaffolds, and d) aligned conditioned medium treated scaffolds.

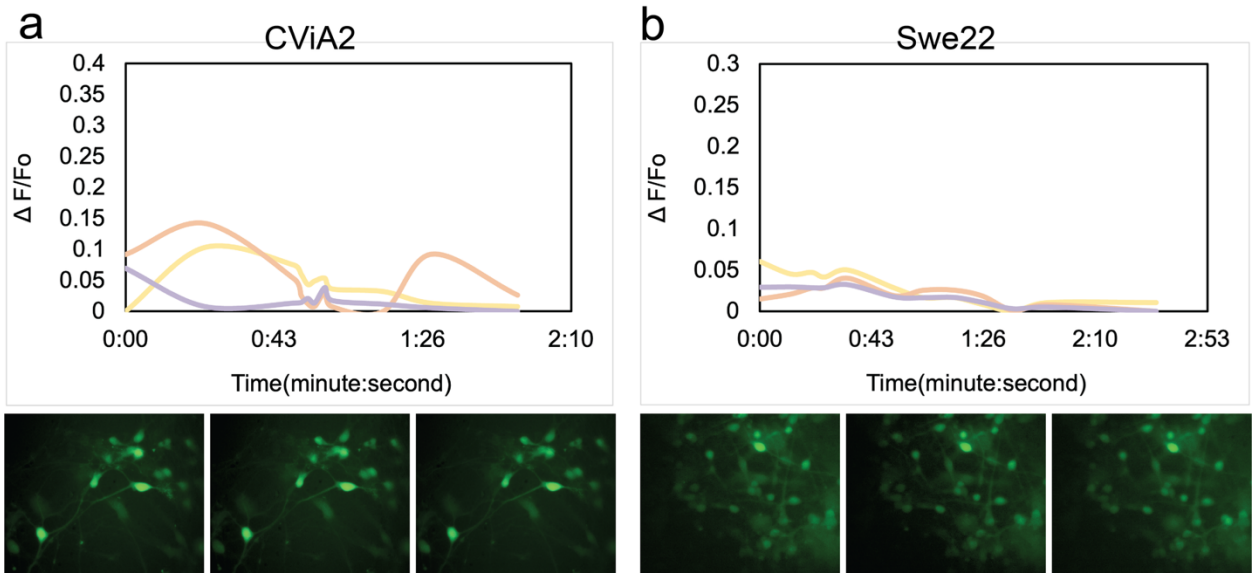


Figure 7.13 Calcium imaging using Fluo4-AM in a) CViA2 and b) Swe22 cells cultured in 2D conditions. Graphs show intracellular uptake of calcium as $\Delta F/F_0$ with representative images below each graph showing calcium uptake and cell morphology.

Figure 7.14 shows the mRNA expression for various genes associated with synaptogenesis and AD pathogenesis. The synaptic markers, synaptogyrin 3 (SYNRG3) and post synaptic density protein (PSD95) generally increased for cells that were grown in 3D scaffolds, particularly for the conditioned medium treated aligned scaffolds. This indicates that the aligned scaffolds were better able to promote differentiation and synaptic connections between cells. The MAPT isoforms, 4RTau and 3RTau were generally upregulated in the aligned scaffold conditions, aside from the 4RTau expression in Swe22 cells. Aβ precursor protein (APP) and microtubule-associated protein tau (MAPT) are two key markers in AD pathogenesis, and they were found to be upregulated in the aligned scaffolds for all 3 cell types. β-site APP cleaving enzyme 1 (BACE1) was also shown to be upregulated in the aligned scaffold conditions for the diseased cell lines. These results indicate that the scaffolds are able to promote more efficient differentiation of cells from hNPCs

into neurons than the 2D controls and generally cause an upregulation of key genes associated for AD pathogenesis.

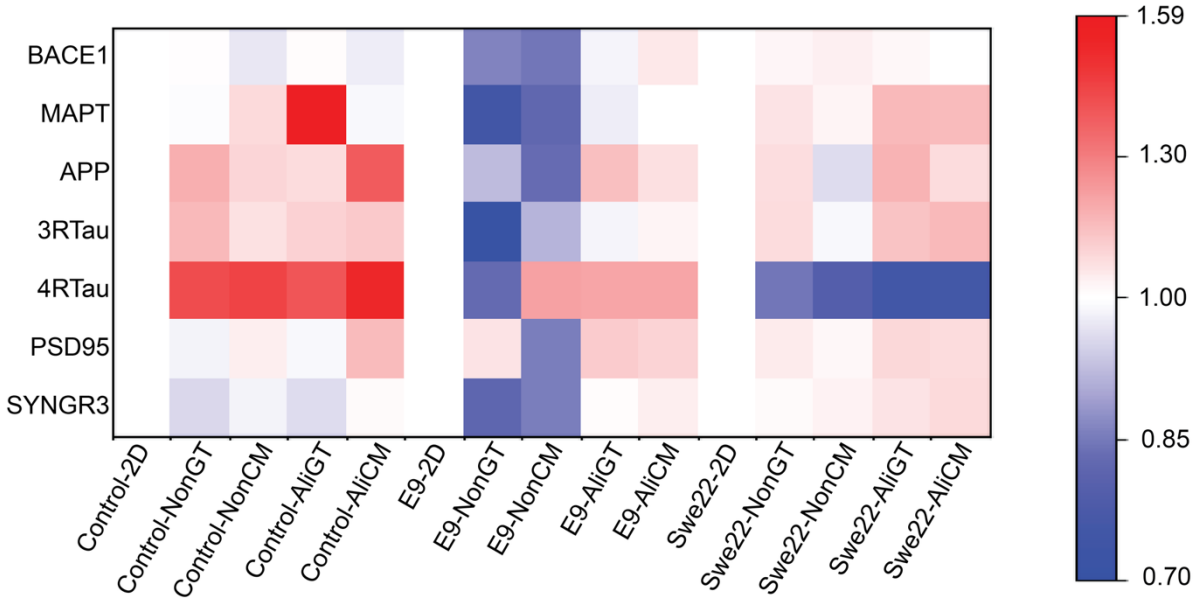


Figure 7.14 The mRNA expression normalized to the 2D cultured cell type for each cell type. The results are presented as fold changes as described previously. [350] The 2D differentiated cells were set as 1-fold for each cell type.

7.3.8 Amyloid Beta Analysis

Medium was collected after the initial 3-week differentiation period before passaging the cells and plating them onto 2D wells. The ratio of Aβ 1-42 to Aβ 1-40 is shown in **Figure 7.15a** and the fold change compared to the 2D control is illustrated in **Figure 7.15b**. In clinical models, a decrease in the Aβ 1-42 to Aβ 1-40 ratio is associated with Alzheimer's disease, as more Aβ 1-42 builds up on the brain as plaque, hindering neuron function. [351,352] In both cell lines, a decrease in the Aβ 1-42 to Aβ 1-40 ratio is seen, indicating that the scaffolds are able to better model the *in vivo* characteristic of Alzheimer's disease, although in the control cell line only a significant change in the nonaligned condition medium treated scaffold is significant. This is likely due to the scaffold's porous structure and surface charge, which allows it to better protect Aβ 1-42 and Aβ

1-40 during medium changes that may otherwise remove them. The scaffolds provide a better model for Aβ accumulation in the brain, which could provide a better model for drug screening.

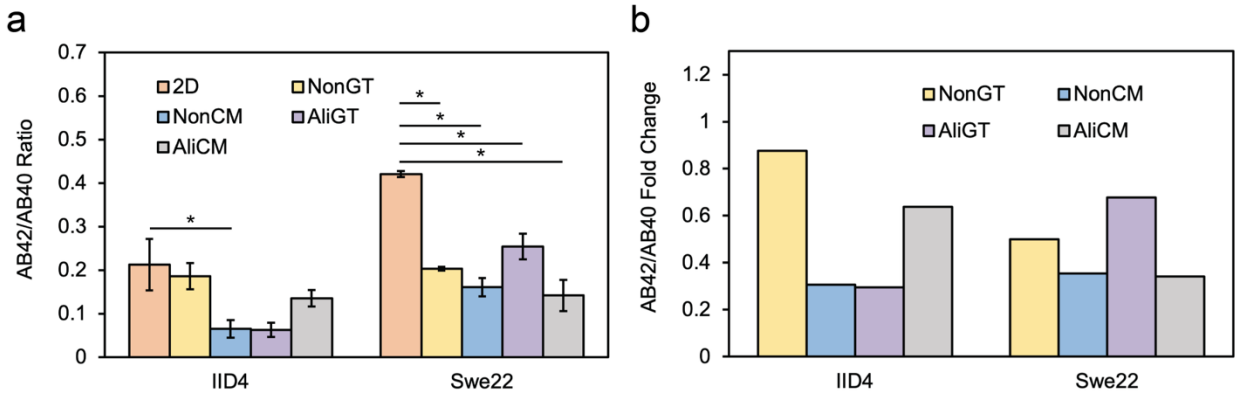


Figure 7.15 Quantification of Aβ 1-42 and Aβ 1-40 shown as the a) Aβ 1-42 to Aβ 1-40 ratio and b) Aβ 1-42 to Aβ 1-40 ratio fold change compared to the 2D control sample for each cell line. An * indicates a *p* value of less than 0.05.

Chapter 8 Summary of Major Findings

This dissertation presents the development and validation of chitosan-based biomaterials as a robust platform for the culture, expansion, and differentiation of human neural stem cells. Through systematic material design and biological evaluation, the research addresses key limitations in current culture systems, including the lack of scalability, inadequate physiological relevance, and non-compliance with regulatory standards for clinical use.

Chapter 3 demonstrates the influence of varying chitosan (CS) ratios within chitosan-alginate (CA) and chitosan-hyaluronic acid (CHA) films on human neural stem cell (hNSC) fate. The fabricated films exhibited consistent topography, favorable hydrophilicity, and a wide range of mechanical properties, enabling a systematic exploration of the impact of polymer composition on hNSC behavior. The 2D nature of these films allows for clear visualization and imaging of the cultured hNSCs. Our findings demonstrated that pure CS films provided the most conducive environment for hNSC adhesion and proliferation, and maintenance of multipotency, as evidenced by light optical imaging, live-dead staining, alamarBlue assays, flow cytometry, and immunostaining. This superior performance was observed despite absence of any exogenous extracellular matrix proteins like laminin or fibronectin in the pure CS films.

The incorporation of chitosan to both alginate and HA films consistently resulted in enhanced cell attachment, proliferation, and maintenance of multipotency compared to films composed of solely of alginate or HA. Conversely, pure alginate or HA films predominantly induced the formation of cell spheroids. While all chitosan-containing films supported adherent cell populations for up to 4 days, except for the CA 1:3 ratio film, the HA films generally exhibited a higher degree of cell adhesion. Collectively, these findings indicate that pure CS surfaces offer a more favorable microenvironment for hNSCs compared to hybrid CA and CHA materials in

terms of cell adhesion, proliferation, and the preservation of multipotency. Furthermore, this study establishes a xeno-free and chemically defined 2D culture substrate that possesses significant potential for migrating to 3D systems for future culture applications.

In Chapter 4, we developed a 3D microcarrier designed to expand hNSCs in dynamic bioreactor culture systems. The microcarrier offers several advantages, such as providing additional growth space and shielding cells from the dynamic environment. Our investigation into the maintenance of hNSCs in dynamic cultures showed that the mechanical properties of the scaffolds, including their compressive elastic moduli and localized micro- to nanoscale elastic moduli, have a crucial impact on cell mechanosensing, structural integrity, and cell fate determination. By utilizing pure chitosan, we successfully achieved xeno-free cultivation of human stem cells suitable for clinical applications. Notably, this is the first study to expand hNSCs using chitosan porous scaffolds in a dynamic culture system. The scaffolds maintained a stable microstructure and demonstrated long-term durability without degradation. The scaffold pores facilitated hNSC adhesion and distribution within a 3D space, while possessing appropriate mechanical properties to support undifferentiated proliferation. When compared to collagen scaffolds, the optimized chitosan scaffolds outperformed them in maintaining the proliferation and multipotency of hNSCs. Moreover, the 4CS chitosan scaffolds were the best at supporting hNSCs in terms of proliferation and multipotency, and we able to support hNSC expansion for up to three weeks. Overall, this study presents a dynamic bioreactor culture platform utilizing chitosan scaffolds as microcarriers capable of scaling up for hNSC production.

Chapter 5 demonstrates a novel continuous-flow rotational bioreactor system designed to address key tissue engineering challenges through an adaptable, efficient, and cost-effective cell culture platform. Its modular design accommodates various flask types and sample configurations,

providing precise control over critical physiological parameters. A unique swivel connector ensures continuous gas and media exchange during rotation, which reduces shear stress and improves mass transport for enhanced reliability. The system successfully cultured cancer cells on chitosan scaffolds and non-adherent cells, demonstrating its versatility. Integration with Arduino and Python platforms supports customization, incorporation of additional sensors, and advanced control algorithms to facilitate high-throughput testing, multi-sample processing, and complex tissue culture models. This bioreactor serves as a powerful tool for tissue engineering research by improving reproducibility, scalability, versatility, and affordability. Its tunable regulation of environmental conditions maintains physiologically relevant cultures, while its user-friendly, modular design accommodates researchers of all levels. These attributes make it suitable for fundamental studies such as stem cell differentiation and tumor modeling, as well as clinical applications in tissue regeneration and personalized medicine. Its cost-effectiveness broadens its potential impact.

In Chapter 6, we fabricated 6CS scaffolds with various coatings or surface treatments to assess their effect on the differentiation of hNSCs. The 6CS scaffolds provided a chemically defined environment that closely mimics *in vivo* conditions, enhancing the efficiency and speed of hNSC differentiation into cortical neurons. Notably, the pre-seeded 6CS scaffolds demonstrated superior coating consistency and protein retention, leading to faster and more effective differentiation. Compared to 2D controls, the pre-seeded scaffolds significantly enhanced the expression of differentiation makers on day 14, with increases of 128% for MAP2B, 309% for GFAP, 153% for DCX, and 42% for TUBB3. Cells grown in pre-seeded scaffolds exhibited improved morphology and better attachment, indicating enhanced differentiation support.

Gene expression analysis further confirmed that cells in the pre-seeded 6CS scaffolds advanced towards mature cortical neuron phenotypes more effectively than those in Geltrex coated scaffolds. Over the 14-day period, gene expression for key differentiation markers decreased for the 3D samples while gene expression in the 2D samples increased, indicating the cells grown in 3D scaffolds are further along in the differentiation process than those in 2D. Even so, GFAP, OLIG2, TBR1, and CTIP2 showed a 144%, 203%, 162%, and a 375% increase when comparing the pre-seeded scaffold to the 2D control on day 14. While gene expression levels in 3D scaffold cultures decreased over the 14-day period, suggesting maturation, expression levels in 2D cultures continued to rise, indicating ongoing differentiation. By day 14, the pre-seeded scaffolds outperformed 2D controls, with increases in GFAP (144%), OLIG2 (203%), TBR1 (162%), and CTIP2 (375%), underscoring their potential in promoting quicker neuron maturation.

Overall, we have demonstrated a chemically defined 3D culture system that can effectively differentiate hNSCs into mature cortical neurons. This 3D culture model could be a promising tool for enhancing the efficiency of hNSC differentiation, potentially accelerating therapeutic strategies for neurodegenerative diseases.

In Chapter 7 we demonstrated that our chitosan scaffolds provided a robust matrix to for AD model constructs in vitro. The 3D culture not only supported hiPSC pluripotency but also supported efficient differentiation into hNPCs and maintenance of the hNPCs. The scaffolds were also able to effectively differentiate from hNPCs into neurons, showing higher levels of expression of key neuron proteins than the 2D controls. The functional study indicates that the scaffolds were able to better capitulate mature neurons and had higher levels of synaptic transmission and expression than the 2D controls. Finally, the scaffolds caused the cells to produce higher levels of

amyloid beta than the 2D controls, making it a more effective model of Alzheimer's disease than the 2D controls.

Collectively, these findings highlight the potential of chitosan-based biomaterials to transform stem cell culture platforms by integrating biocompatibility, scalability, and functional relevance. This work offers a pathway toward clinical translation of hNSC therapies and provides a valuable foundation for the development of high-fidelity disease models. Future studies may expand the platform to include additional neural subtypes, integrate biosensors for real-time phenotype monitoring, or incorporate gene-editing tools to further explore disease mechanisms and therapeutic interventions.

References

1 Schneider, L. S. & Sano, M. Current Alzheimer's disease clinical trials: methods and placebo outcomes. *Alzheimer's & dementia* **5**, 388-397 (2009).

2 Mangialasche, F., Solomon, A., Winblad, B., Mecocci, P. & Kivipelto, M. Alzheimer's disease: clinical trials and drug development. *The Lancet Neurology* **9**, 702-716 (2010).

3 Grochowski, C., Radzikowska, E. & Maciejewski, R. Neural stem cell therapy—Brief review. *Clinical neurology and neurosurgery* **173**, 8-14 (2018).

4 Nam, H., Lee, K.-H., Nam, D.-H. & Joo, K. M. Adult human neural stem cell therapeutics: Current developmental status and prospect. *World journal of stem cells* **7**, 126 (2015).

5 Centeno, E. G., Cimarosti, H. & Bithell, A. 2D versus 3D human induced pluripotent stem cell-derived cultures for neurodegenerative disease modelling. *Molecular neurodegeneration* **13**, 1-15 (2018).

6 Duval, K. *et al.* Modeling physiological events in 2D vs. 3D cell culture. *Physiology* **32**, 266-277 (2017).

7 Tian, X. F. *et al.* Comparison of osteogenesis of human embryonic stem cells within 2D and 3D culture systems. *Scandinavian journal of clinical and laboratory investigation* **68**, 58-67 (2008).

8 Jakel, R. J., Schneider, B. L. & Svendsen, C. N. Using human neural stem cells to model neurological disease. *Nature Reviews Genetics* **5**, 136-144 (2004).

9 Kim, S. U. Human neural stem cells genetically modified for brain repair in neurological disorders. *Neuropathology* **24**, 159-171 (2004).

10 Kim, S. U., Lee, H. J. & Kim, Y. B. Neural stem cell-based treatment for neurodegenerative diseases. *Neuropathology* **33**, 491-504 (2013).

11 Martínez-Morales, P. *et al.* Progress in stem cell therapy for major human neurological disorders. *Stem Cell Reviews and Reports* **9**, 685-699 (2013).

12 Baghbaderani, B. A. *et al.* cGMP-manufactured human induced pluripotent stem cells are available for pre-clinical and clinical applications. *Stem cell reports* **5**, 647-659 (2015).

13 Shelley, B. C., Gowing, G. & Svendsen, C. N. A cGMP-applicable expansion method for aggregates of human neural stem and progenitor cells derived from pluripotent stem cells or fetal brain tissue. *Journal of visualized experiments: JoVE*, 51219 (2014).

14 Coccini, T. *et al.* 3D human stem-cell-derived neuronal spheroids for in vitro neurotoxicity testing of methylglyoxal, highly reactive glycolysis byproduct and potent glycating agent. *Current Research in Toxicology* **7**, 100176 (2024).

15 Zhao, X. & Moore, D. L. Vol. 371 1-6 (Springer, 2018).

16 Clout, A. E., Della Pasqua, O., Hanna, M. G., Orlu, M. & Pitceathly, R. D. Drug repurposing in neurological diseases: an integrated approach to reduce trial and error. *Journal of Neurology, Neurosurgery & Psychiatry* **90**, 1270-1275 (2019).

17 Briggs, R., Kennelly, S. P. & O'Neill, D. Drug treatments in Alzheimer's disease. *Clinical medicine* **16**, 247-253 (2016).

18 Niu, X. *et al.* Silver-loaded microspheres reinforced chitosan scaffolds for skin tissue engineering. *European Polymer Journal* **134**, 109861 (2020).

19 Tamimi, M., Rajabi, S. & Pezeshki-Modaress, M. Cardiac ECM/chitosan/alginate ternary scaffolds for cardiac tissue engineering application. *International Journal of Biological Macromolecules* **164**, 389-402 (2020).

20 Ananthanarayanan, B., Kim, Y. & Kumar, S. Elucidating the mechanobiology of malignant brain tumors using a brain matrix-mimetic hyaluronic acid hydrogel platform. *Biomaterials* **32**, 7913-7923 (2011).
21 Erickson, A. E., Lan Levengood, S. K., Sun, J., Chang, F. C. & Zhang, M. Fabrication and characterization of chitosan–hyaluronic acid scaffolds with varying stiffness for glioblastoma cell culture. *Advanced healthcare materials* **7**, 1800295 (2018).
22 Arulmoli, J. *et al.* Combination scaffolds of salmon fibrin, hyaluronic acid, and laminin for human neural stem cell and vascular tissue engineering. *Acta biomaterialia* **43**, 122-138 (2016).
23 Xie, H. G. *et al.* Effect of surface wettability and charge on protein adsorption onto implantable alginate-chitosan-alginate microcapsule surfaces. *Journal of Biomedical Materials Research Part A: An Official Journal of The Society for Biomaterials, The Japanese Society for Biomaterials, and The Australian Society for Biomaterials and the Korean Society for Biomaterials* **92**, 1357-1365 (2010).
24 Tam, S. K. *et al.* Factors influencing alginate gel biocompatibility. *Journal of Biomedical Materials Research Part A* **98**, 40-52 (2011).
25 Wang, L. *et al.* A physically cross-linked sodium alginate–gelatin hydrogel with high mechanical strength. *ACS Applied Polymer Materials* **3**, 3197-3205 (2021).
26 Wang, Y. *et al.* A study on the performance of hyaluronic acid immobilized chitosan film. *Biomedical Materials* **4**, 035009 (2009).
27 Ghosh, K. in *Natural-based polymers for biomedical applications* 716-737 (Elsevier, 2008).
28 Gorroñogoitia, I., Olza, S., Alonso-Varona, A. & Zaldua, A. M. The Effect of Alginate/Hyaluronic Acid Proportion on Semi-Interpenetrating Hydrogel Properties for Articular Cartilage Tissue Engineering. *Polymers* **17**, 528 (2025).
29 Gachon, E. & Mesquida, P. Mechanical strain alters the surface charge of collagen fibrils. *ACS nano* **15**, 9820-9826 (2021).
30 Rahmanian-Schwarz, A. *et al.* In vivo biocompatibility and biodegradation of a novel thin and mechanically stable collagen scaffold. *Journal of biomedical materials research Part A* **102**, 1173-1179 (2014).
31 Rodrigues, S., Dionísio, M., Remunan Lopez, C. & Grenha, A. Biocompatibility of chitosan carriers with application in drug delivery. *Journal of functional biomaterials* **3**, 615-641 (2012).
32 Funakoshi, T. *et al.* Novel chitosan-based hyaluronan hybrid polymer fibers as a scaffold in ligament tissue engineering. *Journal of Biomedical Materials Research Part A: An Official Journal of The Society for Biomaterials, The Japanese Society for Biomaterials, and The Australian Society for Biomaterials and the Korean Society for Biomaterials* **74**, 338-346 (2005).
33 Costa-Pinto, A. R., Reis, R. L. & Neves, N. M. Scaffolds based bone tissue engineering: the role of chitosan. *Tissue Engineering Part B: Reviews* **17**, 331-347 (2011).
34 Rodríguez-Vázquez, M., Vega-Ruiz, B., Ramos-Zúñiga, R., Saldaña-Koppel, D. A. & Quiñones-Olvera, L. F. Chitosan and its potential use as a scaffold for tissue engineering in regenerative medicine. *BioMed research international* **2015** (2015).
35 LogithKumar, R. *et al.* A review of chitosan and its derivatives in bone tissue engineering. *Carbohydrate polymers* **151**, 172-188 (2016).

36 Busilacchi, A., Gigante, A., Mattioli-Belmonte, M., Manzotti, S. & Muzzarelli, R. A. A. Chitosan stabilizes platelet growth factors and modulates stem cell differentiation toward tissue regeneration. *Carbohydrate polymers* **98**, 665-676 (2013).
37 Sivashankari, P. R. & Prabaharan, M. Prospects of chitosan-based scaffolds for growth factor release in tissue engineering. *International journal of biological macromolecules* **93**, 1382-1389 (2016).
38 Li, J. *et al.* Chitosan-based nanomaterials for drug delivery. *Molecules* **23**, 2661 (2018).
39 Liu, H. *et al.* A functional chitosan-based hydrogel as a wound dressing and drug delivery system in the treatment of wound healing. *RSC advances* **8**, 7533-7549 (2018).
40 Oryan, A. & Sahvieh, S. Effectiveness of chitosan scaffold in skin, bone and cartilage healing. *International Journal of Biological Macromolecules* **104**, 1003-1011 (2017).
41 Chen, E. *et al.* An asymmetric chitosan scaffold for tendon tissue engineering: In vitro and in vivo evaluation with rat tendon stem/progenitor cells. *Acta biomaterialia* **73**, 377-387 (2018).
42 Köwitsch, A., Zhou, G. & Groth, T. Medical application of glycosaminoglycans: a review. *Journal of Tissue Engineering and Regenerative Medicine* **12**, e23-e41 (2018). https://doi.org/10.1002/term.2398
43 Saied-Santiago, K. & Bülow, H. E. Diverse roles for glycosaminoglycans in neural patterning. *Developmental Dynamics* **247**, 54-74 (2018). https://doi.org/10.1002/dvdy.24555
44 Tedesco, M. T. *et al.* Soft chitosan microbeads scaffold for 3D functional neuronal networks. *Biomaterials* **156**, 159-171 (2018).
45 Revkova, V. A. *et al.* Chitosan-g-oligo (L, L-lactide) copolymer hydrogel potential for neural stem cell differentiation. *Tissue Engineering Part A* **26**, 953-963 (2020).
46 Mattotti, M. *et al.* Differential neuronal and glial behavior on flat and micro patterned chitosan films. *Colloids and Surfaces B: Biointerfaces* **158**, 569-577 (2017). https://doi.org/https://doi.org/10.1016/j.colsurfb.2017.07.045
47 Viswanathan, P. *et al.* 3D surface topology guides stem cell adhesion and differentiation. *Biomaterials* **52**, 140-147 (2015).
48 Jensen, C. & Teng, Y. Is it time to start transitioning from 2D to 3D cell culture? *Frontiers in molecular biosciences* **7**, 33 (2020).
49 Liu, R. *et al.* From 2D to 3D co-culture systems: a review of co-culture models to study the neural cells interaction. *International journal of molecular sciences* **23**, 13116 (2022).
50 Magrofuoco, E., Flaibani, M., Giomo, M. & Elvassore, N. Cell culture distribution in a three-dimensional porous scaffold in perfusion bioreactor. *Biochemical Engineering Journal* **146**, 10-19 (2019).
51 Simão, D. *et al.* Perfusion stirred-tank bioreactors for 3D differentiation of human neural stem cells. *Bioreactors in Stem Cell Biology: Methods and Protocols*, 129-142 (2016).
52 Hu, W., Berdugo, C. & Chalmers, J. J. The potential of hydrodynamic damage to animal cells of industrial relevance: current understanding. *Cytotechnology* **63**, 445-460 (2011).
53 Loubière, C. *et al.* Optimization of the impeller design for mesenchymal stem cell culture on microcarriers in bioreactors. *Chemical Engineering & Technology* **42**, 1702-1708 (2019).
54 Pörtner, R., Freiberger, F. & Möller, J. Review on the impact of impeller-induced hydrodynamics on suspension cell culture for production of biopharmaceuticals. *Chemie Ingenieur Technik* **96**, 462-470 (2024).

55 DiStefano, T. *et al.* Accelerated and improved differentiation of retinal organoids from pluripotent stem cells in rotating-wall vessel bioreactors. *Stem cell reports* **10**, 300-313 (2018).
56 Zhang, Y., Wang, X., Pong, M., Chen, L. & Ye, Z. Application of bioreactor in stem cell culture. *Journal of Biomedical Science and Engineering* **10**, 485-499 (2017).
57 Zhang, C.-L., Huang, T., Wu, B.-L., He, W.-X. & Liu, D. Stem cells in cancer therapy: opportunities and challenges. *Oncotarget* **8**, 75756 (2017).
58 Benmelouka, A. Y. *et al.* Neural stem cell-based therapies and glioblastoma management: Current evidence and clinical challenges. *International journal of molecular sciences* **22**, 2258 (2021).
59 Fares, J. *et al.* Neural stem cell delivery of an oncolytic adenovirus in newly diagnosed malignant glioma: a first-in-human, phase 1, dose-escalation trial. *The Lancet Oncology* **22**, 1103-1114 (2021).
60 McGinley, L. M. *et al.* Human neural stem cell transplantation improves cognition in a murine model of Alzheimer's disease. *Scientific reports* **8**, 1-10 (2018).
61 Fleifel, D. *et al.* Recent advances in stem cells therapy: A focus on cancer, Parkinson's and Alzheimer's. *Journal of Genetic Engineering and Biotechnology* **16**, 427-432 (2018).
62 Lu, M.-H. *et al.* Intranasal transplantation of human neural stem cells ameliorates Alzheimer's disease-like pathology in a mouse model. *Frontiers in Aging Neuroscience* **13**, 650103 (2021).
63 Apodaca, L. A. *et al.* Human neural stem cell-derived extracellular vesicles mitigate hallmarks of Alzheimer's disease. *Alzheimer's research & therapy* **13**, 1-18 (2021).
64 Kim, S. W. *et al.* Neural stem cells derived from human midbrain organoids as a stable source for treating Parkinson's disease: Midbrain organoid-NSCs (Og-NSC) as a stable source for PD treatment. *Progress in neurobiology* **204**, 102086 (2021).
65 Lee, E. J., Choi, Y., Lee, H. J., Hwang, D. W. & Lee, D. S. Human neural stem cell-derived extracellular vesicles protect against Parkinson's disease pathologies. *Journal of Nanobiotechnology* **20**, 198 (2022).
66 Chen, G. *et al.* Neural stem cell-like cells derived from autologous bone mesenchymal stem cells for the treatment of patients with cerebral palsy. *Journal of Translational Medicine* **11**, 1-11 (2013).
67 Lv, Z. *et al.* Safety and efficacy outcomes after intranasal administration of neural stem cells in cerebral palsy: a randomized phase 1/2 controlled trial. *Stem Cell Research & Therapy* **14**, 23 (2023).
68 Zhang, C. *et al.* Treatment of multiple sclerosis by transplantation of neural stem cells derived from induced pluripotent stem cells. *Science China Life Sciences* **59**, 950-957 (2016).
69 Brown, C. *et al.* Neural stem cells derived from primitive mesenchymal stem cells reversed disease symptoms and promoted neurogenesis in an experimental autoimmune encephalomyelitis mouse model of multiple sclerosis. *Stem Cell Research & Therapy* **12**, 1-21 (2021).
70 Genchi, A. *et al.* Neural stem cell transplantation in patients with progressive multiple sclerosis: an open-label, phase 1 study. *Nature medicine* **29**, 75-85 (2023).
71 Mazzini, L. *et al.* Human neural stem cell transplantation in ALS: initial results from a phase I trial. *Journal of translational medicine* **13**, 1-16 (2015).

72 Kassi, A. A. Y. *et al.* Enduring neuroprotective effect of subacute neural stem cell transplantation after penetrating TBI. *Frontiers in neurology* **9**, 1097 (2019).
73 Hayashi, Y., Lin, H.-T., Lee, C.-C. & Tsai, K.-J. Effects of neural stem cell transplantation in Alzheimer's disease models. *Journal of biomedical science* **27**, 1-11 (2020).
74 Pluchino, S., Smith, J. A. & Peruzzotti-Jametti, L. Promises and limitations of neural stem cell therapies for progressive multiple sclerosis. *Trends in Molecular Medicine* **26**, 898-912 (2020).
75 Smith, M. J. *et al.* Neural stem cell treatment for perinatal brain injury: A systematic review and meta-analysis of preclinical studies. *Stem cells translational medicine* (2021).
76 Sterneckert, J. L., Reinhardt, P. & Schöler, H. R. Investigating human disease using stem cell models. *Nature Reviews Genetics* **15**, 625-639 (2014). https://doi.org/10.1038/nrg3764
77 Ghourichaee, S. S. & Leach, J. B. The effect of hypoxia and laminin-rich substrates on the proliferative behavior of human neural stem cells. *Journal of Materials Chemistry B* **4**, 3509-3514 (2016).
78 Du, J. *et al.* Comparative evaluation of chitosan, cellulose acetate, and polyethersulfone nanofiber scaffolds for neural differentiation. *Carbohydrate polymers* **99**, 483-490 (2014).
79 Ando, Y., Chang, F.-C., James, M., Zhou, Y. & Zhang, M. Chitosan Scaffolds as Microcarriers for Dynamic Culture of Human Neural Stem Cells. *Pharmaceutics* **15** (2023).
80 Bai, T. *et al.* Neuronal differentiation and functional maturation of neurons from neural stem cells induced by bFGF-chitosan controlled release system. *Drug Delivery and Translational Research* **13**, 2378-2393 (2023).
81 Chang, F.-C. *et al.* 3D chitosan scaffolds support expansion of human neural stem cells in chemically defined condition. *Matter* **6**, 3631-3660 (2023). https://doi.org/10.1016/j.matt.2023.08.014
82 Chang, F. C. *et al.* Effect of degree of deacetylation of chitosan/chitin on human neural stem cell culture. *Macromolecular Bioscience* **23**, 2200389 (2023).
83 Guo, S. *et al.* Parallel Control over Surface Charge and Wettability Using Polyelectrolyte Architecture: Effect on Protein Adsorption and Cell Adhesion. *ACS Applied Materials & Interfaces* **8**, 30552-30563 (2016). https://doi.org/10.1021/acsami.6b09481
84 Ferrari, M., Cirisano, F. & Morán, M. C. Mammalian Cell Behavior on Hydrophobic Substrates: Influence of Surface Properties. *Colloids and Interfaces* **3**, 48 (2019). https://doi.org/10.3390/colloids3020048
85 Xu, K. *et al.* 3D porous chitosan-alginate scaffold stiffness promotes differential responses in prostate cancer cell lines. *Biomaterials* **217**, 119311 (2019).
86 Niculescu, A.-G. & Grumezescu, A. M. Applications of Chitosan-Alginate-Based Nanoparticles—An Up-to-Date Review. *Nanomaterials* **12**, 186 (2022). https://doi.org/10.3390/nano12020186
87 Dhoot, N. O., Tobias, C. A., Fischer, I. & Wheatley, M. A. Peptide-modified alginate surfaces as a growth permissive substrate for neurite outgrowth. *Journal of Biomedical Materials Research Part A* **71A**, 191-200 (2004). https://doi.org/10.1002/jbm.a.30103
88 Bozza, A. *et al.* Neural differentiation of pluripotent cells in 3D alginate-based cultures. *Biomaterials* **35**, 4636-4645 (2014).

89 Lee, K. Y. & Mooney, D. J. Alginate: properties and biomedical applications. *Progress in polymer science* **37**, 106-126 (2012).
90 Rowley, J. A., Madlambayan, G. & Mooney, D. J. Alginate hydrogels as synthetic extracellular matrix materials. *Biomaterials* **20**, 45-53 (1999).
91 Chang, S.-H. & Chian, C.-H. Plasma surface modification effects on biodegradability and protein adsorption properties of chitosan films. *Applied Surface Science* **282**, 735-740 (2013). https://doi.org/10.1016/j.apsusc.2013.06.044
92 Murguía-Flores, D. A., Bonilla-Ríos, J., Canales-Fiscal, M. R. & Sánchez-Fernández, A. Protein adsorption through Chitosan–Alginate membranes for potential applications. *Chemistry Central Journal* **10**, 1-22 (2016).
93 Li, Z., Ramay, H. R., Hauch, K. D., Xiao, D. & Zhang, M. Chitosan–alginate hybrid scaffolds for bone tissue engineering. *Biomaterials* **26**, 3919-3928 (2005). https://doi.org/10.1016/j.biomaterials.2004.09.062
94 Reed, S. & Wu, B. M. Biological and mechanical characterization of chitosan-alginate scaffolds for growth factor delivery and chondrogenesis. *Journal of Biomedical Materials Research Part B: Applied Biomaterials* **105**, 272-282 (2017). https://doi.org/10.1002/jbm.b.33544
95 Abatangelo, G., Vindigni, V., Avruscio, G., Pandis, L. & Brun, P. Hyaluronic Acid: Redefining Its Role. *Cells* **9**, 1743 (2020). https://doi.org/10.3390/cells9071743
96 Pereira, I. *et al.* Hyaluronic acid-based bioink improves the differentiation and network formation of neural progenitor cells. *Frontiers in Bioengineering and Biotechnology* **11**, 1110547 (2023).
97 Liang, Y. *et al.* Impact of hydrogel stiffness on the induced neural stem cells modulation. *Annals of Translational Medicine* **9** (2021).
98 Drozdova, M. G. *et al.* Macroporous Hyaluronic Acid/Chitosan Polyelectrolyte Complex-Based Hydrogels Loaded with Hydroxyapatite Nanoparticles: Preparation, Characterization and In Vitro Evaluation. *Polysaccharides* **3**, 745-760 (2022).
99 Meng, X. *et al.* Chitosan/alginate/hyaluronic acid polyelectrolyte composite sponges crosslinked with genipin for wound dressing application. *International Journal of Biological Macromolecules* **182**, 512-523 (2021).
100 Yamanlar, S., Sant, S., Boudou, T., Picart, C. & Khademhosseini, A. Surface functionalization of hyaluronic acid hydrogels by polyelectrolyte multilayer films. *Biomaterials* **32**, 5590-5599 (2011). https://doi.org/10.1016/j.biomaterials.2011.04.030
101 Sionkowska, A. & Kozłowska, J. Properties and modification of porous 3-D collagen/hydroxyapatite composites. *International journal of biological macromolecules* **52**, 250-259 (2013).
102 Xia, J., Yuan, Y., Wu, H., Huang, Y. & Weitz, D. A. Decoupling the effects of nanopore size and surface roughness on the attachment, spreading and differentiation of bone marrow-derived stem cells. *Biomaterials* **248**, 120014 (2020). https://doi.org/10.1016/j.biomaterials.2020.120014
103 Majhy, B., Priyadarshini, P. & K. Sen, A. Effect of surface energy and roughness on cell adhesion and growth – facile surface modification for enhanced cell culture. *RSC Advances* **11**, 15467-15476 (2021). https://doi.org/10.1039/D1RA02402G
104 Wysotzki, P., Sancho, A., Gimsa, J. & Groll, J. A comparative analysis of detachment forces and energies in initial and mature cell-material interaction. *Colloids and Surfaces*

B: Biointerfaces **190**, 110894 (2020). https://doi.org/https://doi.org/10.1016/j.colsurfb.2020.110894
105 Sarker, B. *et al.* Alginate-based hydrogels with improved adhesive properties for cell encapsulation. *International Journal of Biological Macromolecules* **78**, 72-78 (2015). https://doi.org/https://doi.org/10.1016/j.ijbiomac.2015.03.061
106 Vining, K. H. & Mooney, D. J. Mechanical forces direct stem cell behaviour in development and regeneration. *Nature reviews Molecular cell biology* **18**, 728-742 (2017).
107 Stukel, J. M. & Willits, R. K. Mechanotransduction of neural cells through cell–substrate interactions. *Tissue Engineering Part B: Reviews* **22**, 173-182 (2016).
108 Cavanaugh, M. & Willits, R. K. Mechanotransductive N-cadherin binding induces differentiation in human neural stem cells. *Mechanobiology in Medicine* **3**, 100099 (2025).
109 Marinval, N. & Chew, S. Y. Mechanotransduction assays for neural regeneration strategies: A focus on glial cells. *APL bioengineering* **5** (2021).
110 Zhao, N., Wang, X., Qin, L., Guo, Z. & Li, D. Effect of molecular weight and concentration of hyaluronan on cell proliferation and osteogenic differentiation in vitro. *Biochemical and Biophysical Research Communications* **465**, 569-574 (2015). https://doi.org/10.1016/j.bbrc.2015.08.061
111 Dovedytis, M., Liu, Z. J. & Bartlett, S. Hyaluronic acid and its biomedical applications: A review. *Engineered Regeneration* **1**, 102-113 (2020). https://doi.org/10.1016/j.engreg.2020.10.001
112 Kamiloglu, S., Sari, G., Ozdal, T. & Capanoglu, E. Guidelines for cell viability assays. *Food Frontiers* **1**, 332-349 (2020). https://doi.org/10.1002/fft2.44
113 Liu, Y.-R. *et al.* Sox2 acts as a transcriptional repressor in neural stem cells. *BMC Neuroscience* **15**, 95 (2014). https://doi.org/10.1186/1471-2202-15-95
114 Tang, Y., Yu, P. & Cheng, L. Current progress in the derivation and therapeutic application of neural stem cells. *Cell death & disease* **8**, e3108-e3108 (2017).
115 Zhao, X. & Moore, D. L. in *Cell and tissue research* Vol. 371 1-6 (Springer, 2018).
116 F Lévesque, M., Neuman, T. & Rezak, M. Therapeutic microinjection of autologous adult human neural stem cells and differentiated neurons for Parkinson's disease: five-year post-operative outcome. *The Open Stem Cell Journal* **1** (2009).
117 Mazzini, L. *et al.* Human neural stem cell transplantation in ALS: initial results from a phase I trial. *Journal of Translational Medicine* **13**, 1-16 (2015).
118 Greiner, A. M., Richter, B. & Bastmeyer, M. Micro-engineered 3D scaffolds for cell culture studies. *Macromolecular bioscience* **12**, 1301-1314 (2012).
119 Liu, N., Zang, R., Yang, S. T. & Li, Y. Stem cell engineering in bioreactors for large-scale bioprocessing. *Engineering in Life Sciences* **14**, 4-15 (2014).
120 Li, H., Koenig, A. M., Sloan, P. & Leipzig, N. D. In vivo assessment of guided neural stem cell differentiation in growth factor immobilized chitosan-based hydrogel scaffolds. *Biomaterials* **35**, 9049-9057 (2014).
121 Borys, B. S. *et al.* Overcoming bioprocess bottlenecks in the large-scale expansion of high-quality hiPSC aggregates in vertical-wheel stirred suspension bioreactors. *Stem Cell Research & Therapy* **12**, 1-19 (2021).

122 Galderisi, U., Peluso, G. & Di Bernardo, G. Clinical trials based on mesenchymal stromal cells are exponentially increasing: where are we in recent years? *Stem Cell Reviews and Reports*, 1-14 (2021).
123 Karvelas, N., Bennett, S., Politis, G., Kouris, N.-I. & Kole, C. Advances in stem cell therapy in Alzheimer's disease: a comprehensive clinical trial review. *Stem Cell Investigation* **9** (2022).
124 Lv, Z.-Y., Li, Y. & Liu, J. Progress in clinical trials of stem cell therapy for cerebral palsy. *Neural Regeneration Research* **16**, 1377-1377 (2021).
125 Razeghian-Jahromi, I. *et al.* Surfing the clinical trials of mesenchymal stem cell therapy in ischemic cardiomyopathy. *Stem Cell Research & Therapy* **12**, 1-12 (2021).
126 Trounson, A. & McDonald, C. Stem cell therapies in clinical trials: progress and challenges. *Cell stem cell* **17**, 11-22 (2015).
127 Kretzmer, G. Influence of stress on adherent cells. *Influence of Stress on Cell Growth and Product Formation*, 123-137 (2000).
128 Jeon, K. J. *et al.* Combined effects of flow-induced shear stress and micropatterned surface morphology on neuronal differentiation of human mesenchymal stem cells. *Journal of bioscience and bioengineering* **117**, 242-247 (2014).
129 King, J. A. & Miller, W. M. Bioreactor development for stem cell expansion and controlled differentiation. *Current opinion in chemical biology* **11**, 394-398 (2007).
130 Lu, J. A novel hypothesis of blood-brain barrier (BBB) development and in vitro BBB model: neural stem cell is the driver of BBB formation and maintenance. *J Exp Integr Med* **2**, 39-43 (2012).
131 Olmer, R. *et al.* Suspension culture of human pluripotent stem cells in controlled, stirred bioreactors. *Tissue Engineering Part C: Methods* **18**, 772-784 (2012).
132 Sen, A., Kallos, M. S. & Behie, L. A. Effects of hydrodynamics on cultures of mammalian neural stem cell aggregates in suspension bioreactors. *Industrial & engineering chemistry research* **40**, 5350-5357 (2001).
133 Stevens, K. R., Pabon, L., Muskheli, V. & Murry, C. E. Scaffold-free human cardiac tissue patch created from embryonic stem cells. *Tissue engineering Part A* **15**, 1211-1222 (2009).
134 Velasco, S. *et al.* Individual brain organoids reproducibly form cell diversity of the human cerebral cortex. *Nature* **570**, 523-527 (2019).
135 Baghbaderani, B. A. *et al.* Expansion of human neural precursor cells in large-scale bioreactors for the treatment of neurodegenerative disorders. *Biotechnology progress* **24**, 859-870 (2008).
136 Nemati, S., Abbasalizadeh, S. & Baharvand, H. in *Bioreactors in Stem Cell Biology* 143-158 (Springer, 2015).
137 Simão, D. *et al.* in *Bioreactors in Stem Cell Biology* 129-142 (Springer, 2016).
138 Yan, Y., Song, L., Tsai, A.-C., Ma, T. & Li, Y. in *Bioreactors in Stem Cell Biology* 119-128 (Springer, 2015).
139 dos Santos, F. F., Andrade, P. Z., da Silva, C. L. & Cabral, J. M. S. Bioreactor design for clinical-grade expansion of stem cells. *Biotechnology journal* **8**, 644-654 (2013).
140 Rodrigues, C. A. V., Diogo, M. M., Da Silva, C. L. & Cabral, J. M. S. Microcarrier expansion of mouse embryonic stem cell-derived neural stem cells in stirred bioreactors. *Biotechnology and applied biochemistry* **58**, 231-242 (2011).

141 Skop, N. B., Calderon, F., Levison, S. W., Gandhi, C. D. & Cho, C. H. Heparin crosslinked chitosan microspheres for the delivery of neural stem cells and growth factors for central nervous system repair. *Acta Biomaterialia* **9**, 6834-6843 (2013).
142 Jeske, R. *et al.* Agitation in a microcarrier-based spinner flask bioreactor modulates homeostasis of human mesenchymal stem cells. *Biochemical engineering journal* **168**, 107947-107947 (2021).
143 Rogers, R. E. *et al.* A scalable system for generation of mesenchymal stem cells derived from induced pluripotent cells employing bioreactors and degradable microcarriers. *Stem Cells Translational Medicine* **10**, 1650-1665 (2021).
144 Tsai, A.-C., Liu, Y. & Ma, T. Expansion of human mesenchymal stem cells in fibrous bed bioreactor. *Biochemical Engineering Journal* **108**, 51-57 (2016).
145 Hammel, E. C., Ighodaro, O.-R. & Okoli, O. I. Processing and properties of advanced porous ceramics: An application based review. *Ceramics International* **40**, 15351-15370 (2014).
146 Guo, R. *et al.* Biomimetic 3D bacterial cellulose-graphene foam hybrid scaffold regulates neural stem cell proliferation and differentiation. *Colloids and Surfaces B: Biointerfaces* **200**, 111590-111590 (2021).
147 Lee, Y.-B. *et al.* Bio-printing of collagen and VEGF-releasing fibrin gel scaffolds for neural stem cell culture. *Experimental neurology* **223**, 645-652 (2010).
148 Moore, K. M. *et al.* Impact of composite scaffold degradation rate on neural stem cell persistence in the glioblastoma surgical resection cavity. *Materials Science and Engineering: C* **111**, 110846-110846 (2020).
149 Olson, H. E. *et al.* Neural stem cell–and schwann cell–loaded biodegradable polymer scaffolds support axonal regeneration in the transected spinal cord. *Tissue Engineering Part A* **15**, 1797-1805 (2009).
150 Purcell, E. K., Singh, A. & Kipke, D. R. Alginate composition effects on a neural stem cell–seeded scaffold. *Tissue Engineering Part C: Methods* **15**, 541-550 (2009).
151 Sheets, K. T. *et al.* Developing implantable scaffolds to enhance neural stem cell therapy for post-operative glioblastoma. *Molecular Therapy* **28**, 1056-1067 (2020).
152 Stevanato, L. & Sinden, J. D. The effects of microRNAs on human neural stem cell differentiation in two- and three-dimensional cultures. *Stem Cell Research & Therapy* **5**, 49 (2014). https://doi.org/10.1186/scrt437
153 Ahmed, S. & Ikram, S. Chitosan based scaffolds and their applications in wound healing. *Achievements in the life sciences* **10**, 27-37 (2016).
154 Bhattarai, N., Gunn, J. & Zhang, M. Chitosan-based hydrogels for controlled, localized drug delivery. *Advanced drug delivery reviews* **62**, 83-99 (2010).
155 Neubrech, F. *et al.* Enhancing the outcome of traumatic sensory nerve lesions of the hand by additional use of a chitosan nerve tube in primary nerve repair: a randomized controlled bicentric trial. *Plastic and reconstructive surgery* **142**, 415-424 (2018).
156 Böcker, A., Däschler, S. C., Kneser, U. & Harhaus, L. Relevance and recent developments of chitosan in peripheral nerve surgery. *Frontiers in cellular neuroscience* **13**, 104-104 (2019).
157 Dietzmeyer, N., Förthmann, M., Grothe, C. & Haastert-Talini, K. Modification of tubular chitosan-based peripheral nerve implants: Applications for simple or more complex approaches. *Neural Regeneration Research* **15**, 1421-1421 (2020).

158 Kourgiantaki, A. *et al.* Neural stem cell delivery via porous collagen scaffolds promotes neuronal differentiation and locomotion recovery in spinal cord injury. *NPJ Regenerative medicine* **5**, 12-12 (2020).
159 Li, X. *et al.* Cetuximab modified collagen scaffold directs neurogenesis of injury-activated endogenous neural stem cells for acute spinal cord injury repair. *Biomaterials* **137**, 73-86 (2017).
160 Zou, Y. *et al.* Aligned collagen scaffold combination with human spinal cord-derived neural stem cells to improve spinal cord injury repair. *Biomaterials Science* **8**, 5145-5156 (2020).
161 Moore, L., Skop, N. B., Rothbard, D. E., Corrubia, L. R. & Levison, S. W. Tethered growth factors on biocompatible scaffolds improve stemness of cultured rat and human neural stem cells and growth of oligodendrocyte progenitors. *Methods* **133**, 54-64 (2018).
162 Sood, D. *et al.* Functional maturation of human neural stem cells in a 3D bioengineered brain model enriched with fetal brain-derived matrix. *Scientific reports* **9**, 1-15 (2019).
163 Zheng, K. *et al.* Basic fibroblast growth factor promotes human dental pulp stem cells cultured in 3D porous chitosan scaffolds to neural differentiation. *International Journal of Neuroscience* **131**, 625-633 (2021).
164 O'Rourke, C. *et al.* An allogeneic 'off the shelf'therapeutic strategy for peripheral nerve tissue engineering using clinical grade human neural stem cells. *Scientific reports* **8**, 1-11 (2018).
165 Chang, P.-H., Chao, H.-M., Chern, E. & Hsu, S.-h. Chitosan 3D cell culture system promotes naïve-like features of human induced pluripotent stem cells: A novel tool to sustain pluripotency and facilitate differentiation. *Biomaterials* **268**, 120575 (2021).
166 Indrani, D. J., Lukitowati, F. & Yulizar, Y. in *IOP Conference Series: Materials Science and Engineering.*1 edn 012020-012020 (IOP Publishing).
167 Ren, L. *et al.* Preparation and characterization of porous chitosan microspheres and adsorption performance for hexavalent chromium. *International journal of biological macromolecules* **135**, 898-906 (2019).
168 Fernandez-Megia, E., Novoa-Carballal, R., Quiñoá, E. & Riguera, R. Optimal routine conditions for the determination of the degree of acetylation of chitosan by 1H-NMR. *Carbohydrate polymers* **61**, 155-161 (2005).
169 Pereira, A. G. B., Muniz, E. C. & Hsieh, Y.-L. 1H NMR and 1H–13C HSQC surface characterization of chitosan–chitin sheath-core nanowhiskers. *Carbohydrate polymers* **123**, 46-52 (2015).
170 Gonzalez Badillo, F. *et al.* Tissue-Engineered Stromal Reticula to Study Lymph Node Fibroblastic Reticular Cells in Type I Diabetes. *Cellular and molecular bioengineering* **13**, 419-434 (2020).
171 Laiva, A. L., O'Brien, F. J. & Keogh, M. B. SDF-1α gene-activated collagen scaffold restores pro-angiogenic wound healing features in human diabetic adipose-derived stem cells. *Biomedicines* **9**, 160-160 (2021).
172 Ryan, A. J. & O'Brien, F. J. Insoluble elastin reduces collagen scaffold stiffness, improves viscoelastic properties, and induces a contractile phenotype in smooth muscle cells. *Biomaterials* **73**, 296-307 (2015).
173 Xin, L. *et al.* A collagen scaffold loaded with human umbilical cord-derived mesenchymal stem cells facilitates endometrial regeneration and restores fertility. *Acta biomaterialia* **92**, 160-171 (2019).

174 Ikada, Y. Challenges in tissue engineering. *Journal of the Royal Society Interface* **3**, 589-601 (2006).
175 Trung, T. S., Thein-Han, W. W., Qui, N. T., Ng, C.-H. & Stevens, W. F. Functional characteristics of shrimp chitosan and its membranes as affected by the degree of deacetylation. *Bioresource technology* **97**, 659-663 (2006).
176 Zhang, R. *et al.* Application of chitosan with different molecular weights in cartilage tissue engineering. *Carbohydrate Polymers*, 120890-120890 (2023).
177 Daugherty, A. M., Schwarb, H. D., McGarry, M. D. J., Johnson, C. L. & Cohen, N. J. Magnetic resonance elastography of human hippocampal subfields: CA3-dentate gyrus viscoelasticity predicts relational memory accuracy. *Journal of cognitive neuroscience* **32**, 1704-1713 (2020).
178 Iwashita, M. *et al.* Comparative analysis of brain stiffness among amniotes using glyoxal fixation and atomic force microscopy. *Frontiers in cell and developmental biology* **8**, 574619-574619 (2020).
179 Donzelli, E. *et al.* Mesenchymal stem cells cultured on a collagen scaffold: In vitro osteogenic differentiation. *Archives of oral biology* **52**, 64-73 (2007).
180 Muzzarelli, R. A. A., El Mehtedi, M., Bottegoni, C., Aquili, A. & Gigante, A. Genipin-crosslinked chitosan gels and scaffolds for tissue engineering and regeneration of cartilage and bone. *Marine drugs* **13**, 7314-7338 (2015).
181 Schneider, G. B. *et al.* The effect of hydrogel charge density on cell attachment. *Biomaterials* **25**, 3023-3028 (2004). https://doi.org/10.1016/j.biomaterials.2003.09.084
182 Pottmeier, P., Doszyn, O., Peuckert, C. & Jazin, E. Increased expression of Y-encoded demethylases during differentiation of human male neural stem cells. *Stem Cells and Development* **29**, 1497-1509 (2020).
183 Liu, D. *et al.* Coating Materials for Neural Stem/Progenitor Cell Culture and Differentiation. *Stem Cells and Development* **29**, 463-474 (2020). https://doi.org/10.1089/scd.2019.0288
184 Wang, Q. *et al.* Magnetic lanthanum-doped hydroxyapatite/chitosan scaffolds with endogenous stem cell-recruiting and immunomodulatory properties for bone regeneration. *Journal of Materials Chemistry B* **8**, 5280-5292 (2020).
185 Amiryaghoubi, N., Pesyan, N. N., Fathi, M. & Omidi, Y. Injectable thermosensitive hybrid hydrogel containing graphene oxide and chitosan as dental pulp stem cells scaffold for bone tissue engineering. *International journal of biological macromolecules* **162**, 1338-1357 (2020).
186 Agrawal, P. *et al.* Enhanced chondrogenesis of mesenchymal stem cells over silk fibroin/chitosan-chondroitin sulfate three dimensional scaffold in dynamic culture condition. *Journal of Biomedical Materials Research Part B: Applied Biomaterials* **106**, 2576-2587 (2018).
187 Bhaskar, B., Owen, R., Bahmaee, H., Rao, P. S. & Reilly, G. C. Design and assessment of a dynamic perfusion bioreactor for large bone tissue engineering scaffolds. *Applied biochemistry and biotechnology* **185**, 555-563 (2018).
188 Kanwar, S. & Vijayavenkataraman, S. Design of 3D printed scaffolds for bone tissue engineering: A review. *Bioprinting* **24**, e00167 (2021).
189 Chen, C.-H., Kuo, C.-Y. & Chen, J.-P. Effect of cyclic dynamic compressive loading on chondrocytes and adipose-derived stem cells co-cultured in highly elastic cryogel scaffolds. *International Journal of Molecular Sciences* **19**, 370 (2018).

190 Noroozi, R. *et al.* In vitro static and dynamic cell culture study of novel bone scaffolds based on 3D-printed PLA and cell-laden alginate hydrogel. *Biomedical Materials* **17**, 045024 (2022).
191 Puwanun, S. *et al.* A simple rocker-induced mechanical stimulus upregulates mineralization by human osteoprogenitor cells in fibrous scaffolds. *Journal of tissue engineering and regenerative medicine* **12**, 370-381 (2018).
192 Nguyen, T. D., Kadri, O. E., Sikavitsas, V. I. & Voronov, R. S. Scaffolds with a High Surface Area-to-Volume Ratio and Cultured Under Fast Flow Perfusion Result in Optimal O2 Delivery to the Cells in Artificial Bone Tissues. *Applied Sciences* **9**, 2381 (2019).
193 Pasini, A. *et al.* Perfusion flow enhances viability and migratory phenotype in 3D-cultured breast cancer cells. *Annals of Biomedical Engineering* **49**, 2103-2113 (2021).
194 Patel, D. B., Luthers, C. R., Lerman, M. J., Fisher, J. P. & Jay, S. M. Enhanced extracellular vesicle production and ethanol-mediated vascularization bioactivity via a 3D-printed scaffold-perfusion bioreactor system. *Acta biomaterialia* **95**, 236-244 (2019).
195 Athira, R. K. *et al.* Hydroxyapatite cages with aligned pores for bone grafting–Seeding of human osteoblast-like cells in vitro and their response in dynamic culture mode. *Ceramics International* **47**, 30051-30060 (2021).
196 Chen, H.-C. & Hu, Y.-C. Bioreactors for tissue engineering. *Biotechnology letters* **28**, 1415-1423 (2006).
197 Chen, L., Yang, Y., Ueno, H. & Esch, M. B. Body-in-a-cube: a microphysiological system for multi-tissue co-culture with near-physiological amounts of blood surrogate. *Microphysiological systems* **4** (2020).
198 Rodriguez-Granrose, D. *et al.* Transition from static culture to stirred tank bioreactor for the allogeneic production of therapeutic discogenic cell spheres. *Stem cell research & therapy* **12**, 1-14 (2021).
199 He, L. *et al.* Increased proliferation and adhesion properties of human dental pulp stem cells in PLGA scaffolds via simulated microgravity. *International Endodontic Journal* **49**, 161-173 (2016).
200 Li, Y. *et al.* Three-dimensional simulated microgravity culture improves the proliferation and odontogenic differentiation of dental pulp stem cell in PLGA scaffolds implanted in mice. *Molecular medicine reports* **15**, 873-878 (2017).
201 Varley, M. C., Markaki, A. E. & Brooks, R. A. Effect of rotation on scaffold motion and cell growth in rotating bioreactors. *Tissue Engineering Part A* **23**, 522-534 (2017).
202 Chen, H. J., Miller, P. & Shuler, M. L. A pumpless body-on-a-chip model using a primary culture of human intestinal cells and a 3D culture of liver cells. *Lab on a Chip* **18**, 2036-2046 (2018).
203 He, H. *et al.* Dynamic formation of cellular aggregates of chondrocytes and mesenchymal stem cells in spinner flask. *Cell proliferation* **52**, e12587 (2019).
204 Rödling, L. *et al.* Magnetic macroporous hydrogels as a novel approach for perfused stem cell culture in 3D scaffolds via contactless motion control. *Advanced Healthcare Materials* **7**, 1701403 (2018).
205 Schmid, J. *et al.* A perfusion bioreactor system for cell seeding and oxygen-controlled cultivation of three-dimensional cell cultures. *Tissue Engineering Part C: Methods* **24**, 585-595 (2018).

206 Show, K.-Y., Lee, D.-J. & Chang, J.-S. Bioreactor and process design for biohydrogen production. *Bioresource technology* **102**, 8524-8533 (2011).
207 YekrangSafakar, A., Hamel, K. M., Mehrnezhad, A., Jung, J. P. & Park, K. Development of rolled scaffold for high-density adherent cell culture. *Biomedical microdevices* **22**, 1-10 (2020).
208 Martin, I., Smith, T. & Wendt, D. Bioreactor-based roadmap for the translation of tissue engineering strategies into clinical products. *Trends in biotechnology* **27**, 495-502 (2009).
209 Wendt, D., Riboldi, S. A., Cioffi, M. & Martin, I. Potential and bottlenecks of bioreactors in 3D cell culture and tissue manufacturing. *Advanced materials* **21**, 3352-3367 (2009).
210 Hjelmeland, A. B. *et al.* Acidic stress promotes a glioma stem cell phenotype. *Cell Death & Differentiation* **18**, 829-840 (2011).
211 Antoni, D., Burckel, H., Josset, E. & Noel, G. Three-dimensional cell culture: a breakthrough in vivo. *International journal of molecular sciences* **16**, 5517-5527 (2015).
212 Stoppel, W. L., Kaplan, D. L. & Black Iii, L. D. Electrical and mechanical stimulation of cardiac cells and tissue constructs. *Advanced drug delivery reviews* **96**, 135-155 (2016).
213 Wang, T. *et al.* Programmable mechanical stimulation influences tendon homeostasis in a bioreactor system. *Biotechnology and bioengineering* **110**, 1495-1507 (2013).
214 Raimondi, M. T., Giordano, C. & Pietrabissa, R. Oxygen measurement in interstitially perfused cellularized constructs cultured in a miniaturized bioreactor. *Journal of Applied Biomaterials & Functional Materials* **13**, 313-319 (2015).
215 Seddiqi, H. *et al.* Inlet flow rate of perfusion bioreactors affects fluid flow dynamics, but not oxygen concentration in 3D-printed scaffolds for bone tissue engineering: computational analysis and experimental validation. *Computers in Biology and Medicine* **124**, 103826 (2020).
216 Kondaveeti, H. K., Kumaravelu, N. K., Vanambathina, S. D., Mathe, S. E. & Vappangi, S. A systematic literature review on prototyping with Arduino: Applications, challenges, advantages, and limitations. *Computer Science Review* **40**, 100364 (2021).
217 Morgunova, G. V., Klebanov, A. A., Marotta, F. & Khokhlov, A. N. Culture medium pH and stationary phase/chronological aging of different cells. *Moscow University Biological Sciences Bulletin* **72**, 47-51 (2017).
218 Lee, J. T. Y. *et al.* Cell culture medium as an alternative to conventional simulated body fluid. *Acta Biomaterialia* **7**, 2615-2622 (2011).
219 Bahsoun, S., Coopman, K., Forsyth, N. R. & Akam, E. C. The role of dissolved oxygen levels on human mesenchymal stem cell culture success, regulatory compliance, and therapeutic potential. *Stem Cells and Development* **27**, 1303-1321 (2018).
220 Kagawa, Y., Matsuura, K., Shimizu, T. & Tsuneda, S. Direct measurement of local dissolved oxygen concentration spatial profiles in a cell culture environment. *Biotechnology and Bioengineering* **112**, 1263-1274 (2015).
221 Drljača, J. *et al.* Diazepam diminishes temozolomide efficacy in the treatment of U87 glioblastoma cell line. *CNS Neuroscience & Therapeutics* **28**, 1447-1457 (2022).
222 Rafazi, P., Bagheri, Z., Haghi-Aminjan, H., Rahimifard, M. & Ahvaraki, A. Long-term exposure of human U87 glioblastoma cells to polyethylene microplastics: Investigating the potential cancer progression. *Toxicology Reports* **13**, 101757 (2024).
223 Sengul, E., Sharbati, P., Elitas, M., Islam, M. & Korvink, J. G. Analysis of U87 glioma cells by dielectrophoresis. *Electrophoresis* **43**, 1357-1365 (2022).

224 Nakase, I. *et al.* Environmental pH stress influences cellular secretion and uptake of extracellular vesicles. *FEBS Open bio* **11**, 753-767 (2021).
225 Cai, X., Luo, Y., Zhang, W., Du, D. & Lin, Y. pH-Sensitive ZnO quantum dots–doxorubicin nanoparticles for lung cancer targeted drug delivery. *ACS applied materials & interfaces* **8**, 22442-22450 (2016).
226 Widmer, D. S. *et al.* Hypoxia contributes to melanoma heterogeneity by triggering HIF1α-dependent phenotype switching. *Journal of Investigative Dermatology* **133**, 2436-2443 (2013).
227 Michl, J., Park, K. C. & Swietach, P. Evidence-based guidelines for controlling pH in mammalian live-cell culture systems. *Communications biology* **2**, 144 (2019).
228 Li, W. *et al.* Responses of cellular adhesion strength and stiffness to fluid shear stress during tumor cell rolling motion. *ACS sensors* **4**, 1710-1715 (2019).
229 Costariol, E. Establishing a scalable manufacturing process for the clinical scale production of CAR-T cell therapies in stirred-tank bioreactors. (2021).
230 Sin, W.-X. *et al.* A high-density microfluidic bioreactor for the automated manufacturing of CAR T cells. *Nature Biomedical Engineering*, 1-21 (2024).
231 Vieira, M. S. *et al.* Neural stem cell differentiation into mature neurons: Mechanisms of regulation and biotechnological applications. *Biotechnology Advances* **36**, 1946-1970 (2018). https://doi.org/https://doi.org/10.1016/j.biotechadv.2018.08.002
232 Ottoboni, L., Wunster, B. v. & Martino, G. (2020).
233 Mehta, S. R. *et al.* Human Huntington's disease iPSC-derived cortical neurons display altered transcriptomics, morphology, and maturation. *Cell reports* **25**, 1081-1096. e1086 (2018).
234 Yu, C. *et al.* Decreased BDNF release in cortical neurons of a knock-in mouse model of Huntington's disease. *Scientific reports* **8**, 16976 (2018).
235 Ranjan, V. D. *et al.* A microfiber scaffold-based 3D in vitro human neuronal culture model of Alzheimer's disease. *Biomaterials Science* **8**, 4861-4874 (2020).
236 Horne, M. K., Nisbet, D. R., Forsythe, J. S. & Parish, C. L. Three-dimensional nanofibrous scaffolds incorporating immobilized BDNF promote proliferation and differentiation of cortical neural stem cells. *Stem Cells and Development* **19**, 843-853 (2010). https://doi.org/10.1089/scd.2009.0158
237 Muratore, C. R., Srikanth, P., Callahan, D. G. & Young-Pearse, T. L. Comparison and optimization of hiPSC forebrain cortical differentiation protocols. *PLoS One* **9**, e105807 (2014).
238 Park, J. *et al.* A 3D Human Tri-Culture System Modeling Neurodegeneration and Neuroinflammation in Alzheimer's Disease. *Nature neuroscience* **21**, 941-951 (2018). https://doi.org/10.1038/s41593-018-0175-4
239 Kapałczyńska, M. *et al.* 2D and 3D cell cultures–a comparison of different types of cancer cell cultures. *Archives of medical science* **14**, 910-919 (2018).
240 Fontoura, J. C. *et al.* Comparison of 2D and 3D cell culture models for cell growth, gene expression and drug resistance. *Materials Science and Engineering: C* **107**, 110264 (2020).
241 Knight, E. & Przyborski, S. Advances in 3D cell culture technologies enabling tissue-like structures to be created in vitro. *Journal of anatomy* **227**, 746-756 (2015).

242 Tomaskovic-Crook, E. *et al.* Human neural tissues from neural stem cells using conductive biogel and printed polymer microelectrode arrays for 3D electrical stimulation. *Advanced healthcare materials* **8**, 1900425 (2019).
243 Aisenbrey, E. A. & Murphy, W. L. Synthetic alternatives to Matrigel. *Nature Reviews Materials* **5**, 539-551 (2020). https://doi.org/10.1038/s41578-020-0199-8
244 Lee, H. & Kim, G. Cryogenically fabricated three-dimensional chitosan scaffolds with pore size-controlled structures for biomedical applications. *Carbohydrate Polymers* **85**, 817-823 (2011). https://doi.org/10.1016/j.carbpol.2011.04.001
245 Levental, I., Georges, P. C. & Janmey, P. A. Soft biological materials and their impact on cell function. *Soft Matter* **3**, 299-306 (2007). https://doi.org/10.1039/b610522j
246 Shin, J. E. *et al.* Brain and spinal cord injury repair by implantation of human neural progenitor cells seeded onto polymer scaffolds. *Experimental & molecular medicine* **50**, 1-18 (2018).
247 Song, S. *et al.* Controlling properties of human neural progenitor cells using 2D and 3D conductive polymer scaffolds. *Scientific Reports* **9**, 19565 (2019).
248 Liang, J., Guo, Z., Timmerman, A., Grijpma, D. & Poot, A. Enhanced mechanical and cell adhesive properties of photo-crosslinked PEG hydrogels by incorporation of gelatin in the networks. *Biomedical Materials* **14**, 024102 (2019).
249 Jin, K. *et al.* Transplantation of human neural precursor cells in Matrigel scaffolding improves outcome from focal cerebral ischemia after delayed postischemic treatment in rats. *Journal of Cerebral Blood Flow & Metabolism* **30**, 534-544 (2010).
250 Nierode, G. J. *et al.* High-throughput identification of factors promoting neuronal differentiation of human neural progenitor cells in microscale 3D cell culture. *Biotechnology and bioengineering* **116**, 168-180 (2019).
251 Jaworska, M., Sakurai, K., Gaudon, P. & Guibal, E. Influence of chitosan characteristics on polymer properties. I: Crystallographic properties. *Polymer International* **52**, 198-205 (2003). https://doi.org/https://doi.org/10.1002/pi.1159
252 Liu, Z. *et al.* Effects of chitosan molecular weight and degree of deacetylation on the properties of gelatine-based films. *Food Hydrocolloids* **26**, 311-317 (2012). https://doi.org/https://doi.org/10.1016/j.foodhyd.2011.06.008
253 Kaczmarek, H. & Zawadzki, J. Chitosan pyrolysis and adsorption properties of chitosan and its carbonizate. *Carbohydrate Research* **345**, 941-947 (2010). https://doi.org/https://doi.org/10.1016/j.carres.2010.02.024
254 Rodrigues, S., Dionísio, M., López, C. R. & Grenha, A. Biocompatibility of chitosan carriers with application in drug delivery. *Journal of functional biomaterials* **3**, 615-641 (2012).
255 Younes, I. & Rinaudo, M. Chitin and Chitosan Preparation from Marine Sources. Structure, Properties and Applications. *Marine Drugs* **13**, 1133-1174 (2015). https://doi.org/10.3390/md13031133
256 Ehtesabi, H. & Massah, F. Improvement of hydrophilicity and cell attachment of polycaprolactone scaffolds using green synthesized carbon dots. *Materials Today Sustainability* **13**, 100075 (2021). https://doi.org/10.1016/j.mtsust.2021.100075
257 Kim, C.-H., Park, S. J., Yang, D. H. & Chun, H. J. Chitosan for tissue engineering. *Novel biomaterials for regenerative medicine*, 475-485 (2018).
258 Maeng, Y.-J., Choi, S.-W., Kim, H. O. & Kim, J.-H. Culture of human mesenchymal stem cells using electrosprayed porous chitosan microbeads. *Journal of Biomedical*

Materials Research Part A: An Official Journal of The Society for Biomaterials, The Japanese Society for Biomaterials, and The Australian Society for Biomaterials and the Korean Society for Biomaterials **92**, 869-876 (2010).
259 Li, Y., Wang, X., Wei, Y. & Tao, L. Chitosan-based self-healing hydrogel for bioapplications. *Chinese Chemical Letters* **28**, 2053-2057 (2017). https://doi.org/https://doi.org/10.1016/j.cclet.2017.09.004
260 Gu, Q. *et al.* Functional 3D neural mini-tissues from printed gel-based bioink and human neural stem cells. *Advanced healthcare materials* **5**, 1429-1438 (2016).
261 Feng, X. *et al.* 3D porous chitosan scaffolds suit survival and neural differentiation of dental pulp stem cells. *Cellular and molecular neurobiology* **34**, 859-870 (2014).
262 Cordella, F. *et al.* Human iPSC-Derived Cortical Neurons Display Homeostatic Plasticity. *Life* **12**, 1884 (2022).
263 Kondo, T. *et al.* iPSC-based compound screening and in vitro trials identify a synergistic anti-amyloid β combination for Alzheimer's disease. *Cell reports* **21**, 2304-2312 (2017).
264 Sison, S. L., Vermilyea, S. C., Emborg, M. E. & Ebert, A. D. Using patient-derived induced pluripotent stem cells to identify Parkinson's disease-relevant phenotypes. *Current neurology and neuroscience reports* **18**, 1-14 (2018).
265 Verheijen, M. C. T. *et al.* iPSC-derived cortical neurons to study sporadic Alzheimer disease: A transcriptome comparison with post-mortem brain samples. *Toxicology Letters* **356**, 89-99 (2022).
266 Muratore, C. R. *et al.* The familial Alzheimer's disease APPV717I mutation alters APP processing and Tau expression in iPSC-derived neurons. *Human molecular genetics* **23**, 3523-3536 (2014).
267 Pomeshchik, Y. *et al.* Human iPSC-derived hippocampal spheroids: an innovative tool for stratifying Alzheimer disease patient-specific cellular phenotypes and developing therapies. *Stem Cell Reports* **15**, 256-273 (2020).
268 Knoepfler, P. S. Deconstructing Stem Cell Tumorigenicity: A Roadmap to Safe Regenerative Medicine. *Stem Cells (Dayton, Ohio)* **27**, 1050-1056 (2009). https://doi.org/10.1002/stem.37
269 Gutierrez-Aranda, I. *et al.* Human Induced Pluripotent Stem Cells Develop Teratoma More Efficiently and Faster Than Human Embryonic Stem Cells Regardless the Site of Injection. *Stem Cells* **28**, 1568-1570 (2010). https://doi.org/10.1002/stem.471
270 Ben-David, U. & Benvenisty, N. The tumorigenicity of human embryonic and induced pluripotent stem cells. *Nature Reviews Cancer* **11**, 268-277 (2011). https://doi.org/10.1038/nrc3034
271 Hu, B.-Y. *et al.* Neural differentiation of human induced pluripotent stem cells follows developmental principles but with variable potency. *Proceedings of the National Academy of Sciences* **107**, 4335-4340 (2010). https://doi.org/10.1073/pnas.0910012107
272 Chen, S. *et al.* Fast transformation of 2D nanofiber membranes into pre-molded 3D scaffolds with biomimetic and oriented porous structure for biomedical applications. *Applied Physics Reviews* **7**, 021406 (2020).
273 Nicholas, C. R. *et al.* Functional maturation of hPSC-derived forebrain interneurons requires an extended timeline and mimics human neural development. *Cell stem cell* **12**, 573-586 (2013).
274 O'Brien, L. C., Keeney, P. M. & Bennett, J. P. Differentiation of Human Neural Stem Cells into Motor Neurons Stimulates Mitochondrial Biogenesis and Decreases Glycolytic

Flux. *Stem Cells and Development* **24**, 1984-1994 (2015). https://doi.org/10.1089/scd.2015.0076

275 Alisch, M. *et al.* Identification of the gliogenic state of human neural stem cells to optimize in vitro astrocyte differentiation. *Journal of Neuroscience Methods* **361**, 109284 (2021). https://doi.org/https://doi.org/10.1016/j.jneumeth.2021.109284

276 Tamura, A., HAYASHI, S., Watanabe, I., NAGAYAMA, K. & Matsumoto, T. Mechanical characterization of brain tissue in high-rate compression. *Journal of biomechanical science and engineering* **2**, 115-126 (2007).

277 Aurand, E. R., Wagner, J., Lanning, C. & Bjugstad, K. B. Building biocompatible hydrogels for tissue engineering of the brain and spinal cord. *Journal of functional biomaterials* **3**, 839-863 (2012).

278 Franze, K., Janmey, P. A. & Guck, J. Mechanics in neuronal development and repair. *Annual review of biomedical engineering* **15**, 227-251 (2013).

279 Srimasorn, S. *et al.* Increased Neuronal Differentiation Efficiency in High Cell Density-Derived Induced Pluripotent Stem Cells. *Stem cells international* **2019**, 2018784 (2019).

280 Mercurio, S., Serra, L. & Nicolis, S. K. More than just Stem Cells: Functional Roles of the Transcription Factor Sox2 in Differentiated Glia and Neurons. *International Journal of Molecular Sciences* **20**, 4540 (2019). https://doi.org/10.3390/ijms20184540

281 Bertolini, J. A. *et al.* Mapping the Global Chromatin Connectivity Network for Sox2 Function in Neural Stem Cell Maintenance. *Cell Stem Cell* **24**, 462-476.e466 (2019). https://doi.org/10.1016/j.stem.2019.02.004

282 Capobianco, D. L. *et al.* Human neural stem cells derived from fetal human brain communicate with each other and rescue ischemic neuronal cells through tunneling nanotubes. *Cell Death & Disease* **15** (2024). https://doi.org/10.1038/s41419-024-07005-w

283 Englund, U., Björklund, A. & Wictorin, K. Migration patterns and phenotypic differentiation of long-term expanded human neural progenitor cells after transplantation into the adult rat brain. *Developmental Brain Research* **134**, 123-141 (2002).

284 Islam, M. O. *et al.* Characterization of ABC transporter ABCB1 expressed in human neural stem/progenitor cells. *FEBS letters* **579**, 3473-3480 (2005).

285 Manent, J.-B., Wang, Y., Chang, Y., Paramasivam, M. & LoTurco, J. J. Dcx reexpression reduces subcortical band heterotopia and seizure threshold in an animal model of neuronal migration disorder. *Nature Medicine* **15**, 84-90 (2009). https://doi.org/10.1038/nm.1897

286 Li, H.-L. *et al.* The Effect of Amino Density on the Attachment, Migration, and Differentiation of Rat Neural Stem Cells *In Vitro*. *Molecules and Cells* **35**, 436-443 (2013). https://doi.org/10.1007/s10059-013-0046-5

287 Pevny, L. H. & Nicolis, S. K. Sox2 roles in neural stem cells. *The international journal of biochemistry & cell biology* **42**, 421-424 (2010).

288 Hevner, R. F. *et al.* Tbr1 Regulates Differentiation of the Preplate and Layer 6. *Neuron* **29**, 353-366 (2001). https://doi.org/10.1016/s0896-6273(01)00211-2

289 Forbes, L. H. & Andrews, M. R. Grafted human iPSC-derived neural progenitor cells express integrins and extend long-distance axons within the developing corticospinal tract. *Frontiers in Cellular Neuroscience* **13**, 26 (2019).

290 Hwang, D. H. *et al.* Transplantation of human neural stem cells transduced with Olig2 transcription factor improves locomotor recovery and enhances myelination in the white matter of rat spinal cord following contusive injury. *BMC neuroscience* **10**, 1-16 (2009).
291 Lutz, A.-K. *et al.* SHANK2 Mutations Result in Dysregulation of the ERK1/2 Pathway in Human Induced Pluripotent Stem Cells-Derived Neurons and Shank2 (−/−) Mice. *Frontiers in Molecular Neuroscience* **14** (2021).
292 Limbad, C. *et al.* Astrocyte senescence promotes glutamate toxicity in cortical neurons. *PLOS ONE* **15**, e0227887 (2020). https://doi.org/10.1371/journal.pone.0227887
293 Khatir, I. *et al.* Decoupling of mRNA and Protein Expression in Aging Brains Reveals the Age-Dependent Adaptation of Specific Gene Subsets. *Cells* **12**, 615 (2023). https://doi.org/10.3390/cells12040615
294 Buck, S. A. *et al.* Aging disrupts the coordination between mRNA and protein expression in mouse and human midbrain. *bioRxiv*, 2024.2006.2001.596950 (2024). https://doi.org/10.1101/2024.06.01.596950
295 Sansom, S. N. *et al.* The level of the transcription factor Pax6 is essential for controlling the balance between neural stem cell self-renewal and neurogenesis. *PLoS genetics* **5**, e1000511 (2009).
296 2021 Alzheimer's disease facts and figures. *Alzheimer's & Dementia* **17**, 327-406 (2021). https://doi.org/10.1002/alz.12328
297 Cummings, J., Lee, G., Zhong, K., Fonseca, J. & Taghva, K. Alzheimer's disease drug development pipeline: 2021. *Alzheimer's & dementia (New York, N. Y.)* **7**, e12179 (2021). https://doi.org/10.1002/trc2.12179
298 SL, M., KD, K., JQ, X. & E., A. Mortality in the United States, 2020. *National Center for Health Statistics. 2021* (2021). https://doi.org/10.15620/cdc:112079
299 Veugelen, S., Saito, T., Saido, T. C., Chávez-Gutiérrez, L. & Strooper, B. D. Familial Alzheimer's Disease Mutations in Presenilin Generate Amyloidogenic Aβ Peptide Seeds. *Neuron* **90**, 410-416 (2016). https://doi.org/10.1016/j.neuron.2016.03.010
300 Kametani, F. & Hasegawa, M. Reconsideration of Amyloid Hypothesis and Tau Hypothesis in Alzheimer's Disease. *Frontiers in Neuroscience* **12**, 25 (2018). https://doi.org/10.3389/fnins.2018.00025
301 Kwart, D. *et al.* A Large Panel of Isogenic APP and PSEN1 Mutant Human iPSC Neurons Reveals Shared Endosomal Abnormalities Mediated by APP β-CTFs, Not Aβ. *Neuron* **104**, 256-270.e255 (2019). https://doi.org/10.1016/j.neuron.2019.07.010
302 Karran, E. & Strooper, B. D. The amyloid hypothesis in Alzheimer disease: new insights from new therapeutics. *Nature Reviews Drug Discovery* **21**, 306-318 (2022). https://doi.org/10.1038/s41573-022-00391-w
303 Cummings, J., Feldman, H. H. & Scheltens, P. The "rights" of precision drug development for Alzheimer's disease. *Alzheimer's research & therapy* **11**, 76 (2019). https://doi.org/10.1186/s13195-019-0529-5
304 D'Souza, G. X. *et al.* The application of in vitro-derived human neurons in neurodegenerative disease modeling. *Journal of neuroscience research* **99**, 124-140 (2020). https://doi.org/10.1002/jnr.24615
305 Drummond, E. & Wisniewski, T. Alzheimer's disease: experimental models and reality. *Acta Neuropathologica* **133**, 155-175 (2016). https://doi.org/10.1007/s00401-016-1662-x

306 Vitek, M. P. *et al.* Translational animal models for Alzheimer's disease: An Alzheimer's Association Business Consortium Think Tank. *Alzheimer's & dementia (New York, N. Y.)* **6**, e12114 (2020). https://doi.org/10.1002/trc2.12114
307 Yagi, T. *et al.* Modeling familial Alzheimer's disease with induced pluripotent stem cells. *Human molecular genetics* **20**, 4530-4539 (2011). https://doi.org/10.1093/hmg/ddr394
308 Penney, J., Ralvenius, W. T. & Tsai, L.-H. Modeling Alzheimer's disease with iPSC-derived brain cells. *Molecular Psychiatry* **25**, 148-167 (2020). https://doi.org/10.1038/s41380-019-0468-3
309 Sivandzade, F. & Cucullo, L. Regenerative Stem Cell Therapy for Neurodegenerative Diseases: An Overview. *International Journal of Molecular Sciences* **22**, 2153 (2021). https://doi.org/10.3390/ijms22042153
310 Si, Z. & Wang, X. Stem Cell Therapies in Alzheimer's Disease: Applications for Disease Modeling. *Journal of Pharmacology and Experimental Therapeutics* **377**, 207-217 (2021). https://doi.org/10.1124/jpet.120.000324
311 Sproul, A. A. *et al.* Characterization and molecular profiling of PSEN1 familial Alzheimer's disease iPSC-derived neural progenitors. *PloS one* **9**, e84547 (2014). https://doi.org/10.1371/journal.pone.0084547
312 Alsanie, W. F. *et al.* Generating homogenous cortical preplate and deep-layer neurons using a combination of 2D and 3D differentiation cultures. *Scientific Reports* **10**, 6272 (2020). https://doi.org/10.1038/s41598-020-62925-9
313 Paşca, A. M. *et al.* Functional cortical neurons and astrocytes from human pluripotent stem cells in 3D culture. *Nature methods* **12**, 671-678 (2015). https://doi.org/10.1038/nmeth.3415
314 Raja, W. K. *et al.* Self-Organizing 3D Human Neural Tissue Derived from Induced Pluripotent Stem Cells Recapitulate Alzheimer's Disease Phenotypes. *PloS one* **11**, e0161969 (2016). https://doi.org/10.1371/journal.pone.0161969
315 Rigamonti, A. *et al.* Large-Scale Production of Mature Neurons from Human Pluripotent Stem Cells in a Three-Dimensional Suspension Culture System. *Stem cell reports* **6**, 993-1008 (2016). https://doi.org/10.1016/j.stemcr.2016.05.010
316 Leeuw, S. d. & Tackenberg, C. Alzheimer's in a dish – induced pluripotent stem cell-based disease modeling. *Translational Neurodegeneration* **8**, 21 (2019). https://doi.org/10.1186/s40035-019-0161-0
317 Hernández-Sapiéns, M. A. *et al.* A Three-Dimensional Alzheimer's Disease Cell Culture Model Using iPSC-Derived Neurons Carrying A246E Mutation in PSEN1. *Frontiers in cellular neuroscience* **14**, 151 (2020). https://doi.org/10.3389/fncel.2020.00151
318 Cenini, G. *et al.* Dissecting Alzheimer's disease pathogenesis in human 2D and 3D models. *Molecular and Cellular Neuroscience* **110**, 103568 (2021). https://doi.org/10.1016/j.mcn.2020.103568
319 Gozal, E., Jagadapillai, R., Cai, J. & Barnes, G. N. Potential crosstalk between sonic hedgehog-WNT signaling and neurovascular molecules: Implications for blood–brain barrier integrity in autism spectrum disorder. *Journal of Neurochemistry* **159**, 15-28 (2021). https://doi.org/10.1111/jnc.15460
320 Xu, Y. *et al.* Understanding the role of tissue-specific decellularized spinal cord matrix hydrogel for neural stem/progenitor cell microenvironment reconstruction and spinal cord injury. *Biomaterials* **268**, 120596 (2021). https://doi.org/10.1016/j.biomaterials.2020.120596

321 Cho, A.-N. *et al.* Microfluidic device with brain extracellular matrix promotes structural and functional maturation of human brain organoids. *Nature Communications* **12**, 4730 (2021). https://doi.org/10.1038/s41467-021-24775-5
322 Choi, S. H. *et al.* A three-dimensional human neural cell culture model of Alzheimer's disease. *Nature* **515**, 274-278 (2014). https://doi.org/10.1038/nature13800
323 Leeuw, S. M. d. *et al.* Increased maturation of iPSC-derived neurons in a hydrogel-based 3D culture. *Journal of Neuroscience Methods* **360**, 109254 (2021). https://doi.org/10.1016/j.jneumeth.2021.109254
324 Donato, R. *et al.* Differential development of neuronal physiological responsiveness in two human neural stem cell lines. *BMC Neuroscience* **8**, 36-36 (2007). https://doi.org/10.1186/1471-2202-8-36
325 Meli, L. *et al.* Three dimensional cellular microarray platform for human neural stem cell differentiation and toxicology. *Stem cell research* **13**, 36-47 (2014). https://doi.org/10.1016/j.scr.2014.04.004
326 Arber, C. *et al.* Familial Alzheimer's disease patient-derived neurons reveal distinct mutation-specific effects on amyloid beta. *Molecular Psychiatry* **25**, 2919-2931 (2020). https://doi.org/10.1038/s41380-019-0410-8
327 Miller, Justine D. *et al.* Human iPSC-Based Modeling of Late-Onset Disease via Progerin-Induced Aging. *Cell Stem Cell* **13**, 691-705 (2013). https://doi.org/10.1016/j.stem.2013.11.006
328 Jang, H., Kim, S. H., Koh, Y. & Yoon, K.-J. Engineering Brain Organoids: Toward Mature Neural Circuitry with an Intact Cytoarchitecture. *International Journal of Stem Cells* **15**, 41-59 (2022). https://doi.org/10.15283/ijsc22004
329 Kwak, S. S. *et al.* Amyloid-β42/40 ratio drives tau pathology in 3D human neural cell culture models of Alzheimer's disease. *Nature Communications* **11**, 1377 (2020). https://doi.org/10.1038/s41467-020-15120-3
330 Wray, S. Modelling neurodegenerative disease using brain organoids. *Seminars in Cell & Developmental Biology* **111**, 60-66 (2020). https://doi.org/10.1016/j.semcdb.2020.05.012
331 Wang, Y., Wang, L., Guo, Y., Zhu, Y. & Qin, J. Engineering stem cell-derived 3D brain organoids in a perfusable organ-on-a-chip system. *RSC Advances* **8**, 1677-1685 (2018). https://doi.org/10.1039/c7ra11714k
332 Qian, X. *et al.* Generation of human brain region–specific organoids using a miniaturized spinning bioreactor. *Nature Protocols* **13**, 565-580 (2018). https://doi.org/10.1038/nprot.2017.152
333 Hernández, D. *et al.* Culture Variabilities of Human iPSC-Derived Cerebral Organoids Are a Major Issue for the Modelling of Phenotypes Observed in Alzheimer's Disease. *Stem Cell Reviews and Reports*, 1-14 (2021). https://doi.org/10.1007/s12015-021-10147-5
334 Potjewyd, G., Kellett, K. A. B. & Hooper, N. M. 3D hydrogel models of the neurovascular unit to investigate blood–brain barrier dysfunction. *Neuronal Signaling* **5**, NS20210027 (2021). https://doi.org/10.1042/ns20210027
335 Jorfi, M., D'Avanzo, C., Tanzi, R. E., Kim, D. Y. & Irimia, D. Human Neurospheroid Arrays for In Vitro Studies of Alzheimer's Disease. *Scientific Reports* **8**, 2450 (2018). https://doi.org/10.1038/s41598-018-20436-8

336 Miguel, L. *et al.* Detection of all adult Tau isoforms in a 3D culture model of iPSC-derived neurons. *Stem Cell Research* **40**, 101541 (2019). https://doi.org/10.1016/j.scr.2019.101541
337 Hughes, C. S., Postovit, L. M. & Lajoie, G. A. Matrigel: A complex protein mixture required for optimal growth of cell culture. *PROTEOMICS* **10**, 1886-1890 (2010). https://doi.org/10.1002/pmic.200900758
338 Koroleva, A. *et al.* In vitro development of human iPSC-derived functional neuronal networks on laser-fabricated 3D scaffolds. *ACS Applied Materials & Interfaces* **13**, 7839-7853 (2021).
339 Milovanović, A. *et al.* The effect of time on mechanical properties of biocompatible photopolymer resins used for fabrication of clear dental aligners. *Journal of the Mechanical Behavior of Biomedical Materials* **119**, 104494 (2021). https://doi.org/10.1016/j.jmbbm.2021.104494
340 Moxon, S. R. *et al.* Blended alginate/collagen hydrogels promote neurogenesis and neuronal maturation. *Materials Science and Engineering: C* **104**, 109904 (2019). https://doi.org/10.1016/j.msec.2019.109904
341 Madl, C. M. *et al.* Maintenance of neural progenitor cell stemness in 3D hydrogels requires matrix remodelling. *Nature Materials* **16**, 1233-1242 (2017). https://doi.org/10.1038/nmat5020
342 Madl, C. M., LeSavage, B. L., Dewi, R. E., Lampe, K. J. & Heilshorn, S. C. Matrix Remodeling Enhances the Differentiation Capacity of Neural Progenitor Cells in 3D Hydrogels. *Advanced Science* **6**, 1801716 (2019). https://doi.org/10.1002/advs.201801716
343 Levy, S. *et al.* The Diploid Genome Sequence of an Individual Human. *PLoS Biology* **5**, e254 (2007). https://doi.org/10.1371/journal.pbio.0050254
344 Woodruff, G. *et al.* The Presenilin-1 ΔE9 Mutation Results in Reduced γ-Secretase Activity, but Not Total Loss of PS1 Function, in Isogenic Human Stem Cells. *Cell Reports* **5**, 974-985 (2013). https://doi.org/10.1016/j.celrep.2013.10.018
345 Miyaoka, Y. *et al.* Isolation of single-base genome-edited human iPS cells without antibiotic selection. *Nature methods* **11**, 291-293 (2014). https://doi.org/10.1038/nmeth.2840
346 Young, J. E. *et al.* Stabilizing the Retromer Complex in a Human Stem Cell Model of Alzheimer's Disease Reduces TAU Phosphorylation Independently of Amyloid Precursor Protein. *Stem Cell Reports* **10**, 1046-1058 (2018). https://doi.org/10.1016/j.stemcr.2018.01.031
347 Frankowski, H. *et al.* Knock-Down of HDAC2 in Human Induced Pluripotent Stem Cell Derived Neurons Improves Neuronal Mitochondrial Dynamics, Neuronal Maturation and Reduces Amyloid Beta Peptides. *International Journal of Molecular Sciences* **22**, 2526 (2021). https://doi.org/10.3390/ijms22052526
348 Almenar-Queralt, A. *et al.* Chromatin establishes an immature version of neuronal protocadherin selection during the naive-to-primed conversion of pluripotent stem cells. *Nature genetics* **51**, 1691-1701 (2019). https://doi.org/10.1038/s41588-019-0526-4
349 Williams, L. M. *et al.* Prolonged culturing of iPSC-derived brain endothelial-like cells is associated with quiescence, downregulation of glycolysis, and resistance to disruption by an Alzheimer's brain milieu. *Fluids and Barriers of the CNS* **19**, 10 (2022). https://doi.org/10.1186/s12987-022-00307-1

350 Bustin, S. A. *et al.* MIQE 2.0: Revision of the Minimum Information for Publication of Quantitative Real-Time PCR Experiments Guidelines. *Clinical Chemistry*, hvaf043 (2025).
351 Fandos, N. *et al.* Plasma amyloid β 42/40 ratios as biomarkers for amyloid β cerebral deposition in cognitively normal individuals. *Alzheimer's & Dementia: Diagnosis, Assessment & Disease Monitoring* **8**, 179-187 (2017).
352 Hansson, O., Lehmann, S., Otto, M., Zetterberg, H. & Lewczuk, P. Advantages and disadvantages of the use of the CSF Amyloid β (Aβ) 42/40 ratio in the diagnosis of Alzheimer's Disease. *Alzheimer's research & therapy* **11**, 1-15 (2019).